POLITECNICO
MILANO 1863

Politecnico di Milano
Deparment of Energy
Doctoral Programme in
Energy and Nuclear Science and Technology

Hydrogen-treated titanium dioxide hierarchical nanostructures for water splitting applications

Doctoral Dissertation of:
Luca Mascaretti

Supervisors:
Prof. Andrea Li Bassi
Prof. Carlo S. Casari

Tutor:
Prof. Matteo Passoni

The Chair of the Doctoral Programme:
Prof. Carlo E. Bottani

Year 2017 - Cycle XXX

Abstract

THIS thesis work presents a thorough experimental development and investigation on TiO_2 nanostructured thin films with controlled properties for their applications as photoanode materials for photoelectrochemical (PEC) water splitting applications.

TiO_2 is a well-known photoanode material, but its unsatisfactory efficiency has triggered extensive research aiming at overcoming its intrinsic limitations. For instance, the combination of a vertically oriented nanostructured morphology with hydrogenation or reduction of TiO_2, leading to the so-called *black titania* nanomaterials, or with noble metal nanoparticles, exhibiting plasmonic effects, is a promising strategy to improve the material photoactivity. However, a detailed comprehension of the underlying physical-chemical mechanisms, often related to the complex defect chemistry of TiO_2 and to the peculiar experimental strategy, is still challenging.

In this work, an experimental investigation devoted to the control and optimization of TiO_2 functional properties is presented. First, TiO_2 hierarchical nanostructures are prepared by Pulsed Laser Deposition (PLD) employing oxygen-poor conditions both in the deposition step and in the post-annealing one. The control of the synthesis strategy enables a fine tuning of the material properties, as shown by morphological, structural and optical characterizations, which in turn strongly affect the photoelectrochemical properties of TiO_2 photoanodes. Second, a further strategy, concerning the synthesis of Au nanoparticles and their integration with TiO_2 hierarchical nanostructures with an all physical vapor deposition approach, is also developed, showing how PLD allows the simultaneous growth of a composite Au-TiO_2 film with controlled plasmonic properties.

The results presented in this thesis can provide valuable insights into the possibility to tune the photoactivity of semiconductor materials, for water splitting or other solar energy conversion applications, by controlling their properties at the meso- and nanoscale and their defect concentration.

Sommario

IL presente elaborato di tesi riporta un dettagliato studio sperimentale riguardante film nanostrutturati di TiO_2 con proprietà controllate per la loro applicazione come fotoanodi in esperimenti di fotoelettrolisi dell'acqua.

Il TiO_2 è un materiale ben noto come fotoanodo, ma la sua efficienza ancora inadeguata ha innescato numerose ricerche per ovviare ai suoi limiti intrinseci. Una strategia promettente per aumentarne la fotoattività consiste, ad esempio, nel combinare una morfologia nanostrutturata a orientazione verticale con l'idrogenazione o riduzione del TiO_2, ottenendo nanomateriali di "*black titania*", o con nanoparticelle di metalli nobili dotate di proprietà plasmoniche. Non è ancora stata ottenuta, tuttavia, un'accurata comprensione dei fenomeni fisico-chimici sottostanti, spesso legati alla complessa chimica dei difetti del TiO_2 e al particolare metodo sperimentale adottato.

In questo lavoro viene presentata una analisi sperimentale riguardante il controllo e l'ottimizzazione delle proprietà funzionali del TiO_2. In primo luogo, nanostrutture gerarchiche di TiO_2 sono state preparate con la deposizione laser pulsata (PLD) utilizzando condizioni a basso contenuto di ossigeno sia in fase di deposizione, sia nei trattamenti termici successivi, per ottenere l'idrogenazione o la riduzione del materiale. Il controllo della strategia di sintesi permette l'ottimizzazione delle proprietà del materiale, come mostrato da caratterizzazioni morfologiche, strutturali e ottiche; tali proprietà, a loro volta, influenzano fortemente le proprietà fotoelettrochimiche dei fotoanodi di TiO_2. In secondo luogo, è stata sviluppata una ulteriore strategia riguardante la sintesi di nanoparticelle di Au e la loro integrazione con le nanostrutture gerarchiche di TiO_2 con un approccio completamente da fase vapore, illustrando come la PLD permetta la crescita simultanea di un film composito di entrambi i materiali con proprietà plasmoniche controllate.

I risultati presentati in questa tesi forniscono informazioni riguardo la possibilità di controllare la fotoattività di materiali semiconduttori, per la fotoelettrolisi dell'acqua e altre applicazioni di conversione dell'energia solare,

tramite la padronanza delle loro proprietà alla scala mesoscopica e nanometrica e della loro concentrazione di difetti.

Contents

Introduction

> We're running the most dangerous experiment in history right now, which is to see how much carbon dioxide the atmosphere can handle before there is an environmental catastrophe.
>
> *Elon Musk*

SOLAR energy is essential for any living being: some of them, called *autotrophs* (plants, algae and many bacteria), are able to directly make use of it, starting from simple substances in the surroundings, to produce complex organic compounds; some others, called *heterotrophs* (animals, fungi and many other bacteria), ingest or absorb these organic compounds in order to produce energy and synthesize other organic compounds for themselves. As long as the evolution on Earth has gone on, more complex species, able to use a greater and greater amount of energy, have appeared; this process has culminated with humans, who eventually have learned to use energy for different purposes than their own survival: *Homo erectus* learned how to control fire more than 500 thousand years ago by burning wood and *Homo sapiens* further developed the use of fire for cooking, heating, manufacturing. For millennia, the energy consumption by humans did not substantially change, but after the Industrial Revolution it dramatically escalated in the blink of an eye from the evolutionary point of view, exploiting deposits of organic energy that had been accumulating for millions of years in the form of coal, oil and natural gas.

Today, the rapid decrease of fossil fuel natural reserves and the alarming levels of greenhouse gas emissions are two tough challenges which humanity must solve as soon as possible. Renewable energy sources (such as solar, wind, hydropower, etc.) have already been taken into account and some options have reached a mature stage of technological development, while other ones are still being developed with intense research efforts. Nonetheless, they still account for a minority of the total energy production. Moreover, energy should be both produced and consumed in a renewable way, which is particularly important in the context of fuels.

Speaking of energy carriers, hydrogen is a promising option for two fundamental reasons: it can be obtained from water, by means of the well-known electrolysis (in which the H_2O molecule is split into H_2 and O_2), and its combustion leads back to water (in the form of vapor); the electrical energy required for electrolysis is typically supplied by non-renewable sources, but if solar energy could be exploited for that purpose, then hydrogen would be really a renewable fuel. One of the first reports describing this possibility was published in 1972 by Fujishima and Honda, who found that an electrochemical cell made of a platinum cathode and an anode made of a semiconductor material, titanium dioxide (TiO_2), instead of metal, was able to split water into hydrogen and oxygen with UV illumination. This process is called *photoelectrochemical water splitting* and it is possible thanks to the action of the semiconductor material, which absorbs the solar energy from light and promotes the water splitting reaction; however, it was quite inefficient for several reasons, mostly due to material limitations.

Forty-five years later, the search for an efficient, inexpensive and stable semiconductor material able to bring the water splitting process to the large scale has not been concluded yet. TiO_2 is still one of the most investigated materials thanks to its chemical stability and relatively low cost, but several efforts are being carried out to address its limitations, i.e. to increase its light absorption (it only absorbs UV light) and its overall efficiency (which is lowered by charge recombination).

A strategy recently proposed in the literature consists in the hydrogenation or reduction of TiO_2, for instance by thermal treatments in the presence of H_2, which results in a higher light absorption (its color, from white, turns to grey or even black) and increased photoactivity. These outcomes, however, are not completely understood at present as they strongly depend on the experimental process and on the starting material properties.

Among the properties of materials for energy-related applications, the morphological ones are crucial and this concept is one of the basis of nanotechnology, in which structural, optical, electrical, catalytic properties of TiO_2 (and of course many other materials) can be tuned by controlling its organization at the nanoscale. For instance, nanostructured quasi-one dimensional forms of TiO_2 (such as nanowires, nanotubes and the so-called “tree-like” hierarchical nanostructures, discussed in this thesis) have shown promising results in energy-related applications, including water splitting, attributed to their preferential charge transport along the growth direction.

As a consequence, the realization of novel nanostructured forms of TiO_2

with an increased light absorption or photoactivity (ensured by a hydrogenation/reduction process) could lead to interesting results in the context of photoanodes for water splitting applications. An additional approach devoted to the enhancement of light absorption and photoactivity, on the other hand, consists in combining TiO_2 with nanoparticles made of noble metals (such as gold or silver), which exhibit a peculiar absorption in the visible region of the electromagnetic spectrum, called *localized plasmonic resonance*, which may lead to a better exploitation of the solar energy.

In this context, the main subject of this work is the study and development of hydrogen-treated TiO_2 hierarchically structured materials as photoanodes for solar water splitting applications. This purpose is addressed by experimentally investigating the structure/property relations in TiO_2 thin films by means of Pulsed Laser Deposition (PLD) as synthesis technique and thermal treatments in oxidizing or reducing atmospheres; in addition, photocurrent testing of the obtained films is performed as an effective validation tool in light of the desired application. A different approach also discussed in this work is the introduction of noble metal nanoparticles in TiO_2 thin films, which consists in a further development towards the direction of integrated noble metal-TiO_2 photoanodes. These research activities are reported in the present doctoral dissertation as follows.

Chapter 1 – Photoelectrochemical water splitting: the basic concepts underlying this technology are introduced, with a description of the semiconductor/electrolyte junction and its energetics, the most common definitions of efficiency and the most relevant material requirements.

Chapter 2 – Titanium dioxide for water splitting applications: the fundamental and the functional properties of TiO_2, which allow its application in energy conversion processes, are described, together with the strategies proposed in literature to overcome them; more emphasis is given to those pertaining this thesis work; finally, some important aspects of the defect chemistry of TiO_2, especially in the reduced form, are highlighted.

Chapter 3 – Thesis goals and methods: after the overview on the scientific framework of this thesis work, the specific objectives are explained, followed by the experimental methods employed to achieve them; in particular, a synthetic description of the synthesis technique, i.e. Pulsed Laser Deposition (PLD), is presented.

Chapter 4 – Hydrogen treatments of TiO_2 hierarchical nanostructures: this chapter describes the experimental investigation on hydrogen-treated TiO_2 hierarchical films, in which the hydrogenation/reduction process was addressed both exploiting the deposition conditions as well as the thermal treatments.

Chapter 5 – Tuning the photoelectrochemical properties of TiO_2 hierarchical nanostructures: due to the promising results obtained with the strategy presented in Chapter 4, a deeper investigation aiming at optimizing the performance of TiO_2 nanostructured films is presented, in which the deposition and post-annealing conditions have been extensively studied, finding clear trends in the photoelectrochemical properties of the obtained photoanodes.

Chapter 6 – Photoluminescence properties of annealed TiO_2 hierarchical nanostructures: this chapter reports a further development on the study of reduced TiO_2 nanomaterials, in which the role of defects introduced by the synthesis conditions in determining their photoactivity was addressed by means of photoluminescence spectroscopy.

Chapter 7 – Integration of TiO_2 hierarchical films with plasmonic Au nanoparticles: after a thorough investigation on reduced TiO_2 nanostructured materials, another research strategy was developed (with the aim of fully addressing it in other works beyond this Ph.D. thesis) related to the combination of TiO_2 with gold nanoparticles exhibiting plasmonic effects, with the possibility of extending the photoactivity of this material towards the visible range. This was pursued by employing Pulsed Laser Deposition as a synthesis technique for both materials, as conveniently explained in the chapter.

Chapter 8 – Conclusions and perspectives: this chapter summarizes the main findings of this Ph.D. thesis and presents some possible future developments which may be explored in other research works.

The original contents of this Ph.D. thesis have actively contributed to the publication of the following peer-reviewed papers, ordered by year:

- Mascaretti, L.; Ferrulli, S.; Mazzolini, P.; Casari, C. S.; Russo, V.; Matarrese, R.; Nova, I.; Terraneo, G.; Liu, N.; Schmuki, P.; Li Bassi, A. “Hydrogen-treated hierarchical titanium oxide nanostructures for photoelectrochemical water splitting” *Sol. Energy Mater. Sol. Cells* **2017**, *169*, 19–27 (with data from Chapter 4);
- Mascaretti, L.; Matarrese, R.; Ravanelli, A.; Isacchi, M.; Mazzolini, P.; Casari, C. S.; Russo, V.; Nova, I.; Terraneo, G.; Ducati, C.; Li Bassi, A. “Tuning the photoelectrochemical properties of hierarchical TiO_2 nanostructures by control of pulsed laser deposition and annealing in reducing conditions” *Int. J. Hydrogen Energ.* **2017**, *42*, 26639–26651 (with data from Chapter 5);
- Ghidelli, M.; Mascaretti, L.; Bricchi, B. R.; Zapelli, A.; Russo, V.; Casari, C. S.; Li Bassi, A. “Engineering plasmonic nanostructured surfaces by

pulsed laser deposition" *Appl. Surf. Sci.* **2018**, *434*, 1064–1073 (with data from Section 7.2 with further investigations).

In addition, the results achieved in this thesis work were also presented in several international conferences, presented by myself:

- EMRS2015 Spring Meeting (Lille, France, May 2015); poster contribution: "Hierarchical TiO_2 nanostructures for photoelectrochemical hydrogen production";
- CIMTEC2016 (Perugia, Italy, June 2016); oral contribution: "Quasi-1D hydrogen-treated titanium oxide nanostructures for water splitting applications".
- MRS2017 Spring Meeting (Phoenix, USA, April 2017); poster contribution: "Hierarchical TiO_2-based nanostructures for photoelectrochemical water splitting";
- EMRS2017 Spring Meeting (Strasbourg, France, May 2017); oral contribution: "Hydrogen-treated TiO_2 hierarchical nanostructured films for photoelectrochemical water splitting";

as well as presented by colleagues:

- MRS2016 Spring Meeting (Phoenix, USA, March 2016); poster contribution: "Quasi-1D hydrogen-treated titanium oxide nanostructures for photoelectrochemical water splitting", by A. Li Bassi;
- 9th ICEC2016 (Newcastle, Australia, July 2016); poster contribution: "Quasi-1D black titanium oxide nanostructures for photoelectrochemical water splitting", by R. Matarrese;
- EMRS2017 Spring Meeting (Strasbourg, France, May 2017); oral contribution: "Integration of hierarchical TiO_2 nanostructures with Au plasmonic nanoparticles for photocatalysis applications", by M. Ghidelli;
- NAM25 (Denver, USA, June 2017); poster contribution: "Efficient Black TiO_2 nanostructured photoandes prepared by PLD for photoelectrochemical (PEC) water splitting", by R. Matarrese;
- NAM25 (Denver, USA, June 2017); poster contribution: "Hierarchical TiO_2-based nanostructures prepared by PLD for photoelectrochemical (PEC) water splitting", by R. Matarrese;
- MRS2017 Fall Meeting (Boston, USA, November 2017); oral contribution: "Synthesis and optical properties of plasmonic-metal nanostructures by pulsed laser deposition", by M. Ghidelli.

1

Photoelectrochemical water splitting

This chapter introduces the fundamental aspects of solar water splitting and their relationship with semiconductor materials employed for the extended (but still unfinished) researches on them. First, Section 1.1 illustrates the interest in hydrogen as a green fuel for human activities. The essentials on the water splitting reactions are subsequently described in Section 1.2, while a more detailed description of the photoelectrochemical cell is discussed in Section 1.3. Some important definitions of efficiency are illustrated in Section 1.4, clarifying which was employed in this thesis work. Finally, the material requirements for the realization of efficient photoanodes are described in Section 1.5, with a special attention to the bandgap and introducing the advantages of nanostructured materials (which will be discussed in detail in Chapter 2 for the case of titanium dioxide, TiO_2).

1.1 Hydrogen as solar fuel

The need of renewable energy resources and production methods is becoming increasingly urgent due to the alarming prospects of climate change, which is widely accepted in the scientific community as strongly related to anthropogenic emissions of greenhouse gases, such as carbon dioxide (CO_2). To make matters worse, the energy demand is rising, contributing to the increase of atmospheric CO_2 concentrations and depleting the fossil fuel resources, which currently account for the majority of it[1].

Among the several renewable sources of energy, solar energy is particularly desirable as it is decentralized, inexhaustible and, euphemistically, abundant: the Sun deposits 120000 TW of radiation on the surface of Earth, far exceeding current and future human needs[2]; for instance, the International Energy Agency estimated for the year 2015 a total primary energy supply (closely related to the total energy consumption) of 18 TW[3]. However, due to the daily and seasonal variability of sunlight, solar energy cannot be exploited continuously; in order to address this issue, energy harvested from the sun can be, for instance, converted into chemical fuels, which can be stored, transported and converted back into energy when needed[4].

Hydrogen (H_2) has been identified as one promising clean fuel, as its utilization leads only to water vapor and the energy yield of hydrogen is about 122 kJ/g, almost three times greater than hydrocarbon fuels. However, it is unavailable in nature, as it is combined with other elements in water and many organic compounds (e.g. hydrocarbons), and its production process is costly[1].

Table 1.1 summarizes various hydrogen production techniques available at present, including their feedstock use and efficiency[1]. Hydrogen is mainly produced from non-renewable sources, such as coal, oil and natural gas. The typical process to do so is the so-called *steam reforming* reaction, as shown in Equation (1.1), in which high-temperature steam (700-1000°C) is used to produce hydrogen from methane source (e.g. natural gas); this reaction is endothermic and produces CO and H_2. Subsequently, CO and steam at high temperature react exothermically via the so-called *water-gas shift* reaction (Equation (1.2)) producing additional H_2 and CO_2.

$$\mathrm{CH_4 + H_2O \rightleftharpoons CO + 3\,H_2} \qquad \Delta H_\mathrm{f}^\circ = 206\,\mathrm{kJ/mol} \quad (1.1)$$

$$\mathrm{CO + H_2O \rightleftharpoons CO_2 + H_2} \qquad \Delta H_\mathrm{f}^\circ = -41\,\mathrm{kJ/mol} \quad (1.2)$$

On the other hand, hydrogen can also be obtained from renewable sources, such as biomass, wind energy, geothermal energy and, importantly, solar energy. The latter is particularly interesting due to the abundance of solar energy (as mentioned above) and the possibility to avoid greenhouse gas emissions; indeed, this can be achieved by decomposition of water through the overall mechanism

$$\mathrm{H_2O}\,(l) \rightleftharpoons \frac{1}{2}\,\mathrm{O_2}\,(g) + \mathrm{H_2}\,(g) \qquad \Delta G_\mathrm{f}^\circ = 237\,\mathrm{kJ/mol} \quad (1.3)$$

In the standard water *electrolysis*, the energy required for this reaction is supplied by electricity, which anyway involves greenhouse gas emission if it is produced by fossil fuel combustion. In order to completely avoid CO_2 emission, solar radiation must supply this energy and in this case the process

Table 1.1: Overwiev of the hydrogen production technologies[1].

Technology	Feedstock	Efficiency	Maturity
Steam reforming	Hydrocarbons	70-85%	Commercial
Auto-thermal reforming	Hydrocarbons	60-75%	Near term
Biomass gasification	Biomass	35-50%	Commercial
Electrolysis	H_2O+electricity	50-70%	Commercial
Photolysis	H_2O+sunlight	0.5%	Long term
Thermochemical water splitting	H_2O+heat	N.A.	Long term

is called *photo(electro)lysis* of water, *solar water splitting* or also *photocatalytic/photoelectrochemical water splitting*. The precise term is related to the approach employed; in all cases, in order for solar energy to drive the water splitting reaction, a semiconductor material must be present, which absorbs solar energy and delivers it to water, promoting its decomposition. In the case of photocatalytic water splitting, both oxygen and hydrogen (the products of Equation (1.3)) evolve at the surface of the semiconductor material, which is referred to as *photocatalyst*; in the case of photoelectrochemical (PEC) water splitting, they are produced at separate electrodes. The spatial separation of evolved O_2 and H_2 gases is an advantage of the PEC architecture, which, on the other hand, is more complex than the photocatalytic one. One of the first reports concerning solar water splitting came from Fujishima and Honda in 1972[5] using titanium dioxide (TiO_2) as a semiconductor material in a photoelectrochemical arrangement[a]. From that time, a huge amount of research has been carried out to obtain a light-driven stable and efficient water splitting system; this goal, however, remains elusive basically due to conflicting material requirements, as will be clarified in the following sections. Thus, hydrogen generation from solar energy at the industrial or commercial scale will be determined by the progress in materials science and engineering applied to candidate semiconductor materials for photocatalysts or photoelectrodes[7].

1.2 Water splitting reaction mechanism

The essential “ingredient” for water splitting is a semiconductor material, which exhibits a band structure with a clear distinction between the occupied states (valence band, VB) and the unoccupied states (conduction band, CB), separated by the so-called *bandgap (E_g)*, in which no available states are found. In addition, a semiconductor is able to conduct electricity, and if this happens by means of negative charge carriers, the electrons, it is an n-type semiconductor, while if it happens by means of positive charge carriers, the holes, it is a p-type semiconductor. The Fermi level, E_F, is the chemical potential of electrons[8] and in n-type semiconductors it lies in the bandgap close to the conduction band edge.

A semiconductor material absorbs photons having energy higher than its bandgap; upon light absorption, electrons (e^-) in the valence band are excited to the conduction bands, leaving holes (h^+) in the valence band; thus, the photogeneration of electron/hole pairs can be described by the reaction

---

[a] This paper is extremely well-known in the scientific community of water splitting, even though it has been criticized for different ambiguous descriptions, such as those related to the experimental conditions[6].

$$2\,h\nu \longrightarrow 2\,e^- + 2\,h^+ \tag{1.4}$$

where h is the Planck's constant and ν is the photon frequency. After photoexcitation, if no recombination (either radiative or non-radiative) occurs, holes oxidize water, which consists in the so-called anodic water oxidation half-reaction or *oxygen evolution reaction* (OER), while electrons react with H^+ ions in solution, which is the cathodic H^+ reduction half-reaction or *hydrogen evolution reaction* (HER). These two reactions are written below in Equations (1.5) and (1.6), respectively, both in acidic conditions (pH = 0), and the overall water splitting reaction (already seen in Equation (1.3)) can be obtained as a simple redox reaction involving the two former ones, as shown in Equation (1.7):

$$H_2O + 2\,h^+ \rightleftharpoons 2\,H^+ + \frac{1}{2}\,O_2(g) \qquad E^\circ_{\text{ox,an}} = -1.229 \text{ V vs. SHE} \tag{1.5}$$

$$2\,H^+ + 2\,e^- \rightleftharpoons H_2(g) \qquad E^\circ_{\text{red,cat}} = 0 \text{ V vs. SHE} \tag{1.6}$$

$$H_2O \rightleftharpoons \frac{1}{2}\,O_2(g) + H_2(g) \qquad \Delta E^\circ = E^\circ_{\text{red,cat}} + E^\circ_{\text{ox,an}} \approx -1.23 \text{ V} \tag{1.7}$$

In these reactions, $E^\circ_{\text{ox,an}}$ is the electrode potential for the anodic reaction (the OER), which takes the negative sign as the OER in Equation (1.5) is written in the oxidation direction, and $E^\circ_{\text{red,cat}}$ is the electrode potential for the cathodic reaction; they are both given relative to the standard hydrogen electrode (SHE), which by definition has 0 potential and it is related to the energy scale through the so-called absolute potential, which is 4.44 ± 0.02 V at 25°C, so that its energy is −4.44 eV with respect to the vacuum level[9]. In Equation (1.7), instead, ΔE° is the cell potential or electrochemical cell voltage, which takes the negative sign, meaning that the reaction is not spontaneous (evidently). The OER and HER reactions are usually tabulated in standard electrode potential tables in the direction of reduction, i.e. in terms of O_2/H_2O and H^+/H_2 redox couples,

$$2\,H^+ + \frac{1}{2}\,O_2(g) \rightleftharpoons H_2O + 2\,h^+ \qquad E^\circ_{\text{red},O_2/H_2O} = +1.229 \text{ V vs. SHE} \tag{1.8}$$

$$2\,H^+ + 2\,e^- \rightleftharpoons H_2(g) \qquad E^\circ_{\text{red},H^+/H_2} = 0 \text{ V vs. SHE} \tag{1.9}$$

which are also written at pH = 0 and in which E° is the standard electrode potential[b]. In alkaline electrolyte (pH = 14), Equations (1.8) and (1.9) become

---

[b] The standard electrode potential is given relative to the standard hydrogen electrode (SHE) at the temperature of of 25°C (298.15 K), effective concentration of 1 mol/L, partial pressure of 1 atm (101325 Pa), activity of unity and for one electron transfer (regardless the stoichiometric coefficient in the reaction).

$$H_2O + \frac{1}{2}\,O_2(g) \rightleftharpoons 2\,OH^- + 2\,h^+ \qquad E_{\mathrm{red},O_2/H_2O} = +0.401 \text{ V vs. SHE} \quad (1.10)$$

$$2\,H_2O + 2\,e^- \rightleftharpoons H_2(g) + 2\,OH^- \qquad E_{\mathrm{red},H^+/H_2} = -0.828 \text{ V vs. SHE} \quad (1.11)$$

where their standard potential values are shifted with pH according to the Nernst equation, which can be written in a simple form as $E = E^\circ - 0.059 \cdot \mathrm{pH}$. In this context, it can be useful to refer to the reversible hydrogen electrode (RHE), which is a common and practical reference electrode showing the same pH dependence, so that the O_2/H_2O and H^+/H_2 standar potential values are 1.23 V and 0 V vs. RHE at any pH, respectively. In all cases, the electrochemical cell voltage $\Delta E^\circ = -1.23$ V (Equation (1.7)) remains unchanged; this important quantity is the minimum voltage which must be supplied for the water splitting reaction, $V^\circ_{rev} = 1.23$ V, corresponding to the minimum theoretical bandgap energy of the semiconductor material, $E_g = 1.23$ eV. The quantity ΔE° is related to the free energy of formation seen in Equation (1.3) through the relation

$$\Delta G^\circ_{\mathrm{f}} = -nF\Delta E^\circ \qquad (1.12)$$

where $n = 2$ is the number of electrons transferred in the reaction and $F = 96485$ C/mol is the Faraday constant. It should be noted that the OER and HER reactions are more complex than how emerges from Equations (1.5) and (1.6); indeed, Table 1.2 reports a more detailed description of the individual steps.

The main difference between photocatalytic and photoelectrochemical water splitting depends on the location in which the OER and HER occur, as illustrated by Figure 1.1. In the photocatalytic case (Figure 1.1A), both reactions take place at the semiconductor interface with the electrolyte; in the photoelectrochemical case, they do not: the OER can occur at the surface of an n-type semiconductor, called *photoanode*, and the HER at a metal cathode (Figure 1.1B); conversely, the HER can occur at the surface of a p-type semiconductor, called *photocathode*, and the OER at a metal anode (Figure 1.1C). Figure 1.1, in addition, suggests in a schematic way another important aspect of water splitting: the conduction band minimum (CBM or E_c) must be more negative in the electrochemical scale (more positive in the energy scale) than the HER standard potential, while the valence band maximum (VBM or E_v) must be more positive in the electrochemical scale (more negative in the energy scale) than the OER standard potential. In other words, the band edges must straddle the water reduction and oxidation potentials.

It is important to note that the minimum required voltage of 1.23 V is not the *actual* voltage necessary for the water splitting reaction to occur; indeed, thermodynamic losses[11] (about 0.3–0.4 V) and overpotentials required to

Table 1.2: Elementary reactions involved in water splitting promoted by a photoanode[10].

Reaction	Process description
$H_2O_{(l)} \longrightarrow H_2O^*_{(ads)}$	Adsorption of water molecules on surface active centers, resulting in the formation of catalytically active complexes.
$H_2O^*_{(ads)} \longrightarrow OH^-_{(ads)} + H^*_{(ads)}$	Dissociation of water molecules on the surface of photoanode.
$h\nu \longrightarrow \{e^- + h^+\}_s$	Light-induced formation of electron/hole pair through ionization over bandgap of a semiconductor photoelectrode near the surface.
$\{e^- + h^+\}_s \longrightarrow h_s^+ + e_b^-$	Separation of light-induced charges, formed near the surface, leading to transfer of holes toward the surface and electrons toward the bulk.
$OH^-_{(ads)} + h^+ \longrightarrow O^-_{(ads)} + H^+_{(ads)}$	Reaction of OH^- radicals with holes leading to the formation of O^- chemisorbed species and hydrogen ions.
$O^-_{(ads)} + h^+ \longrightarrow O^*_{(ads)}$	Reaction between the surface O^- species and holes resulting in the formation of atomic oxygen radicals.
$O^*_{(ads)} \longrightarrow O^*_{(gas)} \longrightarrow \frac{1}{2}\,O_{2\,(gas)}$	Desorption of oxygen radicals and their subsequent association leading to the formation of gaseous oxygen.
$H^+_{(ads)} + H_2O \longrightarrow \{H_3O^+\}_a$	Formation of hydronium ions in the vicinity of the anode.
$(e_b^-)_a \longrightarrow (e_s^-)_c$	Transfer of electrons from the bulk of photoanode to the surface of cathode over external circuit.
$\{H_3O^+\}_a \longrightarrow \{H_3O^+\}_c$	Migration of hydronium ions from the vicinity of the photoanode to the vicinity of cathode.
$\{H_3O^+\}_c \longrightarrow \{H^+_{(ads)}\}_c + H_2O$	Adsorption of hydrogen ions on the surface of cathode.
$\{H^+_{(ads)}\}_c + e^- \longrightarrow \{H^*_{(ads)}\}_c$	Reaction between adsorbed hydrogen ions and electrons leading to the formation of hydrogen radicals in the vicinity of cathode.
$H^*_{(ads)} \longrightarrow (H_l^*)_c$	Transfer of hydrogen radicals from the adsorbed layer to the electrolyte in the vicinity of cathode.
$2\,(H_l^*)_c \longrightarrow H_{2\,(gas)}$	Association of hydrogen radicals leading to the formation of gaseous hydrogen molecules.

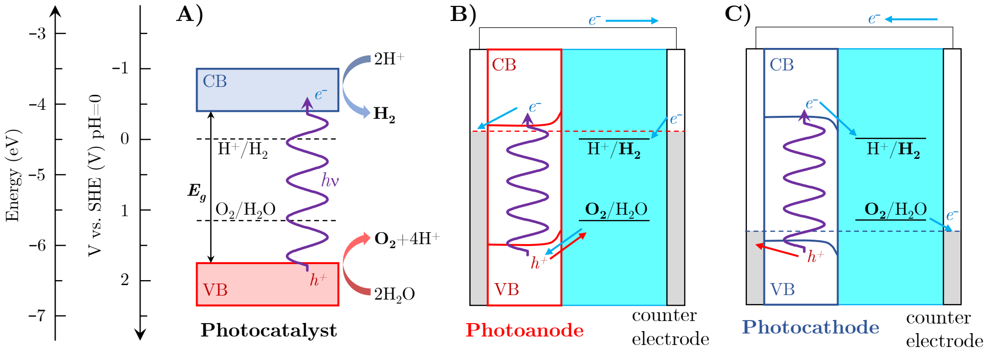

Figure 1.1: Energy diagrams of photocatalytic water splitting **(A)** and photoelectrochemical water splitting using a photoanode **(B)** or a photocathode **(C)**.

ensure sufficiently fast reaction kinetics[12] (about 0.4–0.6 V) raise this value at about 1.9–2.2 V. For instance, the OER at the anode is a quite complex reaction and it implies an overpotential loss (η_a) higher than that related to the HER (η_c). On the other hand, overpotential losses due to ionic conductivity in the solution can also be relevant; indeed, pure water has a ionic conductivity lower than 0.05 S/m, so that weak acid or alkaline solutions with conductivities higher than 10 S/m are typically employed[13]. This means that the minimum bandgap of the semiconductor material must be around 1.9–2.2 eV.

1.3 The photoelectrochemical cell

In this section, the principles of PEC water splitting involving an n-type semiconductor material (i.e. photoanode) will be considered due to the relevance with this thesis work. A huge amount of literature regarding the working principles of water splitting is available at present and an extended discussion is clearly beyond the scope of this section, which is written taking into account in particular Refs. [7, 13, 14].

1.3.1 Semiconductor/electrolyte junction (band diagram)

The description of the semiconductor/electrolyte junction, the charge transfer processes and the resulting band diagram is more complex than how emerging from the simple picture presented in Figure 1.1. The model of the semiconductor/liquid interface was developed by Gerischer starting from 1960 (as reviewed more recently in [15]) by means of a statistical equilibrium model, in which the important connection between the electrochemical potentials of electrons in solution and the Fermi levels in the solid state was made. This statistical description was also employed by Kumar *et al.*[16] in comparison with experimental results on a $SrTiO_3$ photoanode; Salvador[17] further developed this approach by introducing a nonequilibrium thermodynamical description. Finally, in recent years some numerical studies have also been performed[18,19] to determine the band diagram of a PEC cell and to simulate the current-voltage response. In the following, for the sake of simplicity, only the main energetic features of a PEC cell will be discussed, following the scheme illustrated in Figure 1.2.

(a) Before contact (Figure 1.2A). An n-type semiconductor material, connected to a metal back-contact[c] (photoanode), is immersed into an electrolyte, together with the counter electrode (cathode). Before contact, the Fermi level in the photoanode is $E_F = eU_{fb}$, where U_{fb} is the so-called *flatband potential* (see Section 1.3.2).

(b) After contact (Figure 1.2B). When the semiconductor is brought into contact with an electrolyte containing a redox couple, electrons flow from the former to the latter until equilibrium is established, according to the relation[20]

$$E_F = \bar{\mu}_{e,redox} \tag{1.13}$$

where $\bar{\mu}_{e,redox}$ is the electrochemical potential of electrons. For a PEC cell, the redox couples of interest are the H^+/H_2 couple for a p-type semiconductor and the O_2/H_2O couple for an n-type semiconductor[4]. Thus, in Figure 1.2B the Fermi level of the semiconductor is matched with E_{O_2/H_2O}[d]. The electron transfer from the semiconductor to the electrolyte exposes positively charged fixed donor sites, while in the electrolyte negatively charged ions accumulate at the semiconductor surface. The positively charged region in the semiconductor is referred to as *space charge layer* (SCL, with width W_{SC}); in the liquid, instead, all ions in solution are surrounded by a solvation cloud of water molecules, preventing them from approaching the first few Å of the surface; this thin region is called *Helmoltz layer* (with width W_H). An electric built-in field forms between the positive and negative charges; this charge separation in turn originates a potential barrier, which eventually reaches the value ϕ_{SC} and a dynamic equilibrium establishes (in accordance with Equation (1.13)). The potential barrier ϕ_{SC} is referred to as *band bending*[e], due to the drop in electric field strength in the solid, which can effectively

---

[c] The formation of a Schottky rather than an Ohmic contact between the semiconductor and the back-contact is not discussed here, even if it should be taken into consideration for the realization of a photoanode (or photocathode).

[d] In some cases, it is reported that the semiconductor Fermi level must be equal to the solution Fermi level, which coincides with its the electrochemical potential and is in between the redox potentials of the OER and HER[13]. To the best of this author's knowledge, this detail is not fully clarified in the literature.

[e] This situation is completely comparable to the semiconductor/metal Schottky junction and it is assumed that the band edges values at the interface are "pinned" (i.e. $E_{v,s}$ and $E_{c,s}$ do not change); a different situation, called "Fermi level pinning", can occur in the presence of surface states[21].

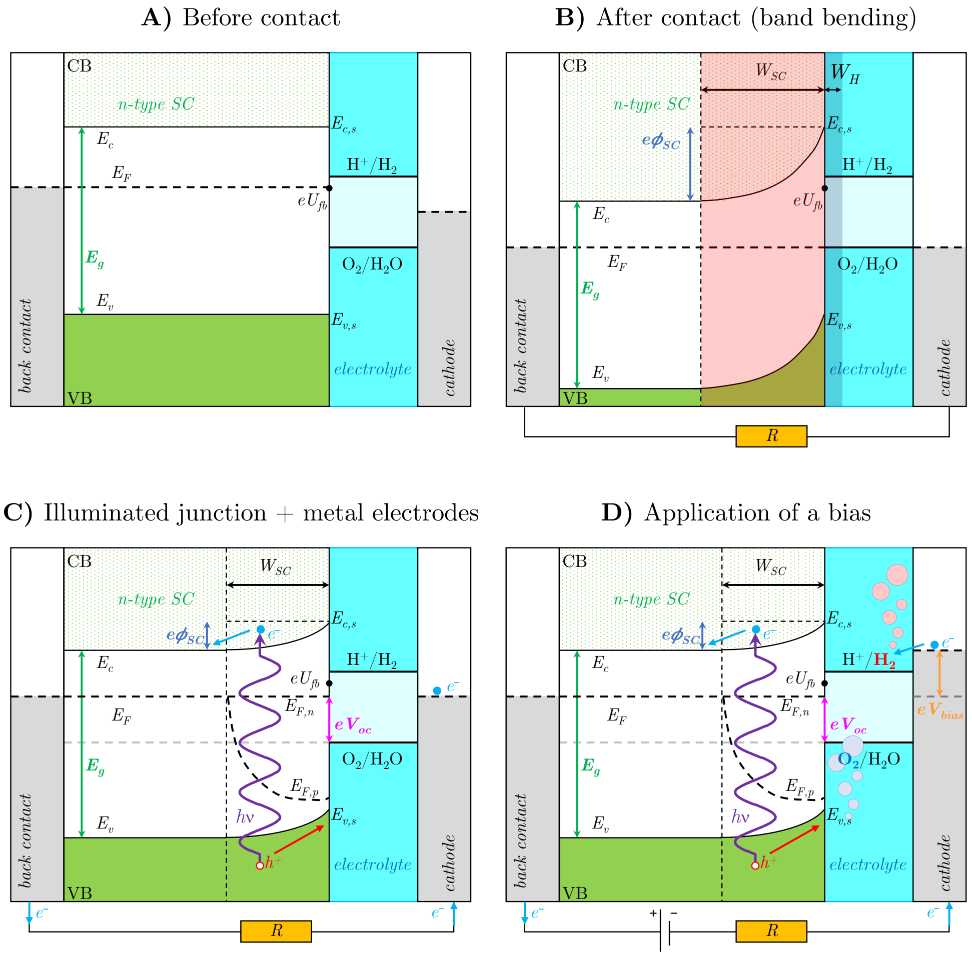

Figure 1.2: Band diagram of a PEC cell with an n-type semiconductor (photoanode). **A)** Photoanode and electrolyte before contact. **B)** Junction formation and equilibration (SC: space charge layer, H: Helmoltz layer). **C)** PEC cell under illumination. **D)** Application of an external bias. **Legend.** CB: conduction band; VB: valence band; E_F: Fermi level; E_g: bandgap; $E_{F,s}$: Fermi level of the electrolyte; eU_{fb}: flat-band potential; W_{SC}: width of the space charge region; ϕ_{SC}: band bending; W_H: Helmoltz layer width; $E_{F,n}$: quasi-Fermi level of electrons; $E_{F,p}$: quasi-Fermi level of holes; V_{oc}: photovoltage; V_{bias}: external applied bias.

separate photoinduced charge carriers (indeed, the electric field in the space charge region can be as high as 10^5 V/cm[22]).

The potential distribution and width of the space charge layer can be estimated, knowing the concentration of donors (N_D) in the material, starting from the Poisson's law and finding the total amount of charge in the SCL[14]:

$$Q_{SC} = \sqrt{2\epsilon_0\epsilon_r e N_D A^2 \left(\phi_{SC} - \frac{kT}{e}\right)} \tag{1.14}$$

where $\epsilon_0 = 8.854 \times 10^{-12}$ F/m is the vacuum permittivity and ϵ_r is the semiconductor relative permittivity. Subsequently, the width of the space charge layer can be obtained:

$$W_{SC} = \sqrt{\frac{2\epsilon_0\epsilon_r}{eN_D}\left(\phi_{SC} - \frac{kT}{e}\right)} \tag{1.15}$$

Typical values of W_{SC} are in the order of hundreds of nm - tens of µm, while the Helmoltz layer width is on the order of few nm.

(c) Illuminated junction (Figure 1.2C). Photon absorption in the space charge region promotes the generation of electron/hole pairs, which can be separated by the built-in electric field. Photoexcited electrons in the CB are driven toward the semiconductor back contact and they travel through the external circuit to the counter electrode (e.g. typically made of platinum). Conversely, photogenerated holes in the VB are driven toward the semiconductor/electrolyte interface, where they can oxidize water. Upon illumination, the Fermi level increases with V_{oc}, the internal photovoltage (or open circuit voltage), which logarithmically depends on the light flux[16,17], and the band bending decreases. The system is no longer in equilibrium, especially in the SCL, thus the use of a single Fermi level is no longer appropriate and the concept of *quasi-Fermi levels* is considered. For an n-type semiconductor, if n_0 is the equilibrium electron concentration and Δn the additional concentration created by illumination, the total electron concentration can be written as $n = n_0 + \Delta n \simeq n_0$; on the contrary, for holes it is possible to write $p = p_0 + \Delta p \simeq \Delta p$ (with the same notation), due to the fact that the excess hole population significantly alters the minority-carrier distribution. As a result, $E_{F,n}$, the quasi-Fermi level of electrons, remains horizontal and identical to the Fermi level, while $E_{F,p}$, the quasi-Fermi level of holes, departs from the bulk Fermi level in the active region.

At this point, it is important to note that in the context of p-n junctions, the quasi-Fermi level splitting defines the open circuit voltage and, so, the usable energy in the device[23]: $\Delta\mu = eV_{oc} = E_{F,n} - E_{F,p}$. This interpretation has also been applied to photoelectrochemical cells[13,24,25]. However, Salvador[17] suggested that this equality does not hold, since

$$\Delta\mu = \Delta G = eV_{oc} = E_{F,n} - E_{O_2/H_2O} \leq E_{F,n} - E_{F,p} = E_g + kT \ln \frac{\Delta n \Delta p}{N_c N_v} \quad (1.16)$$

which implies that $E_{F,n} - E_{F,p} - eV_{oc}$ represents an entropic contribution, defined *photoelectrochemical affinity* in the full nonequilibrium formulation ($a_{ph} = E_{O_2/H_2O} - E_{F,p}$). Thus, the bandgap represents the increase of internal energy of the photoexcited semiconductor after thermalization of the photoexcited carriers: $E_g = \Delta E = \Delta G + T\Delta S = eV_{oc} + T\Delta S$[17]. However, it must be noted that this interpretation is debated by some authors[14] as the predictive value of the quasi-Fermi levels as a thermodynamic driving force may depend on the reaction mechanism.

It can be observed that the *maximum* open circuit voltage corresponds to the flatband conditions (i.e. $eV_{oc,max} = eU_{fb} - E_{O_2/H_2O}$)[21], while the *critical* one, i.e. the one corresponding to a net photoelectrolysis, is $eV_{oc,cr} = E_{H^+/H_2} - E_{O_2/H_2O} = |\Delta E°|$. Consequently, the condition

$$eU_{fb} \geq E_{H^+/H_2} \quad (1.17)$$

must be satisfied for the photoanode to develop an unassisted water splitting reaction.

(d) Application of a bias (Figure 1.2D). The condition for the flatband potential shown in Equation (1.17) is not satisfied by the photoanode depicted in Figure 1.2C. This situation is typical of many photoanodes, such as TiO_2[7] (see also Section 1.5.3). Thus, an external bias is applied to the metal cathode to raise its Fermi level above the HER potential, making water splitting possible. In the water splitting process, photoelectrodes act as *minority carrier* devices[13], as the semiconductor/liquid junction allows the flow of minority carriers , while blocking majority-carriers. For this reason, *n*-type semiconductors are employed as photoanodes and *p*-type semiconductors as photocathodes.

1.3.2 Bias potential and flatband potential

In the previous section, it was shown that the application of a bias between a photoanode and a metal counter electrode can allow the overall water splitting reaction. On the other hand, in most cases, a photoelectrode (either a photoanode or a photocathode) is characterized by means of a three-electrode potentiostat (as explained in Section 1.3.3), which means that the bias is applied with respect to a reference electrode; in this case, the potential difference is distributed over the space charge layer and the Helmholtz layer, both of which are associated with the same charge Q (see Equation (1.14)). The capacitance is defined as $C = Q/V$ and, since these layers act as two capacitance in series, the potential distribution is given by[14]

$$\frac{\Delta V_{SC}}{\Delta V_H} = \frac{C_H}{C_{SC}} \tag{1.18}$$

Since $C_H \gg C_{SC}$ (typical values for C_{SC} are 1–1000 nFcm^{-2} and for C_H are 10–20 µFcm^{-2}[14]), the change in applied bias falls across the depletion layer of the semiconductor, as shown in Figure 1.3: starting from a band bending ϕ_{SC} in a photoanode (Figure 1.3A), application of a negative (cathodic) bias reduces the band bending; the opposite occurs when a positive (anodic) bias is applied. The situation depicted in Figure 1.3B is the so-called *flatband* situation, in which the Fermi level of the semiconductor in contact with the electrolyte has the same value as before contact, i.e. $E_F = eU_{fb}$ (see Figure 1.2A), so that band bending is reduced to zero.

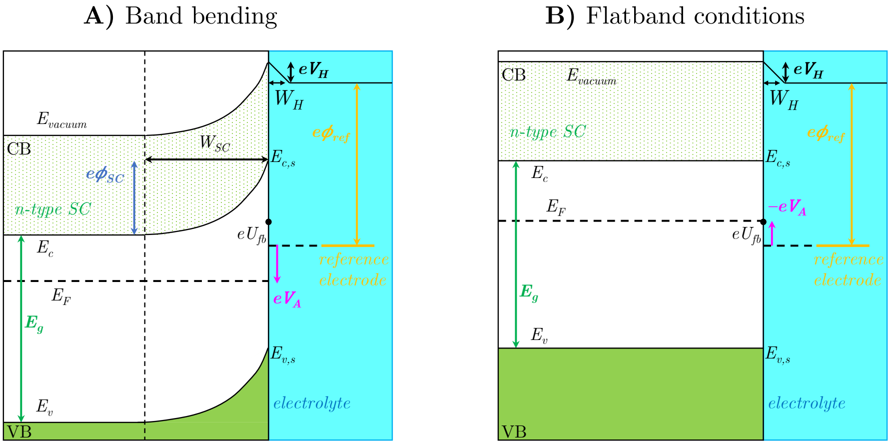
A) Band bending

B) Flatband conditions

Figure 1.3: Effect of bias voltage application (V_A) to an n-type semiconductor. The change in applied potential falls across the space charge layer, while V_H remains constant, so that, when a sufficiently negative bias is applied, the band bending **(A)** can be reduced to zero **(B)**.

Several techniques can be used to determine the flatband potential of a semiconductor. The easiest method consists in measuring the photocurrent onset (see below), but a more appropriate method is the Mott-Schottky analysis (see Figure 1.4), in which the capacitance of the space charge layer, obtained by differentiating Equation (1.14), i.e. $C_{SC} = dQ_{SC}/d\phi_{SC}$, is plotted as its reciprocal square as a function of the applied potential V_A by replacing the potential of the space charge layer, $\phi_{SC} = V_A - U_{fb}$, obtaining the so-called Mott-Schottky equation:

$$\frac{1}{C_{SC}^2} = \frac{2}{\epsilon_0 \epsilon_r e N_D A^2}\left(V_A - U_{fb} - \frac{kT}{e}\right) \tag{1.19}$$

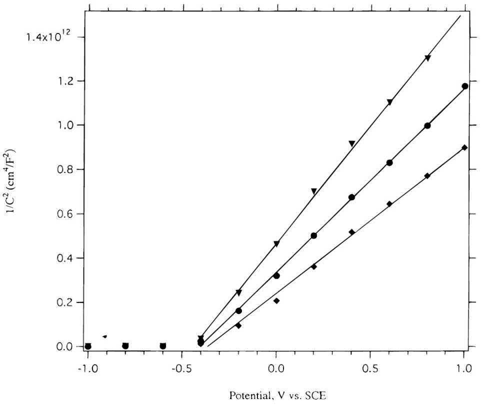

Figure 1.4: Mott-Schottky plots of anatase single crystal electrode in 1 M H_2SO_4 at various frequencies (◆: 100 Hz; ●: 500 Hz; ▼: 1000 Hz), leading to $U_{fb} = -0.4$ V vs. SCE[26].

1.3.3 Photocurrent-voltage characteristics

The quantities described above play an important role in the performance of photoelectrodes, which is evaluated by means of photocurrent testing, i.e. the current produced by the photogenerated charges. Indeed, current-voltage measurements are the most important technique to determine the performance characteristics of photoanodes or photocathodes for water splitting[14], which allow to obtain:

- the photocurrent density and energy conversion efficiency as a function of the applied potential;
- the dark current as a function of the applied potential;
- the sign of the photocurrent (anodic or cathodic);
- the photocurrent onset potential;
- electron or hole transport limitations (comparing front- and back-side illumination);
- transient efficiencies that indicate recombination.

These measurements are performed by means of a three-electrode potentiostat, which means that the working electrode is set at a fixed potential versus this reference electrode and the current at that potential is acquired while sweeping the applied voltage at constant scan rate (such as 1–50 mV/s) in the dark, under constant illumination or also by switching the illumination on and off at a fixed frequency[14]. In this way, a current-voltage plot of the photoelectrode, i.e. its characteristics, is obtained. In this case, the counter electrode performance is not relevant, since the potentiostat supplies whatever voltage between the photoelectrode and the counter electrode to maintain the current at a definite voltage with respect to the reference electrode. Therefore, this kind of measurement do not give cell efficiencies (see Section 1.4.2) but rather photoelectrode efficiencies[27].

Figure 1.5 illustrates a scheme both of the band diagram and the measured photocurrent as a function of the applied bias, V. When $V < U_{fb}$, i.e. under cathodic polarization, an accumulation of majority carriers (i.e. electrons for a photoanode) occurs at the surface, which are transferred to the electrolyte competing with water oxidation (i.e. water reduction). When $V = U_{fb}$, the anodic and cathodic reactions are balanced and the net current is zero. When $V > U_{fb}$, the space charge layer is formed, so that photogenerated electron/hole pairs are separated and holes are transferred to the electrolyte oxidizing water, which results in an anodic photocurrent. However, in real cases, the photocurrent onset (V_{on}, when $J > 0$) is typically higher than U_{fb} due to the overpotential for water oxidation (η_{ox}), as shown by the red curve in Figure 1.5. The electrochemical overpotential on *metallic* electrodes is a well-studied phenomenon and is known to arise from many sources (electrical resistance in the electrode or in the electrolyte, depletion of charge carriers at the surface), but results from using H_2O_2 as a "hole scavenger" in photocurrent tests exclude these possibilities on *semiconductor* electrodes. For the latter, kinetic limitations have been suggested, but this does not explain the large difference between in overpotential observed for photoanodes such as WO_3 and TiO_2 (about 0.2 V) and α-Fe_2O_3 (about 0.5 V). On the other hand, a slow reaction rate for holes in the OER have been suggested, which can be addressed by adding catalysts (such as CoO_x or IrO_2) on the photoanode surface. Moreover, electronic surface traps (or surface states), leading to the so-called Fermi level pinning, can be an additional loss mechanism, although their characterization is particularly challenging[24].

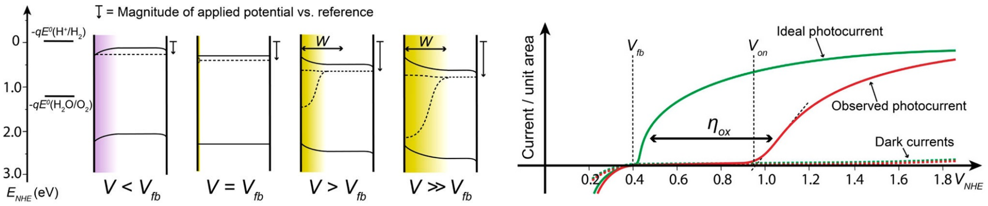

Figure 1.5: Left. Electron energy scheme of an n-type semiconductor photoanode under polarization using a potentiostat at different potentials relative to the flatband potential (V_{fb}). An accumulation of majority carriers (purple shaded region) occurs when $V < V_{fb}$, and a depletion layer (of width W, yellow shaded region) forms when $V > V_{fb}$. **Right.** Idealized photocurrent density versus applied potential curves are shown relative to V_{fb}, and the overpotential for the oxidation reaction, η_{ox}, is shown for a typical electrode with an onset of photocurrent V_{on}.[24]

1.4 Efficiency of a photoelectrochemical cell

The energy conversion efficiency is a fundamental performance indicator of the PEC cell; an ultimate aim of the research on PEC water splitting is indeed the realization of low-cost devices with an efficiency of about 10%. However, much pluralism exists regarding the concept itself of efficiency, due to the fact that several different measures of efficiency exist. Thus, some authors have developed guidelines regarding the correct approach for reporting efficiency values[28–30]. A brief discussion is accordingly reported in this section.

1.4.1 Solar-to-hydrogen conversion efficiency

The so-called *solar-to-hydrogen* (STH) efficiency is the most important efficiency measurement for PEC water splitting devices exposed to Air Mass 1.5 Global (AM 1.5G) illumination under zero bias conditions[29]. This implies that no voltage is applied between the working electrode (WE) and the counter electrode (CE), which should be short-circuit; this means that the STH must be measured in a 2-electrode system. Also, the WE and CE must be immersed in the same pH solution and the electrolyte should not contain any sacrificial donors or acceptors because the redox reactions would no longer reflect true water splitting. The STH is defined as the ratio of the useable energy in the generated hydrogen gas to the total solar energy delivered to the system[14]. For steady-state operations, this is equivalent to the ratio of the power *output* to the power *input*:

$$\frac{P_{out}}{P_{in}} = \frac{\text{(hydrogen production rate)} \times \text{(hydrogen energy density)}}{\text{solar flux integrated over illuminated area}} \tag{1.20}$$

The hydrogen production rate can be measured by analytical methods such as gas chromatography and mass spectrometry, which sometimes is not available in laboratories; thus, the STH efficiency can be written in terms of the measured photocurrent density, i.e. photocurrent per unit illuminated electrode area, $J_{ph} = I_{ph}/A$, as

$$STH = \left[\frac{|J_{ph}| \cdot E^{\circ} \cdot \eta_F}{P_{light}}\right]_{AM1.5G} \rightarrow STH(\%) \simeq 1.23 \cdot J_{ph}\ (\mathrm{mA\,cm^{-2}}) \tag{1.21}$$

where $E^{\circ} = 1.23$ V, η_F is the faradaic efficiency for hydrogen production and P_{light} is the power of incident light (which corresponds to 100 mW/cm^2 for AM 1.5G illumination). The second equality in Equation (1.21) is calculated inserting the explicit values for the quantities in the first term and is useful for a quick estimate of the STH efficiency for a measured photocurrent[14]. It is critical to note that Equation (1.21) is only valid if one confirms stoichiometric gas evolution (H_2 and O_2) in the absence of any sacrificial electron donors or acceptors. Equation (1.21), moreover, is restricted to the condition that the measured photocurrent must correspond directly to the molar H_2 generation rate, i.e. faradaic efficiencies for the hydrogen evolution and oxygen evolution reactions are 100% (i.e. $\eta_F = 1$).

1.4.2 Other efficiencies

If a voltage is applied between the working and the counter electrode, another efficiency must be introduced, the so-called *applied bias photon-to-current efficiency* (ABPE), which is not a true solar-to-hydrogen measurement since the application of a bias involves power consumption; it is defined as[29]

$$ABPE = \left[\frac{|J_{ph}| \cdot (E^\circ - |V_{bias}|)}{P_{light}}\right]_{AM1.5G} \tag{1.22}$$

where J_{ph} is the photocurrent density ($\mathrm{mA\,cm^{-2}}$) obtained under an applied bias V_{bias} (V).

The previous definitions of efficiency are referred to the overall device performance, in which the working electrode is short-circuited with a counter electrode. From a materials research and development point of view, however, it is important to evaluate the fundamental properties of a photoelectrode, since the current state of the art on PEC technology is still far from the commercial scale. Thus, these properties can be determined from photocurrent-voltage analysis of a material in a three-electrode arrangement (i.e. photoelectrode, counter electrode and reference electrode) under illumination[30], as performed for this thesis work. In this case, a measurement of the efficiency of the *single photoelectrode* (and not of the overall PEC cell) can be performed by substituting V_{bias} in Equation (1.22) with the applied potential V_{app}, defined as

$$V_{app} = V_{meas} - V_{a,oc} \tag{1.23}$$

which means that it is the difference between the potential at the working electrode measured with respect to the reference electrode, V_{meas}, and the potential of the photoelectrode under open circuit conditions (i.e. zero current) measured also with respect to the same reference electrode in identical conditions, $V_{a,oc}$ (note that $V_{a,oc} \neq V_{oc}$)[28]. The term $V_{meas} - V_{a,oc}$ makes the following relation for the efficiency independent of the electrolyte pH and the type of reference electrode used[28]:

$$\eta = \frac{|J_{ph}| \cdot (E^\circ - |V_{app}|)}{P_{light}} = \frac{|J_{ph}| \cdot (E^\circ - |V_{meas} - V_{a,oc}|)}{P_{light}} \tag{1.24}$$

Finally, one of the most useful diagnostic efficiencies of photoelectrodes is the *external quantum efficiency* (EQE), also called *incident photon-to-current efficiency* (IPCE), which is defined as[29]

$$IPCE = EQE = \eta_{e^-/h^+}\eta_{tra}\eta_{int} \tag{1.25}$$

where η_{e^-/h^+} is the fraction of electron hole pairs generated per incident photon flux, η_{tra} is the efficiency of the charge transport to the solid-liquid interface and η_{int} is the efficiency of interfacial charge transfer. Thus, Equation (1.25) can be written as

$$IPCE(\lambda) = \frac{\text{electrons cm}^{-2}\,\text{s}^{-1}}{\text{photons cm}^{-2}\,\text{s}^{-1}} = \frac{|J_{ph}| \cdot 1239.8\ (\text{V nm})}{P_{mono} \cdot \lambda\ (\text{nm})} \tag{1.26}$$

where 1239.8 V nm represents the product hc (h is the Planck's constant and c the speed of light), P_{mono} is the calibrated and monochromated illumination power intensity in mWcm^{-2} and λ is the wavelength at which this illumination power is measured[29]. IPCE describes the maximum possible efficiency with which the incoming radiation can produce hydrogen from water, assuming that all the photogenerated charges are used for the evolution of H_2 and O_2, neglecting corrosion or the formation of by-products.

1.5 Materials aspects for photoanodes

The most critical aspect to consider in the development of efficient PEC cells is the choice of appropriate photoanode/photocathode materials. These must satisfy several requirements, some of which are in conflict between each other; indeed, the “perfect” photoanode/photocathode material has not been found yet; in general, the most important requirements a semiconductor material for water splitting should meet are listed below[14] and will be accordingly discussed in detail:

- good light absorption, possibly in the visible range (Section 1.5.1);
- high chemical stability in the dark and under illumination (Section 1.5.2);
- appropriate positions of the band edges, straddling the O_2/H_2O and H^+/H_2 reduction potentials (Section 1.5.3);
- efficient charge transport (Section 1.5.4);
- low overpotentials for reduction/oxidation of water (Section 1.5.5).

1.5.1 Bandgap

The bandgap, E_g, determines the spectral region in which the semiconductor absorbs light: its value corresponds to the minimum energy of incoming photons which will be absorbed. The minimum bandgap for a photoelectrode is about 2.0 eV, as mentioned in Section 1.2. In general, direct bandgap materials (such as GaAs) absorb light more efficiently than indirect bandgap materials (such as Si or TiO_2); photogenerated electron/hole pairs thermalize (within ps) to band-edge levels, losing energy to heat, which implies that high-bandgap semiconductors generate little photocurrent due to poor absorption, but low-bandgap semiconductors can suffer from low conversion efficiency due to thermalization losses[13].

The importance of the bandgap is illustrated in Figure 1.6. In Figure 1.6A, the solar spectrum (AM 1.5G) is shown, and some portions are colored according to the bandgap limits of water splitting: the theoretical minimum (1.23 eV), the practical one (2.00 eV) and that of anatase TiO_2 (3.2 eV), which is a widely investigated material. It is evident how the region starting from $E_g = 2.0$ eV is important since it exhibits the absolute maximum of the solar irradiance. In Figure 1.6B, in addition, the usable solar spectrum region for water splitting is shown and compared to the maximum theoretical STH efficiency (left y axis) and the maximum theoretical photocurrent (right y axis)[31]. The latter was obtained assuming that every photon in the solar spectrum with an energy exceeding the bandgap creates an electron/hole pair, and that all the photoexcited charge carriers are converted to photocurrent. The STH efficiency, on the other hand, is simply obtained by Equation (1.21). Thus, Figure 1.6B shows that anatase TiO_2 can lead to the maximum photocurrent of 1.1 $\mathrm{mA\,cm^{-2}}$, corresponding to only 1.3% STH efficiency, while an optimum photoelectrode having $E_g = 2.0$ eV would produce a photocurrent of 14.5 $\mathrm{mA\,cm^{-2}}$ and a STH efficiency of 17.8%.

Based on the assumptions made to derive them, one may expect that the STH efficiency values in Figure 1.6B do not correspond to experimental values. Indeed, unassisted water splitting with a single material have been only obtained with very high-bandgap oxides, such as $SrTiO_3$[32] and $KTaO_4$[33], with demonstrated STH values close to those of Figure 1.6B; on the other hand, semiconductors with encouraging theoretical STH values, such as α-Fe_2O_3 or $BiVO_4$, develop a low photovoltage under sunlight, insufficient to split water without the assistance of an external bias (consistently with the discussion of Section 1.3.1); this occurs even for TiO_2, having a higher bandgap of 3.0 (rutile)/3.2 (anatase) eV[14].

1.5.2 Chemical stability

An essential requirement for photoelectrodes is the resistance to chemical reactions occurring at the solid/liquid interface which would degrade their properties, such as electrochemical corrosion, photocorrosion and dissolution[7]. Photo- or electrochemical corrosion of a generic AB

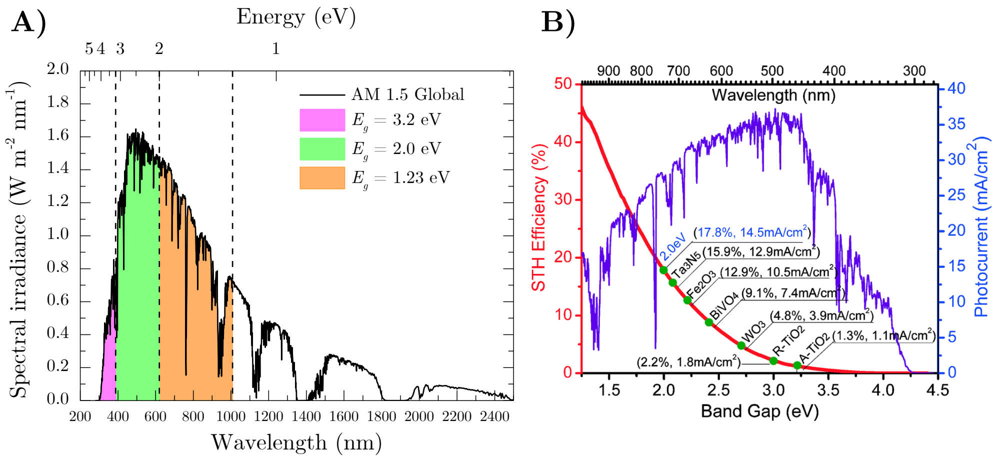

Figure 1.6: **A)** Solar energy spectrum (ASTM G173-03 AM 1.5 Global), of which some portions are colored according to the bandgap limits of water splitting: theoretical (1.23 eV, orange), practical (2.00 eV, green) and of undoped TiO_2 (3.20 eV, magenta). **B)** Dependence of the theoretical maximum solar-to-hydrogen (STH) efficiency and the photocurrent density of photoelectrodes on the bandgap under AM 1.5G irradiation[31].

semiconductor can be written as

$$AB + zh^{+} \rightleftharpoons A^{+z} + B \qquad E_{p,d} \quad \text{(anodic decomposition)} \tag{1.27}$$

$$AB + ze^{-} \rightleftharpoons B^{-z} + A \qquad E_{n,d} \quad \text{(cathodic decomposition)} \tag{1.28}$$

where z is the number of electron or holes, $E_{p,d}$ is the enthalpy change at the anode (anodic decomposition) and $E_{n,d}$ is the enthalpy change at the cathode (cathodic decomposition)[7]. Considering these potentials as energies in eV, the following criteria hold[14]:

1. if $E_{p,d} < E_v$ no anodic decomposition can occur (where E_v is the valence band edge);
2. if $E_{n,d} > E_c$ no cathodic decomposition can occur (where E_c is the conduction band edge).

The actual values of $E_{p,d}$ and $E_{n,d}$ are difficult to know since they may depend on the pH of the solution; however, a useful illustration is given by Figure 1.7, which shows that some metal oxides are thermodynamically stable against cathodic photocorrosion (e.g. TiO_2), but almost all of them are in fact unstable against anodic corrosion, including very well investigated n-type photoanodes such as TiO_2 and hematite (α-Fe_2O_3). Decomposition of these materials is typically not observed due to slow reaction kinetics[14]. A different example is given by Cu_2O, which is thermodynamically unstable against both anodic and cathodic decompositions; however, this material can be successfully employed as photocathode by protecting it with a so-called *protective layer* of more stable oxides; an example of this approach is discussed in Ref. [34].

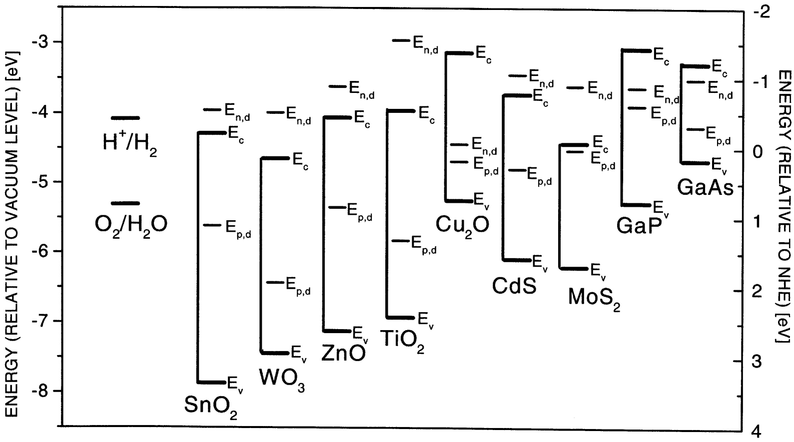

Figure 1.7: Position of decomposition potentials ($E_{p,d}$, $E_{n,d}$) and band edges (E_c, E_v) of selected semiconductors[7].

1.5.3 Proper positioning of band edges

Another requirement for semiconductor materials for PEC water splitting is that the band edges should straddle the water reduction and oxidation potentials, i.e. $E_c < E_{O_2/H_2O}$ and $E_v > E_{H^+/H_2}$. This is illustrated in Figure 1.8, in which the band edges position is shown with respect to the reversible hydrogen electrode (RHE, Section 1.2) and the water redox energy levels. It can be observed that this requirement is not easily achieved for many semiconductors: for instance, α-Fe_2O_3 and WO_3 have the conduction band minimum more positive (in the electrochemical scale) than the H^+/H_2 potential. In addition, the band edges position with respect to the water redox levels is generally fixed since they all exhibit the same pH dependence (i.e. shift with -0.059 V per pH unit)[14]. For this reason, intense efforts are currently being made to synthesizing ternary (or even quaternary) oxides with tuneable bandgap, and thus band edges position, based on cation combination, as shown in Figure 1.8[35].

The proper position of band edges, however, is a *necessary* requirement for a photoanode/photocathode material, but it is not *sufficient* for the unassisted water splitting: as mentioned in Section 1.3.1, indeed, some authors suggest that the quasi-Fermi levels, instead of the band edges, should straddle the water redox potentials; on the other hand, the flat-band potential, U_{fb}, must be more positive (in the energy scale) than the H^+/H_2 standard potential (Equation (1.17)). U_{fb} also shows the same pH dependence as the band edges[20], but it can be modified through surface chemistry[7].

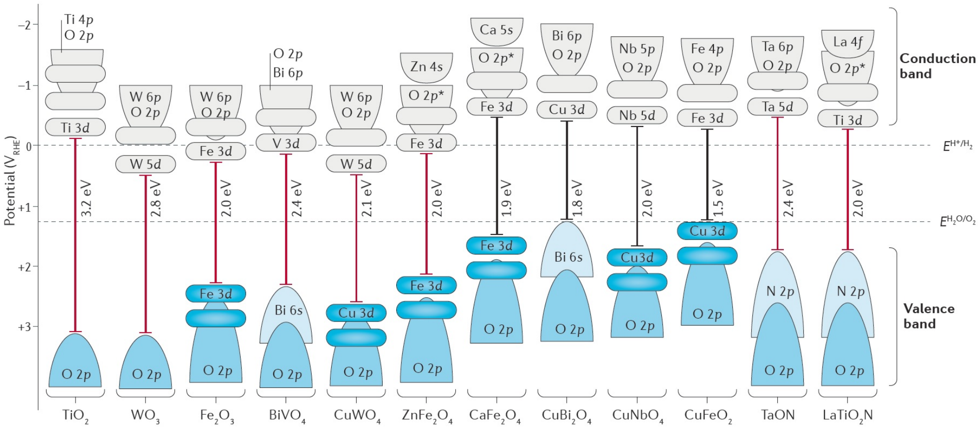

Figure 1.8: Bandgap structure by contribution of metal cation and oxygen anion states to the conduction and valence bands. The band edges position is shown with respect to the reversible hydrogen electrode (RHE) and the water redox energy levels; the bandgap energy is marked with red vertical bars for n-type semiconductors and with black vertical bars for p-type semiconductors[35].

Flat-band potential values of some relevant semiconductors are shown in Figure 1.9.

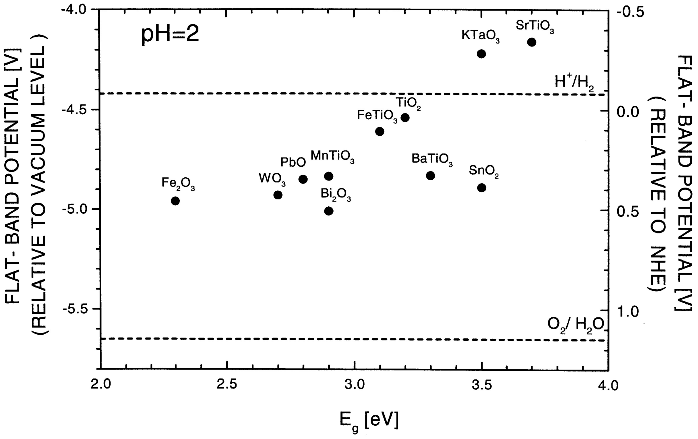

Figure 1.9: Flat-band potential of different oxide semiconductors with respect to their bandgap and the normal hydrogen electrode at pH = 2[7].

1.5.4 Efficient charge transport

Some materials, such as TiO_2 or WO_3, exhibit a good charge transport, while others, such as α-Fe_2O_3, do not; for the latter, an inefficient charge transport facilitates charge recombination, leading to lower photoconversion efficiency[14]. A relevant material parameter in this context is the intrinsic charge carrier mobilities, which are influenced by the material band structure. Considering for instance transition metal oxides, extensive overlap of metal 3d orbitals (which mainly contribute to the conduction band) usually leads to high electron mobilities, while the overlap of O-2p orbitals (which mainly contribute to the valence band) determines the hole mobility. A widely used relation is

$$L_D = \sqrt{D\tau_R} \tag{1.29}$$

which relates the minority carrier diffusion length (L_D) with the diffusivity (D) and the carrier lifetime (τ_R); conversely, the diffusivity can be expressed through the Einstein-Smoluchowski relation for a particle in an electric field as

$$D = \frac{kT\mu}{e} \tag{1.30}$$

where μ is the carrier mobility. Values of L_D range from some nm in some oxides to hundreds of µm in high-purity Si[14].

1.5.5 Low overpotential for water oxidation

Considering n-type semiconductors, the hole transfer across the semiconductor/electrolyte interface should be sufficiently fast to compete with the anodic decomposition reaction (Equation (1.27)). More generally, interfacial charge transfer should be fast enough to avoid carriers accumulation at the surface; if not, a decrease of electric field and a concomitant increase in electron-hole recombination would occur[14]. To improve the kinetics of charge transfer, nm-sized catalysts can be added to the semiconductor surface, as already mentioned in Section 1.3.3; examples of oxygen evolution catalysts are RuO_2, IrO_x and Co-based compounds, while Pt, Rh or NiO_x are employed as catalysts for the hydrogen evolution[14].

1.5.6 Trade-offs and nanostructuring

Apart from the material requirements described in Sections 1.5.1 to 1.5.5, other ones are important for the realization of an efficient photoelectrode material, such as an appropriate choice of the substrate[36], low electrical resistance in the components of the PEC cell[7] and, ultimately, a low cost. For further discussion, the reader is referred to the appropriate references.

Unfortunately, no single material satisfying all these requirements has been found yet; instead, there are some trade-offs between anti-correlated quantities, such as

- the open circuit voltage and the maximum photocurrent: a high bandgap leads to higher V_{oc} (see Equation (1.16)), but also to a low photocurrent, as mentioned in Section 1.5.1; this is particularly detrimental for water splitting systems with a single photoanode/photocathode material (i.e. single junctions cells), which has led to the study of multi-junction semiconductor PEC devices (not discussed in this work)[14];

- the bandgap and the chemical stability: a low bandgap, desirable for better photon absorption, leads to lower chemical stability (as discussed in Section 1.5.2);
- the recombination degree and the catalytic activity: catalytically active surface sites can also act as recombination centers for charge carriers; in addition, catalyst particles on the semiconductor surface for hydrogen or oxygen evolution may enhance the back-reaction between H_2 and O_2, such as Pt[14].

In addition, some quantities are not by themselves correlated or anti-correlated, but they need to be so, as for the photon collection and the charge transport (see the left side of Figure 1.10): in a material with small absorption coefficient (α), such as indirect bandgap metal oxides, charge carriers are generated far away from the surface, which means a high photon collection length (α^{-1}), and they may recombine before reaching the semiconductor/electrolyte interface; as a consequence, a high minority carrier diffusion length (L_D) is needed. However, a material with a small absorption coefficient might also have a low L_D; in order to circumvent this issue, the strategy of nanostructuring the semiconductor material is particularly advantageous, which can also address additional material limitations, as shown in countless studies on nanostructured materials for water splitting applications.

First, a nanostructured morphology dramatically increases the specific surface area, increasing the number of surface sites for reactions. Second, it enables to decouple the overall material thickness with the maximum charge collection length. This is shown in the right side of Figure 1.10: minority carriers (holes) have to travel half the diameter of the nanowire (tens of nm or less) in order to reach the interface with the electrolyte, while the majority carriers (electrons) can travel along the wire axis, reaching the metal back-contact and, finally, the counter electrode. If transport of majority carriers is also an issue, the wire core could be also metallic and, after, coated with a photoactive semiconductor[14].

Another important aspect of nanostructured semiconductors is that the space charge layer can be larger than the nanostructure itself[14,37]; considering, for instance, the radial distribution of electrical potential in an anatase TiO_2 spherical particle with an uniform concentration of donors $N_D = 10^{17}$ cm^{-3} having a size of 50 nm[38,39],

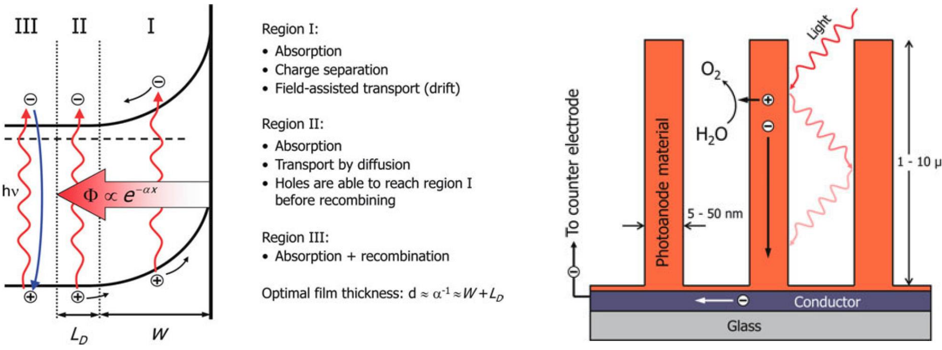

Figure 1.10: Left. Schematic illustration of absorption region in a photoanode: the light intensity (Φ) decreases exponentially with distance from the surface (Lambert-Beer law) and charge carriers generated within a distance $L_D + W$ from the surface contribute to the photocurrent. **Right.** Nanostructuring effects of a photoanode film in nanowires: the photogenerated holes easily react with water molecules, while photogenerated electrons are transported through the wire to the metal back-contact. Adapted from ref. [14].

$$\phi_{SC} = \phi(r) = \frac{eN_D}{6\epsilon_0\epsilon_r}(r - r_W)^2 \left(1 + \frac{2r_W}{r}\right) \tag{1.31}$$

where r_W is the characteristic width of the depletion region and r is the radial coordinate, the maximum achievable band banding is only about 6 meV, which corresponds to the extension of the space charge layer over the whole nanoparticle ($r_W = 0$ in Equation (1.31)); this means that the whole nanoparticle is fully depleted. The band bending, thus, is smaller than the average thermal energy kT, thus it can be neglected. Conversely, if the donor density is 10^{18} cm^{-3}, the maximum ϕ_{SC} is about 60 meV, which is large enough to affect the distribution of charge carriers in the particle[37]. These considerations suggest that the concept of band bending described in Section 1.3.1 may be misleading in nanostructured or mesoporous semiconductors, excluding a significant role of the band bending itself in the charge separation. However, as discussed above, in a nanostructured material minority carriers have to travel a short distance compared to their diffusion length (L_D), which means that the charge transfer kinetics at the semiconductor/electrolyte interface is the main factor ruling the overall charge separation and recombination kinetics in nanosized electrodes[14].

The interest in nanostructured semiconductor materials is one of the main bases of this thesis work. Indeed, the following chapter is devoted to the discussion on the most important aspects related to PEC water splitting of nanostructured titanium dioxide (TiO_2), which is the very first material known for this application[5] but still widely investigated due to its properties and, as such, object of this thesis work.

2

Titanium dioxide for water splitting applications

THIS chapter reports an overview on titanium dioxide nanostructured films related to their applications and the required properties for water splitting. First, the general properties of this material will be introduced (Section 2.1); in the following, an analysis on the approaches presented in the literature to overcome its limitations and enhancing its performances is reported (Section 2.2), where the discussion is focused on the strategies pursued also in this Ph.D. thesis work. As the defect chemistry of TiO_2 is a crucial aspect in determining its photoactivity and is particularly relevant in the discussion of *black titania*, it is presented in a dedicated section (Section 2.3), even though an exhaustive discussion on this aspect exceeds the purposes of this chapter.

2.1 Titanium dioxide as a photoactive material

This section describes the most relevant properties of titanium dioxide in the framework of water splitting applications, considering the material in its undoped form. First, the structural properties of the most common allotropes of TiO_2 will be highlighted (Section 2.1.1), then their electronic properties (Section 2.1.2) and, finally, some basic concepts of photon-induced reactivity of TiO_2 surfaces will be presented (Section 2.1.3).

2.1.1 Structural properties

Titanium dioxide crystallizes in three main different structures: rutile (tetragonal), anatase (tetragonal) and brookite (rhombohedral). Other phases are known as well, such as the TiO_2(B) and TiO_2(II), which form at high pressure[40]. The most relevant structural properties of anatase, rutile and brookite are reported in Table 2.1. Anatase and rutile polymorphs are by far more employed than brookite[41], since the latter is difficult to synthesize. Figure 2.1 illustrates the unit cells of these three phases. In all of them, a Ti atom is surrounded by six O atoms in a more or less distorted octahedral configuration, forming the TiO_6 basic building blocks. Comparing anatase and rutile, in the latter the octahedra show a slight orthorhombic distortion, while in the former the distortion is more significant and the symmetry degree is lower. In anatase, the Ti–Ti distances are larger and the Ti–O distances smaller than in rutile.

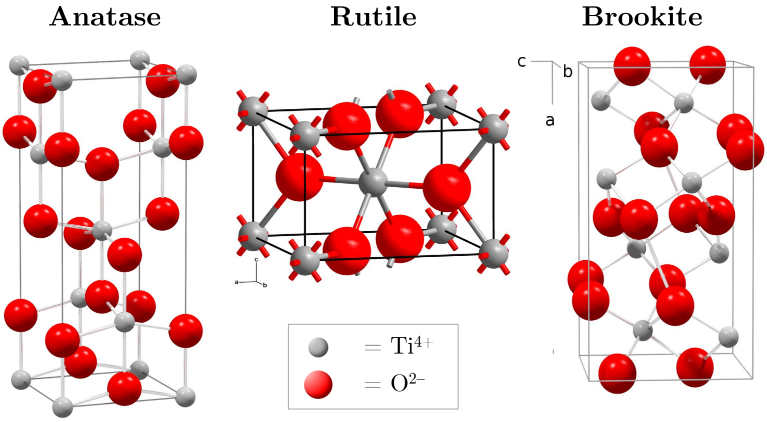

Figure 2.1: Unit cells of the most common TiO_2 crystalline phases: anatase (left), rutile (middle) and brookite (right).

Rutile is the thermodynamically stable phase at high temperatures, but anatase and brookite can be obtained in fine grained materials; for instance, Ranade *et al.*[43] found that the energetic stability crosses over between the three phases depending on the specific surface area: rutile for less than 7 m^2/g, brookite between 7 and 40 m^2/g and anatase for higher values (corresponding to approximately 40 nm crystal size). The phase transformation from anatase to rutile, on the other hand, has been well investigated. Generally, pure bulk anatase begins to transform into rutile in air at about 600°C[44]; however, various transition temperatures have been

Table 2.1: Physical parameters of the most common TiO_2 polymorphs. Data taken from the Mincryst database[42].

	Rutile	**Anatase**	**Brookite**
Density (g/cm^3)	4.25	3.89	4.07
Crystal system	Tetragonal	Tetragonal	Orthorhombic
Space group	$P4_2/mnm$	$I4_1/amd$	$Pbca$
Unit cell parameters (Å)	$a = 4.593$	$a = 3.785$	$a = 9.250$
	$b = 4.593$	$b = 3.785$	$b = 5.460$
	$c = 2.959$	$c = 9.514$	$c = 5.160$
Unit cell volume (Å^3)	62.42	136.30	260.61
Molar volume (cm^3/mol)	18.80	20.52	19.6

reported in the range 400–1200°C due to the influence of several parameters, such as morphology, grain size, presence and species of dopants or impurities, annealing atmosphere[44]. For instance, inert or reducing atmospheres can increase the number of oxygen vacancies (see Section 2.3) in the anatase lattice and promote the transformation into rutile, on the contrary of annealing in air or in pure O_2[44].

The TiO_2 polymorphs exhibit distinct features when analyzed with Raman spectroscopy and X-ray diffraction (for a description of these techniques, see Sections 3.3.2 and 3.3.3, respectively), as illustrated in Figure 2.2, which shows reference data for Raman spectra (A) and XRD patterns (B) of anatase, brookite and rutile phases. Figure 2.2A shows that anatase exhibits five distinct Raman peaks at 144, 197, 399, 516 and 639 cm^{-1}[45,46]; brookite is characterized by several bands, the most intense observed at 150, 244, 320, 553 and 630 cm^{-1}[47]; rutile, finally, can be identified by peaks at 143, 235, 447, 612 and 826 cm^{-1}[48]. In the case of anatase, the most intense peak at 144 cm^{-1}, associated to a E_g mode, is more sensitive to alteration of its crystal structure, such as quantum confinement[49,50], large defectivity[51] or poor oxygen stoichiometry[49,52].

On the other hand, Figure 2.2B shows the XRD patterns of the three phases in powder form with Cu Kα X-ray source (frequently used on lab-scale instruments). For the anatase phase, the most intense diffraction peak is found at $2\theta = 25.303°$, corresponding to the (101) lattice planes; for the brookite phase, two main peaks are observed at $2\theta = 29.364°$ and $2\theta = 35.765°$, corresponding to the (210) and (211) planes, respectively; for rutile, finally, the most intense peak is found at $2\theta = 27.44°$, which corresponds to the (110) planes. In case of samples made of mixed anatase and rutile particles (with diameters in the range 40–80 nm), Spurr and Myers[53] found an empirical method to obtain the weight fractions of anatase (x_a), according to this formula:

$$x_a = \frac{1}{1 + 1.26 I_r / I_a} \tag{2.1}$$

where I_r is the intensity of the rutile (110) peak and I_a that of anatase (101) peak.

2.1.2 Electronic properties

The density of states (DOS) around the Fermi level (E_F) of TiO_2 is obtained by the hybridization of O 2s, O 2p and Ti 3d atomic orbitals[55]. Figure 2.3 illustrates the DOS for rutile, anatase and brookite polymorphs as obtained by density functional theory (DFT) calculations; all of them exhibit similar features: taking as 0 the energy of the valence band maximum (VBM), the lower energy part of the valence band (between −17 and −20 eV) is mainly

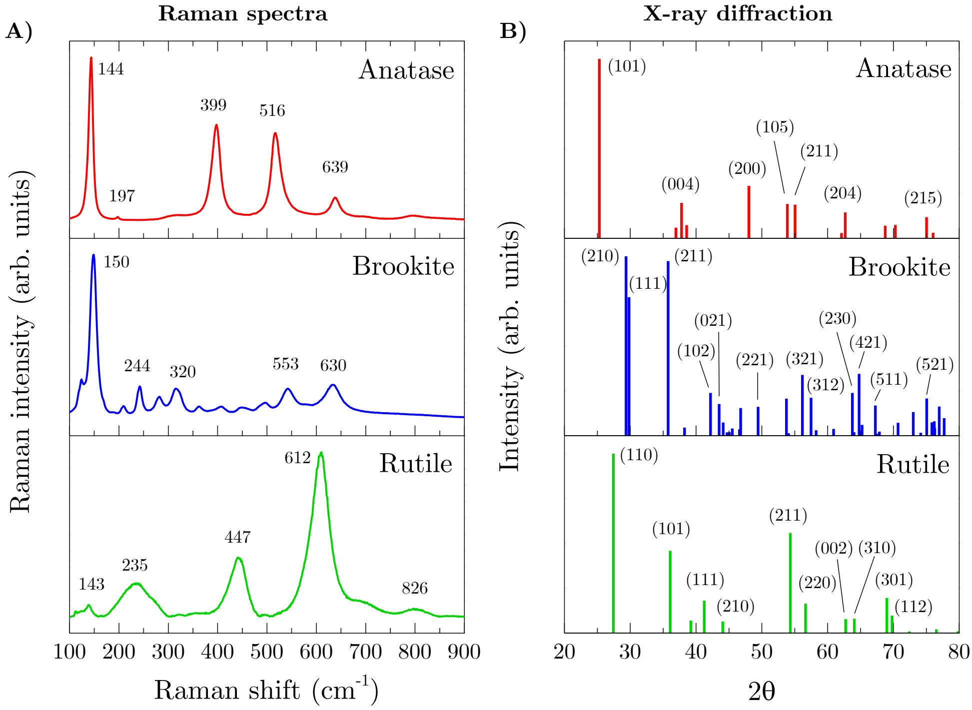

Figure 2.2: Structural analysis of the most common TiO_2 crystalline phases: Raman spectra **(A)** and X-ray powder diffraction patterns with Cu Kα source ($\lambda = 1.54$ Å) **(B)** of anatase (top), brookite (middle) and rutile (bottom). Raman spectra were taken from the RRUFF database[54] and XRD patterns from the Mincryst database[42].

composed by O 2s orbitals, while the upper valence band (between -6 and 0 eV) is composed by Ti 3d orbitals hybridized with O 2p orbitals forming σ and π bonds, with a major contribution of the former (the valence band states are "O 2p-like"). The conduction band is also composed by hybridized Ti 3d and O 2p orbitals, but with a major contribution of the former (the conduction band states are "Ti 3d-like").

As noticeable from Figure 2.3, the DOS between the valence and conduction bands is zero: it is well-known, indeed, that TiO_2 is a wide-bandgap semiconductor, with bandgap values (E_g) slightly different between the phases: experimentally, anatase exhibits an indirect transition with $E_g = 3.2$ eV[57], rutile a direct transition with $E_g = 3.05$ eV[58], while for brookite an indirect bandgap of 3.4 eV was reported[59], although more recent DFT calculations suggest that its bandgap is instead direct[56].

As a final remark, it should be noted that the DOS of TiO_2 may be different than that shown in Figure 2.3 due to the presence of defects or dopants, which may introduce localized states in the bandgap and affect not only the electronic properties of TiO_2 (for instance increasing its

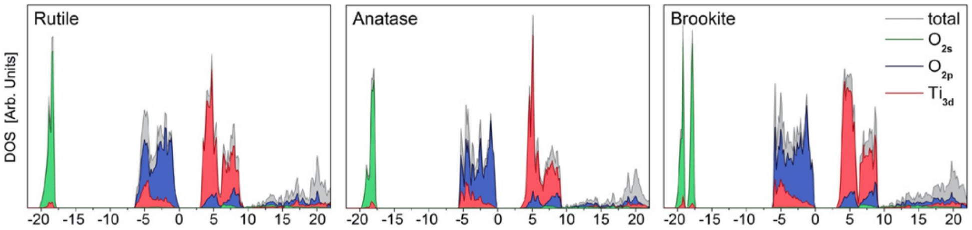

Figure 2.3: Densities of states of rutile, anatase and brookite calculated with the HSE06 XC functional. The contributions of Ti 3d, O 2s and O 2p orbitals are highlighted with red, green and blue colors, respectively[56].

conductivity), but also the structural and optical ones. All of these properties have a key role in determining the photoactivity of the material and for this reason a more detailed discussion on defects in TiO_2 is reported in Section 2.3.

2.1.3 Photon-induced reactivity of titanium dioxide

A fundamental feature of TiO_2 for its application in water splitting studies is its reactivity upon illumination; thus, the basic steps involving the physical and chemical mechanisms and their characteristic time scales should be briefly considered[60–62].

Photo-excitation. The illumination of TiO_2 with photons having energies equal or higher than its bandgap results in the formation of electron-hole pairs (i.e. *excitons*), which occurs with a characteristic time of fs.

Trapping of charge carriers. The charge carriers move within the material until they are "trapped", either on the surface or in the bulk, which occurs in the range of hundreds of fs. In the bulk, electrons can be trapped on Ti^{4+} sites, which become Ti^{3+} ions; holes, conversely, are trapped in O^{2-} sites, which become O^-; these are referred to as *polaronic* states[a]. At the anatase surface, on the other hand, the trapping sites generally correspond to under-coordinated Ti^{3+}_{5c} (electrons in fivefold-coordinated Ti ions) and O^-_{2c} (holes in twofold-coordinated O ions)[63]. The position of hole trapping states varies among rutile and anatase facets and differences in hole trapping strengths can provide a driving force for electron-hole separation and can explain the variation in facets activity toward oxidation processes[64].

At this point, it should be cleared that the charge carriers trapping at the surface of TiO_2 is desired for *photocatalytic* water splitting experiments, in which both the oxygen evolution and hydrogen evolution reactions (OER and HER, see Equations (1.5) and (1.6)) occur at the photocatalyst; on the

---

[a] A polaron is defined as the quasi-particle formed by an electron (or hole) with the surrounding lattice deformation (a cloud of virtual phonons) employed for the description of ionic crystals, in which strong electrostatic interactions are expected. Such a polaron can still move in the crystal with a higher effective mass than the electron/hole, or be self-trapped[8].

contrary, in *photoelectrochemical* water splitting electron/hole trapping may favor charge separation but also their recombination (depending on the trapping sites involved) and, in any case, the electron must be transported to the cathode. The charge carriers separation and transport is facilitated by the presence of a built-in electric field (see Section 1.3.1).

Charge recombination. The recombination of (trapped) charge carriers, either radiatively or non-radiatively, is of course an undesired pathway, competitive with the photocatalytic/photoelectrochemical reactions. It occurs in the timescale from some ps to several ns; if radiative recombinations occur, they can be investigated with techniques such as photoluminescence (PL) spectroscopy (see Section 3.3.2), giving information on the energetic distribution of trap states[61]. It is understood that an efficient separation of electron/hole pairs is of key importance to avoid recombination processes.

Interfacial charge transfer: water oxidation. In the case of photoelectrochemical water splitting with a TiO_2 photoanode, the charge transfer at the semiconductor/electrolyte interface consists in the water oxidation reaction mediated by holes. This is a "complicated" process involving four holes per water molecule evolved (see Equation (1.5)), thus the related time scales can span from few µs[65] to even half a second[66]. The mechanism for this reaction was proposed by Nakato and co-workers for rutile[67–69] considering a nucleophilic attack of a H_2O molecule on a surface-trapped hole on a surface lattice oxygen site accompanied by bond breaking[b]; this is illustrated in Figure 2.4. The quantum efficiency of the reaction, thus, increases by increasing the lifetime of photoexcited electron-hole pairs (i.e. lowering their recombination rate) and the rate of the interfacial charge transfer process[62].

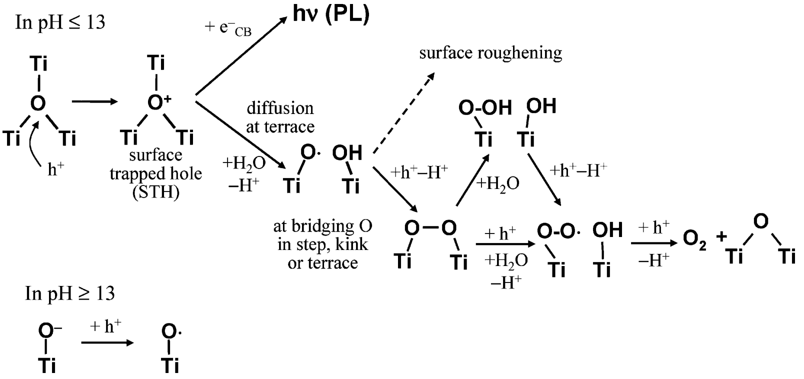

Figure 2.4: Reaction mechanism for water oxidation on a rutile TiO_2 surface[69].

---

[b] This means that a surface Ti−O−Ti bond with a hole trapped at the oxygen atom is broken by the water molecule, which donates an electron pair, resulting in $Ti{-}O^{\bullet}$, HO−Ti and a H^+ ion in solution.

2.2 Modifications of titanium dioxide nanomaterials

Titanium dioxide offers several advantages as a photoanode material for water splitting, as it highly stable over a wide range of pH values in aqueous environment upon illumination[7,70], abundant and relatively inexpensive; also, as discussed in Section 2.1.3, it can react with water through the OER and HER mechanisms (Equations (1.5) and (1.6)). However, it suffers from two main limitations: poor absorption in the visible region, as its bandgap is 3.0–3.2 eV, and limited quantum efficiency due to recombination processes[62]. Consequently, several strategies have been proposed in the literature to overcome these limitations, generally aiming at increase TiO_2 absorption towards the visible range, on the one hand, and increasing its charge carrier transportation/lowering the recombination rate, on the other hand. In this section, some of these approaches will be briefly reviewed; in particular, after a short description of the doping of TiO_2 (Section 2.2.1), those related to this Ph.D. project will be considered: the so-called “black titania” approach (Section 2.2.2), the introduction of noble metal plasmonic nanoparticles in TiO_2 (Section 2.2.3) and, finally, the exploitation of nanostructured forms of TiO_2, in particular hierarchical ones (Section 2.2.4).

2.2.1 Metal and non-metal doping

Metal doping. In order to obtain visible-light activity of TiO_2, several studies have been focused on metal doping[62,71], which results in impurity energy levels within the bandgap, either donors or acceptors, giving visible-light absorption. This is schematically illustrated in Figure 2.5A, for donors, and Figure 2.5B, for acceptors; in addition, Figure 2.5C illustrates the calculated densities of states (DOS) of TiO_2 compounds doped with 3d transition metals (V, Cr, Mn, Fe, Co and Ni), which create an occupied level either in the bandgap or in the valence band; as a result, the charge-transfer transition between the dopant level and the conduction band or valence band of TiO_2 contributes to the photoexcitation under visible light. Moreover, Figure 2.5 shows also the effects of different preparation methods for Cr-doped TiO_2 by Anpo *et al.*[72]: in the case of chemical methods (Figure 2.5D) no shift in the TiO_2 absorption edge is observed, but rather a band at 420 nm due to impurity energy levels in the bandgap, while ion implantation (Figure 2.5E) produces a smooth shift of the absorption onset towards the visible range.

Non-metal doping. On the contrary of metal dopants, non-metal ions are less likely to form donor levels in the bandgap; rather, they produce an upward shift of the valence band, as schematically illustrated in Figure 2.6A, motivated by the substitutional introduction of the non-metal dopant in the O lattice and mixing of 2p orbitals of the dopant and of O[71]. In addition, non-metal doping is considered more favorable than metal doping since the former introduces

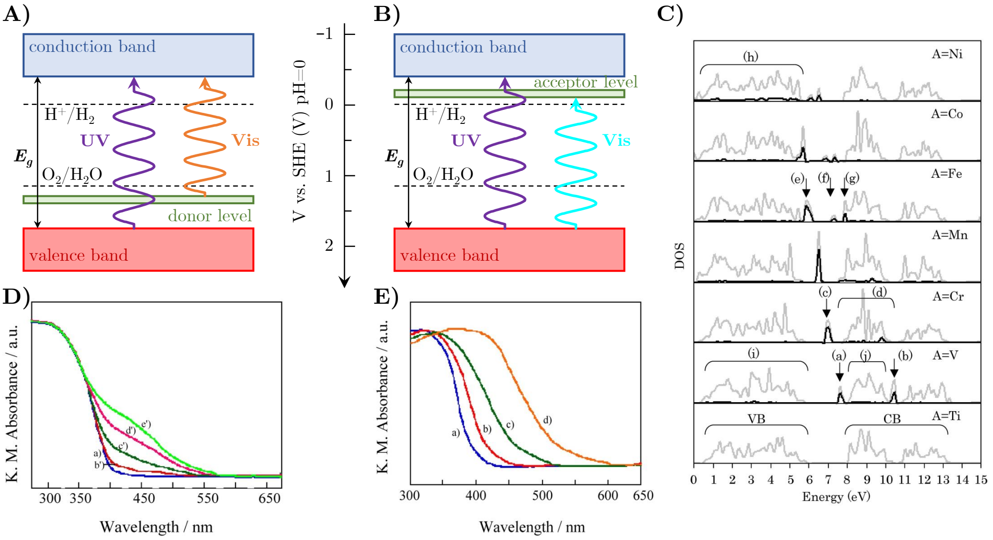

Figure 2.5: Effects of metal doping on the band structure and optical spectra of TiO_2. Schematics of the formation of a donor level **(A)** and an acceptor level **(B)**. **C)** Density of states of $A_xTi_{1-x}O_2$ (A = V, Cr, Mn, Fe, Co or Ni); gray lines: total DOS; black lines: dopant DOS; the states are labeled (a)–(k)[73]. **D)** Absorption spectra of Cr-doped TiO_2 by an impregnation method with different weight fractions, from 0 wt.% (a') to 1 wt.% (e')[72]. **E)** Absorption spectra of Cr-doped TiO_2 by ion implantation method with different weight fractions, from 0 wt.% (a) to 1.3 wt.% (d)[72].

a lower amouunt of recombination centers with respect to the latter[62]. In particular, Chen *et al.*[74] studied the effects of C, N and S dopants on TiO_2 with X-ray photoelectron spectroscopy (XPS), as shown in Figure 2.6B, finding additional electronic levels due to the dopants above the valence band of pure TiO_2. This observation was the basis to explain the "shoulder" and "tail-like" features in the optical spectra of these materials, as shown in Figure 2.6C. Nitrogen-doped TiO_2 (N-TiO_2), among all the other anion-doped forms, has been extensively investigated in the literature, starting from the work of Asahi *et al.*[75] due to its promising visible-light photoactivity (a review by the same authors[76] thoroughly discusses the advancements related to these materials). Finally, it should also be mentioned that the incorporation of multiple non-metal dopants, i.e. co-doping, has also been suggested as means to increase the TiO_2 absorption to the visible range[62]; a remarkable example is given by the so-called "red TiO_2", obtained by co-doping anatase microspheres with B and N (B to weaken the Ti–O bond and N as substitutional dopant), characterized by a bandgap of 1.94 eV on the surface (thus giving the red color) and of 3.22 eV in the core[77].

The various doping strategies briefly discussed above have succeeded in increasing the absorption of TiO_2 to the visible region and improving its photoactivity; however, the doping-induced energy levels can also act as

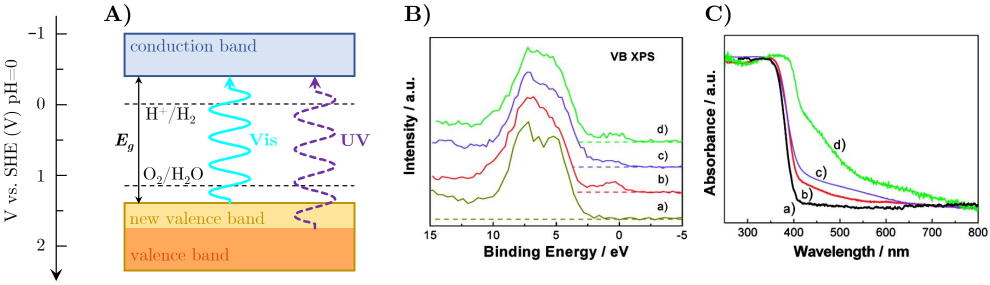

Figure 2.6: Effects of non-metal doping on the band structure and optical spectra of TiO_2. **A)** Schematics of the extension of the valence band. **B)** Valence band XPS spectra of pure TiO_2, C-TiO_2, S-TiO_2 and N-TiO_2[74]. **C)** Absorption spectra of pure TiO_2 (a), C-TiO_2 (b), S-TiO_2 (c) and N-TiO_2 (d)[74].

recombination centers, which has limited the improvements in solar water splitting activities of doped TiO_2, triggering alternative research pathways, as discussed in the following.

2.2.2 *Black titania* nanomaterials

A different approach than doping TiO_2 with aliovalent ions consists in the so-called *black titania* approach, namely hydrogenation/reduction of TiO_2. The purpose of this section is to give an overview on this modified form of TiO_2; a more detailed description can be found in some reviews[78,79] and a whole book[80]. It should be noted that this section will consider mainly the experimental results from a performance point of view, since their understanding is intimately related to the defect states induced in TiO_2, which is instead discussed more properly in Section 2.3.

Hydrogen treatment on TiO_2 crystals has been studied for decades and the consequent darkening of the material was discovered years ago; for instance, in the 50's Cronemeyer studied the absorption and conductivity properties of rutile single crystals, which indeed increased after the reduction treatment[58,81,82]. However, in 2011 Chen and co-workers reported an extensive bandgap decrease of anatase nanoparticles to around 1.5 eV, which indeed turned black (Figure 2.7A and 2.7B) by treating them under a 20 bar pure H_2 atmosphere at 200°C for 5 days[83]. These nanoparticles exhibited a well-ordered crystalline core surrounded by a disordered shell (Figure 2.7C), the presence of Ti–OH bonds and a valence band shift to higher energies (by XPS measurements); a remarkable photocatalytic activity was also demonstrated by decomposition of organic pollutants as well as H_2 generation from water-methanol solution (with 0.6 wt.% Pt co-catalyst). By considering these experimental findings, the authors performed DFT calculations, showing that the disordered shell could induce mid-gap electronic states, while the role of hydrogen was to stabilize the surface disorder by saturating dangling bonds; thus, they proposed the schematic density of states model in Figure 2.7D.

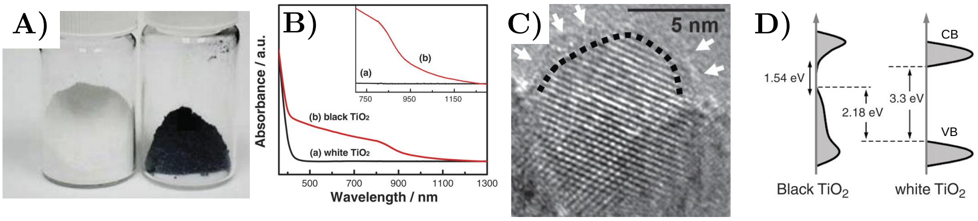

Figure 2.7: Black anatase nanoparticles produced by high-pressure pure hydrogen treatment. **A)** Pictures of white and black TiO_2. **B)** Optical absorption spectra of white (a) and black (b) TiO_2. **C)** High-resolution TEM image of black TiO_2 nanoparticles. **D)** Schematic illustration of the density of states of black TiO_2, compared to that of unmodified anatase (VB: valence band; CB: conduction band). Adapted from [83].

In the same year, Wang *et al.*[84] prepared hydrogenated rutile nanowire arrays by annealing in ultra-high purity H_2 atmosphere at ambient pressure for 3 h at various temperatures, from 200°C to 550°C (Figure 2.8). The hydrogenated nanowires showed a dark color (the darker the higher annealing temperature, Figure 2.8A), no evident structural changes and enhanced photocurrents in three-electrode cell experiments (with a maximum at 350°C annealing temperature, Figure 2.8B). Incident photon-to-current efficiency (IPCE) measurements, on the other hand, showed a substantial increase in the UV range, but negligible activity in the visible one (Figure 2.8C); this observation was related to the increase of charge carrier density, evaluated by Mott-Schottky plots (Equation (1.19)), from pristine TiO_2 ($\sim 5 \cdot 10^{18}\,\mathrm{cm}^{-3}$) to TiO_2 hydrogenated at 350°C ($\sim 10^{22}\,\mathrm{cm}^{-3}$). The authors, consequently, concluded that oxygen vacancies provided more charge carriers (electrons) enhancing the photoactivity in the UV range as well as produced a darkening of the samples without any bandgap narrowing nor visible-light activity.

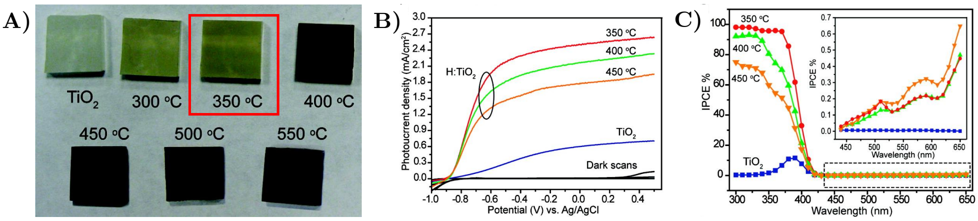

Figure 2.8: Pristine (TiO_2) and hydrogen-treated ($H{:}TiO_2$) rutile nanowire arrays. **A)** Digital pictures. **B)** Photocurrent density curves obtained in a three-electrode cell with Ag/AgCl reference electrode, Pt wire as counter electrode and 1 M NaOH (pH = 13.6) electrolyte under solar simulated illumination (100 $\mathrm{mW/cm^2}$ from a 150 W xenon lamp and AM 1.5G filter). **C)** IPCE spectra collected in the range 300–650 nm at a potential of −0.6 V vs. Ag/AgCl; inset: magnified IPCE spectra highlighted in the dashed box[84].

These first reports triggered a world-wide interest in black TiO_2 nanomaterials[78,79] and several strategies have been employed to produce them; considering only TiO_2 thin films (for a more appropriate comparison to this thesis work), annealing treatments in H_2 at high pressure[85,86], in pure H_2 at environmental pressure[87–89], in Ar/H_2 atmosphere[90–96] and in vacuum[97] have been reported.

In particular, Hoang *et al.*[90] prepared rutile TiO_2 nanowires and compared the effects of thermal treatments in NH_3 and Ar/H_2 (95%-5%) atmospheres (N-TiO_2 and H-TiO_2, respectively), also combining the two annealing treatments (Ar/H_2 annealing followed by NH_3 annealing, H,N-TiO_2), as illustrated in Figure 2.9A and 2.9B. Hydrogen treatment showed a dramatic IPCE increase (Figure 2.9B), similarly to the study of Wang *et al.*[84], but not an increased absorption in the visible range (the color of the film did not change), while NH_3 and, mainly, Ar/H_2+NH_3 treatments resulted in a increased absorption and photoactivity in the visible range (Figure 2.9A), explained with the electron transfer from Ti^{3+} defect states to substitutional N atoms.

On the other hand, as most of the studies mentioned above did not reproduce the original high-pressure hydrogen treatment of Chen *et al.*[83], Liu and co-workers[85] compared the effects of various annealing conditions on anatase TiO_2 nanotubes and rutile TiO_2 nanorods, including a “standard” air annealing, a pure Ar or Ar/H_2 (95%-5%) annealing at environmental pressure and a high-pressure H_2 (HPH) treatment at 20 bar; all of them were performed at 500°C for 1 h. They showed that only the HPH treatment on anatase nanotubes led to open-circuit photocatalytic activity without the need of a co-catalyst, while in the other cases no activity was measured (Figure 2.9C); this was attributed to the formation of Ti^{3+} defect states with different features than all the other conventional reduction treatments, having the role of intrinsic co-catalytic centers. Conversely, in PEC water splitting experiments the Ar/H_2-annealed rutile nanorods showed better performance with respect to HPH-annealed anatase nanotubes thanks to their single-crystal nature and, thus, their higher conductivity.

From the brief discussion above, it is evident how the different morphological/structural properties of the pristine TiO_2 material as well as the hydrogenation/reduction conditions strongly affect the properties and performances of *black titania* nanomaterials reported in the literature by various research groups. In addition, it is important to note that the dark color by itself is not an evidence of visible-light activity: indeed, IPCE measurements on *black titania* thin films obtained with thermal treatments in hydrogen atmosphere[84,89,90,93,95,98] as well as with electrochemical reduction methods[99,100] and with hydrogen plasma treatment[93,101] show that an evident quantum efficiency increase occurs only in the UV range upon hydrogenation, while the enhancement in the visible region (almost)

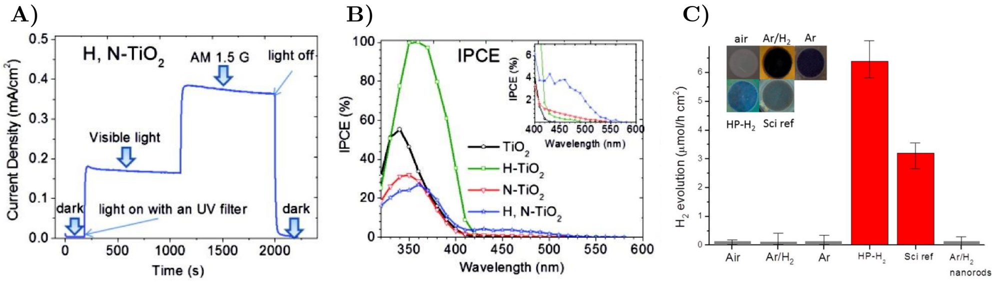

Figure 2.9: **A)** Chronoamperometry at 1.23 V vs. RHE of the H,N-TiO_2 rutile nanowires[90]. **B)** IPCE spectra measured at 1.23 V vs. RHE for pristine TiO_2, H-TiO_2, N-TiO_2 and H,N-TiO_2[90]. **C)** Photocatalytic H_2 production under open circuit conditions in methanol/water (50%-50% vol.) with TiO_2 nanotubes and nanorods treated in different atmospheres[85].

negligible. On the contrary, in the first work by Chen *et al.*[83] the extensive bandgap narrowing could suggest a remarkable visible-light activity.

In all the cases mentioned above the modified properties have been explained with either chemical or structural changes induced by reducing treatments, such as surface lattice disorder, oxygen vacancies, Ti^{3+} ions, Ti–OH and Ti–H bonds[78,79]. These alterations, which can be generally considered as defects in TiO_2, will be discussed in more detail in Section 2.3 in comparison to those expected in untreated TiO_2, which naturally occurs as *n*-type semiconductor due to the presence of oxygen vacancies; some insights on their possible influence on the functional properties of *black titania* nanomaterials will be also provided.

2.2.3 Plasmonic-enhanced water splitting

The decoration of the surface of TiO_2 with noble-metal (Au, Pt) nanoparticles has been extensively exploited in photocatalytic water splitting, since they act as electron traps to collect electrons from the semiconductor, which then react with protons to generate hydrogen[70]; on the other hand, oxygen-evolution co-catalysts, such as IrO_2, are employed in photoelectrochemical arrangements to lower the overpotential associated to the oxygen evolution reaction (OER)[102]. On a different point of view, noble metal nanoparticles can be employed both in photocatalytic and photoelectrochemical water splitting experiments in order to exploit a peculiar properties related to their nanoscale dimension, the so-called *localized surface plasmon resonance* (LSPR)[103–105]. Briefly, this is a phenomenon which occurs when conduction electrons in a nanoparticle harmonically oscillate in response to an oscillating electric field, such as that provided by the electromagnetic radiation; these coherent oscillations of charge density and electric field are called localized surface plasmons and decay in the timescale of 10 fs[104]. The frequency at which the conduction electrons oscillate with minimal power dissipation is called the plasmon resonance frequency. These phenomena are well-known in physics, and the plasmon frequency can be calculated for a single spherical particle with the Mie theory[106]. The LSPR of metal nanoparticles typically results in a well-defined absorption peak in optical spectra, as illustrated in Figure 2.10A, which illustrates that the extinction (defined as the sum between absorption and scattering) spectra of noble metal nanoparticles fall in the visible region of the electromagnetic spectrum. The plasmon resonance frequency depends not only on the chemical species of the metal, but also on the size and shape of metallic nanostructures, as illustrated in Figure 2.10B and 2.10C, and on the surrounding medium[103,104]. This suggests that the plasmon resonance frequency can be tuned by controlling one (or more) of these parameters, which enables the realization of noble metal/semiconductor integrated materials with controllable properties for applications (see below).

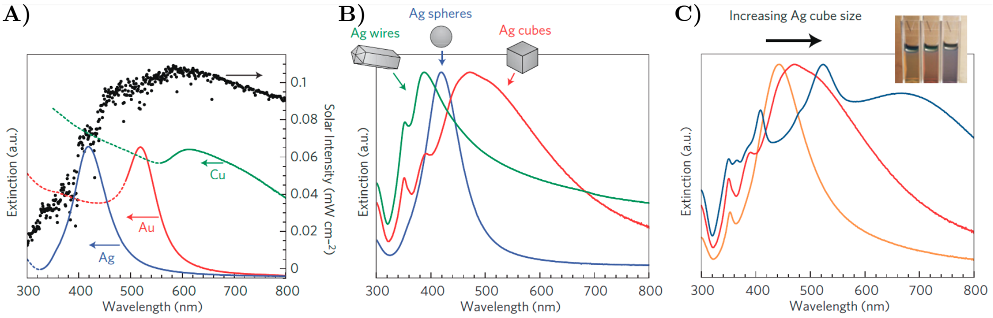

Figure 2.10: Plasmonic properties of noble metal nanoparticles. **A)** Normalized extinction spectra of spherical Ag (38 nm diameter), Au (25 nm) and Cu (133 nm) particles; the AM 1.5G solar spectrum is also shown with black dots, while dashed portions in metal extinction curves represent interband transitions. **B)** Normalized extinction spectra for Ag nanostructures (wires, spheres and cubes). **C)** Normalized extinction spectra of Ag nanocubes as a function of size (from about 56 nm to 130 nm). The inset shows colloidal suspensions of these nanocubes in ethanol[103].

In the limit for small particle radius with respect to the incident wavelength, i.e. $r \ll \lambda$, the extinction cross section mentioned above is defined as $C_{ext} = C_{abs} + C_{scat}$, where $C_{abs} \propto r^3$ is the absorption cross-section and $C_{scat} \propto r^6$ is the scattering cross-section[107]. Thus, the absorption cross-section dominates over the scattering one for small particles (lower than 40-50 nm), while the reverse occurs for bigger dimensions[108]. This observation suggests that different mechanisms can occur upon the decay of a plasmonic excitation. Indeed, after the comprehension of plasmonic enhancement effects in the field of photovoltaics[109], investigations aiming at elucidating those occurring in the case of water splitting were also undertaken. In this context, Figure 2.11 schematically illustrates the most relevant processes induced or affected by the presence of a metal nanoparticle in contact (direct or with a dielectric shell) with a semiconductor material[104]. Without entering in the details (a growing literature on plasmonics for water splitting applications is available[103–105,110,111]), some of these mechanisms relevant for this thesis work (in particular, for the results presented in Chapter 7), will be briefly discussed in the following, considering some "case studies" showing direct evidences beneath.

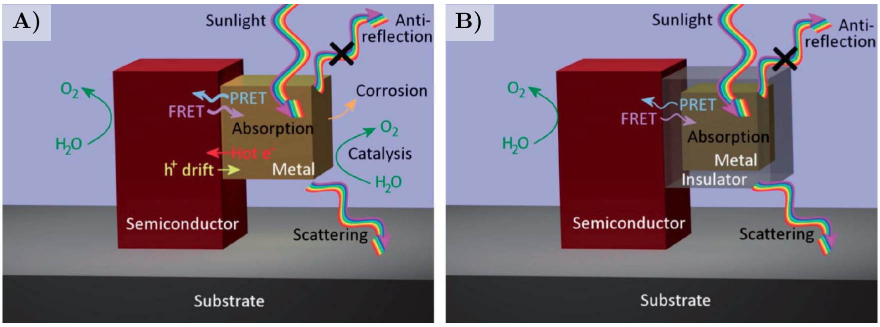

Figure 2.11: Schematic illustration of the most relevant effects of a metal nanoparticle coupled with a semiconductor material. **A)** Direct contact between metal and semiconductor. **B)** The metal nanoparticle is surrounded by a dielectric shell[104].

Plasmonic mechanisms in literature studies

Hot electron injection (or direct electron transfer). After the absorption of incoming photons by the metal nanoparticle and the excitation of the LSPR, the plasmon can decay giving rise to hot electrons, having higher energies with respect to the Fermi level of the metal; subsequently, these can either thermalize or be transfered to an adjacent semiconductor material, since their energy is typically higher than the Schottky barrier at the metal/semiconductor interface (if any), or even by tunneling effect[112]. Thus, an injection of charge carriers in the conduction band of a semiconductor can occur even for photon energies lower than the bandgap, as in the case of noble metal nanoparticles coupled with wide bandgap semiconductors, such as TiO_2. For this mechanism to happen, it is crucial not only a direct metal-semiconductor contact, but also a low size of the metal nanoparticle/nanostructure (10–20 nm), as it is related to a much wider energy distribution of hot electrons produced by the plasmon decay[113].

The first experimental demonstration of this effect was reported by Tian and Tatsuma[114] for a TiO_2 film coupled with Au nanoparticles; they reported that both the open circuit potential and the IPCE curve (measured in a three-electrode cell) followed the trend of the absorption spectrum of the Au-TiO_2 film, exhibiting a LSPR peak at about 550 nm. The authors proposed that the charge separation at the Au nanoparticles involved an electron transfer from the former to the TiO_2 conduction band as well as an electron regeneration provided by an irreversible donor in the electrolyte (methanol), as illustrated in Figure 2.12A. Other studies suggesting a hot electron transfer have been reported in the following years[115–119]. Remarkably, Mubeen *et al.*[117] demonstrated the possibility of performing water splitting with gold nanorod arrays, able to generate all the charge carriers involved in the OER and HER upon the excitation of the localized surface plasmon resonance of the nanorods; these were also covered with a TiO_2 cap layer decorated with Pt nanoparticles (as hydrogen evolution catalysts) and with a cobalt-based oxygen evolution catalyst (Figure 2.12B and 2.12C).

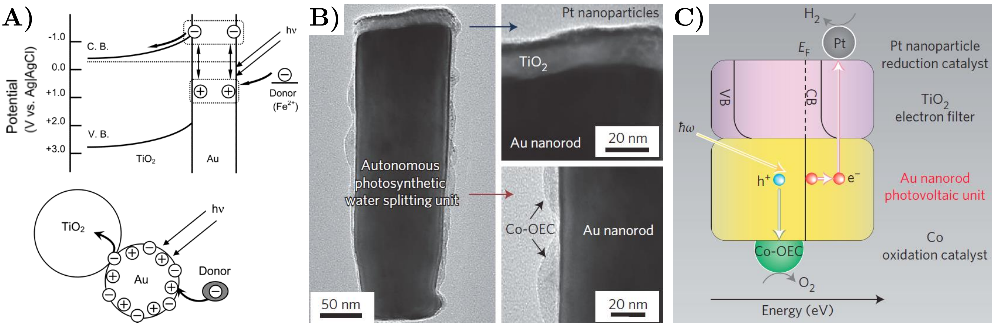

Figure 2.12: A) Illustration of the proposed charge-separation process of the hot electron injection mechanism in Au-TiO_2 under visible light[114]. **B)** TEM image of the plasmonic photosynthetic unit based on Au nanorod, a TiO_2 cap layer decorated with Pt nanoparticles and a cobalt-based oxygen evolution catalyst, while its working mechanism is illustrated in **C)**, where CB and VB are the conduction and valence bands of the TiO_2 cap layer[117].

Plasmon resonant energy transfer (PRET). In this process, the energy of a plasmonic oscillation is transferred from the metal nanoparticle to the semiconductor through an electromagnetic field or a dipole-dipole interaction[104,120]. Indeed, the electromagnetic field close to the plasmonic material (near field) can be intensified by order of magnitudes, so that the generation of electron/hole pairs is greatly enhanced (as it is proportional to the square modulus of the local electric field)[104]. This effect can reduce the thickness required by the semiconductor to completely absorb light; in addition, a spectral overlap between the plasmonic extinction and the semiconductor absorption range must be present (even though a dipole-dipole interaction between the semiconductor and the plasmonic material giving rise to PRET mechanism without spectral overlap has also been reported[121]).

Ingram and Linic[122] studied the photoelectrochemical water oxidation performance of Ag/N-TiO_2 (nitrogen-doped TiO_2) and Au-TiO_2 composites; Ag nanocubes with 120 nm side exhibited LSPR peaks at approximately 410 and 580 nm, while Au nanoparticles of 25 nm diameter showed a peak at 520 nm and a shoulder at 680 nm. Since the N-TiO_2 had an absorption onset at 500 nm, it did not exhibit a spectral overlap with the Au nanoparticles and no enhancement was observed, on the contrary of what happened with Ag nanocubes, consistently with a PRET mechanism (Figure 2.13A). Liu *et al.*[123] prepared a discontinuous Au layer (5 nm) onto a TiO_2 film and a clear increase in photocurrent under visible-light irradiation in correspondence with the localized plasmon resonance wavelength (532 nm) was measured; this was explained by means of finite-difference time domain (FDTD) simulations, suggesting the crucial role of PRET mechanism (Figure 2.13). Finally, a study by Pu and co-workers[124] should be mentioned as it showed how both hot electron injection and PRET mechanisms could occur in the Au-TiO_2 system according to the different excitation wavelength (UV or visible) and the nanostructured form of Au (nanoparticles or nanorods).

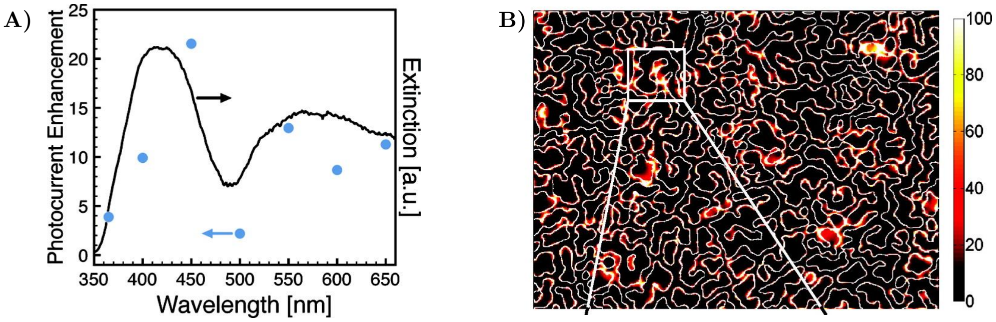

Figure 2.13: A) Photocurrent enhancement factor (left) and optical extinction spectrum (right) of Ag/N-TiO_2[122]. **B)** Electric field intensity at the Au-TiO_2 interface calculated using FDTD methods starting from a top-view SEM image[123].

Other plasmonic mechanisms and final remarks. Apart from hot electron injection and PRET, other plasmonic mechanisms can occur; for instance, scattering effects are maximized for particles larger than 100 nm and can be useful to increase the optical path of the elctromagnetic radiation within the semiconductor; the Förster resonant energy transfer (FRET) is a sort of backward reaction with respect to PRET, and involves a quenching of the excited state in the semiconductor due to the presence of a metal nanoparticle; catalytic and corrosion effects are other mechanisms not related to the localized plasmon resonance, but to the metal/semiconductor contact, and should be discerned (or avoided, in the case of corrosion) in order to correctly interpret the experimental results[104].

In the framework of this thesis work and on the basis of the most frequently reported results, the most interesting plasmonic mechanisms are the hot electron injection and PRET; accordingly, the preparation of Au nanoparticles with sizes (in the range 5–20 nm) compatible with these mechanisms was pursued through dedicated experiments, as well as the integration of the so-obtained nanoparticles with TiO_2 hierarchical nanostructures similar to those which will be presented in the following section. These results will be presented in Chapter 7.

2.2.4 Nanostructured morphologies

The interest in nanostructured semiconductor materials for water splitting applications has already been introduced in Section 1.5.6, where it was motivated in terms of increase of specific surface area and decoupling the overall thickness with the maximum charge collection length. In addition, a mesoporous structure has been adopted to reduce the probability of charge-carrier recombination because such a structure is composed of particles of smaller size[70]. However, it should be mentioned that the nanoscale architecture can create quite different localized processes. Therefore, a well-designed nanostructured material should be realized by taking into consideration the following aspects[125].

- Reflections: with an appropriate design, reflected photons can be scattered within the material porosity to increase the absorption probability.
- Charge carrier transport/recombinations: a reduced particle size allows a shorter diffusion length for charge carriers to the electrolyte, but it may also decrease the mobility and the diffusion coefficient of electrons due to higher electron-phonon interactions (polarons) at inter-particle interfaces such as grain boundaries. In addition, electron-hole recombination is more likely at active sites such as vacancies, defective surfaces, etc., which are increased by nanostructuring. Sintering effects between nanoparticles/nanocrystals, by means of thermal treatments, usually lower the number of grain boundaries, favoring an efficient charge transport, while surface pre-treatments or introduction of electrocatalysts can minimize surface recombination.
- Surface structure: charge transfer at the semiconductor/electrolyte interface can undergo different mechanisms depending on the exposed crystal facets; for instance, the {001} facet of anatase crystals exhibited a lower reactivity than the {101} one in photooxidation reactions for generating OH radicals[126].
- Lattice disorder: oxygen vacancies are beneficial for PEC performance, e.g. they can act as electron donors[84]; however, defects are also active sites for charge carrier recombination, thus their role is not straightforward and both effects must be taken into consideration.

Among the various nanostructured morphologies discussed in the literature, one-dimensional (1D) nanostructures (such as nanowires, nanotubes, nanorods...) are considered favorable for charge transfer and thus reduced recombination of electron-hole pairs, and they have attracted more and more attention in photocatalytic/photoelectrochemical applications. For instance, Grimes and co-workers prepared TiO_2 nanotubes with a length of 45 µm by an anodizing method, achieving a photocurrent of 26 $mA\,cm^{-2}$ under UV irradiation[127]. TiO_2 nanotubes by Ti anodization, indeed, have been extensively studied in literature[128,129]. In the following, thus, the discussion will be focused on a particular kind of *quasi*-1D nanostructures, characterized by a hierarchical morphology, which are the object of this thesis work.

Titanium dioxide hierarchical nanostructures

Titanium dioxide hierarchical nanostructures, also called "nanoforests" or "tree-like" nanostructured films, have been frequently prepared by hydrothermal synthesis and applied for many energy related purposes; these type of architectures, combining 1D and 3D elements, could be more interesting than nanorod arrays due to their higher porosity, specific surface areas and light-scattering properties[130]. An alternative method, in the framework of physical vapor deposition (PVD) techniques, is pulsed laser deposition (PLD), which is described in detail in Section 3.2.1. The peculiar hierarchical growth of these nanostructures, as illustrated in Figure 2.14, is characterized by features at different length scales: the whole assembly (the "forest", Figure 2.14A) with thickness of typically few µm, the single columnar structures (the "trees", Figure 2.14B and 2.14E) with a diameter of 100-200 nm and the nanometric particles (the "leaves", Figure 2.14C). TEM images of such nanostructures are shown in Figure 2.14D and 2.14E, the former at higher magnification, showing the high crystallinity (anatase phase) of individual nanoparticles obtained after air annealing at more than 400°C.

Pulsed laser deposition has been employed for the realization of TiO_2 hierarchical nanostructures by researchers at Micro- and Nanostructured Materials Laboratory[133–138], as well as by other groups[132,139–142]. In these studies,it was shown that the properties of the as-deposited TiO_2 hierarchical film can be controlled with the PLD process parameters (as explained also in Section 3.2.1)[131]: the morphology and density can vary from a compact, columnar film (with a porosity of about 50%) for low background pressure values to aerogel- or foam-like structures (with a porosity higher than 90%) obtained at high background pressures (such as 100 Pa of synthetic air)[133]; accordingly, the specific surface area can be controlled from tens to hundreds of m^2/g[133,137,141]; the crystalline structure can be also controlled directly during the growth by increasing the background O_2 gas pressure[134], even though in most typical conditions an amorphous material is obtained and a crystallization thermal treatment (such as in air at 400 or 500°C) is

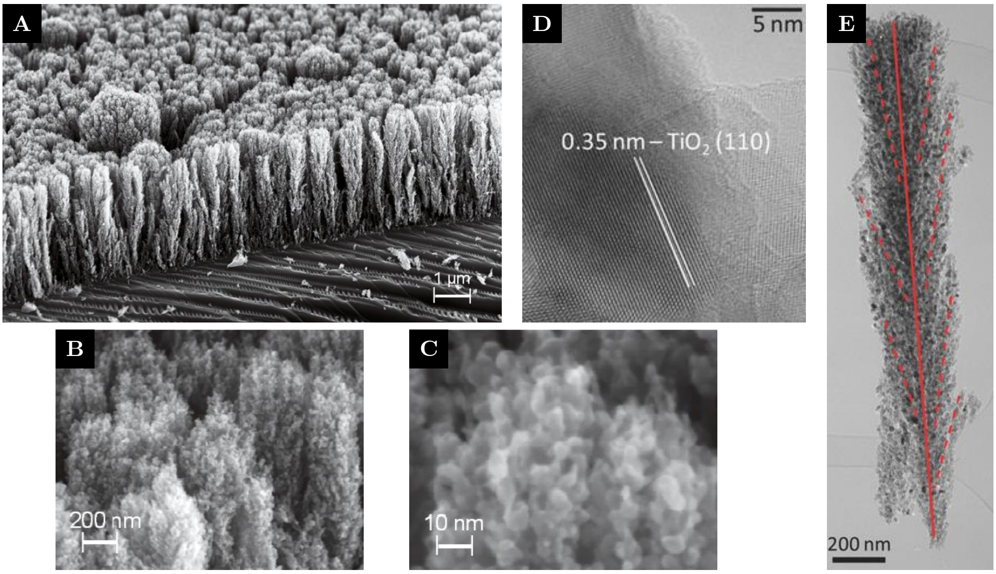

Figure 2.14: TiO_2 hierarchical nanostructures prepared by PLD: SEM images **(A–C)** of a TiO_2 film deposited at 40 Pa of O_2 at different magnifications[131] and TEM images **(D, E)** of a film deposited at 7 Pa of O_2[132].

needed[133,135,137,141]; the oxide phase obtained after annealing can also be influenced by the background gas pressure[133].

All the aforementioned properties of TiO_2 hierarchical nanostructures make them interesting for applications where the surface plays a central role; indeed, in the past years they were applied to photocatalysis[133], solar cells[132,135,139–142] and water splitting[137,138].

In particular, more recent studies on water splitting should be considered in more detail as they represent the prelude for this Ph.D. thesis. In a previous work, indeed, the correlation between the morphology of TiO_2 nanostructured films (depending mainly on O_2 background gas pressure) and their photoelectrochemical properties was investigated[137]. Three different morphologies were explored, as illustrated in Figure 2.15A–C, which exhibited a clear trend in photocurrent results under UV illumination (Figure 2.15D), resulting in an optimum performance for the photoanode obtained at 5 Pa of O_2 background gas. This was ascribed to an optimized balance between a large enough specific surface area and a good charge carrier separation and transport with reduced recombinations, ensured by nanoparticles connectivity and crystallinity; higher background gas pressures would lead to excessive porosity and surface defects. In addition, the effect of annealing temperature was also evaluated (not shown), showing that optimum results were obtained at 650°C, due to an effective sintering effect between nanocrystals, while at 800°C a high coalescence within the hierarchical structure leading to the decrease of surface area was observed. The most effective morphology emerging from this study, thus, i.e. TiO_2 hierarchical film obtained at 5 Pa of pure O_2, will be considered as a benchmark for the experimental investigations presented in Chapter 4.

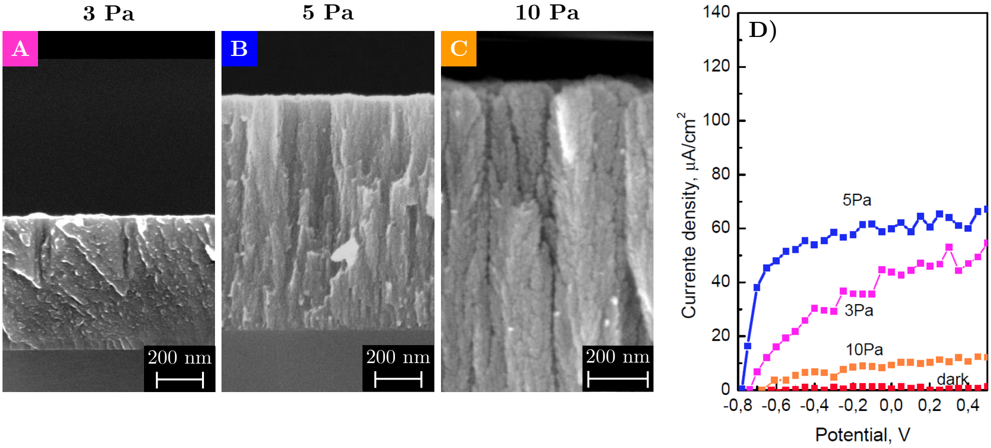

Figure 2.15: TiO_2 hierarchical photoanodes for photoelectrochemical water splitting, obtained by ablating a TiO_2 target in various O_2 background pressures (from 3 to 10 Pa) with post-annealing treatments in air at various temperatures (500°C, 650°C and 800°C). SEM images of the as-deposited films **(A–C)** and photocurrent results **(D)**[137].

2.3 Defect chemistry of (reduced) titanium dioxide

Bulk titanium dioxide, both in the anatase and rutile crystalline forms, is a non-stoichiometric compound with an intrinsic n-type conductivity[143]; both oxygen vacancies and Ti interstitials are considered as the predominant defects and typically the formula TiO_{2-x} is assumed, where x represents the oxygen deficiency. Conversely, p-type conductivity may be obtained with prolonged oxidation of TiO_2, which promotes the formation of Ti vacancies[143]; in this case, the correct formula is TiO_{2+x}.

Typically, TiO_2 is described as a fully ionic solid, in which the oxidation states are +4 for Ti and −2 for O. Assuming the correctness of this description[c], the typical intrinsic defects in TiO_2 can be divided into two categories: ionic defects, such as oxygen vacancies or Ti interstitials, and electronic defects, such as holes located on O^- lattice ions and electrons localized on Ti^{3+} lattice ions[143]. The typical defects found in TiO_2 are summarized in Table 2.2 using

---

[c] The assumption of +4 and −2 as the oxidation states of Ti and O atoms, respectively, has been recently criticized by Koch and Manzhos[144], who suggested a +3 charge state for Ti by means of DFT calculations; however, these results have been debated[145,146].

the traditional and Kröger-Vink notations[147]; even though the latter is more precise, the former is more intuitive and it will be adopted in the following.

Table 2.2: Ionic and electronic defects in TiO_2 according to the traditional and Kröger-Vink notations.

Description	Trad.	Kröger-Vink
Ti^{4+} ion in the titanium lattice site	Ti_{Ti}^{4+}	$Ti_{Ti}^{\times}$
O^{2-} ion in the oxygen lattice site	O_{O}^{2-}	$O_{O}^{\times}$
Ti^{3+} ion in the titanium lattice site (quasi-free electron)	Ti_{Ti}^{3+}	e'
O^{-} ion in the oxygen lattice site (quasi-free hole)	O_{O}^{-}	$h^{\bullet}$
Ti^{4+} ion in the interstitial site	Ti_{i}^{4+}	$Ti_{i}^{\bullet\bullet\bullet\bullet}$
Ti^{3+} ion in the interstitial site	Ti_{i}^{3+}	$Ti_{i}^{\bullet\bullet\bullet}$
Titanium vacancy (tetra-valent)	V_{Ti}	$V_{Ti}^{''''}$
Oxygen vacancy (doubly-ionized)	V_{O}	$V_{O}^{\bullet\bullet}$

Among the defects in TiO_2, oxygen vacancies have received a particular attention since they are typically found in undoped TiO_2, as mentioned above, which, even without intentional modifications, exhibits a slight n-type conductivity; the conductivity, then, can be enhanced by employing thermal treatments in reducing atmospheres, as shown since the 50's by Cronemeyer for rutile[58,81,82]. Indeed, oxygen vacancies have been extensively studied both theoretically and experimentally and they affect the electronic structure, charge transport and surface properties of TiO_2[148].

Fully-ionized oxygen vacancies (V_O) have a +2 charge and they are expected at equilibrium at elevated temperatures; however, at moderate temperature their ionization degree may vary, thus singly-ionized oxygen vacancies (V_O^-) or neutral oxygen vacancies (V_O^{2-}) can be found[143,148,149]. Their formation mechanisms are shown in Equations (2.2) to (2.4) and, in a simplified pictorial way, in Figure 2.16. First, starting from a perfectly stoichiometric TiO_2 lattice (Figure 2.16A), an oxygen atom is removed, resulting in a doubly-ionized oxygen vacancy as well as two lattice Ti^{3+} sites, as shown in Equation (2.2) and Fig. 2.16B; then, both of them can return to a full ionization degree (+4 charge) by Equations (2.3) and (2.4), in which the ionization degree of the oxygen vacancy changes as well (from doubly-ionized to neutral).

$$O_O^{2-} + 2\,Ti_{Ti}^{4+} \rightleftharpoons V_O + 2\,Ti_{Ti}^{3+} + \frac{1}{2}\,O_2(g) \qquad \text{formation of } F^{++} \text{ centers} \tag{2.2}$$

$$V_O + Ti_{Ti}^{3+} \rightleftharpoons V_O^{-} + Ti_{Ti}^{4+} \qquad F^{++}/F^{+} \text{ centers} \tag{2.3}$$

$$V_O^{-} + Ti_{Ti}^{3+} \rightleftharpoons V_O^{2-} + Ti_{Ti}^{4+} \qquad F^{+}/F \text{ centers} \tag{2.4}$$

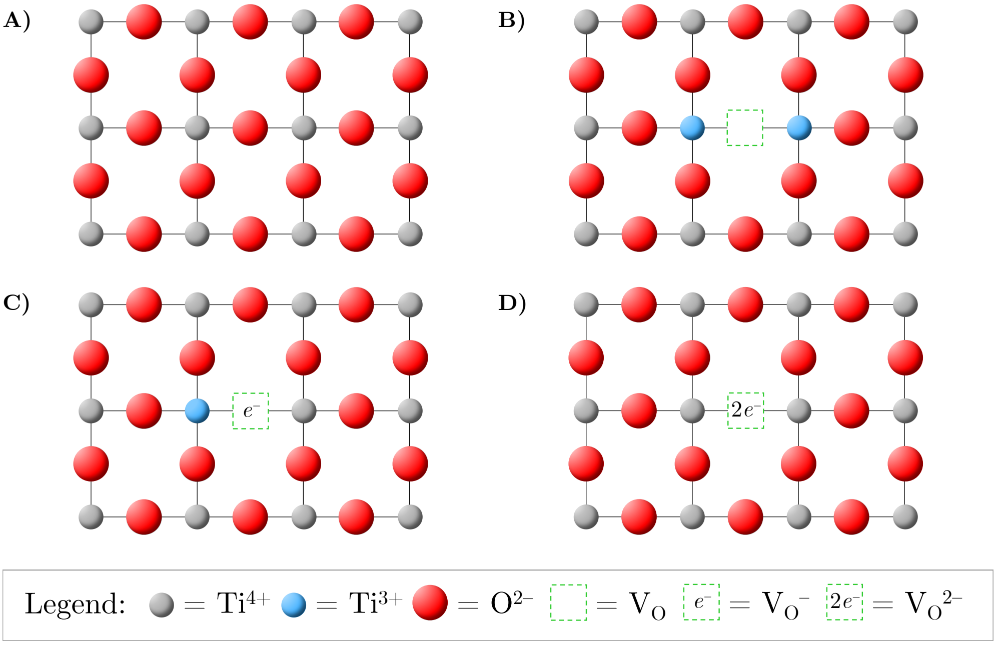

Figure 2.16: Schematic representation of a TiO_2 lattice with perfect stoichiometry **(A)** and oxygen vacancies with different ionization degrees **(B–D)**.

Oxygen vacancies are an example of the so-called *color centers* or *F-centers* (from the German word for color, *Farbe*); for this reason, Equations (2.2) to (2.4) are labeled with an F letter displaying also the ionization degree. When an electron is trapped in an oxygen vacancy (more generally in an anionic vacancy), it can absorb light in the visible spectrum, giving rise to a coloration of an otherwise transparent material. This is illustrated in the following mechanisms[150]: above-bandgap excitation results in the formation of electron-hole pairs (Equation (2.5)); electrons in the conduction band can be trapped in oxygen vacancies, changing the ionization degree of the vacancy (Equation (2.6)); then, the interaction of the vacancy "filled" by electrons with a hole in the valence band can lead to a radiative recombination (Equation (2.7)). In addition to that shown in Equations (2.5) to (2.7), other recombination pathways can also be present, such as involving other kinds of traps[151] (i.e. photoexcited electrons trapped in Ti_{Ti}^{3+} ions or photoexcited holes trapped in O_O^- ions), resulting in different emission energies, or non-radiative ones.

$$TiO_2 + h\nu \longrightarrow e_{CB}^- + h_{VB}^+ \qquad \text{photoexcitation} \tag{2.5}$$

$$V_O^- + e_{CB}^- \rightleftharpoons V_O^{2-} \qquad \text{electron trapping} \tag{2.6}$$

$$V_O^{2-} + h_{VB}^+ \longrightarrow V_O^- + h\nu \qquad \text{radiative recombinations} \tag{2.7}$$

The complexity of studying the defect states in TiO_2, typically considering n-type/reduced TiO_2, may be already evident from the brief discussion above; moreover, it is increased by the similarity between oxygen vacancies and titanium interstitials (which have not been considered above) from the energetic or spectroscopic points of view, as they typically induce localized states in the bandgap of TiO_2 with a wide spectrum of energetic positions with respect to their ionization degree and the allotropic phase (i.e. anatase or rutile). Considering only anatase (as the materials studied in this thesis work are typically crystallized in this phase), DFT calculations by Di Valentin *et al.*[152] suggest that Ti^{3+} species in bulk anatase have different energies according to their nature: a) sixfold-coordinated Ti^{3+} species bound to OH groups, i.e. $Ti^{3+}_{6c}-OH$, associated to H doping, have an energy of 0.4 eV below the conduction band minimum (CBM); b) under-coordinated bulk Ti^{3+}_{5c} species, associated with oxygen vacancies formed upon thermal treatment, have an energy of 0.7 eV below the CBM; c) interstitial Ti^{3+} sites, moreover, are located 0.8 eV below the CBM and they can be formed by diffusion phenomena upon high temperature annealing. DFT calculations also suggest that oxygen vacancies are more stable at subsurface rather than surface sites in anatase, whereas they are favored in bridging sites[d] on the (110) surface of rutile[153], which could suggest a good stability of oxygen vacancies with respect to environmental exposure, explaining the typically observed n-type behavior of anatase. On the other hand, different energetic positions for oxygen vacancies with different ionization degrees have been computed, resulting in a *shallow* behavior for neutral ones and *deep* behavior for singly- or doubly-ionized ones[154–156]. Further theoretical insights on the role of oxygen vacancies and other defects in TiO_2 investigated with theoretical methods can be found in reviews[157].

Oxygen vacancies have been directly observed with STM experiments, typically on the (110) surface of rutile[41], where their direct role in the dissociation of the water molecule has also been observed[158,159]. Apart from these delicate experiments, oxygen vacancies (and other defects in TiO_2) can be investigated with spectroscopic techniques, such as X-ray photoelectron spectroscopy (XPS), electron paramagnetic resonance (EPR) spectroscopy and photoluminescence (PL) spectroscopy[148]. More insights related to photoluminescence spectroscopy are discussed in detail in relation to experimental results presented in Chapter 6, thus they will not be discussed in the present section. Considering EPR spectroscopy, instead, Nakamura *et al.*[160] performed a plasma treatment on TiO_2 samples and assigned a spectral feature at $g = 2.004$ in EPR measurements at 77 K to electrons trapped in oxygen vacancies (thus V_O^-), formed by the plasma irradiation

---

[d] Twofold-coordinated O_{2c} oxygen atoms between two parallel rows of fivefold-coordinated Ti_{5c} atoms[41].

treatment. An interesting experiment in this regard, also in the framework of *black titania*, is that reported by Liu and co-workers[161], who performed EPR experiments during a hydrogen thermal treatment, as illustrated in Figure 2.17. During the process, the interaction between H_2 and TiO_2 can be divided into three steps:

- for $T < 300$ °C, hydrogen removes the adsorbed oxygen on the TiO_2 surface, as shown by the disappearance of its EPR signals;
- for $T > 300$ °C, formation of oxygen vacancies occurs, forming H_2O molecules;
- for $T \simeq 450$ °C, electrons from H atoms are transferred to Ti^{4+} sites forming Ti^{3+} defects;
- for $T \simeq 560$ °C, more energy is supplied to electrons located on oxygen vacancies, which are removed away and transferred to Ti^{4+} ions, resulting in a decrease of the EPR signal for oxygen vacancies and increase for that of Ti^{3+} sites, up to $T = 600$ °C.

Moreover, it has been reported that Ti interstitials can also be formed by hydrogen treatment and that they form more probably in rutile with respect to anatase and in more severe conditions (i.e. high temperature or vacuum annealing)[148].

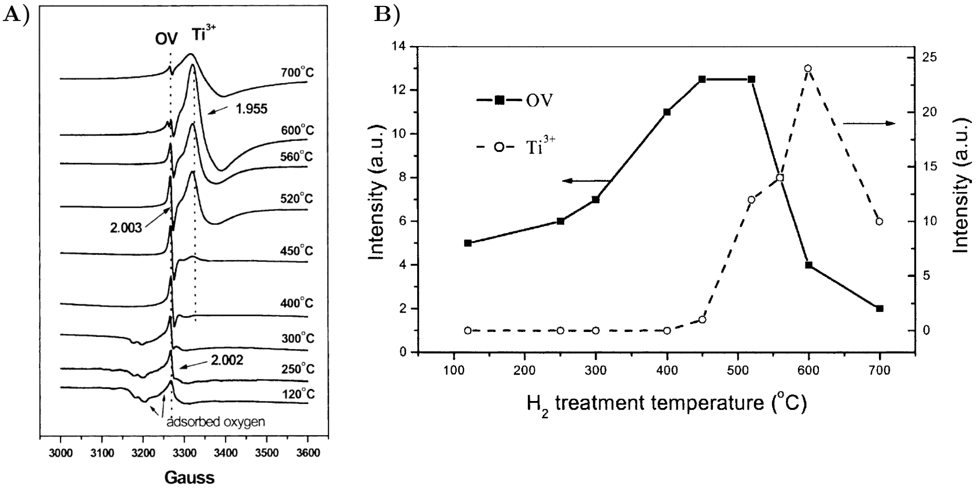

Figure 2.17: A) EPR spectra of oxygen vacancies and Ti^{3+} ions in TiO_2 during H_2 treatment. **B)** EPR intensity of Ti^{3+} and V_O with respect to temperature during the H_2 treatment.[161].

2.3.1 Defects in *black titania* nanomaterials

The above discussion should naturally conclude on the defects expected in *black titania* nanomaterials, as this aspect was not covered in Section 2.2.2. As already mentioned above, a thermal treatment in hydrogen atmosphere is expected to induce oxygen vacancies, Ti^{3+} states and even Ti interstitials, depending on the thermal treatment conditions. The first reports on black titania reported either a bandgap narrowing related to surface disorder[83] or an increased donor density due to oxygen vacancies[84]. Thus, the situation appears equally complex as in the case of "regular" n-type TiO_2. Following investigations added more insights on the issue of defects introduced in black titania, but did not lead to an univocal answer, as the results are strongly dependent on the experimental conditions of both the starting material and the thermal treatment[78,79]. Naldoni *et al.*[162] suggested that black TiO_2 nanoparticles prepared by pure H_2 annealing at 500°C showed a core/shell structure, with a disordered stoichiometric shell, giving rise to band tailing evidenced by valence band XPS spectra, and a crystalline anatase core with oxygen vacancies, evidenced by cathodoluminescence (CL) measurements (Figure 2.18A); in addition, these results were found starting from an amorphous TiO_2 powder, and not with a commercial crystalline powder.

DFT calculations were employed also in this case to gain more information on the effect of hydrogenation treatment. In the original work of Chen *et al.*[83], lattice disorder in hydrogenated anatase nanocrystals resulted in the appearance of two groups of states in the bandgap, at 1.8 eV and 3.0 eV from the valence band maximum (VBM), related to hybridized O 2p/Ti 3d orbitals and only to Ti 3d orbitals, respectively, the former being occupied at room temperature and, thus, leading to valence band shift. Liu and co-workers[163] further studied the effects of hydrogenation on the surface of TiO_2, both considering bulk terminations and a nanocrystal, showing that hydrogen treatment could promote the breaking of Ti–O surface bonds, forming Ti–H bonds, while in the bulk the reverse mechanism occurred (Ti–H bonds rupture and Ti–O bonds formation), thus leading to a disordered surface; moreover, they suggested the preferential localization of photoexcited holes on the disordered surface, thus on states within the bandgap, on the contrary of photoexcited electrons, reducing their recombination and increasing the photocatalytic activity. Further studies of Chen *et al.*[164], both from the experimental and theoretical points of view, confirmed the importance of the disordered shell surrounding crystalline TiO_2 nanoparticles in the bandgap narrowing, while no evident features of Ti^{3+} ions were detected by X-ray emission and absorption spectroscopy (XAS and XES). In particular, as shown in Figure 2.18B, the authors simulated by DFT methods the structure and the density of states of two TiO_2 cluster models: a crystalline one (model A), and a hydrogenated one (model B); the latter exhibited a disordered shell after annealing and relaxation processes, and a clear bandgap narrowing as well, related to the hydrogen-induced disordering of the outer shell.

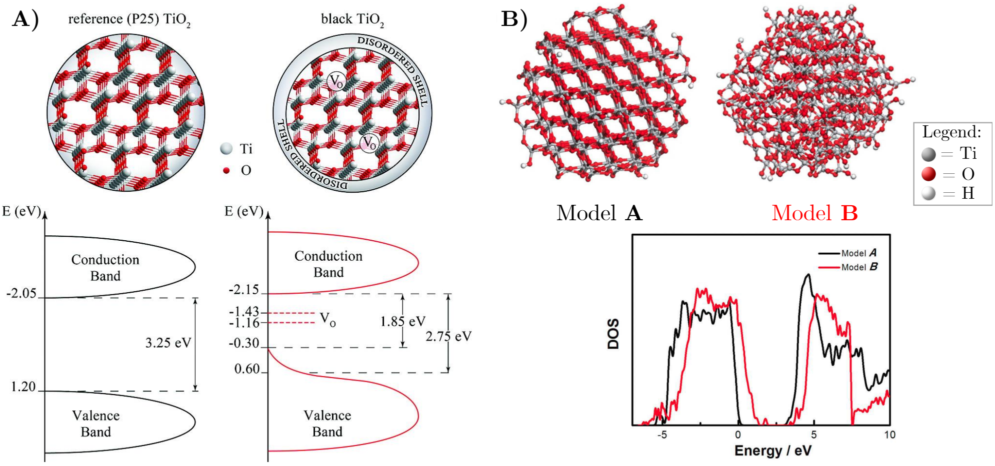

Figure 2.18: Bandgap narrowing in hydrogen-treated TiO_2 nanoparticles with a disordered shell. **A)** Schematics of nanoparticle density of states for P25 TiO_2 (left) and black TiO_2 (right), based on synchrotron X-ray powder diffraction, cathodoluminescence, UV-vis spectroscopy and XPS analysis[162]. **B)** *Ab initio* DFT calculation results on large TiO_2 clusters: structure of crystalline $Ti_{210}O_{420}H_{12}$ (model A), structure of disordered $Ti_{218}O_{436}H_{70}$ (model B) and calculated DOS of models A and B[164].

From the experimental point of view, an interesting analysis was reported by the group of P. Schmuki[85], as already mentioned in Section 2.2.2, who compared the high-pressure pure hydrogen treatment (HPH) with a Ar/H_2 treatment at environmental pressure performed on anodic anatase TiO_2 nanotubes. The authors suggested that the ability of the HPH treatment to produce hydrogen in photocatalytic experiments in open circuit conditions may be related to Ti^{3+} sites with intrinsic co-catalytic activity (i.e. promoting the hydrogen evolution reaction), differently than those found in conventional reduced TiO_2, in which an increase of conductivity should be expected. However, a direct evidence of these intrinsic co-catalytic sites was challenging, even employing spectroscopic techniques such as EPR and proton nuclear magnetic resonance (^1H NMR)[85]. P. Schmuki and co-workers, moreover, obtained H_2 production in open circuit conditions with “black” TiO_2 nanotubes irradiated with high-energy protons (30 keV) and they similarly ascribed these findings to intrinsic co-catalytic centers[165].

To conclude, defects in titanium dioxide, typically occurring as oxygen vacancies, Ti^{3+} sites and Ti interstitials, exhibit similar spectroscopic/energetic features; when hydrogen or generally reducing thermal treatments are performed on TiO_2, with the aim of obtaining the so-called *black titania* nanomaterials, even more defects can occur, such as surface disorder and Ti–OH or Ti–H groups[78,79]. This wide spectrum of defects in TiO_2 is strictly correlated to its photoactivity properties, thus their control, even though anything but straightforward, is of fundamental importance. For these reasons, most of the experimental work performed in this Ph.D. project was related to this issue, with the purpose of increasing the photoelectrochemical properties of TiO_2 hierarchical nanostructured films presented in Section 2.2.4. This will be conveniently clarified in the following chapters.

3

Thesis goals and methods

THIS chapter presents the specific goals of this thesis and illustrates the research methodology followed to achieve them. The specific motivations and objectives are presented in Section 3.1. The materials synthesis approach is illustrated in Section 3.2. In particular, Pulsed Laser Deposition (PLD) and annealing treatments have been extensively exploited to tune the material defectivity and, as a consequence, its photoactivity. The former is described in Section 3.2.1 and the latter in Section 3.2.2. The characterization techniques are presented in Section 3.3, while the photoelectrochemical testing in water splitting experiments is described in Section 3.4.

3.1 Specific goals of the thesis

This Ph.D. thesis aims to study modified TiO_2 hierarchical nanostructures for water splitting applications by means of an experimental investigation mainly conducted at the Micro- and Nanostructured Materials Laboratory (NanoLab), Politecnico di Milano; a close collaboration with the Laboratory of Catalysis and Catalytic Processes (LCCP), Politecnico di Milano, allowed to perform the functional testing in photoelectrochemical cells. Laboratory-scale equipment and techniques have been exploited throughout this work, which are described in the following sections. The main tasks of this thesis were the following:

(*a*) to introduce intrinsic defects in TiO_2 hierarchically nanostructured photoanodes in a controllable way during the deposition process and/or during the annealing one and to study their influence on the material morphological, structural, optical and photoelectrochemical properties;

(*b*) to study in detail the correlation between synthesis conditions and material photoresponse to find an optimization of the experimental strategy;

(*c*) to investigate with dedicated experiments the presence of intrinsic defects in the material;

(*d*) to lay the foundations of another approach, based on the integration of plasmonic nanoparticles with the TiO_2 hierarchical nanostructures, to go beyond the single-material photoanodes.

Tasks (*a*) and (*b*) represent the "core activity" of this Ph.D. thesis and are motivated by a relative lack of knowledge in the field of *black titania* approaches, as explained in the following.

As mentioned in Section 2.2.2, annealing in a dilute Ar/H_2 mixture at atmospheric pressure has been proposed only in few literature studies as a more feasible way to enhance the water splitting performance of nanostructured TiO_2 thin films[91–93], instead of using a pure H_2 gas[84] and, moreover, a high pressure treatment[85]. In addition, this procedure may have an intrinsic interest in view of application development (not only for water splitting, but more in general for photocatalysis and photovoltaics). Alternatively to hydrogen annealing, vacuum annealing has also been proposed, which shows some potentiality in enhancing the material photoactivity[97,166]. Since TiO_2 hierarchical nanostructures, without any hydrogenation/reduction treatment, have been extensively investigated at NanoLab but only recently in PEC water splitting experiments[137,138], they have been modified with reducing treatments (in Ar/H_2 mixture and in vacuum) with the aim not only to enhance their photoresponse, but also to increase the understanding on the effects of intrinsic defects in hydrogenated/reduced TiO_2 nanomaterials.

In addition, PLD (described in Section 3.2.1) offers an advantage from the aforementioned thermal treatment approach, which is peculiar of this technique: the possibility to tune the material properties, and, in this case, the defectiveness, directly during its growth. For TiO_2 nanomaterials, this can be performed by depositing with a mixed oxygen/intert gas background mixture, keeping fixed the total pressure, as opposed to a deposition in pure oxygen (as performed previously[137,138]). The same approach, for instance, was exploited to tune the electrical properties of Al-doped ZnO nanostructured films[167].

Task (*a*), which represents the first part of this activity (both from the logical and temporal points of view), is presented in Chapter 4; in addition, this experimental campaign was performed in collaboration with a student and constituted her Master thesis project[168]. Subsequently, Chapter 5 is related to task (*b*) and it reports the optimization of the material photoresponse, arising from the most promising results of Chapter 4. On the other hand, it must be noted that the detailed understanding of the nature and the role of intrinsic defects in TiO_2 nanomaterials is particularly challenging, as also pointed out in Section 2.3. Nevertheless, task (*c*) was tentatively addressed with photoluminescence (PL) experiments, and the related results are shown in Chapter 6.

Finally, task (d) represents the last development of this Ph.D. project, which is related to the introduction of plasmonic effects in TiO_2 hierarchical nanostructures by means of noble metal (Au) nanoparticles, with the aim of obtaining a photoactivity in the visible range of the electromagnetic spectrum, where TiO_2 poorly absorbs light. Since in recent years these effects have been introduced in TiO_2 and other oxides for photovoltaic[109] and water splitting applications[104], as briefly discussed in Section 2.2.3, the consistency of the same approach applied to hierarchical nanostructures is also evident. In addition, PLD is a suitable technique to deposit not only TiO_2 nanostructured films, but also noble metal nanoparticles, suggesting the opportunity to perform the synthesis of the whole composite material with the same process. This task have been performed in collaboration with a thesis student, so only the main findings are presented in Chapter 7; for the whole discussion, the reader is referred to ref. [169]. In addition, further investigations on the integration of Au nanoparticles with TiO_2 hierarchical nanostructures are still being carried out and represent one of the active research areas of NanoLab.

As previously mentioned, this Ph.D. thesis was mainly conducted at Politecnico di Milano. In some cases, however, collaborations have been set up to perform characterizations unavailable at NanoLab or LCCP, both within Politecnico or externally: XRD measurements, described in Section 3.3.3, pertain to the first case, while IPCE measurements, performed at the Department of Materials Science WW4-LKO at the University of Erlangen-Nuremberg (see the results presented in Section 4.4.2), and TEM analysis, carried out at the Department of Materials Science & Metallurgy, University of Cambridge (see the results in Section 5.2.1), pertain to the second case.

3.2 Material synthesis

As already mentioned, film production was carried out by controlling PLD process parameters; this technique is described below. The annealing facilities, employed to tune the crystallinity and photoactivity of as-deposited films, are presented in Section 3.2.2.

3.2.1 Pulsed Laser Deposition

Nanosecond Pulsed Laser Deposition (PLD) belongs to the class of Physical Vapor Deposition (PVD) techniques, in which the material to be deposited is brought in the vapor phase by means of a physical process; in the case of PLD, such process is *laser ablation*, which originates from the interaction between a high-energy pulsed laser and a solid target: a small part of its surface is vaporized and expands in the form of a supersonic plasma with a characteristic *plume* shape. The plume expansion can occur in vacuum or in the presence of a background gas, either inert (e.g. helium, argon) or reactive (e.g. oxygen, nitrogen, hydrogen. . .). Subsequently, the ablated species in the plasma plume (which can be molecules, atoms, ions, electrons and small aggregates) reach the substrate, where condensation and film growth take place. These are only the fundamental processes of PLD; indeed, a complete and detailed description of the involved physical processes is extremely complex and it is beyond the scope of this section (the reader is referred to textbooks[170,171] for a complete treatise of the subject).

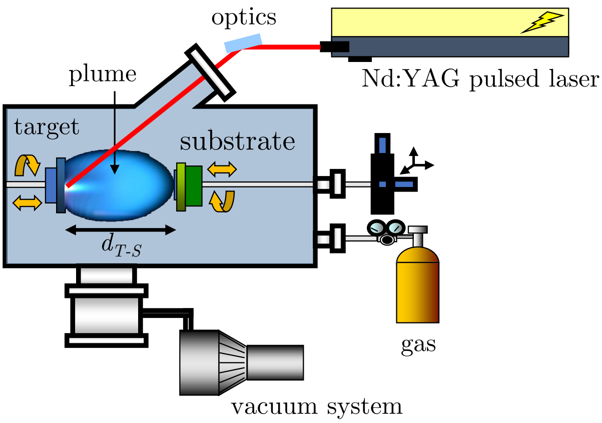

Figure 3.1: Scheme of a typical PLD apparatus. The laser path is indicated by the red line.

A typical scheme of a PLD apparatus is presented in Figure 3.1. A laser source is placed close to a vacuum chamber, which hosts the target and the substrate; the laser pulses are focused by an optical system onto the target surface (the laser path is marked by the red line in Figure 3.1). The ratio between the pulse energy and the size of the focused spot determines the energy density on the target (known as *fluence*), which is one of the critical PLD parameters. Indeed, there is a threshold in its value for ablation to occur, which depends on target properties, laser wavelength and pulse duration. In typical ablation conditions for ns PLD, the laser power on the target is of the order of 10–100 MW, corresponding to fluence values of several J/cm^2. The movement of the ablated species towards the substrate occurs in the plume (colored in blue in Figure 3.1), whose properties are strongly dependent on the laser fluence, on the laser spot size on the target and on the atmosphere inside the deposition chamber. The chamber is evacuated to high vacuum conditions (10^{-3} Pa) by a pumping system and can then be filled with a background gas at a controlled pressure in known flow conditions.

The background atmosphere (gas type and pressure) can be modified to achieve control of the plume shape, length and ionization degree, affecting the plume expansion dynamics and allowing to move between different deposition regimes, which can be sketched as follows[172]:

- a low-pressure "vacuum-like" regime with a forward directed flow and reduced scattering of the ablated species;
- a transition regime with strong momentum transfer to the background gas and formation of a shock wave at the front of the expanding plume;
- a regime characterized by diffusion of the ablated particles at high pressure.

This is illustrated in Figure 3.2. In low pressure conditions, the species ablated from the target proceed almost without collisions and reach the substrate with high kinetic energy, leading to atom-by-atom deposition of compact and bulk-like films. If pressure is increased, the background gas molecules and the ablated species undergo collisions which can lead to the spatial confinement of the ablation plume: the plume edge is better defined due to the presence of a travelling shock wave front which slows down until it reaches the so-called stopping distance. Upon collisions, clusters are formed in the gas phase and the kinetic energy with which the substrate is reached is lower. At higher pressures, the diffusion of clusters in the gas is favored, and their kinetic energy is further decreased (from tens of eV/atom for low pressure conditions to fractions of eV/atom for high pressure conditions[131]).

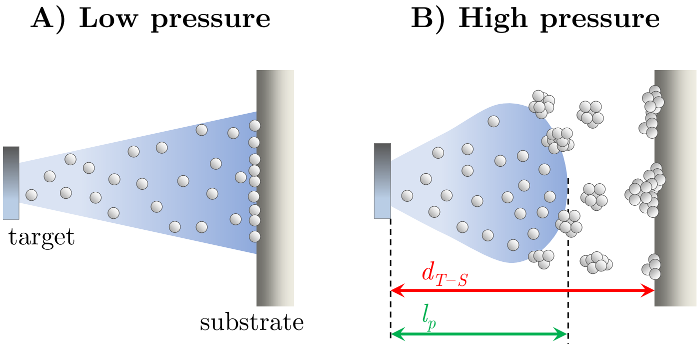

Figure 3.2: Schematic picture of PLD conditions for different pressure regimes: **A)** low pressure, **B)** high pressure; d_{T-S} is the target-to-substrate distance and l_p is the time-integrated visible plume length.

Another aspect shown in Figure 3.2 is the following. A convenient way to identify these deposition regimes consists in introducing a non-dimensional parameter L, defined as the ratio between the target-to-substrate distance, d_{T-S}, and the time-integrated visible plume length, l_p, at each laser pulse[131]. When $L < 1$ the substrate is placed "in plume" and collisions are not sufficient to induce significant clustering, resulting in a compact film. If $L > 1$ (substrate “out of plume”), plume confinement induced by collisions reduces the kinetic energy of the ablated species, favoring cluster nucleation[173], and leads to the deposition of cluster-assembled nanostructured materials; this situation is sketched in Figure 3.2B. The intermediate situation, when $L \simeq 1$ (substrate “at the plume edge”), is instead favorable for the hierarchical morphology widely investigated at NanoLab[131]. Indeed, the morphology can be controlled by varying the properties of the ablation plume, which depend both on laser fluence and deposition pressures, or by varying d_{T-S}. In addition, in the case of PLD of oxide materials, the effect of a reactive (oxygen-rich) deposition atmosphere must be taken into account[174]. Indeed, when an oxide target is ablated, oxygen from the background atmosphere can interact with the “building blocks” which assemble into the film in order to obtain different stoichiometry, which is of primary importance for tuning the functional properties.

Finally, a few drawbacks of PLD as a deposition technique should also be mentioned: first, the deposited films have uniform thickness only over a small area (of the order of 1 cm^2). Thickness uniformity can be increased by performing off-axis depositions and rotating the substrates, in order to obtain a circular corona of several cm^2 with uniform thickness, at the expense of decreasing the total deposition rate. Second, during the ablation process, molten particles are ejected in the form of *droplets*, which appear in the film as spherical protrusions of various sizes (from hundreds of nm to several µm) and are detrimental in case low surface roughness is required.

Instrumentation

The PLD system employed for this work is shown in Figure 3.3 and it consists of a solid state laser, optics to direct the laser beam to the target, a high vacuum chamber, a pumping system and a set of remote-controlled motors for the motion of the target and the substrate. The laser is a Continuum-Quantronix Powerlite 8010 pulsed Q-switched Nd:YAG laser, which generates ns pulses (7 ns) at the fundamental wavelength $\lambda = 1064$ nm (IR), with a maximum repetition rate of 10 Hz. Pulse energy is measured by an external power meter (Gentec QE25LP-H-MB-QED). Modifying the delay time between pulse generation and the maximum efficiency of the amplification module, it is possible to range the pulse energy between 350 mJ and 1800 mJ. Non-linear crystals allow to double and quadruple the fundamental wavelength, obtaining $\lambda = 532$ nm (green, with maximum energy 800 mJ) and $\lambda = 266$ nm (UV, with maximum energy 160 mJ). For this thesis work, green wavelength with energies from 100 to 170 mJ was chosen. As generated, the laser beam spot has a circular profile with a diameter of 9 mm. The laser beam impinges on the target at an angle of 45°, so its projection is elliptical. The beam is focused by a plano-convex lens with focal length of 50 mm. The fluence onto the target is the ratio between the pulse energy and the laser spot on it and the employed values have been 2 and 3.5 J/cm^2. Depositions were performed with a background gas selected on the basis of the specific experiment; the details are conveniently reported at the beginning of the following chapters (Sections 4.1.1, 5.1.1, 6.1.1, 7.1.1 and 7.1.2).

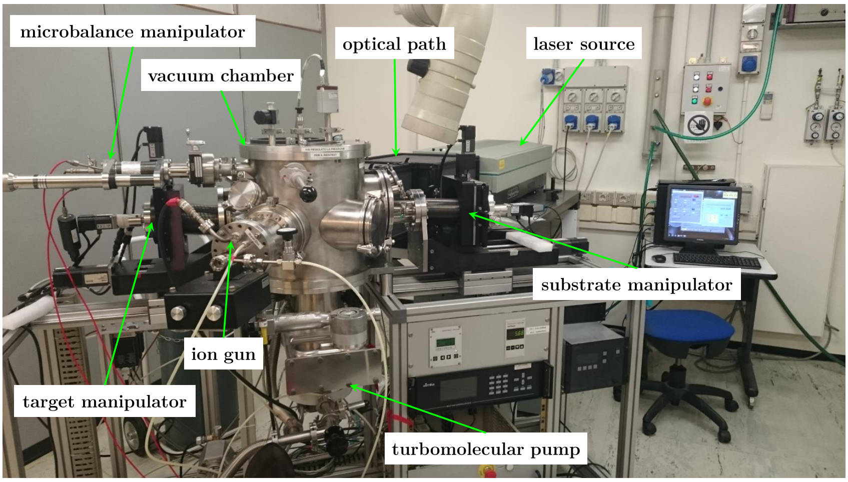

Figure 3.3: Photographs of PLD apparatus at NanoLab.

The high vacuum chamber is a stainless steel cylinder equipped with different components: a pumping system, a laser window, target and substrate holders, a quartz microbalance, a gas inlet and an ion gun. Viton o-rings are used to guarantee the vacuum seal. The pumping system is made up of a primary scroll pump and a turbomolecular pump (TMP). The scroll pump works in a viscous flow regime and allows to reach a pressure of about 10^{-1} Pa. TMP works in molecular flow conditions and can bring the system to the nominal pressure of 10^{-4} Pa (a base pressure of 10^{-3}–10^{-2} Pa prior to each deposition is typically reached). The pressure is measured by a capacitance gauge (operational range 10^{-1}–10^{3} Pa) and by a full range gauge (Pirani and Bayard-Alpert sensor combination, operational range 10^{-4} – 10^{5} Pa). The gas inlet is controlled by a mass-flow meter system (MKS 2179A). A PID controller is able to regulate the gas mass flow in order to maintain the desired pressure (from 10^{-1} up to 10^{2} Pa) with 100 and 1000 sccm controllers. The locked manipulators allow to translate both in vertical and horizontal directions and to rotate around their axis. These motions are commanded by software-controlled stepper motors. A dedicated Labview software allows to control target and substrate motion during the deposition process; in particular, target roto-translation is set up to obtain a spiral-like motion of the laser beam on its surface, which ensures uniform ablation; the substrate manipulator allows a manual off-axis shift of the substrate holder in the horizontal direction, which, combined to its rotation, can lead to achieve film planarity over several cm^2. Deposition rate is measured with an Infcon XTC/2 quartz crystal microbalance.

3.2.2 Annealing treatments

Annealing treatments are widely employed in material science to alter the physical (or sometimes chemical) properties of a material. In the specific case of TiO_2 thin films deposited by PLD, since in the typical experimental conditions employed for this thesis work the as-deposited material is amorphous, annealing in air is employed to obtain the anatase crystalline phase with a temperature greater than 400°C[133]. On the other hand, thermal treatments in reducing conditions have been applied to TiO_2 to increase its conductivity since the 50's[81]; however, in recent years a great interest in reducing treatments, especially in hydrogen atmosphere, has arisen due to the outstanding photocatalytic activity obtained by Chen and coworkers[83]; a short discussion on the so-called *black titania* is presented indeed in Section 2.2.2. In this section, it must be mentioned that for this thesis work thermal treatments in air were employed for crystallization purpose, while in reducing atmospheres (Ar/H_2 mixture, pure Ar or vacuum) were employed to introduce defects (such as oxygen vacancies) in the material to increase its photoelectrochemical activity.

Instrumentation

The apparatus employed for air annealing consists of a Lenton Muffle furnace (ECF type), which has a maximum operating temperature of 1200°C (Figure 3.4A). The temperature uniformity is provided by two side wall-heating elements manufactured from high temperature resistance wire spirals embedded into cast refractory slabs; an exhaust chimney is also present. The annealing chamber is insulated from the outside environment with an insulating door; its double skin construction allows natural air convection to maintain a cool outer case. The annealing temperature is set up with a PID controller (Lenton type 3216), which can be employed either as a simple controller or to perform a profile with some ramp/dwell pairs. In this work, the typical temperature profile employed was the following: from room temperature to 500°C with 4°C/min heating ramp, 2 hours dwell and cooling back to room temperature spontaneously (the total treatment time was about 24 h). In some cases, the dwell temperature of 650°C was also employed.

Thermal treatments in controlled atmospheres are performed in a home-made furnace which consists of a high vacuum chamber, a heater stage connected to a PID controller and a pumping system (Figure 3.4B). The high

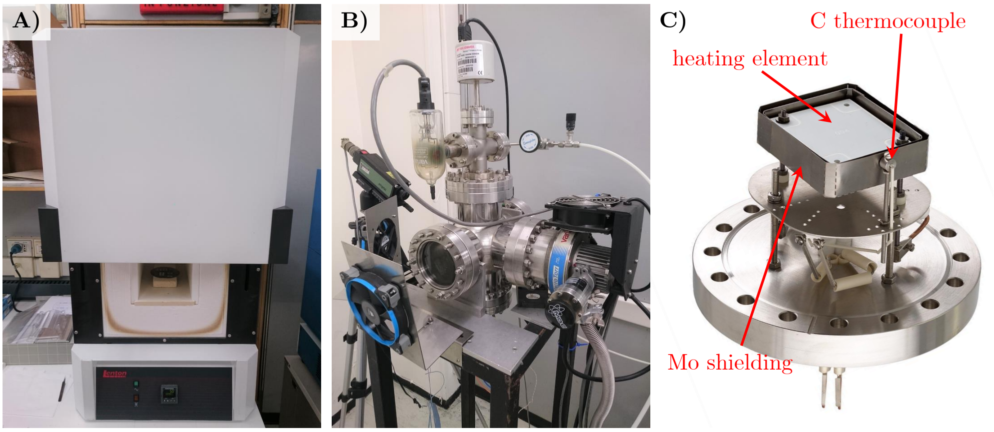

Figure 3.4: **A)** Muffle furnace. **B)** Home-made furnace for thermal treatments in controlled atmospheres; the heater stage is reported in **C)**.

vacuum chamber is a stainless steel sphere equipped with different components: a pumping system, viewports, diagnostic instruments and a gas inlet. Copper o-rings are used to guarantee the vacuum seal; the pumping system consists of a primary rotative pump and a TMP and it allows to reach a nominal pressure of about 10^{-6} Pa. The pressure is measured by a capacitance gauge (BOC Edwards Barocel Pressure Sensor, operational range 10^2–10^5 Pa) and by a Varian Bayard-Alpert gauge (operational range 10^{-8}–10^{-2} Pa). The gas inlet ensures the possibility to introduce a gas flow during annealing treatments to perform them in a desired atmosphere or, also, to speed up the cooling process. The heater stage, its power supply and its controller are provided by Tectra; the former is illustrated in Figure 3.4C. The heating element, commercially called Boralectric®, is made of pyrolitic boron nitride (pBN, a dielectric ceramic material) and pyrolitic graphite (pG, an electrical conductor). By flowing an electrical current through the graphite contacts and exploiting the Joule effect, it is possible to bring the system to the desired temperature, measured by a C thermocouple, using a proper controlling system, consisting of a standard PID controller (Yudian AI-518P). A molybdenum shield, covering the heating element, can be installed to reduce the irradiated power, keeping the other components safe (especially the front viewport, which otherwise can reach excessive temperatures) and, in addition, to ensure a more uniform temperature distribution. This system can reach very high temperatures (the maximum operating temperature is 1200°C) with heating ramps up to 100°C/s. In addition, an optical pyrometer (Impac IGA 140) is also employed to check the actual temperature on the heating stage (only if it is not covered by the molybdenum shielding). The temperature profiles acquired both by the pyrometer and the temperature controller are recorded on a PC by means of RS232 connections and a

Labview home-made program. In this work, the typical temperature profile was the following: from room temperature to 500°C (measured by the thermocouple) with 10°C/min heating ramp, 3 hours dwell and cooling back to room temperature again with 10°C/min. In some cases, the dwell temperature of 650°C was also employed. The annealing atmosphere was a Ar/H_2 mixture (97:3) at environmental pressure in flowing conditions; in some cases, also annealing in vacuum ($P = 10^{-4}$ Pa) was tested.

3.3 Material characterization techniques

The materials synthesized with the methods described above have been characterized from the morphological, structural, optical and photoelectrochemical point of view by exploiting different techniques, which are described below.

3.3.1 Scanning Electron Microscopy (SEM)

In a scanning electron microscope (SEM), a high-energy (0.2–30 keV) electron beam is focused on a fine probe that scans the surface of the sample to be analyzed. The interaction between the specimen and the electron probe *(primary electrons)* produces *back-scattered electrons* (BSE), *secondary electrons* (SE) and X-rays (Figure 3.5).

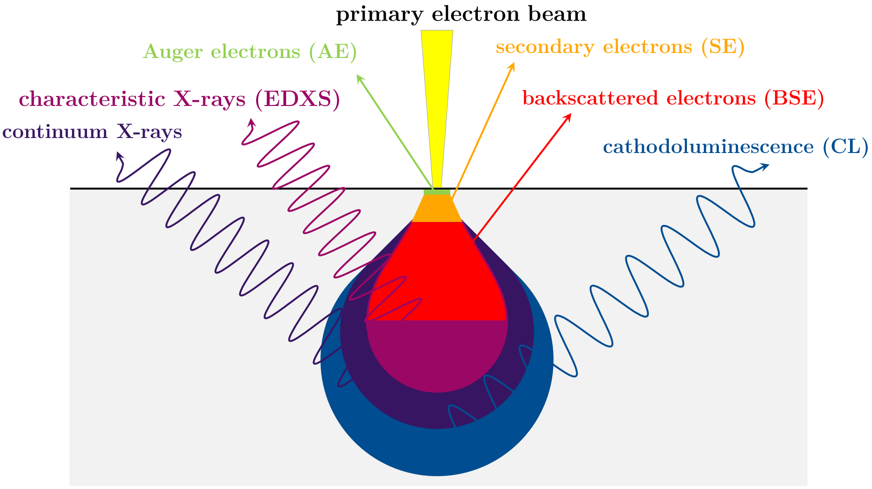

Figure 3.5: Schematics of the interaction depth profile between the incident electron beam and the sample surface.

BSE are produced by elastic scattering events between primary electrons and atomic nuclei. Due to the big difference between electrons and nuclei masses, the former lose little energy in these events. Since backscattering cross-section is proportional to Z^2, the higher the specimen atomic number, the more BSE are produced. For this reason, BSE can provide qualitative information about the sample composition. Primary electrons can also interact inelastically with the sample, i.e. with electrons bound in atoms. If the energy transferred is sufficient, SE are generated. Generally, SE have a kinetic energy lower than 50 eV, but they need a higher energy than the material work function to escape from the sample's surface and reach the detector. For this reason, typically, only the SE generated in the first nm from the surface can be detected. Other signals come from the sample surface upon the interaction with the primary beam, such as X-rays (analyzed with Energy Dispersive X-ray Spectroscopy, EDXS), Auger electrons, catholuminescence etc., but these are not considered in this work.

Instrumentation

The SEM employed for this thesis is a high resolution Field Emission-SEM Zeiss Supra 40 based on the Gemini column, equipped with an Oxford EDXS spectrometer. The accelerating voltage ranges from 1 kV up to 30 kV (in this work, 5–7 kV were typically used). The sample holder is connected with five software-controlled motors (x, y, z, rotation and tilt). The EDXS detector is a solid-state silicon lithium detector protected by a beryllium window with an energy resolution of about 10 eV. The SEM images reported in this thesis, if not specified otherwise, were obtained acquiring SE electrons with an In-Lens detector, which, compared to a standard SE detector, allows to achieve a higher contrast thanks to local differences in work function on the surface.

3.3.2 Raman and photoluminescence spectroscopy

Raman scattering

Raman spectroscopy is a spectroscopic technique based on inelastic scattering of monochromatic light, usually from a laser source, due to the excitation of vibrational modes in crystals or in molecules. As a consequence of the inelastic scattering, the energy of the re-emitted photons is shifted up or down in comparison to the original monochromatic frequency, which is called *Raman effect.* This shift provides information about vibrational, rotational and other low-frequency transitions in materials.

In a typical apparatus for Raman spectroscopy, a sample is illuminated with a laser beam (with frequency ω_L). The light coming from the illuminated spot is sent through a monochromator. The scattered radiation that has not changed its wavelength (i.e., that underwent elastic scattering, known as Rayleigh scattering, which is the large majority of the outgoing light) is filtered out, while the remaining collected light is dispersed onto a detector and spectroscopically analyzed. A Raman spectrum consists in a plot of the scattered light intensity as a function of the Raman shift, defined as the difference in wavenumbers (in cm^{-1}, remembering that $1\ \text{cm}^{-1} = 1.24 \cdot 10^{-4}$ eV $= 30$ GHz) between the scattered radiation and the laser source. The spectral region with frequencies higher than ω_L is called *anti-Stokes* scattering, the one with frequencies lower than ω_L *Stokes* scattering. The intensity of the former is considerably weaker than the latter, so typically only Stokes spectral lines are acquired.

From the physical point of view, the classical theory of the Raman effect for a molecule[175] is based on the fact that the incident electromagnetic field induces in the system a time-dependent dipole moment, $\mathbf{M}(t)$, which is related to the electric field $\mathbf{E}(t) = \mathbf{E}_0 \cos(\omega_L t)$ through the electronic polarizability tensor α: $\mathbf{M} = \alpha\mathbf{E}$. α is a function of the electronic charge distribution and is thus sensitive to molecular vibrations. For small displacements of the nuclei with respect to the equilibrium position, it is possible to express α using a Taylor series as a function of the normal coordinates Q. If the molecule vibrates with the frequency ω_s, at the first order $Q = Q_0 \cos(\omega_s t)$ and we can find

$$\mathbf{M}(t) = \alpha_0 \mathbf{E}_0 \cos(\omega_L t) + \frac{1}{2}\left(\frac{\partial \alpha}{\partial Q}\right)_0 Q_0 \mathbf{E}_0 \{\cos[(\omega_L - \omega_s)t] + \cos[(\omega_L + \omega_s)t]\} \tag{3.1}$$

From Equation (3.1) it can be deduced that the condition to have Raman effect is that $\partial\alpha/\partial Q \neq 0$. The classical theory, so, exactly predicts the position of the peaks in the Raman spectrum, but not the correct intensity ratio between the Stokes and the anti-Stokes branches. This issue is resolved by the quantum theory of Raman scattering[175]; in this context, phonons are the quantum-mechanical counterpart of the classical normal modes of vibration, in which lattice atoms or molecules uniformly oscillate at a single frequency. Raman scattering is thus described as an anelastic collision between the incident photon and a phonon in the lattice; in the Stokes process a phonon $\omega_j(\mathbf{q})$ is created, while in the anti-Stokes process the phonon $\omega_j(\mathbf{q})$ is annihilated. Conservation of energy and momentum between the initial and the final states leads to the fundamental conservation rule $\mathbf{q} \simeq 0$, which implies that in first order Raman scattering only optical phonons at the Brillouin zone center can be excited. Moreover, the correct intensity ratio between the Stokes and the anti-Stokes branches can be found by taking into account the population of states according to the Bose-Einstein statistics:

$$\frac{I_{Stokes}}{I_{anti-Stokes}} = \left[\frac{\omega_L - \omega_j(\mathbf{q})}{\omega_L + \omega_j(\mathbf{q})}\right]^4 \exp\left[\frac{\hbar\omega_j(\mathbf{q})}{k_B T}\right] \tag{3.2}$$

These considerations were derived for crystalline materials; for the amorphous or nanocrystalline ones, the fundamental selection rule is relaxed, so that the spectrum typically exhibits broad bands instead of well-defined peaks. However, a detailed treatment of Raman scattering is quite complex; the reader is referred to textbooks[175] for an appropriate discussion.

In this thesis work, Raman spectroscopy was employed to discern the crystalline phase of TiO_2 hierarchical films and to ascertain any influence of sub-stoichiometry or defectivity to the spectrum[49] induced by depositions and/or annealing treatments in reducing conditions.

Photoluminescence (PL) spectroscopy

Photoluminescence (PL) is the spontaneous emission of light from a material under optical excitation; the excitation energy and intensity are chosen to investigate a variety of materials. PL spectroscopy, indeed, is a selective and sensitive probe of discrete electronic states: the PL spectrum provides transition energies, which can be used to determine electronic energy levels, many of which lie near surfaces and interfaces. In addition, PL spectroscopy is simple, versatile and non-destructive, while transient PL (i.e. time-resolved photoluminescence, TRPL) is more challenging, since it implies sample illumination by a short pulse of light and then the analysis of charge carriers decay at the nanosecond scale[176].

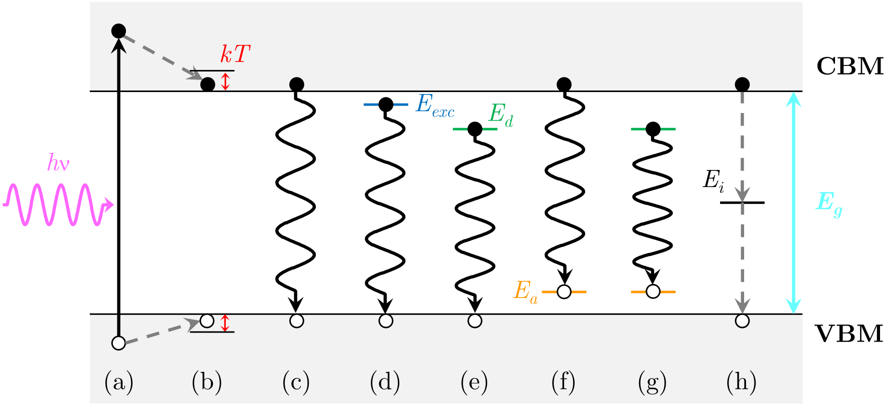

Figure 3.6: Schematics of optical transitions in solids, where VBM is the valence band minimum, CBM is the conduction band maximum, E_g is the bandgap energy and kT is the thermal energy. (a) Photoexcitation by an incoming photon with energy $E = h\nu > E_g$. (b) Thermalization of photo-excited charges in a region $\sim kT$ wide at the CBM or VBM. (c–g) Radiative recombination paths, across the bandgap (c) or mediated by a free or bound exciton (d), a donor level (e), an acceptor level (f) or both of them (g). (h) Non-radiative recombination via an intermediate state.

Considering the bandgap of a semiconductor material, we can consider the radiative processes that can take place across it[177], as illustrated in Figure 3.6. (a) An incoming photon with energy greater than the bandgap excites an electron-hole pair; then, (b) both the electron and the hole thermalize quickly with the lattice and reside in a region $\sim kT$ at the conduction band minimum (CBM) or at the valence band maximum (VBM), respectively; thermalization is generally achieved by phonon emission. (c) The electron and the hole can recombine with photon emission (bandgap recombination or interband photoluminescence); this process, however, is less probable in *indirect* semiconductors, in which the VBM and the CBM do not both occur at the Brillouin zone center and a phonon must take part in the process providing an additional momentum. (d) The electron can be trapped non-radiatively by a donor (an extrinsic impurity purposely introduced or an intrinsic defect) in a localized state within the bandgap (E_d) and, subsequently, radiatively recombine with the hole. (f) Similarly, the hole can be trapped by a non-radiative transition by an acceptor in a localized state E_a and radiatively recombine with the electron. (g) The electron trapped in a donor state can radiatively recombine with the hole trapped in the acceptor state. All these radiative recombinations are competing process with each other and with non-radiative ones, such as the ones mediated by intermediate states (E_i) produced by impurities or defects (h). It is important to underline that the PL spectrum provides the transition (i.e. emission) energies, which can be used to determine the electronic energy levels with some care: for instance, an emission with the same energy E could originate from either of the processes (e) and (f) in Figure 3.6, so the presence of a certain species of dopants/impurities should be known. Nevertheless, PL spectroscopy is a powerful tool in the characterization of surfaces and interfaces, and it can give additional information if performed at cryogenic temperature, to obtain the highest spectral resolution, and with multiple excitation energies, to probe different regions of the sample (as the absorption coefficient depends of most materials depends on energy).

In this thesis work, PL spectroscopy was employed to detect the presence of defects in the TiO_2 hierarchical films exposed to reducing thermal treatments and compare them to films annealed in air; the reader is referred to Chapter 6 for a detailed discussion on this subject.

Instrumentation

For Raman spectra, a Renishaw InVia Raman spectrometer has been used. The exciting radiation is the 514.5 nm line produced by a Ar^+ laser. Spectra have been acquired by a 1800 greeds/mm grating, a super-notch filter (cutoff at 100 cm^{-1}) and a Peltier-cooled CCD camera, allowing a spectral resolution of about 3 cm^{-1}. Laser power on samples was kept below 1 mW to avoid thermal modification. For photoluminescence spectra, as different excitation wavelengths have been exploited, different facilities have been employed: for UV excitation (λ = 325 nm) another Renishaw InVia Raman spectrometer, with a 2400 greeds/mm grating with laser power of about 0.6 mW; for green excitation ($\lambda = 514.5$ nm) the same instrument as for Raman spectra (only the measurement spectral range was extended); for blue ($\lambda = 457$ nm) and red ($\lambda = 633$ nm) a Jobin Yvon Labram HR800 spectrometer with a HeNe laser source, 600 greeds/mm grating and a power on samples of about 1 mW (blue) and 3 mW (red).

3.3.3 X-Ray Diffraction

X-Ray Diffraction (XRD) is a powerful non-destructive technique that enables the identification of the different phases present in the analyzed sample, as well as its structural properties (e.g. crystallite size, preferential growth orientation). The X-rays are diffracted by the crystalline planes of the material. Constructive interference occurs when the path length difference between X-ray beams scattered from successive crystal planes is an integer multiple of the incident radiation wavelength λ. This is known as Bragg's law:

$$n\lambda = 2d_{hkl} \sin \theta_{hkl} \tag{3.3}$$

where d_{hkl} is the distance between crystal planes with Miller indexes (hkl) and θ_{hkl} is the angle between these planes and the incident X-ray beam. This is illustrated in Figure 3.7. From Equation (3.3) it is clear that the detector of the diffracted X-rays must be placed at an angle $2\theta_{hkl}$ with respect to the direction of the incident beam.

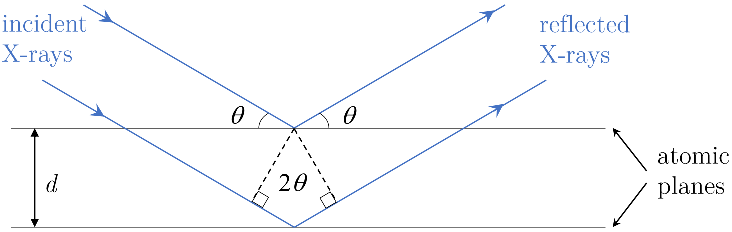

Figure 3.7: Schematic view of Bragg's law.

Instrumentation

In this work, XRD spectra have been acquired by G. Terraneo at the Laboratory of Nanostructured Fluorinated Materials, Department of Chemistry, Materials and Chemical Engineering "G. Natta", Politecnico di Milano. The instrument employed was a Bruker D8 Adavance diffractometer, operating in reflection mode ($\theta/2\theta$) with Ge-monochromated Cu Kα1 radiation ($\lambda = 1.5406$ Å) and a linear position-sensitive detector, with a 2θ range 10–70°, a step size of 0.038°and time/step 1.5 s. Samples were mounted in a sample holder with motorized z-position (4.3 mm). Diffraction patterns were collected at room temperature. The peak position and the full-width at half maximum height (FWHM) of the peaks were then obtained using TOPAS software (Bruker). The crystallite sizes were estimated through the Scherrer formula[178]:

$$\tau = \frac{K\lambda}{\beta \cos\theta} \tag{3.4}$$

where τ is the mean size of the crystal domains, K is a dimensionless shape factor ($K = 0.9$), λ is the x-ray wavelength, β is the FWHM and θ is the Bragg angle.

3.3.4 UV-Vis-NIR spectroscopy

Ultraviolet-visible-near infrared (UV-Vis-NIR) spectroscopy is a non-destructive technique which allows to probe optical transitions of molecules and solids, which are related to the electronic transitions since they typically occur in this spectral region. The optical characterization is particularly relevant for semiconductor materials involved in solar-energy applications, as in this case. The instrument employed in UV-Vis-NIR spectroscopy is a spectrophotometer, which measures the intensity of light passing through the sample (I) and compares it to the intensity of a reference beam, which does not interact with the sample (I_0); the ratio I/I_0 is called (total) *transmittance* (T). On the other hand, a spectrophotometer can measure the intensity of light reflected from the sample, and in this case the ratio I/I_0 is called (total) *reflectance* (R). The fraction of light absorbed by the sample, called *absorbance*, can be simply estimated as

$$A = 1 - (T + R) \tag{3.5}$$

Some samples can also induce a considerable light scattering, so it can be valuable a measurement of the transmittance (or reflectance) by excluding the specular component (i.e. the one transmitted or reflected with the same angle as the incident one): the so-called *diffuse* transmittance, $T_{diff} = T - T_s$ (or diffuse reflectance, $R_{diff} = R - R_s$), is thus obtained, where the subscript s represents the *specular* component, and the so-called *haze factor*, evaluated as $H = T_{diff}/T$ (or $H = R_{diff}/R$), gives an idea of the fraction of scattered light from the sample.

From transmittance and reflectance measurements in the proximity of the bandgap of a material, it is also possible to estimate its optical bandgap with a method derived by Tauc[179]. First, the absorption coefficient must be determined making use of the Lambert-Beer's law:

$$\alpha = -\frac{1}{d}\ln\left(\frac{T}{1-R}\right) \tag{3.6}$$

where d is the thickness of the material. Then, the theoretical value of the absorption coefficient for photons of energies $h\nu$ just above the optical bandgap E_g is given by

$$\alpha = C(h\nu - E_g)^{1/r} \tag{3.7}$$

where C is a constant dependent on the optical transition matrix element and r indicates the type of transition in the considered material ($r = 2$ for direct bandgap transitions and $r = 1/2$ for indirect transitions). From Equation (3.7) we can note that the function α^r must have a linear behavior as a function of $h\nu$; the intercept of its linear fit with the energy axis represents the optical bandgap of the material ($\alpha = 0$ for $h\nu = E_g$). In some cases, $(\alpha h\nu)^r$ is plotted rather than α^r: this is due to the properties of the constant prefactor C in Equation (3.7), which, in the case of a heavily filled and energy dispersed conduction band needs to be multiplied by $h\nu$ for a more accurate realization of the Tauc plot[180].

Instrumentation

In this work, optical characterization was performed with a Perkin Elmer Lambda 1050 spectrophotometer with a 150 mm diameter Spectralon®-coated integrating sphere (reflectance > 95% in the 250–2000 nm range, > 99% in the 400–1500 nm range). The total and diffuse transmittance spectra were measured in the wavelength range between 250 and 2000 nm, whereas the reflectance spectra between 290 and 600 nm. The detector was a R6872 photomultiplier in the UV-vis range and an InGaAs photodetector in the NIR range. For reflectance measurements, the sample was mounted with a 8° inclination to let specular reflected light (R_s) to be detected. The total transmitted light intensity T over the whole solid angle at each wavelength was normalized dividing the contribution of the substrate (glass), whose transmittance was also measured. A schematic illustration of the instrumentation and of the transmittance and reflectance measurement configurations is shown in Figure 3.8.

3.4 Photoelectrochemical experiments

The working principles of the photoelectrochemical (PEC) cell has been described in Chapter 1; thus, in this section only the technical details of the photoelectrochemical experiments performed for this thesis work will be given.

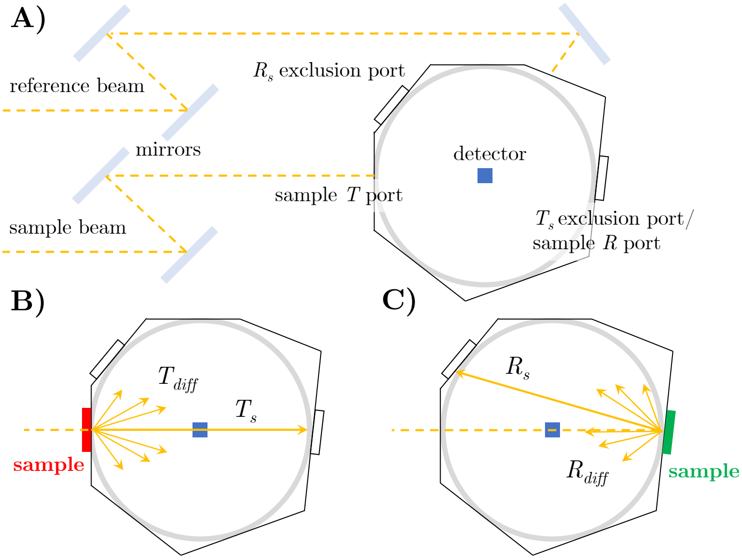

Figure 3.8: **A)** Schematic illustration of the Perkin Elmer Lambda 1050 spectrophotometer with the integrating sphere. **B)** Transmittance measurements configuration. **C)** Reflectance measurements configuration.

All these experiments were performed by R. Matarrese and I. Nova at the Laboratory of Catalysis and Catalytic Processes (LCCP), Politecnico di Milano.

For the photocurrent testing of TiO_2 nanostructured materials reported in this thesis, a three-electrode PEC cell (see discussion in Section 1.3.3) with the following parameters is employed. The electrodes are: as working electrode (photoanode), a TiO_2 film deposited on half-masked Ti plate (with working area of 1 cm^2); as counter electrode (cathode), a platinum grid; as reference electrode, a saturated calomel electrode (SCE)[a]. The electrolyte is an aqueous KOH solution (0.1 M) and the cell is equipped with a flat quartz window. The light source is a solar simulator Lot Quantum Design LS0306 equipped with a 300 W Xe arc lamp and an AM 1.5G filter Lot Quantum Design LSZ389; a UV filter can also be applied to measure the photoactivity under visible light. A light intensity of 100 mW/cm^2 is measured prior to the experiments using a light meter HD2302.0 (Delta OHM). The performance of photoanodes is evaluated by measuring the photocurrent under external bias provided by a potentiostat Amel 7050 performing potential ramps from −0.8 V to about 0.5 V, with a scan rate of 5 mV/s. PEC experiments are also performed under fixed bias potential (0.4 V) for 6 hours to evaluate the photoanodes stability. The photocurrent measurement apparatus is illustrated in Figure 3.9.

Finally, the photoconversion efficiency of TiO_2 photoanodes is obtained according to Equation (1.24) presented in Section 1.4.2, written in percentage

---

[a] The SCE redox potential is +0.244 V vs. SHE (standard hydrogen electrode) at 25°C.

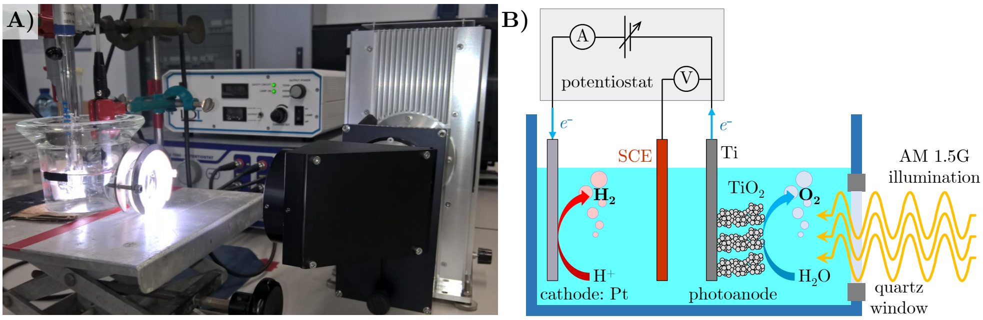

Figure 3.9: Photocurrent measurement apparatus employed for this thesis work: **A)** digital picture and **B)** schematic illustration.

as

$$\eta(\%) = \frac{|J_{ph}| \cdot (E^{\circ} - |V_{app}|)}{P_{light}} \cdot 100 = \frac{|J_{ph}| \cdot (E^{\circ} - |V_{meas} - V_{a,oc}|)}{P_{light}} \cdot 100 \qquad (3.8)$$

in which J_{ph} is the photocurrent density ($\mu\mathrm{A\,cm^{-2}}$), $E^{\circ} = 1.23$ V is the standard reversible potential for water splitting, V_{app} is defined in Equation (1.23) as the difference between the potential at the photoanode, V_{meas}, and the potential at the photoanode in open circuit conditions (with $J_{ph} = 0$), $V_{a,oc}$, both measured with respect to the same reference electrode in the same experimental run, and $P_{light} = 100\,\mathrm{mW/cm^2}$. A more detailed discussion on efficiency measurements is reported in Section 1.4 and in various reports[28–30].

The photocurrent and photoconversion efficiency curves reported in the following chapters are representative data selected among repeated measurements over some months. The TiO_2 photoanodes tested in this Ph.D. thesis are always crystalline (typically in the anatase phase), as obtained after thermal treatments; indeed, photocurrent measurements on as-deposited amorphous TiO_2 lead to very poor results, as well as those on bare Ti plates (the substrate employed for these measurements), i.e. less than 10 $\mu\mathrm{A\,cm^{-2}}$ at 0.5 V vs. SCE (not shown).

4

Hydrogen treatments of TiO_2 hierarchical nanostructures

This chapter reports an explorative investigation on hydrogen-treated TiO_2 hierarchical nanostructures; indeed, the adopted strategy, as described in Section 4.1, consisted in pursuing hydrogenation/reduction effects during both the deposition process and the annealing one. This approach was further investigated and optimized afterwards, and the related results are presented in Chapter 5. The morphological and structural effects produced by the different deposition background atmospheres are described in Section 4.2, while those produced by the annealing treatments (including a detailed optical analysis) are presented in Section 4.3. The photoelectrochemical analysis of all the annealed films and the possible mechanisms explaining these results are discussed in Section 4.4. The study of additional films, prepared to support the arguments presented in this chapter, is reported in Section 4.5; finally, a summary of the obtained results and concluding remarks are presented in Section 4.6. It should be noted that, as already mentioned in Introduction, this chapter reports more extensively the results published in a peer-reviewed article[181]; indeed, my personal contribution consisted in the whole experimental activity presented here, apart from the photoelectrochemical measurements (Section 3.4), X-ray diffraction (Section 3.3.3) and quantum efficiency measurements (as conveniently clarified in Section 4.4.2).

4.1 Experimental strategy

The adopted strategy to obtain hydrogenated/reduced hierarchical TiO_2 nanostructures and to study the corresponding effect on the photoelectrochemical activity was based on the control of both deposition and annealing conditions. The morphology and the approximate thickness of films (1.4 µm), however, was not changed, in order to obtain a more consistent comparison to previous investigations[137,138], in which the optimized background pressure leading to the highest photoelectrochemical response was 5 Pa (as summarized in Section 2.2.4). Thus, on the one hand, three deposition atmospheres were selected, keeping the total pressure at 5 Pa, as follows:

- pure oxygen ("**O_2-TiO_2**", reference);
- Ar/O_2 (50%-50%) mixture ("**Ar/O_2-TiO_2**");
- Ar/H_2 (97%-3%) mixture ("**Ar/H_2-TiO_2**").

The last two approaches were intended as a means to induce oxygen sub-stoichiometry and/or hydrogenation in a partially reducing environment, directly in the synthesis step. On the other hand, three post-deposition thermal treatments were tested for each of the deposition conditions, as follows:

- air, 500°C, 2 h, labeled as **[Air]** (as reference);
- Ar/H_2 (97%-3%) atmosphere at environmental pressure, 500°C, 3 h, labeled as **[Ar/H_2]**;
- "double treatment": [Air] annealing followed by [Ar/H_2], labeled as **[Air+Ar/H_2]**.

For example, a film deposited in pure O_2 atmosphere and annealed in air is labeled as O_2-TiO_2-[Air]. The idea behind the "double treatment" was that of ensuring a good crystallization with a "standard" thermal treatment in air before performing the hydrogenation annealing step. For each deposition condition (i.e. background atmosphere) the effect of three different annealing procedures on twin samples deposited in the same PLD experimental run was evaluated. Accordingly, all the samples were characterized from a morphological, structural and optical point of view and, finally, tested in a photoelectrochemical cell. More details on the deposition parameters are reported in Section 4.1.1 (while the general description on the PLD setup and the details on thermal treatments are reported in Section 3.2.1 and Section 3.2.2, respectively). An additional set of Ar/H_2-TiO_2 films was prepared at 10 Pa instead of 5 Pa and these are treated separately in Section 4.5; the reasons of this choice will be conveniently clarified by the results presented in the following sections.

4.1.1 Deposition parameters

TiO_2 nanostructured films were deposited by ablating a TiO_2 (99.9%) target with the ns-PLD system described in Section 3.2.1 (using $\lambda = 532$ nm and repetition rate 10 Hz). The laser fluence on the target was set at about 3.5 J/cm^2 and the laser pulse energy was 170 mJ. Silicon (100) (University

Wafer, thickness 0.5 mm), soda-lime glass (thickness 1 mm) and titanium plates (Sigma-Aldrich, thickness 0.25 mm, 99.7% purity) were used as substrates, mounted on an off-axis rotating sample holder at a fixed d_{T-S} = 50 mm. All the substrates were kept at room temperature and titanium plate substrates of 2 × 1 cm^2 were half masked during deposition to leave a clean surface for electrical contacts for photoelectrochemical measurements. The deposited mass was fixed at about 0.3 mg/cm^2, as estimated from quartz microbalance measurements, corresponding to a density of 2.1 g/cm^3 and to a nominal thickness of about 1.4 µm; the deposition rate changed between 6 and 16 nm/min depending on the background gas atmosphere. The depositions were performed at a fixed background gas pressure of 5 Pa in three different gas atmospheres (as described previously).

4.2 Deposition background atmosphere effects

The morphology of as-deposited titanium oxide films obtained in different background atmospheres, keeping the total pressure fixed at 5 Pa, is presented in the SEM images in Figure 4.1. The O_2-TiO_2 film surface (Figure 4.1A) exhibits a granular appearance and a nanoscale porosity, with the presence of some “nano-canyons”. Cross-sectional images (Figure 4.1D) show a morphology organized in vertically-oriented nanostructures, which, at higher magnification (Figure 4.1G) appear to be composed by nanoparticles. Similarly, the Ar/O_2-TiO_2 film shows very similar features both from the top-view analysis (Figure 4.1B) as well as from the cross-sectional one (Figure 4.1E and 4.1H): also this film shows a morphology characterized by oriented porous columnar structures composed of nanoparticles. Conversely, the Ar/H_2-TiO_2 film presents a smoother surface (Figure 4.1C) and grows denser and more compact (Figure 4.1F and 4.1I), with a lower thickness (i.e. 1 µm instead of 1.4 µm).

Raman spectra allow to investigate the degree of structural order and the oxide phase. As shown in Figure 4.2, all the Raman spectra of as-deposited films are characterized by broad bands, typical of highly disordered materials. O_2-TiO_2 and Ar/O_2-TiO_2 films show similar spectra with three very large features, while Ar/H_2-TiO_2 shows a spectrum with even broader features, which is an indication of a higher degree of local disorder. This difference is probably related to the lower oxygen content in the Ar/H_2-TiO_2 sample induced by the deposition in a reducing atmosphere[174].

The observed morphological effects are related to clustering and diffusion phenomena occurring in the expanding ablation plume during the deposition process. It can be expected that O_2 and Ar/O_2 atmospheres affect the growth in a very similar way, considering that the molecular mass of O_2 and Ar are

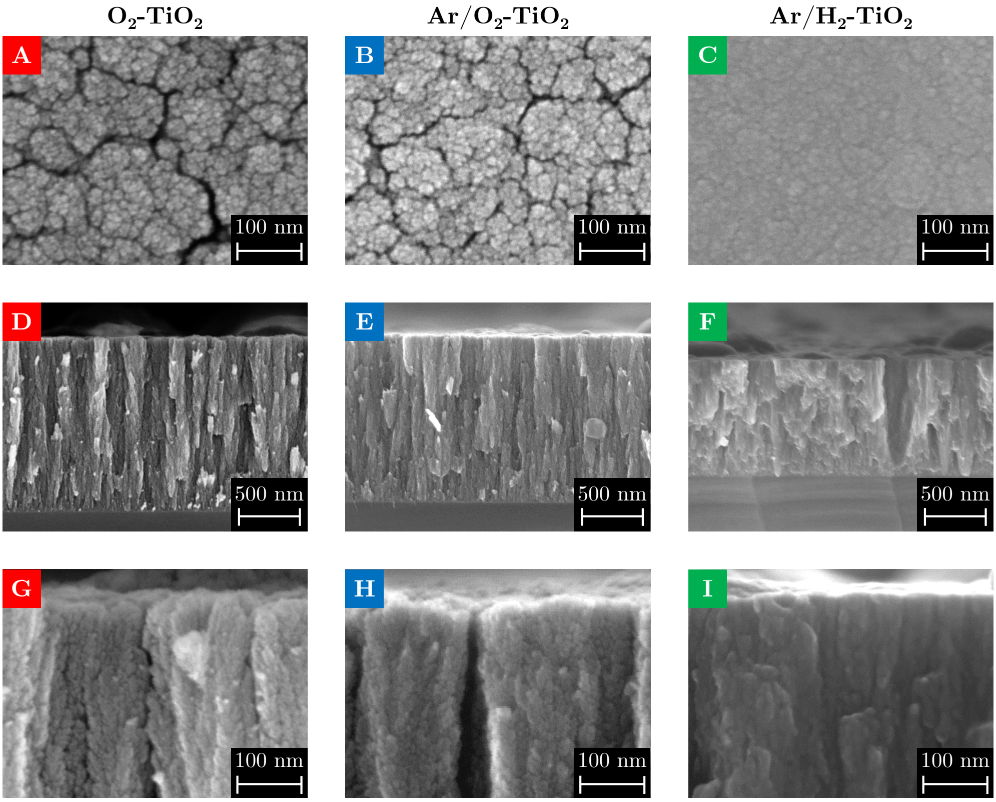

Figure 4.1: Top-view **(A–C)** and cross-sectional **(D–I)** SEM images of TiO_2 films as-deposited with PLD. **(A, D, G)** O_2-TiO_2; **(B, E, H)** Ar/O_2-TiO_2; **(C, F, I)** Ar/H_2-TiO_2.

very similar, and thus the associated elastic scattering process[182]. On the other hand, deposition in Ar/H_2 results in a different morphology, possibly related to different chemical reactions occurring during expansion, thus affecting the dynamics of the plume; this likely leads to a different kinetic energy of the deposited species and, possibly, to a strongly under-oxidized material.

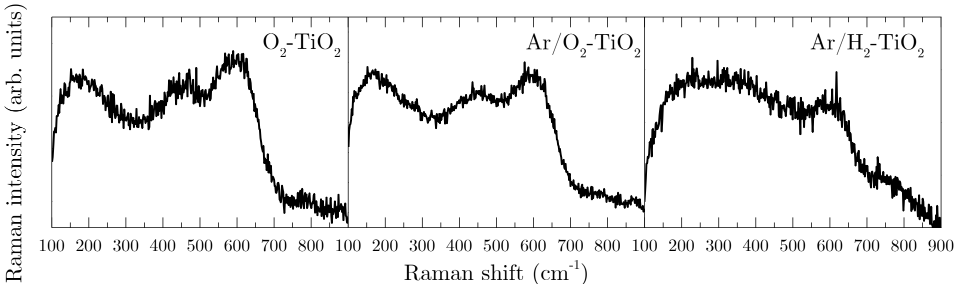

Figure 4.2: Raman spectra of as-deposited TiO_2 films with different background gas: pure O_2 (left), Ar/O_2 mixture (middle) and Ar/H_2 mixture (right).

4.3 Annealing treatments effects

All the films presented in the previous section were heated with the three post-deposition thermal treatments described in Section 4.1; accordingly, their effect on the morphological, structural and optical properties is presented in Section 4.3.1, Section 4.3.2 and Section 4.3.3, respectively.

4.3.1 Morphological analysis

The influence of thermal treatments on the morphological features of the O_2-TiO_2 films was investigated with SEM analysis, as reported in Figure 4.3. In the first row (Figure 4.3A–C), the images of the as-deposited film are shown as reference. On the other hand, the SEM images of O_2-TiO_2 films annealed with [Air], [Ar/H_2] and [Air+Ar/H_2] treatments are reported in the second row (Figure 4.3D–F), third row (Figure 4.3G–I) and fourth row (Figure 4.3J–L), respectively. Thermal treatments do not affect the overall film morphology and thickness, as evidenced by low-resolution cross-sectional images (Figure 4.3B, E, H, K). However, top-view images (Figure 4.3A, 4.3D, 4.3G and 4.3J) show the formation of polygonal nanoparticles, with an estimated size of tens of nm, which can be identified with nanocrystals (as confirmed by the structural characterization, see Section 4.3.2); this is clearer for films annealed in air (either alone or followed by Ar/H_2 annealing). A similar observation can be made from high-resolution cross-sectional images (Figure 4.3C, 4.3F, 4.3I and 4.3L): polygonal nanocrystals appear and they partially merge between each other due to a sintering effect induced by annealing. This leads to an increase in coalescence and connectivity among nanoparticles; indeed, crystalline vertical “channels” can be observed. The fact that this effect is more evident upon annealing in air could be also related to the slower heating/cooling rate of the muffle furnace (Section 3.2.2).

The morphological analysis by SEM images of the Ar/O_2-TiO_2 films is presented in Figure 4.4, with the same layout as in the previous case. As observed for the O_2-TiO_2 films, the crystallization and sintering of nanoparticles occurs, which assume a polygonal shape and become closely connected to each other; this effect is stronger for [Air]- and [Air+Ar/H_2]-annealed films (Figure 4.4D–F and 4.4J–L). On the whole, the morphological effects of thermal treatments on O_2- and Ar/O_2-TiO_2 films are completely comparable.

The morphological analysis of annealed Ar/H_2-TiO_2 films, reported in Figure 4.5, shows a different outcome. The as-deposited film is already denser and more compact with respect to the as-deposited O_2- and Ar/O_2-TiO_2 films (Figure 4.1), but a vertically-oriented morphological organization is still discernible. Upon annealing, while the surface morphology remains almost unchanged (Figure 4.5A, 4.5D, 4.5G and 4.5J), the cross-sectional analysis

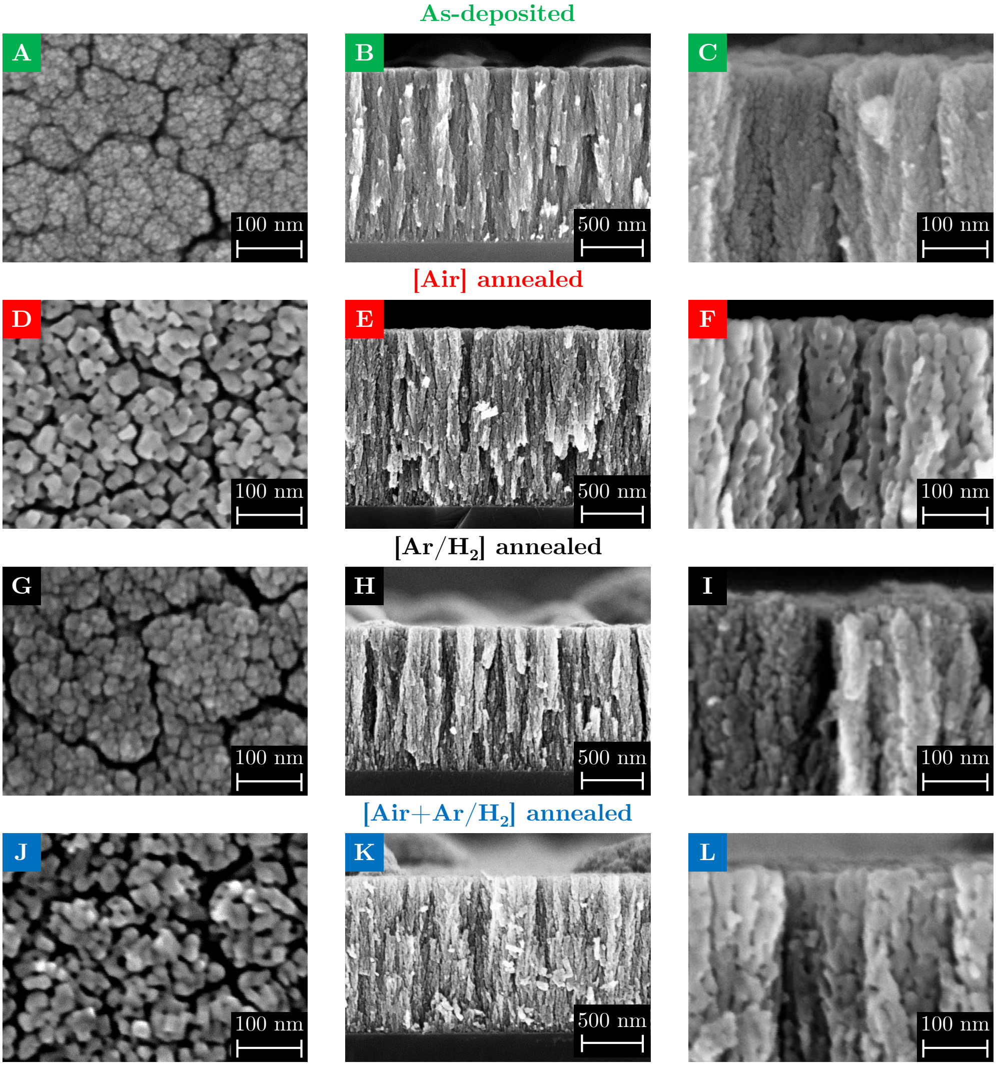

Figure 4.3: SEM images of O_2-TiO_2 films. **(A–C)** As-deposited; **(D–F)** [Air] annealed; **(G–I)** [Ar/H_2] annealed; **(J–L)** [Air+Ar/H_2] annealed.

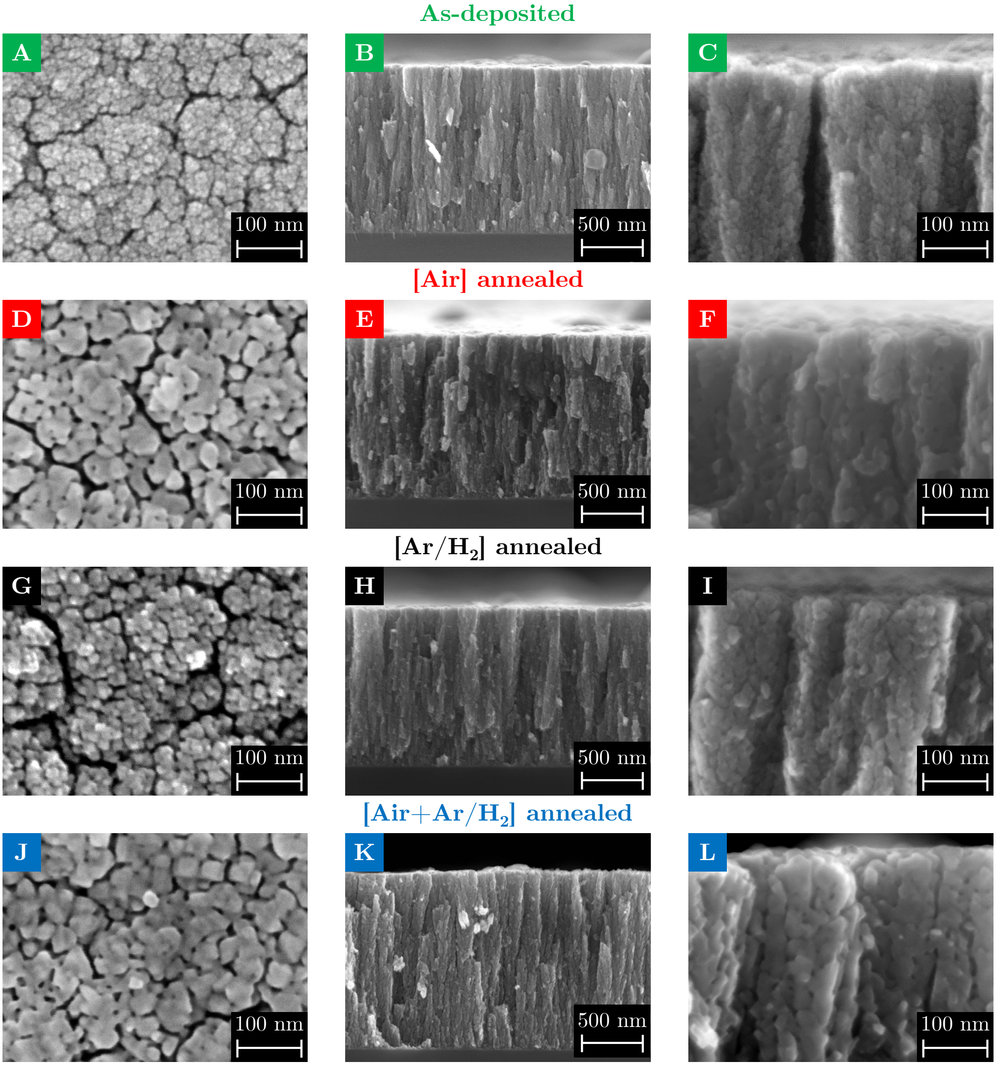

Figure 4.4: SEM images of Ar/O_2-TiO_2 films. **(A–C)** As-deposited; **(D–F)** [Air] annealed; **(G–I)** [Ar/H_2] annealed; **(J–L)** [Air+Ar/H_2] annealed.

shows an evident compacting, so that no indication of columnar structures persists (Figure 4.5E, H, K). High-resolution images (Figure 4.5F, 4.5I and 4.5L), moreover, do not allow to discern the presence of nanoparticles or nanocrystalline domains, which may be completely merged with each other. To sum up, on the contrary of O_2- and Ar/O_2-TiO_2 films, annealed Ar/H_2-TiO_2 films show an overall more compact morphology with respect to the as-deposited one without significant differences between the thermal treatment employed.

The very low porosity, and thus the expected surface area (not measured in this work), of these films does not appear favorable for the application in water splitting cells, as confirmed by the functional tests (Section 4.4). In addition, a comparison of photoelectrochemical properties of TiO_2 films with the same morphology was desired. For this reason, an additional deposition in Ar/H_2 was performed at higher pressure (10 Pa), aiming at recovering the same hierarchical morphology of O_2- and Ar/O_2-TiO_2 films. The discussion on the characterization and photoelectrochemical properties of these films is presented in Section 4.5.

4.3.2 Structural analysis

The crystalline structure of the annealed films was first investigated by means of Raman spectroscopy, as shown in the first column of Figure 4.6, where Raman spectra of O_2-TiO_2 (Figure 4.6A), Ar/O_2-TiO_2 (Figure 4.6C) and Ar/H_2-TiO_2 (Figure 4.6E) samples are shown. For all the films, all thermal treatments induce crystallization in the anatase phase: indeed, the five characteristic peaks of this phase at 144, 198, 399, 517 and 638 cm^{-1} are present in all the spectra, while the sixth weak A_{1g} active mode expected at 513 cm^{-1} is covered and merges into the peak at 517 cm^{-1}[46,183]. Moreover, no significant variation of position or width of the peaks is observed (the analysis of the $E_g(1)$ peak is reported in the insets in Figure 4.6). Therefore, relevant effects related to quantum confinement[49,50], large defectivity[51] or poor O stoichiometry[49,52] can be excluded.

In addition, a photoluminescence (PL) background appears under the Raman peaks for the [Ar/H_2] and [Air+Ar/H_2] annealed films, but not for the [Air] annealed one. As a consequence, PL spectra excited at room temperature by the same laser line used for Raman measurements (514.5 nm, i.e. 2.41 eV, thus smaller than the bandgap) were acquired for the annealed O_2-, Ar/O_2- and Ar/H_2-TiO_2 films and they are reported respectively in Figure 4.6B, 4.6D and 4.6F. A large PL band is observed in the spectral region from 550 to 900 nm (1.3–2.3 eV), composed by a few components. Since these PL features are absent for the [Air] annealed film, it is assumed that they are related to defect levels in the oxide gap induced by the hydrogenation treatment, such as oxygen vacancies (V_O) or Ti^{3+} sites, as

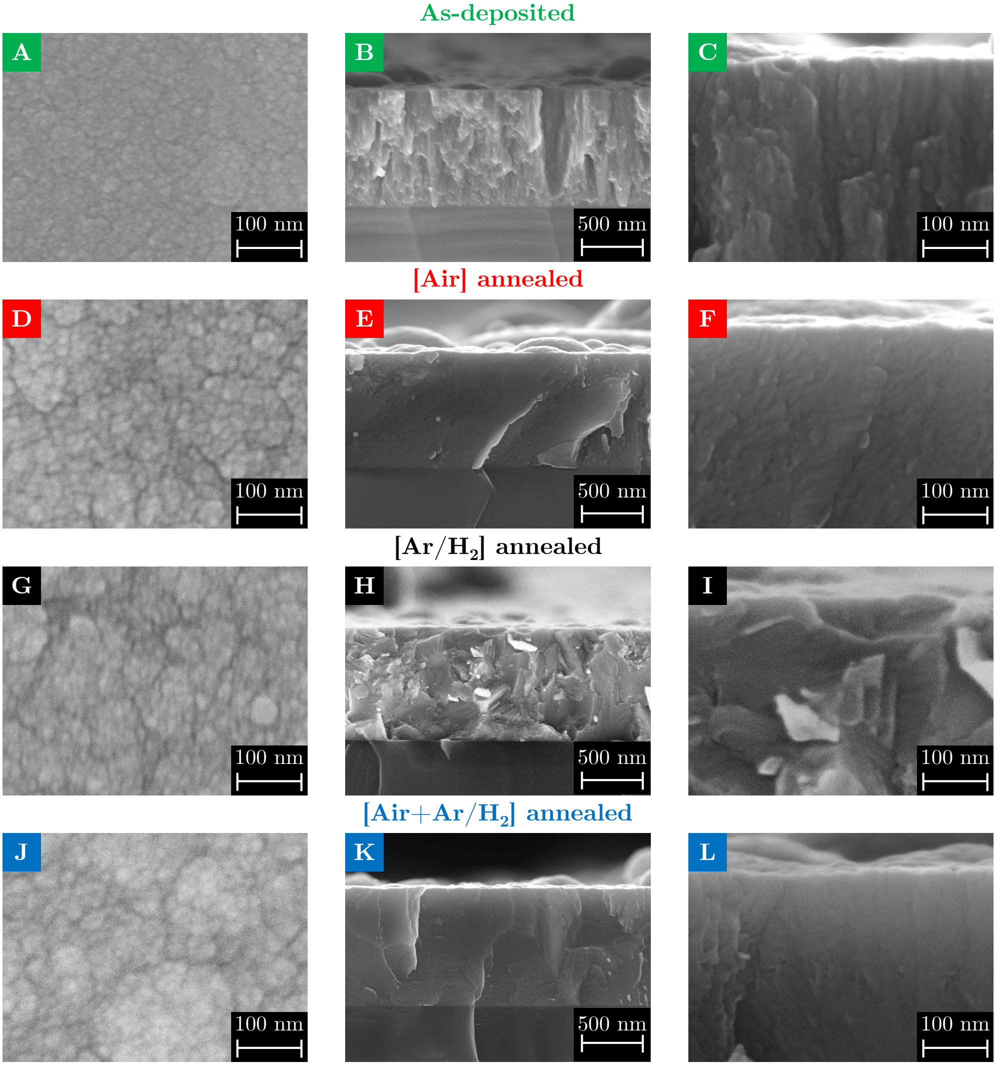

Figure 4.5: SEM images of Ar/H_2-TiO_2 films. **(A–C)** As-deposited; **(D–F)** [Air] annealed; **(G–I)** [Ar/H_2] annealed; **(J–L)** [Air+Ar/H_2] annealed.

reported for instance for hydrogen-treated TiO_2 nanoparticles[162]; indeed, these defects are typically foreseen in reduced TiO_2 materials[157]. As the nature of H-induced defects and disorder in hydrogenated/reduced TiO_2 is still a complex and partially open issue[78,79], and since PL analysis of TiO_2 nanomaterials is also quite complex[184], a detailed discussion is out of the scope of this chapter. Indeed, preliminary X-ray photoelectron spectroscopy (XPS) measurements[a] on the Ar/O_2-TiO_2-[Air+Ar/H_2] film did not evidence any distinct presence of Ti^{3+} sites or other defects, nor any clear spectral difference with respect to the [Air]-annealed film. More detailed PL experiments with different excitation wavelengths were addressed afterwards and they are presented in Chapter 6. Here, the PL background in Raman spectra can be considered as an indication of radiative recombination through defect states, induced by thermal treatments in a reducing atmosphere; as such, these defects could be present only in a limited amount in [Air] annealed films, thus not giving rise to a PL signal.

By comparing the three depositions, it can be observed that they all show the same behavior at the same annealing conditions; however, the PL background for the Ar/H_2-TiO_2 film is weaker with respect to the other two depositions (as evident from the low signal/noise ratio in Figure 4.6F), which may suggest a lower amount of surface defects giving rise to radiative recombinations, due to the lower surface area, or also a higher degree of non-radiative recombination pathways.

Further information on the crystalline structure was obtained by X-ray diffraction (XRD), as shown in Figure 4.7. On the top (Figure 4.7A), a reference anatase powder diffractogram is reported, while below (Figure 4.7B) the diffraction patterns of Ar/O_2-TiO_2 films are reported. One the one hand, the as-deposited film does not exhibit any diffraction peak, so that it is amorphous, consistently with Raman analysis (Figure 4.2); on the other hand, all the annealed Ar/O_2-TiO_2 films exhibit the characteristic peaks of anatase phase without evident shift or broadening, suggesting that no major distortion or disorder is present. The same results are obtained also for annealed O_2-TiO_2 films and, moreover, for the Ar/H_2-TiO_2-[Ar/H_2] film (not shown). The table on the right of Figure 4.7 shows the analysis of anatase (101) and (004) peaks, i.e. the most intense ones in the diffractograms, and reveals that their positions in all the investigated samples is almost the same. In addition, the crystal domain size, evaluated with the Scherrer's formula, leads to an average value of about 44 nm for the (101) peaks and 36 nm for the (004), which is consistent with the estimate made by high-resolution SEM images.

---

[a] G. Bussetti of Department of Physics, Politecnico di Milano is greatly acknowledged for XPS measurements.

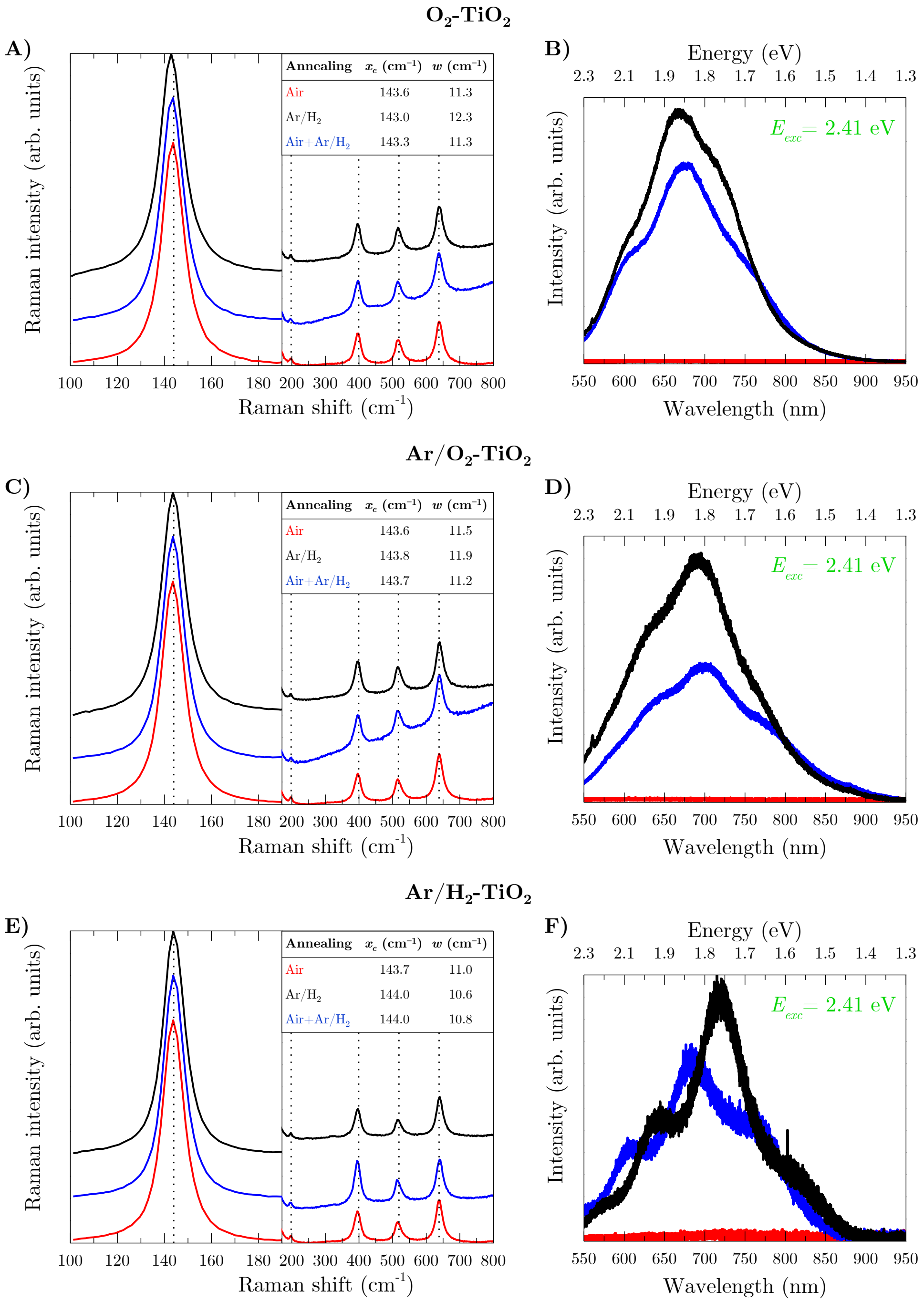

O_2-TiO_2

Annealing	x_c (cm^{-1})	w (cm^{-1})
Air	143.6	11.3
Ar/H_2	143.0	12.3
Air+Ar/H_2	143.3	11.3

Ar/O_2-TiO_2

Annealing	x_c (cm^{-1})	w (cm^{-1})
Air	143.6	11.5
Ar/H_2	143.8	11.9
Air+Ar/H_2	143.7	11.2

Ar/H_2-TiO_2

Annealing	x_c (cm^{-1})	w (cm^{-1})
Air	143.7	11.0
Ar/H_2	144.0	10.6
Air+Ar/H_2	144.0	10.8

Figure 4.6: Raman (first column) and PL (second column) spectra of annealed O_2-TiO_2 films **(A, B)**, Ar/O_2-TiO_2 films **(C, D)** and Ar/H_2-TiO_2 films **(E, F)** (red: [Air]; black: [Ar/H_2]; blue: [Air+Ar/H_2]). The inset tables show the analysis of the $E_g(1)$ peak performed with a Lorentian fitting (x_c: peak position, w: full-width at half-maximum).

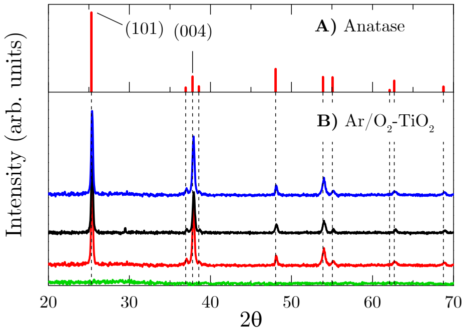

Crystal size domain evaluation

	(101) peak		(004) peak	
Annealing	2ϑ	d (nm)	2ϑ	d (nm)
As-dep.	-	-	-	-
Air	25.39	40	37.93	34
Ar/H_2	25.35	42	37.94	38
Air+Ar/H_2	25.39	49	37.91	36

Figure 4.7: XRD analysis of Ar/O_2-TiO_2 films grown on glass substrates (green: as deposited; red: [Air]; black: [Ar/H_2]; blue: [Air+Ar/H_2]). **A)** Anatase reference powder diffractogram taken from a database[42]; **B)** Ar/O_2-TiO_2. The table on the right reports the analysis of (101) and (004) peaks with the estimated crystal domain sizes.

4.3.3 Optical analysis

In this section, the optical properties of the TiO_2 films are presented; as mentioned in Section 3.3.4, they were evaluated with transmittance and reflectance spectra measured with a spectrophotometer equipped with an integrating sphere. It should be reminded that the total transmittance of all the films was normalized with respect to the glass substrate.

The optical analysis of Ar/O_2-TiO_2 films[b] is presented in Figure 4.8. Figure 4.8A shows the transmittance spectra and the photographs of films grown on glass substrates. It can be easily observed by the unaided eye that the color of films is influenced by the thermal treatment: the as-deposited film is almost transparent, the [Air] annealed one is white, the [Ar/H_2] annealed one is dark-grey and the [Air+Ar/H_2] annealed one is light-grey. This qualitative color difference is experimentally confirmed by a change in transmittance curves, especially in the visible region: in proximity of the optical bandgap, the absorption edge is smoother for the films annealed in Ar/H_2 atmosphere with respect to the sample only annealed in air, and all of the annealed films have a lower transmittance with respect to the as-deposited one. In the spectra, fringes in the high-transparency region appear as a consequence of interference phenomena and they depend on sample thickness morphology, thickness and optical constants. Figure 4.8B, on the other hand, shows the diffuse transmittance spectra (solid lines) and the haze factor curves (dashed lines), which show that the light scattering ability of the TiO_2 hierarchical films is maximum in proximity of the optical bandgap and gradually decreases at higher wavelengths. Also, the film with the highest scattering ability is the [Air] annealed one. Figure 4.8C,

---

[b] These films are presented before and in more detail with respect to the O_2-TiO_2 ones due to their more promising photoactivity, as discussed in Section 4.4.

furthermore, shows the reflectance curves, evaluated in the UV-visible range, which globally lie between 10 and 25% without major differences between them (the reflectance of [Ar/H_2] and [Air+Ar/H_2] annealed films is slightly higher in the UV range). Figure 4.8D, accordingly, shows the absorbance curves of all the films. In this case, the [Ar/H_2] annealed film shows a more pronounced absorption tail in the visible range, while the as-deposited one shows the lowest absorbance. In addition, some fringes still persist in the curves, which arise from a measurement performed in a region of thickness unevenness (this issue was not solved after repeated measurements but does not affect the observed trends). Finally, the Tauc plots of the annealed films are reported in Figure 4.8E, while the obtained bandgap values are reported in Table 4.1, together with the ones of the O_2-TiO_2 and Ar/H_2-TiO_2 films. The values of the optical bandgap for all the Ar/O_2-TiO_2 samples are around 3.2 eV, the typically expected value of anatase.

The appearance of the absorption tail in the visible range without a change in the bandgap value is related to the presence of a limited amount of defect states in the bandgap, introduced by annealing in Ar/H_2 atmosphere, or surface states. The presence of defects is supported also by PL spectra, which suggest radiative emission upon excitation with photon energy below the bandgap (2.4 eV). However, a precise identification of these defect states requires specific investigations. As already mentioned, the reader is referred to Chapter 6 for investigations on PL emission of these materials.

The optical analysis of O_2-TiO_2 films is reported in Figure 4.9. These films exhibit qualitatively similar optical properties to the Ar/O_2-TiO_2 films. Indeed, Figure 4.9A shows that the transmittance curves follow the trend [Air] $>$ [Air+Ar/H_2] $>$ [Ar/H_2], confirming the qualitative color difference (see photographs in Figure 4.9B). However, the O_2-TiO_2-[Air] film is more transparent in the visible region than the corresponding Ar/O_2-TiO_2 film (see Table 4.1). On the other hand, Figure 4.9B shows the absorbance spectra of all the annealed O_2-TiO_2 films, which confirm the trend observed with transmittance curves; also in this case, as for the Ar/O_2-TiO_2 films (see Figure 4.8D), an absorption tail in the visible range appears for the [Ar/H_2] and [Air+Ar/H_2] annealed films; thus, the same argument can be applied also for these films, i.e. defect states in the bandgap or surface states giving rise to this absorption tail.

The optical analysis of Ar/H_2-TiO_2 films is presented in Figure 4.10. These films show a different behavior with respect to the Ar/O_2-TiO_2 ones (Figure 4.8). First, the as-deposited film is almost black (inset in Figure 4.10B) and, accordingly, it exhibits a very low transmittance (Figure 4.10A) and a very high absorbance (Figure 4.10D); upon annealing, its color turns into greyish without major differences between the different thermal treatments (insets in Figure 4.10B), which is confirmed by transmittance and absorbance spectra (Figure 4.10A and 4.10D). Slight

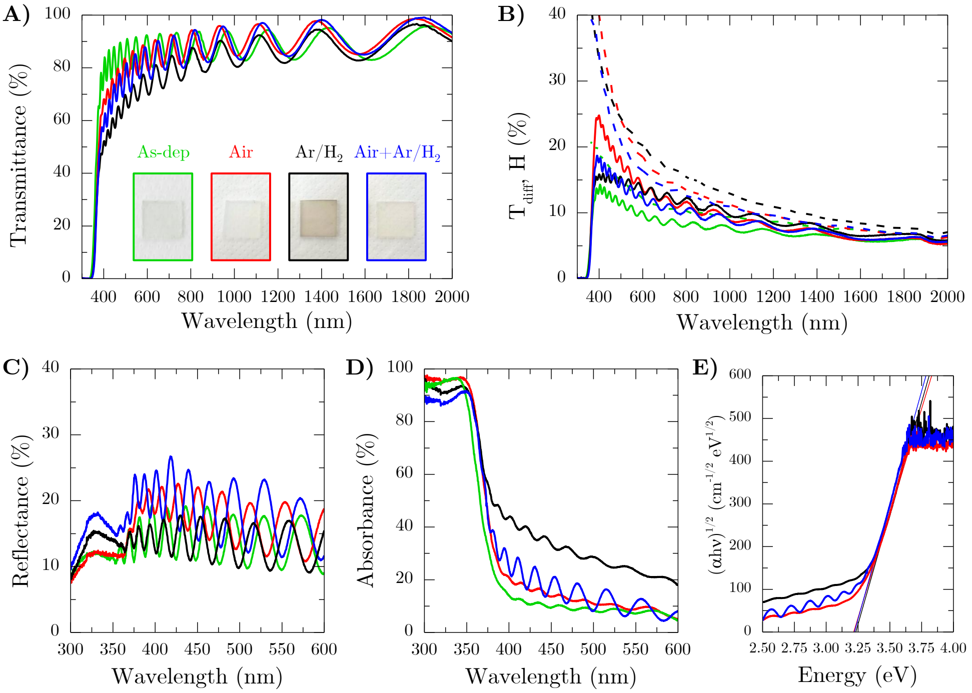

Figure 4.8: Optical analysis of Ar/O_2-TiO_2 films (green: as-deposited; red: [Air]; black: [Ar/H_2]; blue: [Air+Ar/H_2]). **A)** Transmittance curves (optical photographs of the films are shown as insets); **B)** diffuse transmittance (solid lines) and haze factor (dashed lines) curves; **C)** reflectance curves; **D)** absorbance curves; **E)** Tauc plot curves.

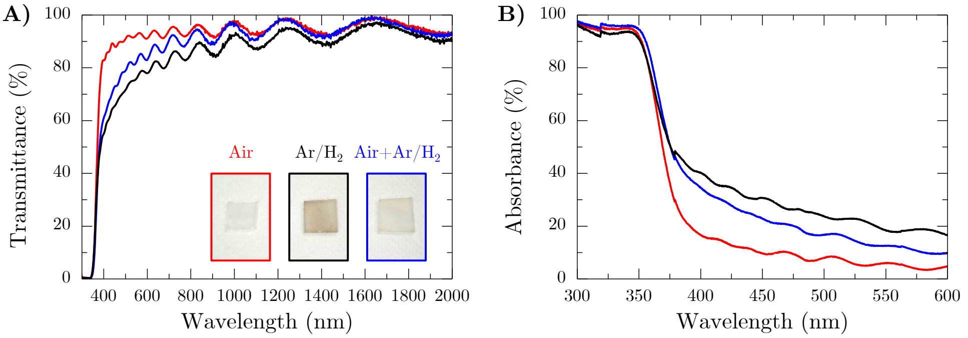

Figure 4.9: Optical analysis of O_2-TiO_2 films (red: [Air]; black: [Ar/H_2]; blue: [Air+Ar/H_2]). **A)** Transmittance curves (optical photographs of the films are shown as insets); **B)** absorbance curves.

differences between the annealed films appear in the diffuse transmittance spectra (Figure 4.10B), where the trend [Air] > [Air+Ar/H_2] > [Ar/H_2] appears, and in reflectance spectra (Figure 4.10C), where the [Ar/H_2] film exhibits slightly higher values. Furthermore, the bandgap energy for all the annealed films is still about 3.2 eV (Figure 4.10E).

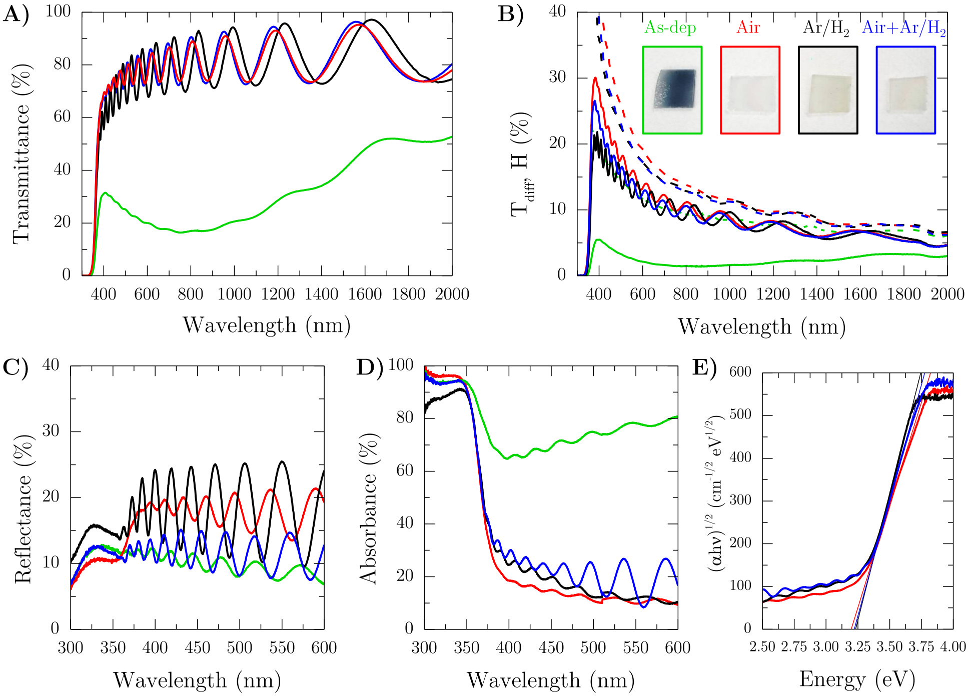

Figure 4.10: Optical analysis of Ar/H_2-TiO_2 films (green: as-deposited; red: [Air]; black: [Ar/H_2]; blue: [Air+Ar/H_2]). **A)** Transmittance curves; **B)** diffuse transmittance (solid lines) and haze factor (dashed lines) curves (optical photographs of the films are shown as insets); **C)** reflectance curves; **D)** absorbance curves; **E)** Tauc plot curves.

By comparing the Ar/H_2-TiO_2 and the Ar/O_2-TiO_2 films, three main differences appear:

- the as-deposited Ar/H_2-TiO_2 film is almost black, darker than the corresponding annealed films (Figure 4.10A and 4.10B), while the as-deposited Ar/O_2-TiO_2 is clearer than the corresponding annealed ones (Figure 4.10A and 4.10B); this effect can be understood considering that deposition in Ar/H_2 atmosphere leads to a very disordered material, more than deposition in pure O_2 or in Ar/O_2 mixture (also suggested by Raman spectroscopy, see Figure 4.2), while annealing promotes crystallization in anatase (Figure 4.6E), restoring its optical properties;
- the transmittance and absorbance curves for annealed Ar/H_2-TiO_2 films

Table 4.1: Tauc optical bandgap (E_g) and mean transmittance in the visible range (T_{vis}, with $400 \leq \lambda \leq 700$ nm) of the annealed O_2-, Ar/O_2- and Ar/H_2-TiO_2 films.

Sample	Annealing	E_g (eV)	T_{vis} (%)
O_2-TiO_2	Air	3.26	90.8
	Ar/H_2	3.26	73.9
	Air+Ar/H_2	3.21	80.4
Ar/O_2-TiO_2	Air	3.22	80.2
	Ar/H_2	3.23	68.6
	Air+Ar/H_2	3.22	76.9
Ar/H_2-TiO_2	Air	3.20	76.6
	Ar/H_2	3.20	73.0
	Air+Ar/H_2	3.22	76.6

are very similar to each other irrespectively of the annealing treatment (Figure 4.10A and 4.10D), while for the annealed Ar/O_2-TiO_2 (Figure 4.8A and 4.8D) and O_2-TiO_2 (Figure 4.9) films a trend emerges; this can be tentatively ascribed to a different effect of Ar/H_2 annealing on Ar/H_2-TiO_2 films since they show a more compact morphology, thus a lower surface area, with respect to the other films, and this qualitative morphological difference is increased with thermal treatments (see Figure 4.5 compared to Figures 4.3 and 4.4);

- the fringes in the visible and infrared region in the optical spectra of Ar/H_2-TiO_2 films are more intense with respect to the other films; this can be related to the higher density and lower surface roughness of the Ar/H_2-TiO_2 films, which promote coherent optical phenomena.

Optical characterizations, to conclude, in particular the appearance of the absorption tail in the visible range without a change in the bandgap value, suggest that annealing in Ar/H_2 atmosphere (either as a single treatment or preceded by annealing in air) induces a limited amount of defects or disorder confined to the nanoparticles surface layers, while probably their crystalline (anatase) core is not affected. The presence of defects is supported by PL spectra (Figure 4.6B, 4.6D and 4.6F), while XRD diffractograms and Raman spectra show that the “bulk” crystallinity of the material is not affected (Figures 4.6 and 4.7). In the recent literature on *black titania*, indeed, theoretical and experimental evidences show that various defects can be formed depending on the hydrogenation/reduction procedure, such as oxygen vacancies/Ti^{3+} sites, surface disorder, Ti–OH and Ti–H bonds[78,79] (as discussed in Section 2.3). As a consequence, these defects induce electronic states in the bandgap, which can act as trapping sites for photogenerated charges, retarding their recombination[79]. Thus, the next step of this analysis consists in the evaluation of the annealing effects on the photoelectrochemical properties of TiO_2 hierarchical films.

4.4 Photoelectrochemical properties

The whole set of annealed TiO_2 films, described in the previous section, were tested from the functional point of view with photocurrent measurements with the setup and parameters described in Section 3.4 and the results are presented in Section 4.4.1. Moreover, for the most promising photoanodes (i.e. the Ar/O_2-TiO_2 films), quantum efficiency measurements were also performed (thanks to a collaboration with P. Schmuki's group, University of Erlangen-Nuremberg) to understand in more detail the photocurrent enhancement (Section 4.4.2). Finally, a discussion on the whole set of photoelectrochemical results is presented in Section 4.4.3

4.4.1 Photocurrent measurements of the annealed TiO_2 films

The photocurrent measurements and the photoconversion efficiency curves (η(%)), calculated with Equation (3.8), for the whole set of annealed TiO_2 films are shown in the first row and in the second row, respectively, of Figure 4.11. All of the investigated photoanodes exhibit negligible anodic current (less than $5\,\mu A\,cm^{-2}$) under dark conditions (not shown) over all the investigated potential range, which indicates that insignificant photoelectrochemical water oxidation occurred at the anodes surface. On the contrary, upon illumination, photocurrent generation is observed.

For the O_2-TiO_2 photoanodes (Figure 4.11A), the best performances are associated with the [Air] annealed film: photocurrent onset is observed at approximately -0.75 V; then, the photocurrent density gradually increases with the applied bias potential, because of the efficient charge carriers separation under the effect of the applied bias[185–187], until a saturated photocurrent density of ca. 40 $\mu A\,cm^{-2}$ is observed. The photoresponse decreases for the [Ar/H_2]- and the [Air+Ar/H_2]-annealed films: in these cases, the photocurrent onset is observed at higher potential value (about -0.45 V) and a lower saturated photocurrent density is measured (i.e. reaching values near 20 and 15 $\mu A\,cm^{-2}$ at 0.5 V, respectively), which suggests a less efficient generation and transfer of photogenerated charge carriers and major recombination losses, as well[188–190].

In the case of Ar/O_2 photoanodes (Figure 4.11B), the [Air+Ar/H_2] annealed film outperforms the [Air] and [Ar/H_2] annealed ones. Indeed, it shows the highest photocurrent densities through the entire potential window, and the saturated photocurrent reaches a value of 110 $\mu A\,cm^{-2}$ at 0.5 V, which represents a 3-fold increase of the photocurrent response if compared to the other thermal treatments. As a control experiment, Figure 4.11B shows also the results obtained for another Ar/O_2-TiO_2 film annealed in air for 5 h instead of 2 h, as for all the other [Air] annealed films. As it clearly appears, a photocurrent density comparable to that of the 2 h air-annealed sample is attained, thus indicating that the increase of photocurrent observed in the case of the double-treated photoanode is not related to the total annealing time, but it likely depends on the hydrogenation treatment.

Finally, the effect of the annealing treatments was also evaluated for the Ar/H_2-TiO_2 films (Figure 4.11C); in this case, quite low photocurrents are observed, with a negligible effect of the different annealing conditions on the photoactivity.

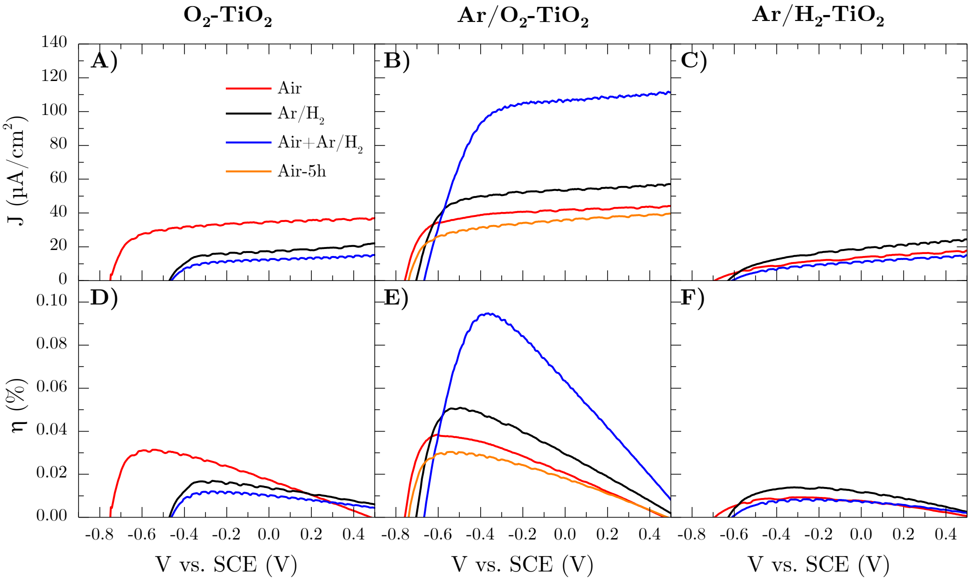

Figure 4.11: Photoelectrochemical results for the annealed TiO_2 photoanodes: photocurrent measurements **(A, B, C)** and photoconversion efficiency curves **(D, E, F)** for O_2-TiO_2 films **(A, D)**, Ar/O_2-TiO_2 films **(B, E)** and Ar/H_2-TiO_2 films **(C, F)**. The color coding is red: [Air]; black: [Ar/H_2]; blue: [Air+Ar/H_2]; orange: [Air] for 5 h).

Comparing, on the other hand, the photoconversion efficiencies of the annealed O_2-TiO_2 (Figure 4.11D), Ar/O_2-TiO_2 (Figure 4.11E) and Ar/H_2-TiO_2 films (Figure 4.11F), it is possible to observe that the highest photoconversion efficiencies are found for films deposited in Ar/O_2 atmosphere (Figure 4.11E), followed by those deposited in pure O_2 (Figure 4.11D). On the other hand, the lowest values are found for samples deposited in Ar/H_2 mixture (Figure 4.11F). The maximum photoconversion efficiency of ca. 0.095% is obtained for the Ar/O_2-TiO_2-[Air+Ar/H_2] photoanode (Figure 4.11E).

Due to their higher photoresponse with respect to all the other investigated films, the Ar/O_2-TiO_2 films were investigated from the stability point of view. Accordingly, Figure 4.12A shows the photocurrent measured over time with applied bias potential of 0.4 V for the [Air], [Ar/H_2] and [Air+Ar/H_2] annealed films. In line with the above results, the [Air+Ar/H_2] annealed sample shows the highest photocurrent results and, notably, possesses the highest photostability. Namely, after 6 h of continuous illumination the photocurrent drops within about 5% vs. 15% and 20% for samples annealed with [Air] and [Ar/H_2] treatments, respectively. Moreover, the photostability of this photoanode was further confirmed by photocurrent measurements over several months, which showed very similar results as those presented in Figure 4.11; indeed, Figure 4.12B shows that the photocurrent exhibited by the Ar/O_2-TiO_2-[Air+Ar/H_2] photoanode dropped from about 110 to about 100 $\mu A\,cm^{-2}$ at 0.5 V, which is a moderate performance decrease.

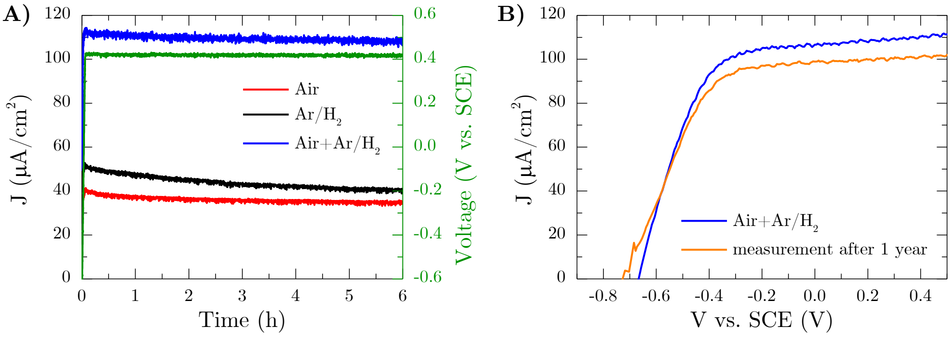

Figure 4.12: Photostability of annealed Ar/O_2-TiO_2 photoanodes: **A)** measured by photocurrent over time with applied bias potential of 0.4 V vs. SCE; **B)** measured by *J–V* curves acquired one year after the first measurement.

4.4.2 Quantum efficiency of Ar/O_2-TiO_2 films

The most efficient photoanode emerging from this study, i.e. Ar/O_2-TiO_2-[Air+Ar/H_2], was further investigated by means of incident photon-to-electron conversion efficiency (IPCE) measurements, alongside the corresponding [Air] annealed film, performed in collaboration with N. Liu and P. Schmuki at the Department of Materials Science WW4-LKO of the University of Erlangen-Nuremberg. These measurements were carried out in the range 300–600 nm at an applied potential of 0.5 V using a three electrode arrangement (Ag/AgCl, 3 M KCl as reference and Pt as counter electrode) in an electrochemical cell equipped with a quartz window in 0.1 M Na_2SO_4 solution. The illumination setup consisted of an Oriel 6356 150 W Xe arc lamp as a light source and an Oriel XCornerstone 7400 1/8 monochromator.

The IPCE results are presented in Figure 4.13, which shows that the quantum efficiency of the [Air+Ar/H_2] annealed film is markedly higher than that of the [Air] annealed film in the UV range; indeed, an enhancement by a factor > 3 emerges. On the other hand, the quantum efficiency of both films in the visible range is negligible. Therefore, IPCE measurements confirm the beneficial effect of [Air+Ar/H_2] annealing and explain the photocurrent increase for the Ar/O_2-TiO_2 films (Figure 4.11B).

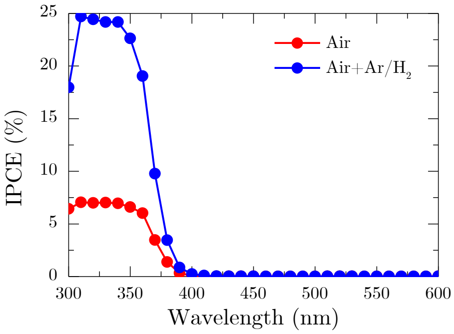

Figure 4.13: IPCE spectra of annealed Ar/O_2-TiO_2 photoanodes (red: [Air]; blue: [Air+Ar/H_2]).

4.4.3 Discussion

The results presented above suggest that the deposition atmosphere composition and the annealing atmosphere/procedure strongly influence the photoelectrochemical performance, as shown in Figure 4.11; an explanation of these findings is not straightforward, also considering the various results and related discussions in the framework of *black titania* nanomaterials[78,79], as mentioned in Section 2.2.2 .

Annealing effects. Considering, first, the effects of thermal treatments, previous literature works concerning TiO_2 nanomaterials annealed in Ar/H_2 or N_2/H_2 mixtures at atmospheric pressure[85,90–94,96] generally show a photocurrent enhancement with respect to the pristine air-annealed material. In particular, the photocurrent values reported in ref. [93] are the closest to those reported in Figure 4.11A–4.11C; however, a direct comparison between these values is not straightforward due to differences in experimental conditions (e.g. electrolyte, illumination) or in material properties (e.g. thickness, crystalline phase, morphology).

In this investigation, a significant beneficial effect only if preceded by annealing in air, which is fundamental because it leads not only to crystallization, but also to significant sintering between nanoparticles, as shown in SEM images (Figures 4.3 and 4.4), thus reducing defects/recombinations and improving electron mobility through the formation of crystalline vertical channels (with reduced grain boundaries), where electrons can be efficiently transported to the external circuit, as observed with TEM in previous works[132,141].

For the Ar/O_2-TiO_2 films, in particular, IPCE spectra suggest that the increased absorption in the visible range (Figure 4.8) does not lead to visible-light activity; conversely, the photoactivity increase of the [Air+Ar/H_2]-annealed with respect to the [Air]-annealed one (Figure 4.11B and 4.11E) is explained by a quantum efficiency increase only in the UV range. This outcome is in agreement with previous works on *black titania* nanomaterials, as mentioned in Section 2.2.2, in which this effect was mainly ascribed to a decrease of recombinations or to an improvement in charge transport, which is generally suggested as an effect arising from any hydrogenation/reduction treatment of TiO_2 thin films[85,98,191].

In particular, previous works on 1D TiO_2 nanomaterials suggest the introduction of defects, such as oxygen vacancies (V_O)/Ti^{3+} sites in the surface layers[91,93,94] promoted by Ar/H_2 thermal treatments. Moreover, an increase of charge carriers, promoted by oxygen vacancies, in hydrogen-treated rutile nanowires has been proposed[84,92].

As a consequence, the hypothesis presented at the end of Section 4.3.3, i.e. the presence of surface defects upon annealing in Ar/H_2 atmosphere giving rise to photoluminescence emission (Figure 4.6) and to absorption tail in the visible range (Figures 4.8 and 4.9), appears consistent with previous literature results. These defects, thus, could increase the conductivity or decrease the recombination rate of TiO_2 hierarchical nanostructures.

Effect of the deposition atmosphere. The functional performance of the material is heavily affected by the initial deposition atmosphere too. The [Air] annealing step is expected to heal sub-stoichiometry or crystalline defects that may arise from a deposition in oxygen-poor atmosphere; indeed, structural characterization (Section 4.3.2) indicates no detectable difference between films deposited in all the explored atmospheres. However, it can be hypothesized that slight differences, probably related to a small oxygen deficiency in the nanoparticle core and leading to better conduction, are important in terms of photoelectrochemical performance, so that a *"memory"* effect (with respect to deposition atmosphere) is clear in these results, and particularly for the best performing sample, as [Air+Ar/H_2] annealing on O_2- or Ar/O_2-TiO_2 films leads to completely different results (Figure 4.11).

The Ar/H_2-TiO_2 films, finally, show the lowest photoresponse, as shown in Figure 4.11C and 4.11F. This outcome can be understood considering that the oxygen deficiency during the deposition process is too high with respect to deposition in Ar/O_2 mixture. In order to confirm this hypothesis and to ascertain this effect from an influence of the more compact morphology (see Figure 4.1), another set of Ar/H_2-TiO_2 films with the same hierarchical morphology of the O_2- and Ar/O_2-TiO_2 films was prepared by increasing the deposition background pressure; the results are presented in the following section.

4.5 Depositions in Ar/H_2 at 10 Pa

As shown by SEM images in Figures 4.1 and 4.5, the Ar/H_2-TiO_2 films deposited at 5 Pa exhibited a more compact morphology with respect to O_2-TiO_2 (Figures 4.1 and 4.3) and Ar/O_2-TiO_2 (Figures 4.1 and 4.4) films. For this reason, a new set of Ar/H_2-TiO_2 films was deposited at higher background pressure, i.e. 10 Pa, in order to obtain a similar morphology to O_2- and Ar/O_2-TiO_2 films, which was evaluated by SEM observations (surface area measurements were not performed in this thesis work). Hereinafter, these films are labeled as **Ar/H_2 (10 Pa)-TiO_2**; the same annealing treatments described in Section 4.1 were applied also for these films and, accordingly, the same characterization and testing procedure was followed.

Figure 4.14 shows the morphological analysis of Ar/H_2 (10 Pa)-TiO_2 films. Clearly, the pressure increase from 5 to 10 Pa produces a more porous morphology (Figure 4.14A–C), in which the vertically-oriented domains are easily distinguishable (Figure 4.14B); also, the hierarchical morphology of these domains is revealed with high-resolution images (Figure 4.14C), which show the nm-sized nanoparticle assemblies composing the film. Upon annealing, the same effects observed for O_2- and Ar/O_2-TiO_2 films (Figure 4.3 and Figure 4.4, respectively) occur: the nanoparticles constituting the material crystallize, increase in size and coalesce with each other, forming vertically-connected “channels”, without major changes to the overall morphology. This effect is less evident for the [Ar/H_2] annealed film, similarly as for the O_2- and Ar/O_2-TiO_2 films. In conclusion, SEM analysis assessed that the Ar/H_2 (10 Pa)-TiO_2 films were completely comparable to O_2- and Ar/O_2-TiO_2 films from the morphological point of view.

Raman characterization of the Ar/H_2 (10 Pa)-TiO_2 films is presented in Figure 4.15. Also for these samples, no evident shift for the $E_g(1)$ peak is evident, even though a slight FWHM increase is measured for the [Ar/H_2] annealed film (Figure 4.15A and inset therein). On the other hand, contrarily to the Ar/H_2-TiO_2 films deposited at 5 Pa (Figure 4.6F) but similarly to the O_2- and Ar/O_2-TiO_2 films (Figure 4.6B and 4.6D), the PL signal for [Ar/H_2] and [Air+Ar/H_2] annealed films is very intense and broad (the [Air] annealed film still shows a negligible response). This outcome may suggest that thermal treatments in Ar/H_2 atmosphere induce a higher amount of defect/surface states in the 10 Pa depositions rather than in the 5 Pa ones due to their higher surface area.

Finally, the photoelectrochemical response of Ar/H_2 (10 Pa)-TiO_2 photoanodes is illustrated in Figure 4.16. The photocurrent densities of all the annealed films (Figure 4.16A) are quite low; indeed, the [Air] and [Ar/H_2]

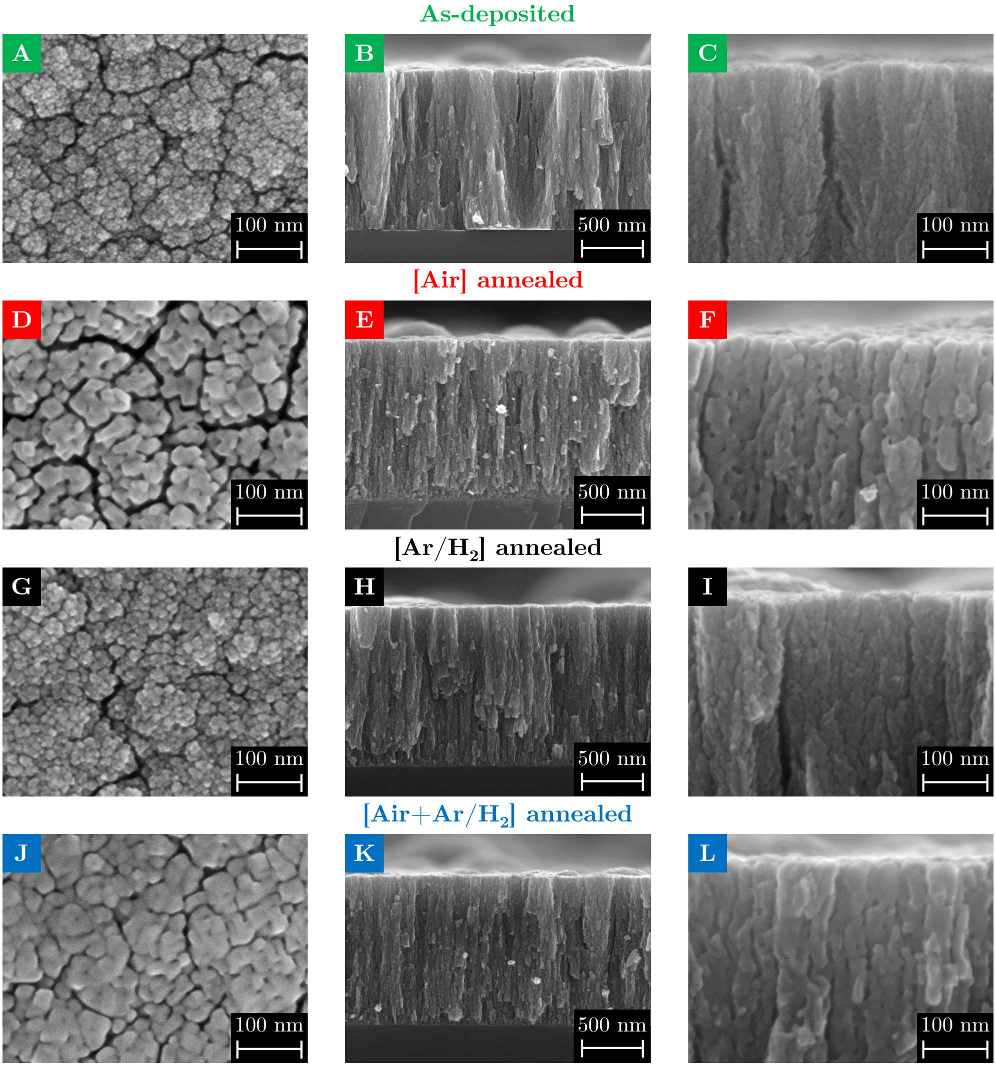

Figure 4.14: SEM images of Ar/H_2 (10 Pa)-TiO_2 films. **(A–C)** As-deposited; **(D–F)** [Air] annealed; **(G–I)** [Ar/H_2] annealed; **(J–L)** [Air+Ar/H_2] annealed.

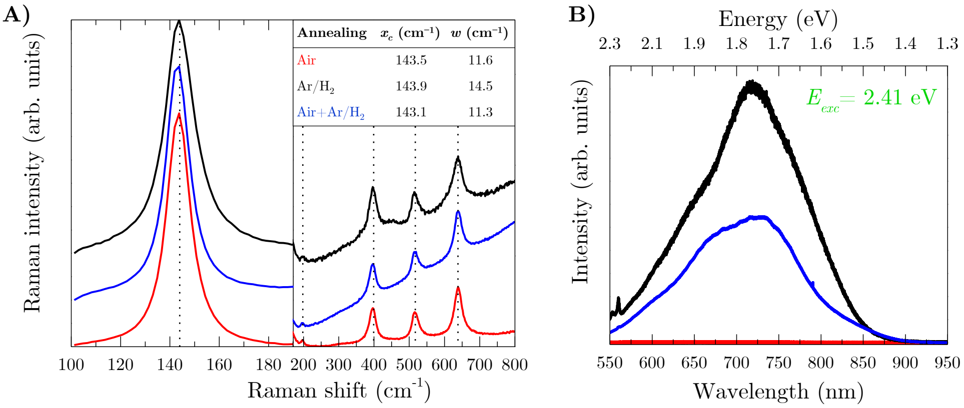

Annealing	x_c (cm^{-1})	w (cm^{-1})
Air	143.5	11.6
Ar/H_2	143.9	14.5
Air+Ar/H_2	143.1	11.3

Figure 4.15: Raman **(A)** and PL **(B)** spectra of annealed Ar/H_2 (10 Pa)-TiO_2 films (red: [Air]; black: [Ar/H_2]; blue: [Air+Ar/H_2]). The inset table shows the analysis of the $E_g(1)$ peak performed with a Lorentian fitting (x_c: peak position, w: full-width at half-maximum).

annealed photoanodes show a similar response, reaching the saturated value of about 15 μA cm^{-2}, but the latter exhibit a higher onset (-0.4 V) with respect to the former (-0.7 V), which is undesirable for practical applications. On the other hand, the maximum photoresponse is observed for the [Air+Ar/H_2] annealed film, reaching the photocurrent density of about 20 μA cm^{-2}. Accordingly, photoconversion efficiency curves confirm this trend, reaching quite low values (Figure 4.16B).

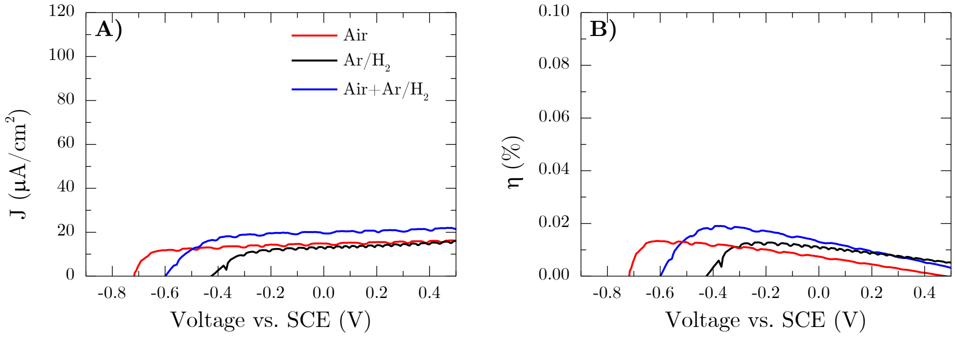

Figure 4.16: Photoelectrochemical behavior of annealed Ar/H_2 (10 Pa)-TiO_2 films (red: [Air]; black: [Ar/H_2]; blue: [Air+Ar/H_2]). **(A)** *J–V* curves; **(B)** photoconversion efficiency curves.

Overall, Figure 4.16 shows that the photoelectrochemical response of Ar/H_2 (10 Pa)-TiO_2 films is definitely lower than that exhibited by the Ar/O_2-TiO_2 films (Figure 4.11B) and also by the reference photoanode, i.e. O_2-TiO_2-[Air] (Figure 4.11A). Nonetheless, by comparing Figure 4.11C to Figure 4.16A, one can conclude that:

- the increase of porosity, and thus surface area, for the Ar/H_2-TiO_2 films produces an increase in photoresponse;
- this photoelectrochemical activity is anyhow insufficient, since ablation of a TiO_2 target with a Ar/H_2 background gas mixture is expected to induce the presence of an excessive amount of defects in the material, independent from the deposition background gas pressure and the post-deposition thermal treatment.

4.6 Summary

This chapter presented an explorative experimental campaign on hydrogenated/reduced TiO_2 hierarchical nanostructured films studied as photoanodes for photoelectrochemical water splitting. In this investigation, the controlled introduction of composition/crystalline defects into the material, in order to increase its photoresponse, was explored both during the deposition step and the annealing step. In particular, depositions were performed at 5 Pa of background gas with pure O_2 (as reference) and in atmospheres with reduced oxygen content (Ar/O_2 50%-50% mixture) or even without (Ar/H_2 97%-3% mixture); thermal treatments were performed in air (as reference) and in Ar/H_2 mixture at atmospheric pressure in substitution to or in combination with air annealing. Another set of films, prepared by deposition in Ar/H_2 atmosphere at 10 Pa, were also investigated to strengthen the arguments explaining the observed results.

The characterization results, obtained with SEM, Raman scattering, PL spectroscopy, X-ray diffraction and UV-visible-IR spectroscopy, show that thermal treatments in the presence of hydrogen do not affect the overall morphology and structure of the material, which always crystallizes in anatase, but they induce the onset of an absorption tail in the visible range. In addition, as evidenced by photocurrent experiments, they influence the material photoactivity, which is also affected by the deposition gas employed (a sort of *"memory"* effect). It was found that some shortage of oxygen in the deposition step (but not its complete absence) as well as a double thermal treatment (in air and, subsequently, in the Ar/H_2 mixture) leads to a clear enhancement in TiO_2 photoresponse with respect to all the other investigated conditions. The performance increase is associated to the presence of defects (such as oxygen vacancies or surface disorder) introduced by the synthesis conditions with a reduced oxygen content as well as thermal treatments in Ar/H_2 gas atmosphere, even though their precise identification remains elusive.

The results presented in this chapter leave much room for development of the approach. For instance, further optimization of the material could be addressed both by considering a fine tuning of the deposition atmosphere and other reducing or inert annealing conditions, such as in vacuum or in pure Ar, which may help to understand what is the specific role of hydrogen. Accordingly, these development possibilities were investigated in detail and are presented in Chapter 5.

5

Tuning the photoelectrochemical properties of TiO_2 hierarchical nanostructures

After the explorative investigation on hydrogen-treated TiO_2 hierarchical nanostructures presented in Chapter 4, this chapter reports the development and optimization of that approach. Section 5.1 illustrates in detail the experimental strategy employed to fulfill this purpose. Briefly, the approach consisted in controlling in detail the PLD synthesis conditions (Sections 5.2 and 5.3) and the post-annealing atmosphere/temperature (Sections 5.4 and 5.5). Finally, the results presented throughout this chapter are summarized in Section 5.6, together with concluding remarks. Similarly as for Chapter 4, some of the results presented here were published in a peer-reviewed article[192] (specifically, those discussed in Sections 5.2 and 5.4.1, and my personal contribution consisted in the whole experimental activity, apart from photoelectrochemical and X-ray diffraction measurements, unless differently specified.

5.1 Experimental strategy

The adopted strategy to optimize the photoelectrochemical properties of hydrogenated/reduced TiO_2 hierarchical nanostructures is based on the control of reducing conditions in both the deposition and annealing steps, similarly as in Chapter 4, but in more detail, as described in the following.

1) Optimization of target-atmosphere combination (Section 5.2). The results presented in Chapter 4 showed that ablation of a TiO_2 target in an oxygen-poor atmosphere was critical to obtain a significant enhancement of photoactivity of the film, when followed by the double thermal treatment [Air+Ar/H_2], to control crystallinity and reduction/hydrogenation. As a consequence, in order to deeply investigate this effect and optimize the process conditions, five different Ar/O_2 background gas mixtures (from pure O_2 to pure Ar) were tested not only with the ablation of a TiO_2 target, but also of a Ti target, keeping the total pressure at 5 Pa, thus investigating different deposition conditions with a low (or even null) presence of oxygen. All the films deposited in this study, with their corresponding labels, are illustrated in Table 5.1.

Table 5.1: Set of the different deposition conditions explored and corresponding sample names.

Atmosphere	TiO_2 target	Ti target
100% O_2	O_2-TiO_2	O_2-Ti
75% O_2, 25% Ar	Ar/O_2 (25:75)-TiO_2	Ar/O_2 (25:75)-Ti
50% O_2, 50% Ar	Ar/O_2 (50:50)-TiO_2	Ar/O_2 (50:50)-Ti
25% O_2, 75% Ar	Ar/O_2 (75:25)-TiO_2	Ar/O_2 (75:25)-Ti
100% Ar	Ar-TiO_2	Ar-Ti

On the basis of the results of Chapter 4, two of the three annealing treatments described in Section 4.1 were performed on all these films: **[Air]**, as reference, and **[Air+Ar/H_2]**, i.e. the most effective annealing treatment in Chapter 4. Detailed characterization and photoelectrochemical tests of these photoanodes allowed to find the optimal deposition conditions for both targets.

2) Increase of deposition pressure (Section 5.3). The deposition background gas pressure for the optimal conditions with TiO_2 target was increased from 5 Pa to 8 Pa to investigate the interaction of a more open morphology, and thus of a higher specific surface area, with the Ar/H_2 atmosphere during annealing.

3) Annealing treatments in other reducing atmospheres (Section 5.4). Photoanodes obtained in the optimized PLD conditions were thermally treated not only with the "standard" [Air] and [Air+Ar/H_2] treatments, but also in other reducing atmospheres in the same home-made furnace (described in Section 3.2.2) and with the same temperature profile (10°C/min heating and cooling ramps, 3 h dwell at 500°C), labeled as follows:

- vacuum ($P < 3 \cdot 10^{-4}$ Pa): **[Vac]**;
- double treatment [Air] followed by [Vac]: **[Air+Vac]**;
- double treatment [Air] followed by annealing in pure Ar (99.9995%) atmosphere at environmental pressure: **[Air+Ar]**.

In this case, the aforementioned atmospheres were tested to understand in more detail the specific role of the annealing atmosphere when different reducing (or inert) conditions were employed.

4) Increase of annealing temperature (Section 5.5). The last optimization approach was based on the increase of annealing temperature, from 500°C to 650°C, either for the air annealing or the Ar/H_2 treatment;

accordingly, these thermal treatments are labeled as **[Air-650+Ar/H_2]** and **[Air+Ar/H_2-650]**, respectively.

5.1.1 Deposition parameters

TiO_2 nanostructured films were deposited by ablating a TiO_2 (99.9%) or Ti (99.99%) target with the ns-PLD system described in Section 3.2.1 (using λ = 532 nm and repetition rate 10 Hz). The laser fluence on the target was set at about 3.5 J/cm^2 and the laser pulse energy was 170 mJ. Silicon (100) (University Wafer, thickness 0.5 mm), soda-lime glass (thickness 1 mm) and titanium plates (Sigma-Aldrich, thickness 0.25 mm, 99.7% purity) were used as substrates, mounted on an off-axis rotating sample holder at a fixed d_{T-S} = 50 mm. All the substrates were kept at room temperature and titanium plate substrates of 2 × 1 cm^2 were half masked during deposition to leave a clean surface for electrical contacts for photoelectrochemical measurements. The depositions were performed at a fixed background gas pressure of 5 Pa in different Ar/O_2 mixtures, (as shown in Table 5.1) and at 8 Pa in Ar/O_2 (50:50) mixture (only for Section 5.3). The nominal film thickness was set at about 1300 nm (the actual thickness, measured by SEM, varied between 1000 and 1400 nm). The deposited mass ranged between 0.15 and 0.35 mg/cm^2, as estimated from quartz microbalance measurements, and the deposition rate ranged between 3 and 11 nm/min, depending on the specific conditions.

5.2 Optimization of target-atmosphere combination

The discussion on the optimization of target-atmosphere combination in PLD experiments at 5 Pa, keeping fixed the *ex-situ* annealing treatments ([Air] and [Air+Ar/H_2]), is presented in two parts: first, the morphological, structural and optical properties of films are considered (Section 5.2.1); second, the photoelectrochemical characterization of all the investigated photoanodes is addressed (Section 5.2.2), including comments on the results and hypotheses on the possible mechanisms leading to them.

5.2.1 Morphological, structural and optical properties

The morphology of all the as-deposited films, obtained from TiO_2 and Ti targets in various Ar/O_2 background gas atmospheres at 5 Pa, is presented in the SEM images in Figure 5.1; only cross-sectional images are shown for the sake of brevity. Films deposited from TiO_2 target (first row in Figure 5.1) as well as those deposited from Ti target (second row in Figure 5.1) show a vertically-oriented morphology; for films deposited in the presence of oxygen, some porosity is also evident, while films deposited in pure Ar show a more compact appearance. These observations are highlighted by SEM images of [Air+Ar/H_2]-annealed films, presented in Figure 5.2; in this case, one can notice the effect of the double annealing, which induces the formation of polygonal crystallites merged with each other as a result of coarsening and sintering, forming crystalline vertical channels. However, the Ar-TiO_2-[Air+Ar/H_2] film shows again a more compact morphology and a lower degree of porosity, so that these "channels" are almost completely merged with each other. An even denser appearance is exhibited by the Ar-Ti-[Air+Ar/H_2] film, which is no more characterized by vertically-oriented nanostructures and exhibits a rougher and more irregular surface with respect to all the other films.

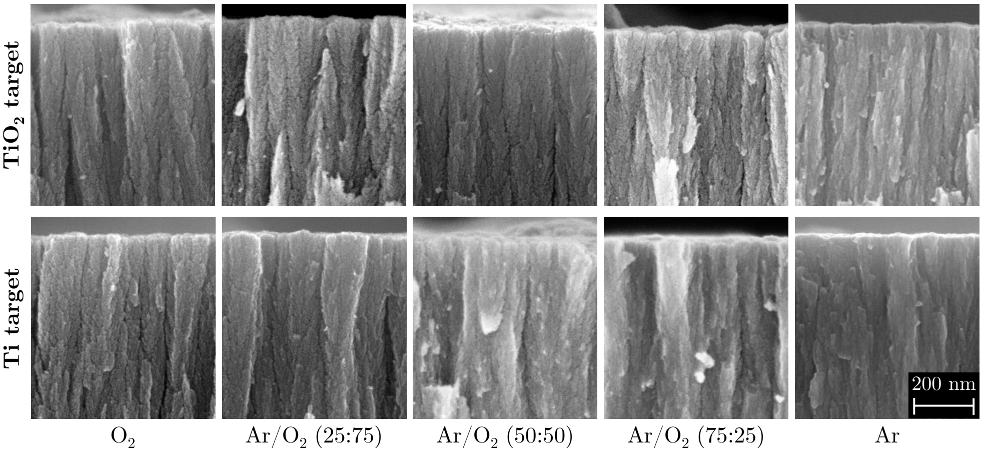

Figure 5.1: SEM images of as-deposited films from TiO_2 target (first row) and from Ti target (second row) with varying Ar/O_2 gas mixture at 5 Pa.

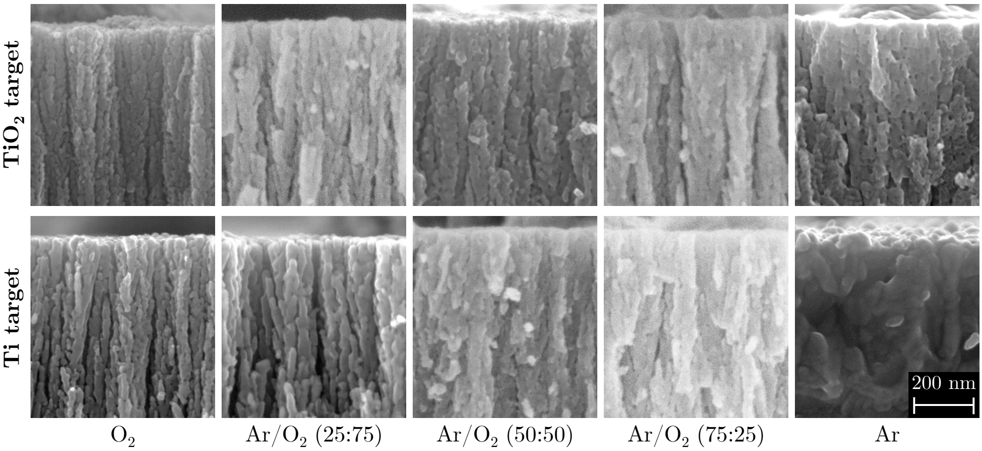

Figure 5.2: SEM images of [Air+Ar/H_2]-annealed films deposited from TiO_2 target (first row) and from Ti target (second row) with varying Ar/O_2 gas mixture at 5 Pa.

The more compact morphology obtained when depositing in pure Ar atmosphere (with respect to O_2-containing atmospheres) is in agreement not only with the previous results presented in Section 4.3.1, but also with previous literature studies[134,136]; this effect is due to the fact that the kinetic energy of Ti ions ablated from a TiO_2 target in 5 Pa of Ar is higher than that of Ti ions ablated in 5 Pa of pure O_2, as evidenced by optical emission spectra of the plasma plume[193]. On the other hand, provided that some O_2 is present in the background gas (in this case at least 25%), the same hierarchical morphology of the O_2-TiO_2 film is achieved, regardless the precise relative composition of the gas atmosphere.

For the Ar/O_2 (25:75)-Ti-[Air+Ar/H_2], i.e. the most photoactive film (see the photocurrent reults in Section 5.2.2), a more detailed morphological analysis with high resolution TEM (transmission electron microscope) images was carried out, comparing this film with the [Air]-annealed one, as shown in Figure 5.3. TEM analysis was performed thanks to the collaboration with C. Ducati at the Department of Materials Science & Metallurgy, University of Cambridge, using a FEI Tecnai F20 microscope operated at 200 kV and equipped with a OneView camera. Both the [Air]-annealed film (Figure 5.3A) and the [Air+Ar/H_2]-annealed one (Figure 5.3B) consist of an assembly of nanocrystals with approximate size of tens of nm; however, the [Air+Ar/H_2]-annealed film shows apparently larger crystals having a more regular shape and surfaces; this effect can be ascribed to the second annealing step experienced by the [Air+Ar/H_2]-annealed film.

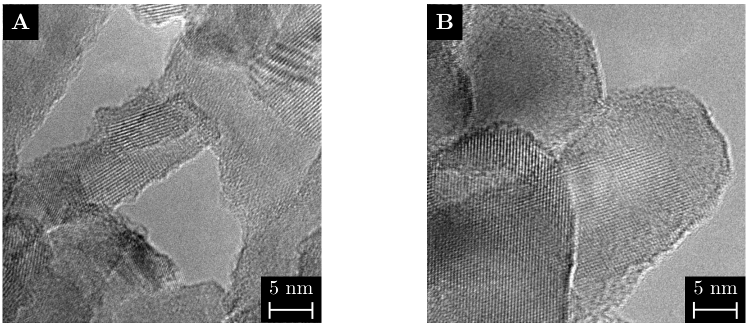

Figure 5.3: TEM analysis of Ar/O_2 (25:75)-Ti film. **A)** [Air]-annealed; **B)** [Air+Ar/H_2]-annealed.

In this section, henceforth, the structural and optical analyses of three films deposited from TiO_2 target and three deposited from Ti target, instead of the whole set of samples, will be presented. Specifically, the films deposited in pure O_2, pure Ar and the optimized Ar/O_2 mixture (on the basis of photoelectrochemical results in Section 5.2.2) for each target will be discussed. In particular, the optimized deposition atmosphere for TiO_2 target ablation was Ar/O_2 (50:50), while for Ti target Ar/O_2 (25:75).

The crystalline structure of [Air+Ar/H_2]-annealed films was evaluated with Raman spectroscopy, as presented in Figure 5.4 (as-deposited films in these experimental conditions are amorphous, as already discussed in Section 4.2). For films deposited from TiO_2 target (Figure 5.4A), the five characteristic peaks of anatase are present in all the spectra without significant shift or broadening, irrespectively of the deposition background gas composition. This effect is in agreement with previous results (see Figure 4.6). On the other hand, for films deposited from Ti target (Figure 5.4B), the same holds for O_2-Ti-[Air+Ar/H_2] and Ar/O_2 (25:75)-Ti-[Air+Ar/H_2] films, but not for the Ar-Ti-[Air+Ar/H_2] film. Indeed, this film is characterized by weak and broad Raman peaks, corresponding to a mixture of anatase and rutile phases (see the rutile E_g and A_{1g} peaks at 440 cm^{-1} and 610 cm^{-1}, respectively) with a large degree of disorder and consistent with a partially oxidized film. This observation can be related to the fact that the deposition of Ar-Ti film occurs in the absence of oxygen (apart from possible impurities), so that the as-deposited film is metallic and undergoes partial oxidation during the annealing process.

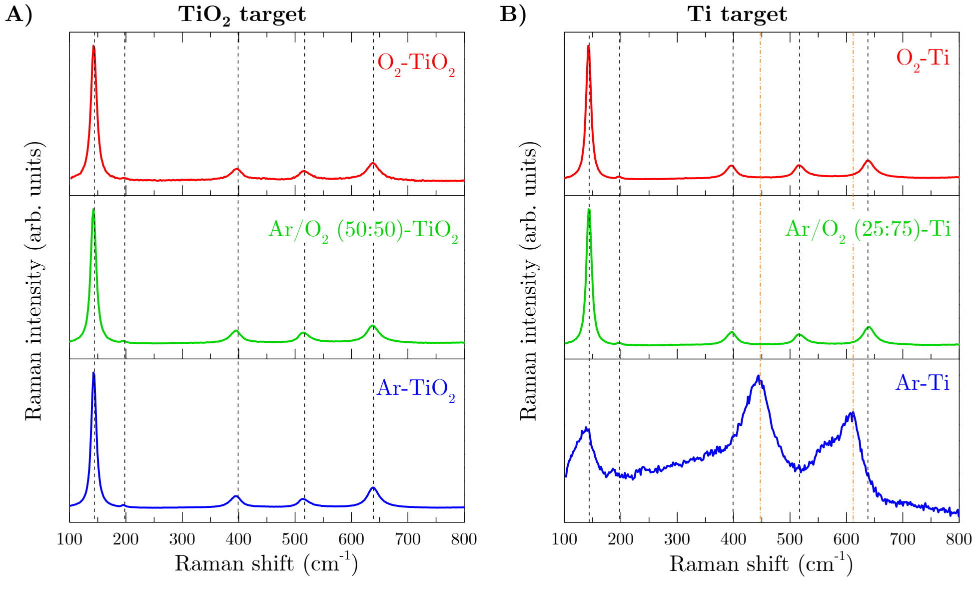

Figure 5.4: Raman spectra of [Air+Ar/H_2]-annealed films deposited from TiO_2 target **(A)** and from Ti target **(B)**. Vertical dashed lines (black) and dashed-dotted lines (orange) are also reported as reference to anatase and rutile peaks, respectively.

The structural information gained with Raman spectroscopy was confirmed with XRD measurements, performed for the films deposited in pure Ar, as shown in Figure 5.5. The Ar-TiO_2-[Air+Ar/H_2] film, indeed, exhibits the typical peaks of the anatase phase without evident shift, confirming a good crystallinity of the material; the crystal domain size, estimated through the Scherrer formula for the (101) and (004) peaks, is 58 nm and 43 nm, respectively. On the contrary, the Ar-Ti-[Air+Ar/H_2] film shows very weak and broadened features, corresponding to both anatase and rutile phases, but the low signal/noise ratio prevents the evaluation of a crystallite size in this case; this is consistent with a strongly under-oxidized and disordered material.

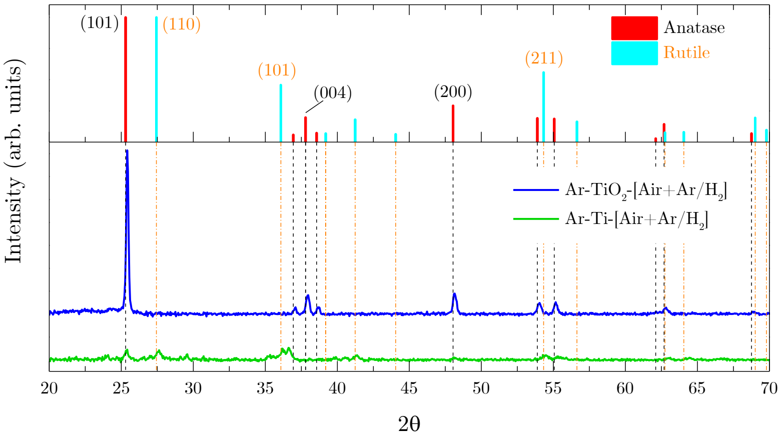

Figure 5.5: XRD analysis of [Air+Ar/H_2]-annealed films deposited in pure Ar from TiO_2 (blue line) and Ti (green line) targets on glass substrates. Vertical dashed lines (black) and dashed-dotted lines (orange) are reported as reference to anatase and rutile peaks, respectively; anatase and rutile reference diffractograms, on top, were taken from a database[42].

The optical properties of [Air+Ar/H_2]-annealed films deposited from TiO_2 and Ti targets in different background gas atmosphere are reported in Figure 5.6. The first row (Figure 5.6A and 5.6B) shows the results for films deposited from TiO_2 target; the transmittance curves of O_2- and Ar/O_2 (50:50)-TiO_2 films (Figure 5.6A) mostly superimpose with each other, whereas that of Ar-TiO_2 film reaches lower values in the whole transparency region (400–2000 nm); absorbance curves (Figure 5.6B) of O_2-TiO_2 and Ar/O_2 (50:50)-TiO_2 films are very close to each other, similarly as transmittance curves, whereas the absorbance of Ar-TiO_2 film is slightly lower in the UV range and higher in the visible range. Moreover, Figure 5.6B shows also the reflectance curves (dashed lines), which reveal that Ar-TiO_2 films exhibit higher values than O_2- and Ar/O_2 (50:50)-TiO_2 films in the whole investigated range, which accounts for the slight absorbance difference between the Ar-TiO_2 film and the other two ones. Globally, Figure 5.6A and 5.6B suggest that thin films deposited from TiO_2 target in 5 Pa of pure O_2 or mixed Ar/O_2 atmosphere show comparable optical properties, while the same does not occur by depositing in pure Ar atmosphere, which results in a lower transmittance and higher reflectance. This effect can be related to the more compact morphology and higher surface flatness exhibited by the Ar-TiO_2

film (see Figures 5.1 and 5.2). For all these films, the estimated optical bandgap is 3.2 eV (not shown), which is still the expected value for anatase, in agreement with the results of Chapter 4 (see Table 4.1).

On the other hand, the second row (Figure 5.6C and 5.6D) shows the results for films deposited from Ti target. Also in this case, the films deposited in pure O_2 or in mixed Ar/O_2 atmospheres (in this case the composition is Ar/O_2 25:75) exhibit analogous transmittance (Figure 5.6C), absorbance and reflectance (Figure 5.6D) curves; on the other hand, the Ar-Ti film shows a completely different behavior: it is opaque (except for a 2% transmittance around 500 nm, Figure 5.6C) and, accordingly, it shows a very high absorbance, between 70 and 80% (Figure 5.6D); indeed, all the light which is not absorbed is reflected, as shown by the reflectance curve in Figure 5.6D. These results suggest that the optical properties exhibited by films deposited in pure O_2 or in mixed Ar/O_2 atmospheres from Ti target are comparable (indeed, the bandgap value of 3.2 eV is obtained also in these cases), while the film deposited in pure Ar has a completely different behavior, consistent with a strongly under-oxidized and disordered material, in agreement with the results of Raman spectroscopy (Figure 5.4) and X-ray diffraction (Figure 5.5).

In addition, by comparing the results for films obtained with the two targets, it is possible to conclude that the optical properties of films obtained by ablating either TiO_2 or Ti targets in the presence of oxygen are qualitatively comparable (a slightly higher absorbance is found for films deposited from Ti target, see Figure 5.6D compared to Figure 5.6B); on the contrary, the choice of a metallic Ti target leads to completely different results with respect to the oxide, TiO_2, in the case of pure Ar background gas atmosphere, since it leads to a strongly under-oxidized film with nearly zero transmittance (Figure 5.6C) and high absorbance in the whole investigated range (Figure 5.6D).

5.2.2 Photoelectrochemical properties

All the photoanodes prepared by PLD and presented in Table 5.1, which exhibit the morphological, structural and optical properties described in the previous section, were tested in a photoelectrochemical cell, with the methods described in Section 3.4. The objective of this analysis was to assess the influence of the deposition conditions, i.e. background gas composition and target material, on the films photoactivity and to find the optimal background atmosphere composition for each target employed, i.e. TiO_2 and Ti. In all cases, under dark conditions negligible photocurrents are observed (not shown), indicating that no reaction occurred at the photoanodes in the absence of light illumination, while under irradiation photocurrent evolution is observed as a result of the water oxidation reaction at the photoanodes.

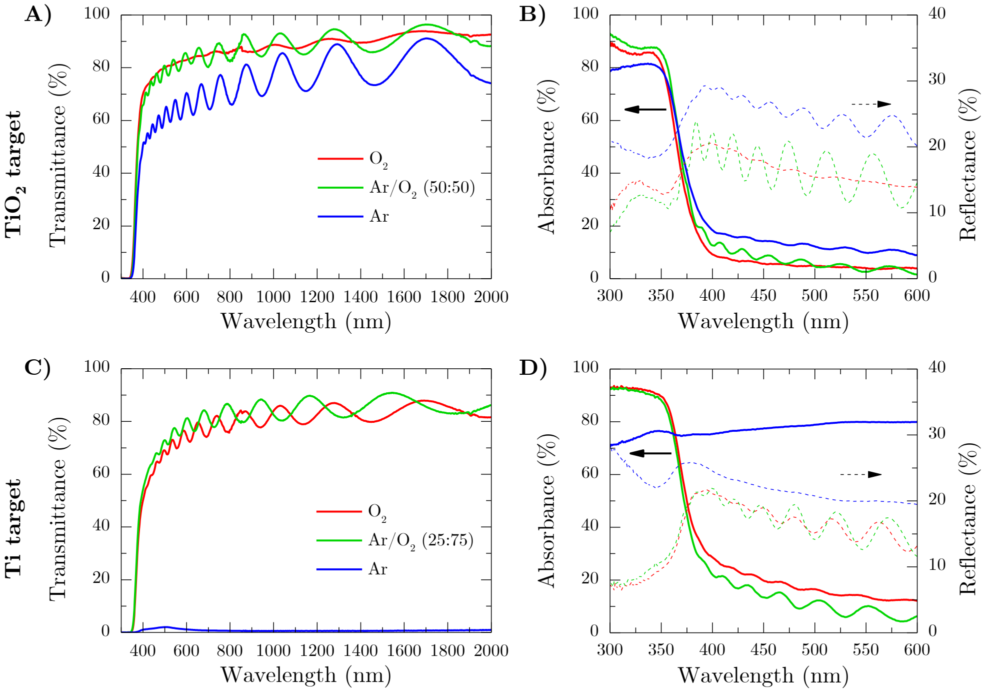

Figure 5.6: Optical analysis of [Air+Ar/H_2]-annealed films deposited from TiO_2 and Ti targets in different background gas atmospheres. **A)** Transmittance spectra (red: O_2; green: Ar/O_2 (50:50); blue: Ar); **B)** absorbance (straight lines) and reflectance (dashed lines) spectra (same colors as **A**). **C)** Transmittance spectra (red: O_2; green: Ar/O_2 (25:75); blue: Ar); **D)** absorbance (straight lines) and reflectance (dashed lines) spectra (same colors as **C**).

The results for photoanodes deposited from TiO_2 target are presented in Figure 5.7, where in the first row (Figure 5.7A and 5.7B) photocurrent density values are reported for [Air]- and [Air+Ar/H_2]-annealed films, respectively, while in the second row (Figure 5.7C and 5.7D) photoconversion efficiency values calculated with Equation (3.8) are shown for [Air]- and [Air+Ar/H_2]-annealed films, respectively. By observing these data, it is possible to assert that:

- the photocurrent onset for all the investigated films is about at −0.75 V vs. SCE;
- the [Air]-annealed films exhibit a saturation photocurrent density in the range 20–35 $\mu A\,cm^{-2}$ at 0.5 V vs. SCE (Figure 5.7A) and maximum photoconversion efficiencies near 0.03% (Figure 5.7C), corresponding the films deposited at intermediate O_2 contents (i.e. 50% and 25%) in the background gas atmosphere;
- the [Air+Ar/H_2]-annealed films exhibit clear differences in photocurrents depending on the deposition background gas composition: an optimum O_2 concentration exists in the deposition atmosphere, i.e. 50%, leading to the maximum saturated photocurrent density (80 $\mu A\,cm^{-2}$ at 0.5 V vs. SCE, Figure 5.7B) as well as to the maximum photoconversion efficiency (about 0.06%, Figure 5.7D) for the Ar/O_2 (50:50)-TiO_2 film; this result represents a clear photoactivity improvement with respect to all the [Air]-annealed films.

The results for photoanodes deposited from Ti target are presented in Figure 5.8, with the same layout as in the previous case. In this case, it is possible to observe that:

- all the films deposited in the presence of O_2 in the background gas exhibit a photocurrent onset at about −0.8-−0.75 V vs. SCE (Figure 5.8A and 5.8B);
- the Ar-Ti film shows the highest photocurrent onset (−0.65 V vs. SCE) and the lowest photocurrent densities, with only a slight increase from the [Air]-annealed film to the [Air+Ar/H_2]-annealed one; this can be related to the different morphology, crystallinity and composition of this sample (as discussed in Section 5.2.1)
- all the other films show clear trends in photocurrent densities and photoconversion efficiencies both after [Air] annealing (Figure 5.8A and 5.8C) as well as after [Air+Ar/H_2] annealing (Figure 5.8B and 5.8D);
- the best results are achieved by films deposited with the highest O_2 contents in the deposition background gas atmosphere, i.e. 75% and 100%; in particular, the Ar/O_2 (75:25)-Ti film reaches the maximum

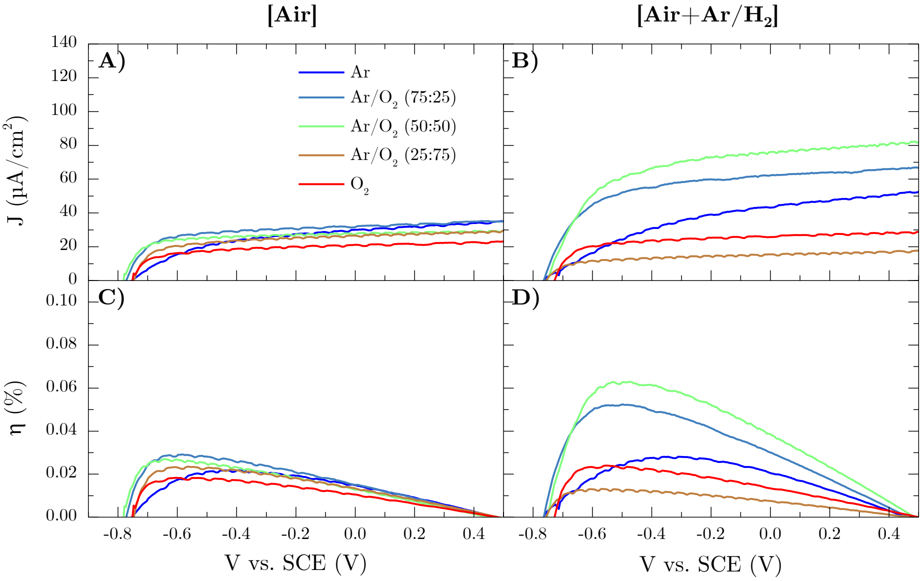

Figure 5.7: Effect of the deposition atmosphere on the performances of photoanodes deposited from TiO$_2$ target and annealed with [Air] **(A, C)** and [Air+Ar/H$_2$] **(B, D)** treatments: photocurrent **(A, B)** and photoconversion efficiency **(C, D)** results.

photocurrent density of almost 120 μA cm^{-2} at 0.5 V vs. SCE (Figure 5.8B) and the maximum photoconversion efficiency of 0.1% (Figure 5.8D).

In order to analyze the above results in more detail and to compare the results obtained for the two targets, the maximum photoconversion efficiency values shown in Figures 5.7C, 5.7D, 5.8C and 5.8D are reported in Figure 5.9A as a function of the different deposition background gas mixtures. The data points and error bars in this figure depict the average and standard deviation values over at least six measurements during several months of testing, in which photocurrent density and photoconversion efficiency values similar to those presented in Figures 5.7 and 5.8 were obtained, providing a first indication on the good reproducibility of the experiments and of the sample structural stability.

Considering the films deposited from Ti target, Figure 5.9A points out that the best performance is achieved by the Ar/O$_2$ (25:75)-Ti film, both with [Air] and [Air+Ar/H$_2$] thermal treatments. Besides, it is clear that [Air+Ar/H$_2$]-annealed photoanodes outperform the [Air]-annealed ones. In the case of films deposited from TiO$_2$ target, the photoresponse is maximized for the Ar/O$_2$ (50:50)-TiO$_2$ film; again, the photoactivity is higher for [Air+Ar/H$_2$]-annealed films than for the [Air]-annealed ones. Considering, finally, the target effect, it can be noted that the most efficient [Air+Ar/H$_2$]-annealed films deposited

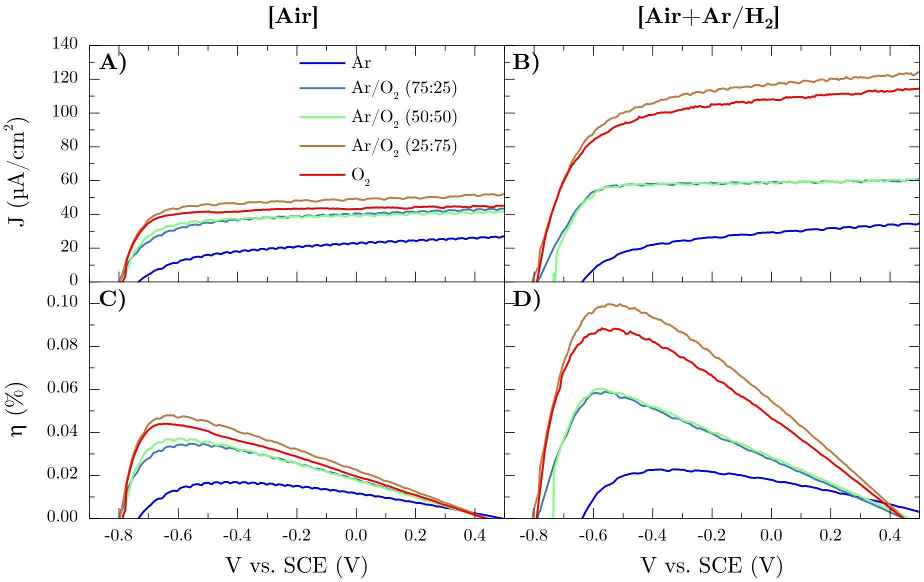

Figure 5.8: Effect of the deposition atmosphere on the performances of photoanodes deposited from Ti target and annealed with [Air] **(A, C)** and [Air+Ar/H_2] **(B, D)** treatments: photocurrent **(A, B)** and photoconversion efficiency **(C, D)** results.

from Ti target (i.e. with 75% and 100% O_2 in the background gas mixture) show higher photoactivities than those deposited from TiO_2 target with the same background atmosphere.

The photostability of the Ar/O_2 (50:50)-TiO_2-[Air+Ar/H_2] and Ar/O_2 (25:75)-Ti-[Air+Ar/H_2] films (i.e. the photoanodes that showed the best performances) was further investigated. Figure 5.9B shows the photocurrents measured over six hours with applied bias potential of 0.4 V. The Ar/O_2 (25:75)-Ti-[Air+Ar/H_2] film shows a better photostability than the Ar/O_2 (50:50)-TiO_2-[Air+Ar/H_2]: after 6 h of continuous illumination, the photocurrent drops by about 8% and 4% for the latter and for the former, respectively. The same films with [Air] annealing, in addition, exhibit a lower stability: after 6 h, the photocurrent drops by about 17% and 19% for Ar/O_2 (50:50)-TiO_2-[Air] and Ar/O_2 (25:75)-Ti-[Air] films, respectively.

Discussion

The photocurrent and photoconversion efficiency results presented above (Figures 5.7 and 5.8) confirm those presented in the previous chapter (see Section 4.4, both considering the effects of the deposition conditions and of thermal treatments. In particular, the increase of photocurrent for the [Air+Ar/H_2]-annealed films with respect to the [Air]-annealed ones (at least of the optimal ones) can be explained with the same arguments as those

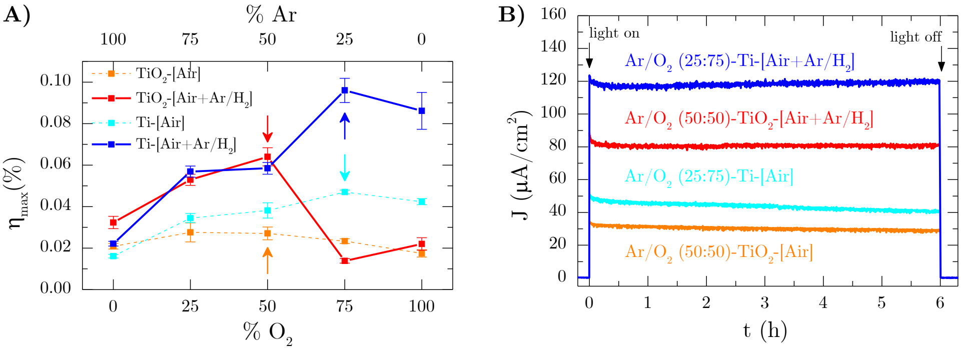

Figure 5.9: **A)** Effect of the deposition atmosphere on the maximum photoconversion efficiency for photoanodes deposited from TiO_2 target annealed with [Air] (orange-dashed line) and with [Air+Ar/H_2] (red-solid line) and from Ti target annealed with [Air] (light blue-dashed line) and with [Air+Ar/H_2] (blue-solid line). **B)** Photostability of the optimal photoanodes, marked with an arrow in **A**, measured by photocurrent over time with applied bias potential of 0.4 V vs. SCE.

discussed in Section 4.4.3, i.e. improved conductivity or decreased recombination rate ensured by a thermal treatment in reducing atmosphere on an already well-crystallized TiO_2 material, probably related to defect states.

On the other hand, with respect to previous results, more insights on the effects of deposition conditions on the photoelectrochemical response of photoanodes can be obtained. First, for films deposited in pure Ar, a more compact morphology is observed (Figure 5.2) and a lower oxygen content is expected, which does not prevent the formation of a crystalline anatase phase for the Ar-TiO_2-[Air+Ar/H_2] film but leads to a less ordered structure for the Ar-Ti-[Air+Ar/H_2] film (Figures 5.4 and 5.5); the latter, moreover, has zero transmittance (Figure 5.6C). These observations can suggest an excessive amount of defects in the material, which in turn can account for the moderately low efficiency of these photoanodes.

Considering, instead, [Air+Ar/H_2]-annealed films deposited in mixed Ar/O_2 atmospheres, two clear trends with two different optimal deposition conditions for the two target materials have been found, as discussed above. The optimized photoresponse for the Ar/O_2 (50:50)-TiO_2 film is consisted with the results presented in Chapter 4, in which a TiO_2 film prepared in identical conditions exhibited the most promising photocurrent results (see Section 4.4). The optimized photoresponse for films deposited from Ti target is found in correspondence to a higher percentage of O_2 in the deposition background atmosphere, i.e. Ar/O_2 (25:75)-Ti film, and the pure O_2 deposition shows a good photocurrent as well. These findings can be discussed by considering the deposition process: the oxygen content in the film is both related to the target material and the background gas mixture in the case of depositions from TiO_2 target, but only to the gas mixture in the case of depositions from Ti target, so a higher concentration of oxygen in the gas is beneficial in the second case.

Photocurrent results, thus, suggest that some degree of oxygen shortage in the deposition process (and a consequent slight oxygen sub-stoichiometry in the film) leads to better photoelectrochemical performance, confirming the results presented in Chapter 4. The oxygen-related effect during deposition is not canceled by the subsequent first annealing step in air, so it is reasonable to expect that it mainly concerns the nanoparticles core (while the hydrogenation step mainly affects the surface, as discussed above). The beneficial effect can be tentatively ascribed to a better conductivity within the slightly reduced material constituting the film[194], similarly to what hypothesized in Section 4.4.3.

5.3 Increase of deposition pressure

The above presented results show that, starting from TiO_2 target, the deposition background gas mixture leading to the highest photoresponse was Ar/O_2 (50:50). On this basis, another set of films was deposited with the same relative composition in the gas atmosphere, but with a higher total pressure, i.e. 8 Pa. The increase of background gas pressure leads to a more open morphology (i.e. higher porosity)[131]; indeed, the purpose of this investigation was to study the interaction of a TiO_2 hierarchical film with a higher porosity, and thus a higher expected surface area (not measured in this work, see previous results discussed in Section 2.2.4), with the Ar/H_2 thermal treatment atmosphere. For the sake of brevity, these films will be referred to as **8 Pa-TiO_2** hereinafter.

The morphological analysis of 8 Pa-TiO_2 films is presented in Figure 5.10. Considering the as-deposited film, top-view SEM images (Figure 5.10A) show that the surface has a granular appearance and is crossed by various fissures with different widths (from few nm to tens of nm). Cross-sectional images (Figure 5.10B) show a vertically-oriented morphology with a thickness of about 1.2 µm; at higher magnification (Figure 5.10C), the hierarchical organization in nanoparticles becomes evident. [Air] annealing promotes the crystallization of nanoparticles in polygonal domains (Figure 5.10D and 5.10F) without changing the overall morphology (Figure 5.10E). It is also possible to discern the “trees” constituting the film between each other (Figure 5.10F). [Air+Ar/H_2] annealing produces the same effects as [Air] annealing (Figure 5.10G–5.10I), in agreement with the results presented in Chapter 4.

By comparing the morphological properties of the 8 Pa-TiO_2 film (Figure 5.10) to those of Ar/O_2 (50:50)-TiO_2 films, deposited at 5 Pa (Figures 4.1D–4.1F, 4.4, 5.1 and 5.2), it is possible to discern the different degree of porosity induced by the two different background pressure values, of

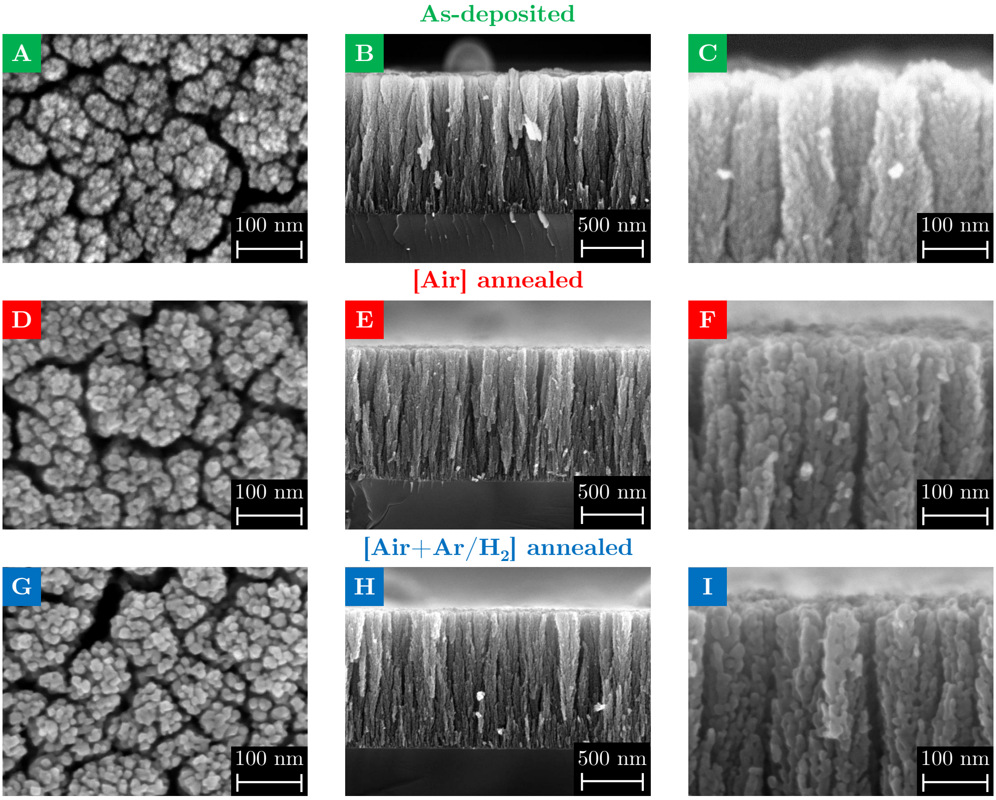

Figure 5.10: SEM images of 8 Pa-TiO_2 films. **(A–C)** As-deposited; **(D–F)** [Air] annealed; **(G–I)** [Ar/H_2] annealed; **(J–L)** [Air+Ar/H_2] annealed.

course higher in the case of 8 Pa-deposited films; this is in agreement with previous observations (see Section 2.2.4) and to the physical phenomena occurring in the plasma plume during the PLD process (see Section 3.2.1). For instance, the "trees" in the 5 Pa-deposited film are merged and connected with each other, with very thin cracks or voids between them, while the 8 Pa-deposited film exhibits various fissures and a lower connectivity.

The structural analysis of annealed 8 Pa-TiO_2 films was performed with Raman spectroscopy, as illustrated in Figure 5.11; the spectra show the characteristic peaks of the anatase phase both after [Air] and [Air+Ar/H_2] treatments. In addition, the $E_g(1)$ peak does not exhibit any significant shift or broadening (inset table in Figure 5.11).

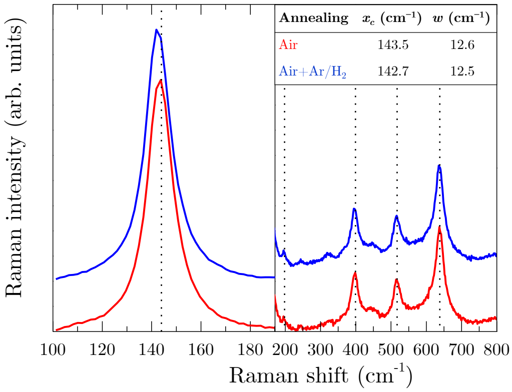

Annealing	x_c (cm^{-1})	w (cm^{-1})
Air	143.5	12.6
Air+Ar/H_2	142.7	12.5

Figure 5.11: Raman spectra of annealed Ar/O_2 (50:50)-TiO_2 films deposited at 8 Pa (red: [Air]; blue: [Air+Ar/H_2]). The inset table shows the analysis of the $E_g(1)$ peak performed with a Lorentian fitting (x_c: peak position, w: full-width at half-maximum).

The photoelectrochemical response of 8 Pa-TiO_2 films is illustrated in Figure 5.12. The photocurrent density of the [Air]-annealed photoanode (Figure 5.12A) shows the onset at about -0.67 V and reaches a saturated value of about 12 μA cm^{-2}, while the [Air+Ar/H_2]-annealed film reaches 16 μA cm^{-2}. Even though the relative photocurrent increment from [Air]-annealed photoanode to [Air+Ar/H_2]-annealed one is significant (about 33%), the absolute performance is evidently lower with respect to the film deposited at 5 Pa. Similarly, photoconversion efficiencies (Figure 5.12B) confirm the photoactivity enhancement from [Air]- to [Air+Ar/H_2]-annealed photoanode, but with low absolute values (the latter exceeds only 0.01%).

Considering the overall results regarding the 8 Pa-TiO_2 films, it can be concluded that their photoelectrochemical performance is clearly lower than that exhibited by the films deposited in 5 Pa (Figure 5.7). This result can be interpreted by considering the morphological features of these films: on the one hand, the mass of the active material is lower at the same thickness of

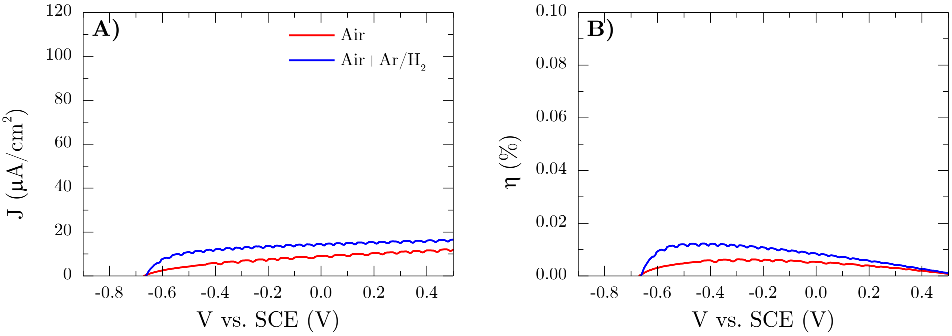

Figure 5.12: Photoelectrochemical behavior of annealed Ar/O_2 (50:50)-TiO_2 films deposited at 8 Pa (red: [Air]; blue: [Air+Ar/H_2]). **(A)** *J–V* curves; **(B)** photoconversion efficiency curves.

5 Pa-deposited films; on the other hand, the degree of connectivity between crystalline domains is also lower. Consequenlty, less photoexcited electron/hole pairs and shorter diffusion paths for them can be expected, resulting in a poorer charge transport; this argument was also considered to explain the poorer photoelectrochemical performance of films deposited at 10 Pa with respect to those deposited at 5 Pa in previous investigations[137,138] (as summarized in Chapter 2).

Nonetheless, an increase of photoresponse upon the second annealing step in Ar/H_2 mixture was found also in this case, confirming the beneficial effects of a double thermal treatment, in agreement with the results presented in Chapter 4 and Section 5.2.2. In addition, the higher porosity obtained for these films could be interesting for other experimental approaches related to photocatalysis. Indeed, the introduction of noble metal nanoparticles on the surface of hierarchical TiO_2 nanostructured films was one of the strategies pursued for the integration between these two materials; accordingly, it is one of the subjects of Chapter 7.

5.4 Annealing treatments in other reducing atmospheres

In the previous sections, various approaches related to the deposition conditions of TiO_2 hierarchical films aimed at optimizing their photoresponse were discussed. In this section and in the following one (Section 5.5), conversely, different approaches related to the annealing step are addressed. Here, the investigations on the role of the reducing annealing atmosphere are illustrated, which consisted in exploring thermal treatments in vacuum (Section 5.4.1) and in pure Ar (Section 5.4.2); in Section 5.5, on the other hand, the effect of changing the annealing temperature (from 500°C to 650°C) will be shown.

5.4.1 Annealing in vacuum

The results presented in Chapter 4 and Sections 5.2 and 5.3 show that the photoelectrochemical performance of TiO_2 hierarchical films can be improved by annealing in Ar/H_2 mixture after annealing in air, and this effect was interpreted as due to the introduction of defects with the thermal treatment in the reducing atmosphere combined with a good degree of crystallization, ensured by annealing in air. Another reducing atmosphere typically employed at the laboratory scale is vacuum, which typically induces oxygen vacancies or Ti^{3+} sites in TiO_2, increasing its conductivity[194–196]. In the specific field of *black titania* nanomaterials, vacuum annealing has also been proposed as an alternative to hydrogen annealing to enhance the photocatalytic activity of TiO_2[97,166]. Based on these literature data, two kinds of vacuum annealing were employed, as explained in Section 5.1: a single-step treatment, labeled as [Vac], and a double annealing, labeled as [Air+Vac]. The samples considered for this investigation were the two deposited in optimal conditions according to the above reported investigation (Section 5.2), i.e. Ar/O_2 (50:50)-TiO_2 and Ar/O_2 (25:75)-Ti. The morphological, structural and optical results will be presented only for the latter, due to the similar effects between the two films, while the photoelectrochemical results of both will be shown.

The morphological analysis of Ar/O_2 (25:75)-Ti film is presented in Figure 5.13, in which the effects of [Air+Ar/H_2], [Vac] and [Air+Vac] thermal treatments are shown. The SEM images reveal that annealing in vacuum produces analogous results as annealing in Ar/H_2 mixture: the single [Vac] treatment does not lead to any sintering/coarsening between nanoparticles (Figure 5.13B and 5.13E), similarly to [Ar/H_2] thermal treatment (Figures 4.3 and 4.3), while the double treatment, [Air+Vac], induces this effect (Figure 5.13C and 5.13F), similarly to [Air+Ar/H_2] thermal treatment (Figure 5.13A and 5.13D).

The structural effects of vacuum annealing were investigated with Raman spectroscopy, as illustrated in Figure 5.14, in which the spectra of [Vac]- and [Air+Vac]-annealed films are shown, in comparison to the one of [Air+Ar/H_2]-annealed film. In all three cases the anatase phase is obtained, but annealing in vacuum leads to a stronger photoluminescence background than [Air+Ar/H_2] (which was removed from the spectra shown in Figure 5.14), so that the [Vac]- and [Air+Vac]-annealed film exhibit a lower signal/noise ratio. In addition, even though the $E_g(1)$ peak is not shifted from its typical frequency, i.e. 144 cm^{-1}, it is slightly broadened for the [Vac]-annealed film (see inset table in Figure 5.14). In addition, for the [Vac]-annealed film an additional peak appears at 244 cm^{-1}, which might be assigned to the A_{1g} mode of brookite at 247 cm^{-1}[48,197]; with this argument,

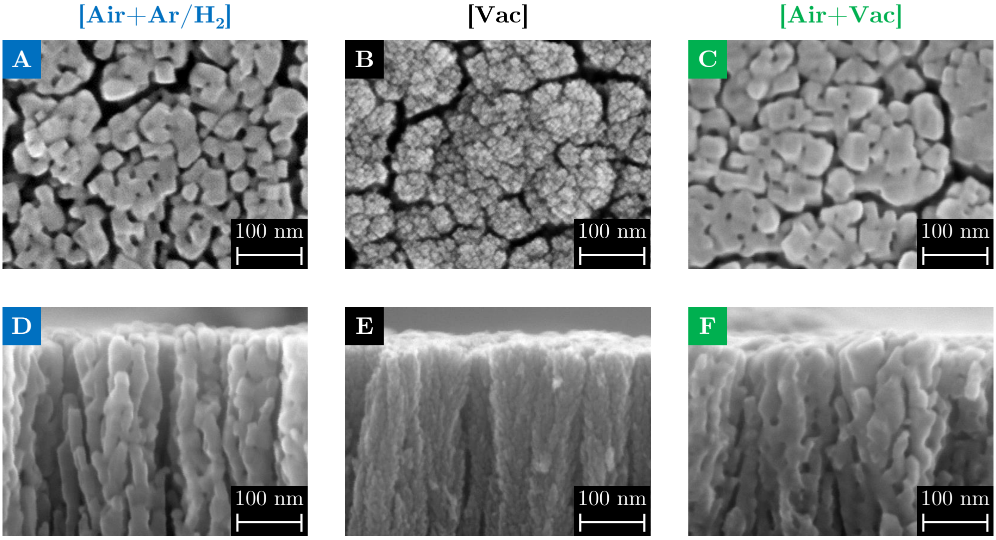

Figure 5.13: Morphological effects of [Air+Ar/H_2] **(A, D)**, [Vac] **(B, E)** and [Air+Vac] **(C, F)** thermal treatments on Ar/O_2 (25:75)-Ti films: top-view (first row) and cross-sectional (second row) SEM images.

the low-intensity signals at about 329, 365 and 450 cm^{-1} could also be assigned to that phase (see also Figure 2.2A). However, the occurrence of brookite phase in the [Vac]-annealed film is not understood and must be considered only hypothetical, waiting for further investigations. XRD measurements for the [Air+Vac]-annealed films, on the other hand, evidenced the presence of a pure anatase phase (not shown).

Further analysis on the effects of vacuum annealing was performed by optical spectroscopy measurements, presented in Figure 5.15, in which also the [Air]- and [Air+Ar/H_2]-annealed films are reported. The [Vac]-annealed film shows the lowest transmittance (both total and diffuse, Figure 5.15A and 5.15B) and reflectance (Figure 5.15C), which results in a pronounced absorption tail in the visible range; indeed, its color is dark-grey. Nonetheless, [Vac] annealing does not induce an evident change in the bandgap energy (3.16 eV). The [Air+Vac]-annealed film, on the other hand, compared to the [Air+Ar/H_2]- and the [Air]-annealed films[a], exhibits a slightly darker color (inset photograph in Figure 5.15A), a lower diffuse transmittance (Figure 5.15B) and lower reflectance (Figure 5.15C).

The effects of [Vac] and [Air+Vac] annealing treatments shown above for the Ar/O_2 (25:75)-Ti films were also similar for the Ar/O_2 (50:50)-TiO_2 films, so they were not reported here. On the other hand, the photoelectrochemical results for both set of films are shown in Figure 5.16, since in this case a

---

[a] The optical analysis of the [Air+Ar/H_2]-annealed film is inserted here for an easier comparison even though it has already been shown in Figure 5.6C and 5.6.

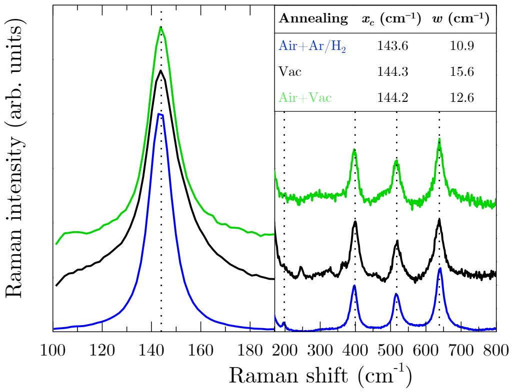

Figure 5.14: Raman spectra of annealed Ar/O_2 (25:75)-Ti films (blue: [Air+Ar/H_2]; black: [Vac]; green: [Air+Vac]). The inset table shows the analysis of the $E_g(1)$ peak performed with a Lorentian fitting (x_c: peak position, w: full-width at half-maximum).

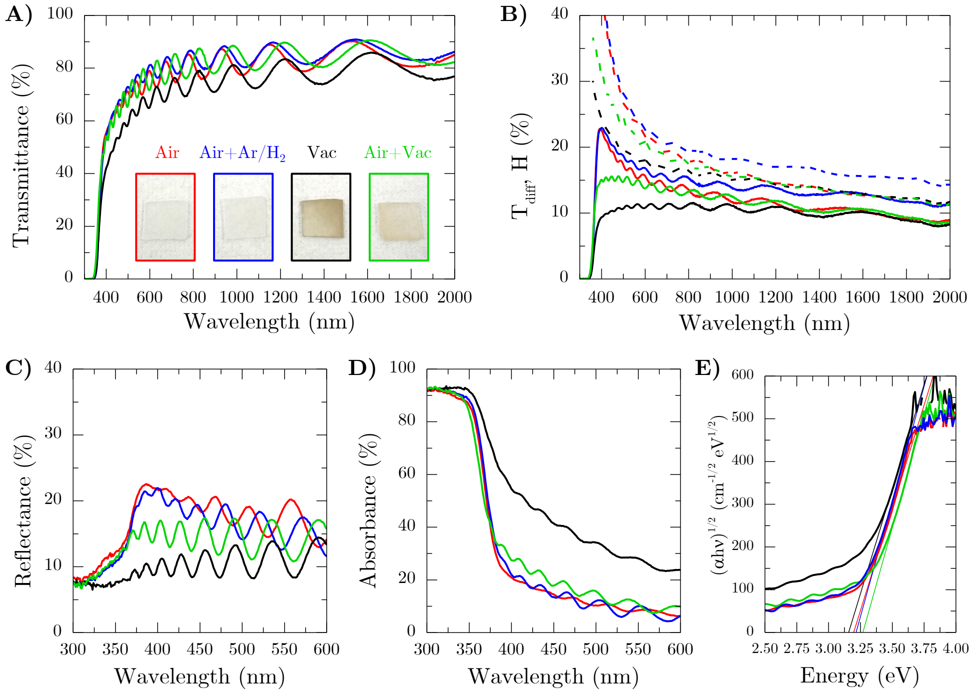

Figure 5.15: Optical analysis of Ar/O_2 (25:75)-Ti films (blue: [Air+Ar/H_2]; black: [Vac]; green: [Air+Vac]). **A)** Transmittance curves (optical photographs of the films are shown as insets); **B)** diffuse transmittance (solid lines) and haze factor (dashed lines) curves; **C)** reflectance curves; **D)** absorbance curves; **E)** Tauc plot curves.

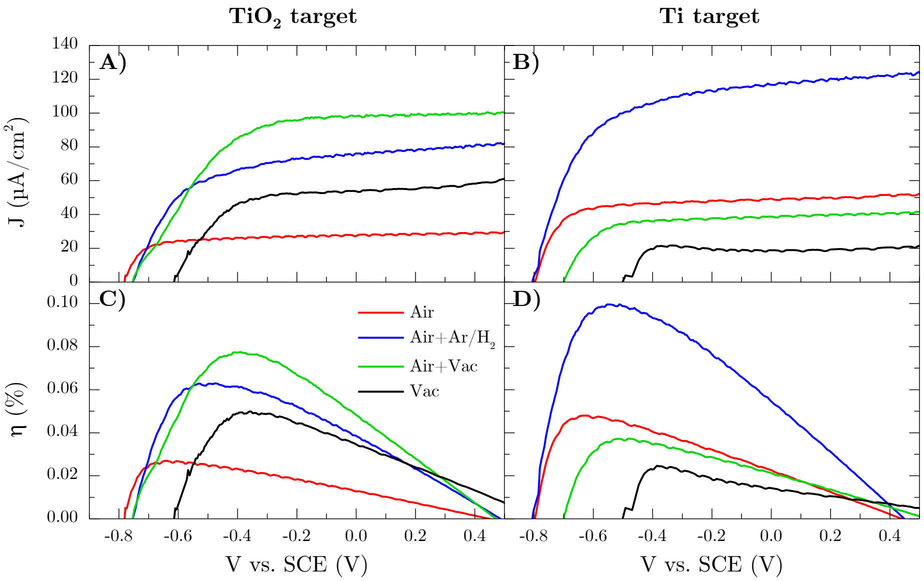

Figure 5.16: Annealing effects on the performances of optimal photoanodes deposited from TiO_2 **(A, C)** and Ti **(B, D)** targets (red: [Air]; blue: [Air+Ar/H_2]; black: [Vac]; green: [Air+Vac]): photocurrent **(A, B)** and photoconversion efficiencies **(C, D)** results.

substantial difference emerged. Indeed, the effects of [Vac] and [Air+Vac] treatments are opposite for the two films: on the one hand, they increase the photoelectrochemical response for the optimized film deposited from TiO_2 target, as illustrated by photocurrents in Figure 5.16A and photoconversion efficiencies in Figure 5.16C; in this case, a maximum photoconversion efficiency close to 0.08% for the Ar/O_2 (50:50)-TiO_2-[Air+Vac] film is obtained. On the other hand, they decrease the photoelectrochemical performance of the optimized film deposited from Ti target, as illustrated by photocurrents in Figure 5.16B and photoconversion efficiencies in Figure 5.16D. This effect is currently unclear and further investigations are needed to elucidate it. However, it can be observed that in both cases the [Air+Vac] thermal treatment leads to better results than the single [Vac] annealing, suggesting the beneficial effect of a crystallization/sintering treatment before an annealing in reducing conditions, as emerged from Chapter 4. This hypothesis is also in agreement with a literature work[166], in which vacuum annealing at 500°C was performed on already air-annealed TiO_2 nanocrystals to obtain an increase of photocatalytic activity.

5.4.2 Annealing in pure argon

Annealing in pure argon is less frequently employed to obtain reduced TiO_2 nanomaterials, as it is an inert gas, and usually “special” kinds of starting TiO_2

are needed. For instance, Tian *et al.* annealed ultra-small (< 5 nm) amorphous TiO_2 nanoparticles, obtained by PLD, at 700°C in Ar for 2 h obtaining black Ti_2O_3/rutile core-shell nanoparticles[198]. In this thesis work, annealing in pure argon was employed to discern the actual role of hydrogen in the Ar/H_2 mixture, since it constituted only 3% of that mixture. Accordingly, as mentioned in Section 5.1, a double treatment with the second step in pure Ar, labeled as [Air+Ar], was performed instead of [Air+Ar/H_2] treatment on Ar/O_2 (50:50)-TiO_2 film.

The morphological analysis of the [Air+Ar]-annealed film is not reported here, due to the fact that it does not significantly affect the hierarchical morphology of the already [Air]-annealed TiO_2, as for the other reducing treatments described previously (i.e. [Ar/H_2] and [Vac]). In addition, the [Air+Ar] treatment neither affects the Raman spectrum of the Ar/O_2 (50:50)-TiO_2 film with respect to [Air] annealing, as shown in Figure 5.17; indeed, not only the peak positions and widths are the same as for the [Air]-annealed film, but also no photoluminescence background appears after annealing in argon atmosphere (not shown). Raman and PL analyses suggest that, in these experimental conditions, annealing in pure Ar is less effective than annealing in Ar/H_2 mixture in promoting the formation of defects in the material.

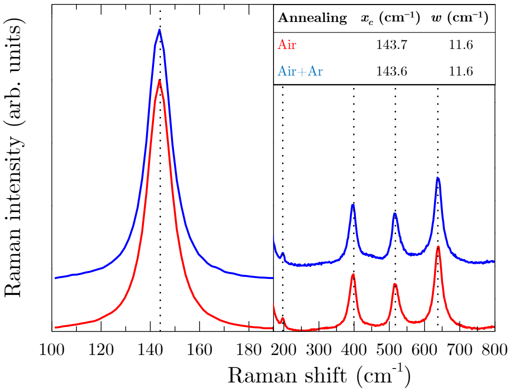

Annealing	x_c **(cm⁻¹)**	w **(cm⁻¹)**
Air	143.7	11.6
Air+Ar	143.6	11.6

Figure 5.17: Raman spectra of [Air]- and [Air+Ar]-annealed Ar/O_2 (50:50)-TiO_2 films (red: [Air]; blue: [Air+Ar]). The inset table shows the analysis of the $E_g(1)$ peak performed with a Lorentian fitting (x_c: peak position, w: full-width at half-maximum).

The photoelectrochemical properties of the [Air+Ar]-annealed film are shown in Figure 5.18, which also includes the results for the corresponding [Air]-annealed film as reference. The photocurrent curve (Figure 5.18A) of the former reaches higher values than that of the latter (i.e. 40 µA cm^{-2} at 0.5 V vs. 30 µA cm^{-2}), but it shows a higher open circuit voltage (about −0.75 V vs. about −0.8 V). Accordingly, the [Air+Ar]-annealed film shows a higher photoconversion efficiency than the [Air]-annealed one (Figure 5.18B), i.e. 0.033% vs. 0.026%.

The only slight increase in photoactivity for the [Air+Ar]-annealed film, compared to the [Air]-annealed one, together with the results of Raman spectroscopy (Figure 5.17), suggests that hydrogen in the Ar/H_2 (97:3) mixture plays an active role in ehnancing the photoelectrochemical behavior of TiO_2 hierarchical films, as its absence is related to a much lower enhancement effect. In support of this hypothesis, a previous literature work[198] reports that annealing P25-like TiO_2 nanoparticles in pure Ar did not lead to any substantial change in the material properties nor in its photoactivity; conversely, that annealing treatment was effective when performed on ultra-small amorphous TiO_2 nanoparticles.

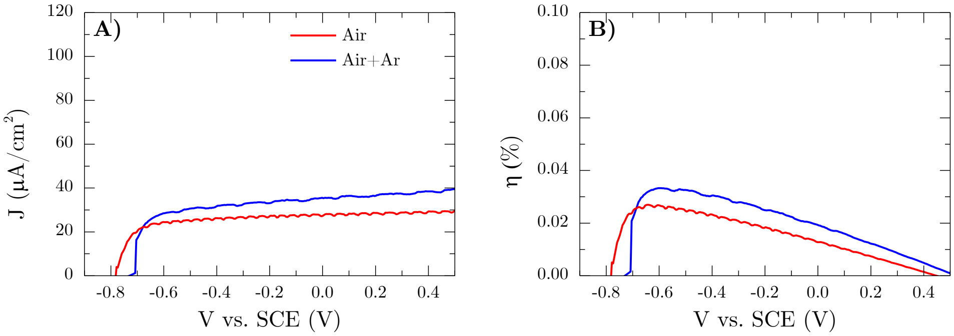

Figure 5.18: Photoelectrochemical behavior of [Air]- (red) and [Air+Ar]-annealed (blue) Ar/O_2 (50:50)-TiO_2 films. **(A)** *J–V* curves; **(B)** photoconversion efficiency curves.

To conclude, annealing in pure Ar atmosphere after [Air] annealing did not show remarkable effects on the photoactivity of TiO_2 hierarchical films and was excluded as a promising strategy for the tuning of their photoresponse.

5.5 Increase of annealing temperature

The last approach aimed at improving the photoelectrochemical properties of TiO_2 hierarchical nanostructures was to increase the annealing temperature from 500°C to 650°C, as mentioned in Section 5.1. This was based on previous works[137,138], in which the best photoresponse in water splitting experiments were obtained for films annealed in air at 650°C. In this case, pursuing the double treatment strategy, the temperature increase from 500°C to 650°C was approached either for the step in air or for the step in Ar/H_2 mixture; accordingly, the thermal treatments were labeled as **[Air-650+Ar/H$_2$]** or **[Air+Ar/H$_2$-650]**. The former was applied on an optimal film deposited from TiO_2 target, i.e. Ar/O_2 (50:50)-TiO_2, while the latter on a non-optimal film deposited from Ti target, i.e. Ar/O_2 (50:50)-Ti, due to unavailability of an optimal one.

The morphological results of obtained employing the aforementioned annealing treatments are shown in Figure 5.19, which also reports the SEM images of an [Air]-annealed film as reference. The [Air-650+Ar/H_2] (Figure 5.19B and 5.19E) and [Air+Ar/H_2-650] (Figure 5.19C and 5.19F) treatments induce clear different effects. [Air-650+Ar/H_2] annealing promotes a stronger coarsening of nanoparticles and higher connectivity with respect to [Air] annealing, as observed by cross-sectional SEM images (Figure 5.19D and 5.19E), and apparently to nanocrystals with more regular shapes (see top-view images in Figure 5.19). On the other hand, [Air+Ar/H_2-650] annealing does not apparently change the morphology of the already [Air]-annealed film (see Figure 5.19A and 5.19D vs. Figure 5.19C and 5.19F). The results for the [Air-650+Ar/H_2] annealing are in agreement with the aforementioned previous observations[137,138]. The outcome for the [Air+Ar/H_2-650] treatment, on the other hand, does not substantially change the morphology of an already [Air]-annealed film, similarly to a second annealing step in reducing conditions at 500°C shown in previous SEM observations (see Sections 4.3.1, 5.2.1 and 5.4.1).

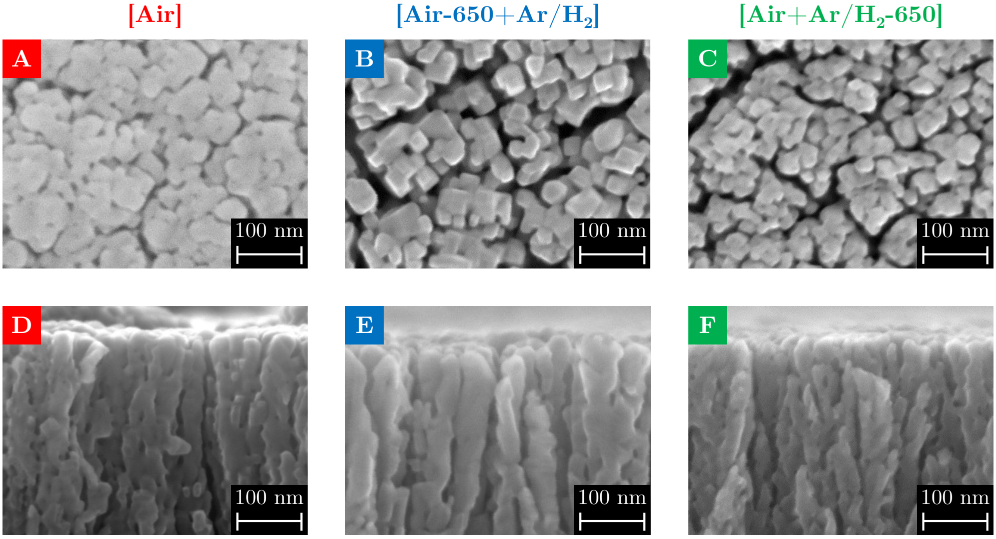

Figure 5.19: Morphological effects of thermal treatments at 650°C: top-view (first row) and cross-sectional (second row) SEM images. **A, D)** Ar/O_2 (50:50)-TiO_2-[Air]; **B, E)** Ar/O_2 (50:50)-TiO_2-[Air-650+Ar/H_2]; **C, F)** Ar/O_2 (50:50)-Ti-[Air+Ar/H_2-650].

The structural analysis on these films, performed with Raman spectroscopy, is shown in Figure 5.20; the spectra for the [Air-650+Ar/H_2]- and [Air+Ar/H_2-650]-annealed films are completely comparable to that of a reference [Air]-annealed film, i.e. the characteristic peaks of anatase are present, without any detectable presence of the rutile phase. Phase transformation from anatase to rutile, indeed, is affected by several parameters (such as morphology, grain size, dopants or impurities)[44] and for TiO_2 hierarchical films deposited at 5 Pa usually starts at higher temperatures[138]. In addition, phase transformation from anatase to rutile does not occur also in reducing conditions, i.e. for the [Air+Ar/H_2-650]-annealed film, even though they can promote it by introducing oxygen vacancies in the anatase lattice[44].

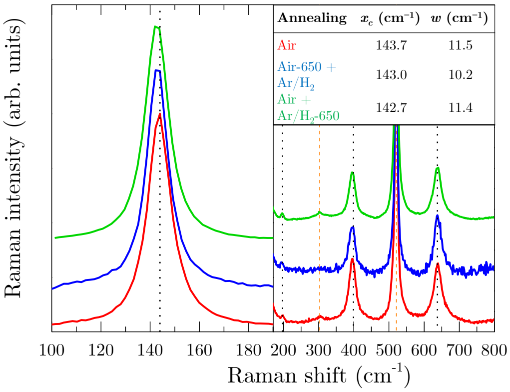

Annealing	**x_c (cm^{-1})**	**w (cm^{-1})**
Air	143.7	11.5
Air-650 + Ar/H_2	143.0	10.2
Air + Ar/H_2-650	142.7	11.4

Figure 5.20: Raman spectra of TiO_2 films annealed at 650°C(red: Ar/O_2 (50:50)-TiO_2-[Air]; light-blue: Ar/O_2 (50:50)-TiO_2-[Air-650+Ar/H_2]; dark-green: Ar/O_2 (50:50)-Ti-[Air+Ar/H_2-650]). The inset table shows the analysis of the $E_g(1)$ peak performed with a Lorentian fitting (x_c: peak position, w: full-width at half-maximum). Dotted lines (black) and dashed lines (orange) are also reported as reference to anatase and silicon (substrate) peaks, respectively.

Finally, the photoelectrochemical response of photoanodes annealed at 650°C was evaluated with photocurrent measurements and compared to the corresponding films annealed with the [Air+Ar/H_2] treatment (already presented in Figures 5.7 and 5.8 and inserted here for a better comparison). In particular, Figure 5.21A compares the photocurrent of the Ar/O_2 (50:50)-[Air-650+Ar/H_2] to that of the [Air+Ar/H_2]-annealed film deposited in identical conditions; the former shows a better performance than the former, reaching a saturated photocurrent density value of about 110 $\mu A\,cm^{-2}$ at 0.5 V vs. SCE. Accordingly, Figure 5.21C shows the photoconversion efficiency curves for these two films, and it confirms the superior performance for the [Air-650+Ar/H_2]-annealed film (0.08%) with respect to the [Air+Ar/H_2]-annealed one (0.6%).

A different situation is depicted by Figure 5.21B, which shows the results for the two films deposited from Ti target, i.e. Ar/O_2 (50:50)-Ti films. The [Air+Ar/H_2-650]-annealed film shows a lower photocurrent density value, but, more significantly, a clearly higher photocurrent onset with respect to the

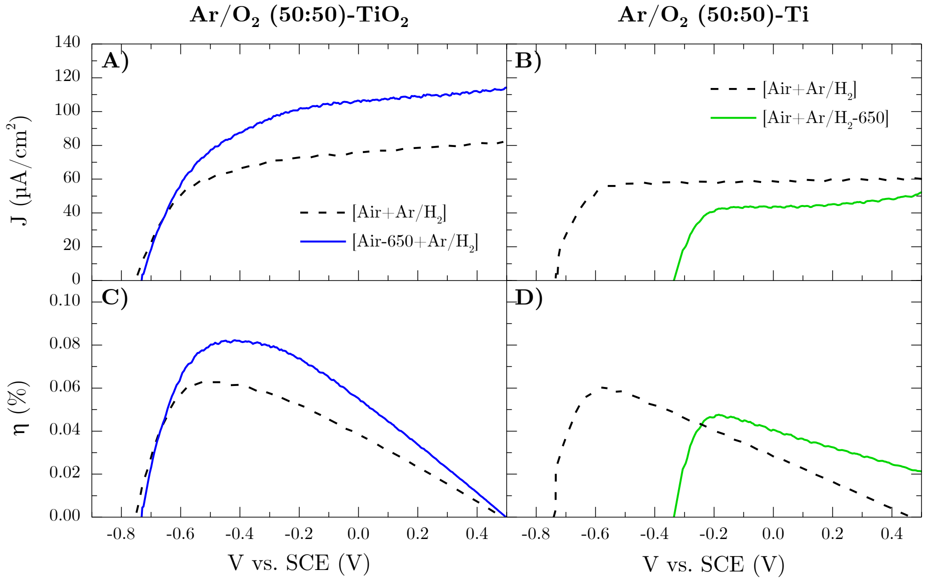

Figure 5.21: Photoelectrochemical response of TiO_2 films annealed at 650°C deposited from TiO_2 target **(A, D)** and from Ti target **(B, D)**: photocurrent **(A, B)** and photoconversion efficiencies **(C, D)** results.

[Air+Ar/H_2]-annealed film, i.e. about -0.33 V vs. SCE of the former and about -0.75 V vs. SCE of the latter. Finally, the photoconversion efficiency curves in Figure 5.21D confirm the lower performance of the [Air+Ar/H_2-650]-annealed film with respect to the [Air+Ar/H_2]-annealed one, as the maximum $\eta(\%)$ for the former is obtained at about -0.2 V vs. SCE, clearly a higher value than -0.6 V vs. SCE for the latter.

The positive effect of air annealing at 650°C (Figure 5.21A and 5.21C) is in agreement with previous investigations[137,138], so that it can be understood in terms of improved crystallinity and, thus, electron conductivity along the vertically-oriented hierarchical nanostructures towards the metal contact at the substrate. The opposite occurs, however, when the annealing at 650°C is performed in Ar/H_2 mixture (Figure 5.21B and 5.21D). In this case, an increase of the overpotential for the oxygen evolution reaction (OER) is observed, which could be attributed to an extensive amount of surface traps (see Section 1.3.3)/defect states on TiO_2 hierarchical nanostructures induced by the high-temperature annealing in a reducing environment. These defects may favor the recombination of charge carriers, lowering the performance of the [Air+Ar/H_2-650]-annealed photoanode.

5.6 Summary

This chapter illustrated various different approaches to develop and optimize the findings of Chapter 4, with the aim to finely tune the photoelectrochemical response of reduced/hydrogenated TiO_2 hierarchical nanostructures. This was mainly explored by gradually decreasing the oxygen content in the PLD deposition process, either coming from the target material or the background gas atmosphere at fixed pressure, keeping fixed the post-deposition thermal treatments, i.e. air annealing followed by thermal treatment in Ar/H_2 mixture; a "standard" air annealing was also employed as reference. Other investigations were performed by testing the effects of a higher deposition pressure (8 Pa) on photoelectrochemical properties, by considering thermal treatments in other reducing atmospheres (vacuum and pure Ar) and by increasing the annealing temperature from 500°C to 650°C. On the basis of the results of photoelectrochemical measurements, two optimal deposition conditions were identified, one for ablation of TiO_2 target and one for Ti target, and other strategies for further increasing their performance were identified.

While clear trends or enhancements were found in photocurrent curves, their interpretation with physical mechanisms related to deposition and annealing conditions is not straightforward; it is suggested that different amounts of defects are introduced either during the synthesis or the post-annealing steps, but their effects on morphological, structural and optical properties is elusive in most cases, hindering their identification in absence of more specific characterization techniques. It should be noted, moreover, that the issue of enhancing mechanisms in *black titania* nanomaterials has not been completely elucidated yet, as they are strongly dependent on process conditions and on the specific morphology/structure of TiO_2 nanomaterials[78,79]. A better understanding of the nature of defect states in the bandgap of TiO_2 hierarchical nanostructures was addressed by means of photoluminescence (PL) spectroscopy experiments, as presented in Chapter 6.

This chapter and the previous one, to conclude, aimed at showing that, by carefully tuning the synthesis and annealing conditions with laboratory facilities, it is possible to induce a (probably) low amount of defects in TiO_2 nanostructured films which lead to significant improvement in photoactivity, leaving also some room for improvement of the results presented in these chapters; a similar approach to that presented in these chapters may be applied to other oxide photoanode materials, such as WO_3 or α-Fe_2O_3, to enhance their photoactivity; on the other hand, other kinds of thermal treatments, such as rapid annealing in vacuum[195], could be employed to obtain a rapid crystallization of TiO_2 with a limited interaction with the surrounding atmosphere.

6

Photoluminescence properties of annealed TiO_2 hierarchical nanostructures

Following the investigations concerning reduced TiO_2 hierarchical nanostructures discussed in Chapters 4 and 5, this chapter presents an analysis of their photoluminescence (PL) properties. The general aim of PL spectroscopy, as introduced in Section 3.3.2, is to probe electronic states of a material, and in the specific case of the TiO_2 hierarchical nanomaterials was to gain information on the defect states introduced (or, if already present, affected to some degree) by thermal treatments in Ar/H_2 or vacuum atmospheres. An important role of these defects (for instance, oxygen vacancies) has been claimed to explain the photocurrent results presented in the previous chapters, on the basis of previous literature studies, and has been indicated by the results of optical spectroscopy (see Figures 4.8 to 4.10) and of preliminary PL measurements (see Figure 4.6). However, a systematic PL analysis was beyond the scope of previous investigations. Consequently. the strategy specifically adopted to pursue the analysis of defect states in the bandgap of hydrogenated/reduced TiO_2 hierarchical nanostructures is presented in Section 6.1. It should be noted, moreover, that a general consensus on the PL properties of TiO_2 nanomaterials has not been achieved yet in the literature: accordingly, a brief survey of the most relevant existing results is presented in Section 6.2. This discussion is also useful for a better understanding of the results obtained in this work, which are illustrated in Section 6.3. It is important to note that a conclusive interpretation of the results has not been achieved yet and future investigations will be necessary. The future perspectives of this work, as well as a summary of the most important findings, are finally presented in Section 6.4.

6.1 Experimental strategy

The systematic study of photoluminescence properties of reduced TiO_2 hierarchical nanostructures was performed on TiO_2 thin films deposited from

TiO_2 target with the same nominal parameters as the optimal deposition discussed in Chapters 4 and 5, i.e. Ar/O_2 (50:50)-TiO_2, with three thermal treatments: [Air], [Air+Ar/H_2] and [Air+Vac], with the same meaning as explained in Sections 4.1 and 5.1. The [Air+Vac]-annealed film was considered not only due to its promising photoactivity (see Figure 5.16), but also (and more importantly) to possibly obtain insights on the role of the reducing atmosphere in the introduction of defects in TiO_2 by comparing it to the [Air+Ar/H_2]-annealed film. Instead of 1.4 µm thick films, thin films (of about 280 nm) were chosen in order to avoid interference fringes[199] (such as those appearing in Figures 4.6 and 4.15, preventing an accurate fit of the photoluminescence curve). These three films, for the sake of brevity, will be labeled only with the thermal treatment, thus: **[Air]**, **[Air+Ar/H_2]** and **[Air+Vac]**.

The three films mentioned above were investigated with four different excitation energies, in order to probe different electronic transitions in TiO_2, one higher than the bandgap (UV at 3.82 eV) and three lower (blue at 2.71 eV, green at 2.41 eV and red at 1.96 eV); the detailed parameters are described below.

6.1.1 Deposition, annealing and photoluminescence parameters

TiO_2 nanostructured films were deposited by ablating a TiO_2 (99.9%) target with the ns-PLD system described in Section 3.2.1 (using $\lambda = 532$ nm and repetition rate 10 Hz). The laser fluence on the target was set at about 3.5 J/cm^2 and the laser pulse energy was 170 mJ. Silicon (100) (University Wafer, thickness 0.5 mm) was employed as substrate material, since it has no PL contribution in the investigated region (it only exhibits a band-to-band recombination peak in the region 0.9–1.3 eV at room temperature[200]). The depositions were performed at room temperature and at a fixed background gas pressure of 5 Pa in Ar/O_2 (50:50) mixture. The deposition time was set at 30 min, giving a thickness of about 280 nm (as evaluated with SEM images, not shown).

The following thermal treatments were employed (as in Chapter 5 and with the instrumentation described in Section 3.2.2): [Air], [Air+Ar/H_2] and [Air+Vac], all of them at 500°C.

Photoluminescence spectra were acquired at room temperature with four excitation laser lines of Raman spectrometers: UV, $\lambda = 325$ nm or $E_{exc} = 3.82$ eV with 0.6 mW power, blue, $\lambda = 457$ nm or $E_{exc} = 2.71$ eV with 1 mW power, green, $\lambda = 514.5$ nm or $E_{exc} = 2.41$ eV with 1 mW power, and red, $\lambda = 633$ nm or $E_{exc} = 1.96$ eV with 3 mW power (see Section 3.3.2 for further details).

6.2 Previous photoluminescence studies on anatase TiO_2

The first experimental investigation on PL emission of anatase single crystals was reported by Tang and co-workers in 1993[201], who found a broad peak in the visible range (2.3 eV at cryogenic temperature or 2.5 eV at room temperature) upon UV excitation and assigned it to the radiative recombinations of self-trapped excitons on the basis of the strong electron-phonon coupling expected in anatase TiO_2 (in other words, as expected in a material where polarons can be formed, as metioned in Section 2.1.3). Sekiya *et al.*[202] also studied the PL of anatase single crystals at cryogenic temperature finding again a broad band in the visible range; moreover, this band could be decomposed in Gaussian peaks at various energies: 2.40 eV, assigned to exciton recombinations mediated by Ti^{3+} sites, 2.15 eV, assigned to self-trapped excitons, and 1.95 eV, related to oxygen vacancies.

Due to the growing interest in energy-related applications of TiO_2 (DSSCs, photocatalysis, water splitting), further studies have mainly been performed on nanocrystalline forms of anatase; however, various or even contradicting results have been reported. The reasons behind this conflicting literature on the PL of nanocrystalline anatase are several[184]: as an indirect semiconductor, the PL from anatase is weak at room temperature, oxygen can quench it by scavenging electrons from the conduction band, intensity and shape of the emission spectrum can be affected by the nanoparticle environment, etc. Nonetheless, many studies show that nanocrystalline anatase exhibit a PL emission peaked in the green region. For instance, Zhang *et al.* found a broad emission peaked in the range 2.15–2.3 eV depending on the excitation energy (2.4–2.7 eV), and assigned it to radiative recombinations mediated by surface Ti^{4+}, Ti^{3+}, Ti^{2+} states[203]. Shi and co-workers studied *in situ* (i.e. in controlled environment, placing the samples in a home-made quartz cell) the evolution of PL from anatase powders with the annealing temperature using oxygen, hydrogen and nitrogen as oxidation, reduction and inert atmospheres, respectively[204]; they found a band centered at 505 nm (2.46 eV, green), which transformed into a band at 835 nm (1.48 eV, NIR) upon phase transformation into rutile and they attributed the visible PL of anatase to oxygen vacancies associated with Ti^{3+}, which increased after H_2 annealing. Cavigli *et al.* performed a time-resolved PL study of anatase nanoparticles (in the range 20–130 nm) at low temperature and found an emission centered at 2.1 eV made of two components, one at higher energy, related to self-trapped excitons, and one at lower energy, related to (sub)-surface oxygen vacancies or Ti^{3+} sites[205]. Preclíková and co-workers studied both the influence of excitation wavelength (325 nm vs.

442 nm) and of the surrounding atmosphere (air at atmospheric pressure or air at 5 Pa) on the PL emission of annealed anatase nanoparticles and found a wide band at about 2.2-2.4 eV[206]; in the case of UV excitation, the measured PL band at low pressure was easily quenched at environmental pressure, while in the case of blue excitation this band was narrower and less dependent on the surrounding atmosphere. The authors, consequently, suggested that above-bandgap excitation resulted mainly in radiative recombination mediated by self-trapped excitons, while below-bandgap excitation in recombinations mediated by a continuum of trap states within the bandgap.

A systematic analysis of PL properties of TiO_2, both in the anatase and rutile phases, has been performed by the group of J. L. McHale during the last 10 years, by considering thin films of TiO_2 nanoparticles (both P25, i.e. 75% anatase - 25% rutile, and pure anatase) illuminated by UV excitation (350 nm); in their studies, they have considered the effects of $TiCl_4$ treatment[207], the dependence on contact medium (such as air, Ar, water, ethanol, see Figure 6.1A)[208], the film porosity[209], the film morphology (nanoparticles vs. nanotubes vs. nanosheets)[210]; moreover, they have performed spectroelectrochemistry studies[211,212], in which the PL measurement was performed on TiO_2 as a working electrode in a three-electrode electrochemical cell (Figure 6.1B).

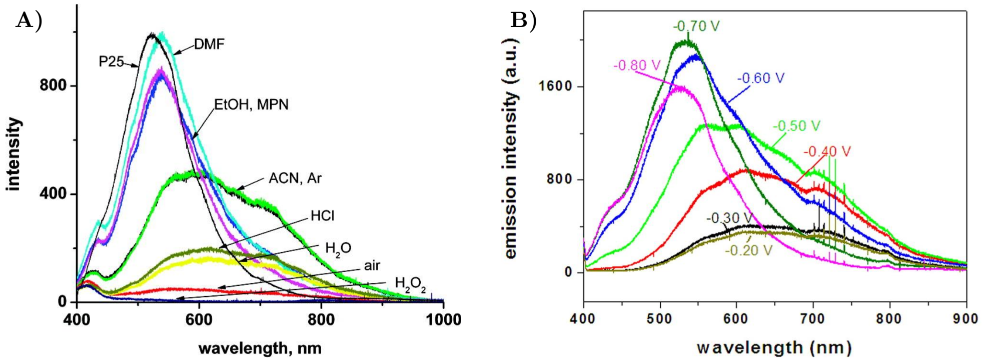

Figure 6.1: Photoluminescence studies on anatase thin films by prof. McHale's group. **A)** PL of a sintered anatase film, excited at 350 nm, in contact with various media (for comparison, the spectrum of a P25 film in contact with EtOH is also shown)[208]. **B)** PL spectra of nanocrystalline TiO_2 at pH 1.8 in 0.2 M $NaClO_4$ excited at 350.7 nm at different applied potentials vs. Ag/AgCl[211].

Although several studies (as discussed above) have addressed the PL properties of anatase nanomaterials, only few of them propose an interpretative model. McHale and co-workers, indeed, developed a scheme for the PL phenomena of anatase (also of rutile, which is not discussed here) represented in Figure 6.2. Upon UV excitation, electron-hole pairs are generated, which relax to the bottom of conduction band (electrons) and of the valence band (holes); electrons are then rapidly trapped into shallow traps, close to the conduction band edge (e.g. about 0.2 eV, which is a typical value for the Urbach energy of anatase[213]), which can participate in carrier transport. Spatial superposition between such an electron and a hole results in a self-trapped exciton, which can radiatively recombine giving a PL peak at about 420 nm (2.95 eV, blue arrow in Figure 6.2), which does not depend on the crystalline phase nor on the surrounding medium[207,208,212] and its intensity is low (as in Figure 6.1A and 6.1B), thus it is not further considered. On the other hand, holes can be trapped in "hole traps" and radiatively recombine with electrons in shallow traps, giving rise to an emission in the green region (about 550 nm or 2.25 eV, green arrow in Figure 6.2); conversely, mobile electrons can be trapped in deep traps and radiatively recombine with holes in the valence band, giving rise to an emission in the red region (between 500 and 800 nm, approximately peaked at 2.0 eV, red arrow in Figure 6.2)[208]:

$$\text{Type 1 PL:} \quad e^-_{CB} + h^+_{tr} \rightarrow h\nu_{green} \tag{6.1}$$

$$\text{Type 2 PL:} \quad h^+_{VB} + e^-_{tr} \rightarrow h\nu_{red} \tag{6.2}$$

Figure 6.2, moreover, illustrates the quenching mechanisms for these emissions: both of them are quenched by O_2 or water, which scavenge electrons from the conduction band and from shallow traps, while ethanol (EtOH) is an efficient hole scavenger and inhibits only type 2 PL[208]; this explains the results illustrated in Figure 6.1A, which illustrates that, taking as reference the PL measured in Ar, quenching of the red PL mechanism results in narrower spectra peaked in the green region (as with EtOH), while (partial) quenching of both mechanisms results in weaker and broader spectra (as with water, air or H_2O_2). The exact nature of electron and hole traps, on the other hand, is rather challenging, and the authors suggested that oxygen vacancies, more prevalent on (101) surfaces, can give rise to hole traps, while under-coordinated Ti ions (Ti_{5c}), more prevalent on (001) surfaces, can trap electrons (lowering their oxidation state to +4 to +3)[210].

Somehow similar results have been obtained by J. T. Yates' group, who studied PL emissions from P25 nanoparticles (pressed in thin disks) excited at 320 nm in vacuum with a dedicated IR/PL setup, also recording the PL emission during time, and by considering exposure to gases such as CO, NH_3 and, in particular, O_2[214–216]. They found a broad PL peak centered at 530 nm (green region) whose intensity increased in vacuum with prolonged UV exposure and reversibly decreased due to NH_3 and CO adsorption[214]. On the other hand, the exposure to O_2 resulted in a more complex mechanism: on the one hand, first O_2 molecularly chemisorbs by extracting electrons from TiO_2, increasing the band bending and lowering the PL intensity; second, further O_2 exposure heals surface defects (such as oxygen vacancies), decreasing the band bending and increasing the PL intensity[216]. In this case, the description of the

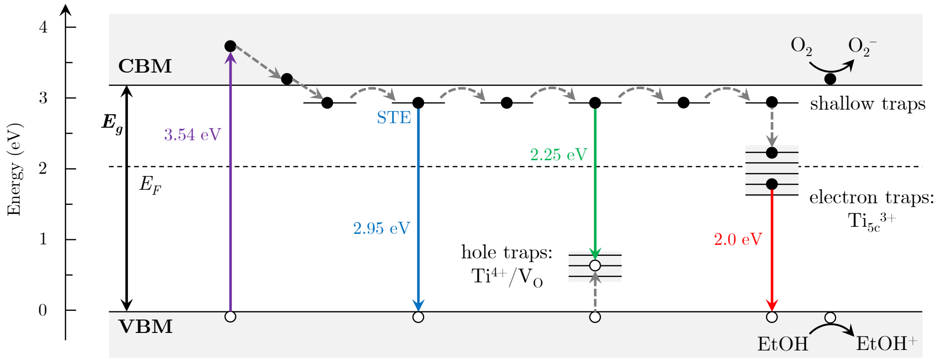

Figure 6.2: Model for PL mechanisms in anatase; colored solid lines indicate radiative transitions, while gray dashed lines non-radiative pathways. Adapted from [208].

observed PL intensity trends was based on the band bending approximation[215], while McHale and co-workers, on the contrary, suggested that nanoparticle films of TiO_2 cannot sustain a macroscopic field[184], excluding any role of band bending.

Recently, Pallotti and co-workers have also investigated the PL mechanisms of nanocrystalline films of TiO_2, both considering anatase and rutile phases, confirming and somehow developing the results obtained by McHale's group[217,218]; in the case of anatase, for instance, they also found a green PL emission, attributed to oxygen vacancies or adjacent Ti sites and easily quenched in the presence of oxygen, as well as a red PL emission, predominating for below-bandgap excitations, less influenced by the presence of oxygen and related, for this reason, to sub-surface oxygen vacancies[218].

Photoluminescence studies of *black titania*

The complex framework discussed above for PL emissions does not explicitly take into account hydrogenated or reduced forms of TiO_2, i.e. *black titania* nanomaterials. Indeed, to this author's knowledge, very few works thoroughly address the PL properties of hydrogen-treated nanomaterials; not surprisingly, McHale and co-workers[219] performed spectroelectrochemical experiments on hydrogenated rutile nanowire arrays produced with the same method as in the work of Wang *et al.*[84]. Notably, in addition to the typical rutile PL emission in the NIR, they found a weak green PL, similar to the green component of anatase, and it was accordingly attributed to oxygen vacancies. Still oxygen vacancies, with defect states in the bandgap at 2.36 and 2.63 eV with respect to the valence band edge, were also suggested by Naldoni *et al.*[162] as defects introduced by hydrogenation in the bulk of TiO_2 nanoparticles, even though these data were obtained by cathodoluminescence spectroscopy rather than photoluminescence.

On the other hand, PL measurements have been more often included in studies concerning black titania nanomaterials as characterization tools, sometimes with gross misinterpretations, as pointed out (again) by McHale and co-workers[220]; conversely, in other cases more insights on the defects introduced by hydrogenation treatments have been obtained. For instance, Yan *et al.*[221] treated P25 nanoparticles with a H_2 plasma at 150°C and studied their PL emission with 266 nm excitation (4.66 eV), finding similar results to McHale and co-workers: a broad "green PL" emission centered at 505 nm (2.46 eV) was observed and attributed to radiative recombinations between mobile electrons and holes trapped in localized states, at 0.7–1.4 eV above the valence band maximum, related to oxygen vacancies. On the other hand, Liu *et al.*[222] prepared hydrogenated anatase nanoparticles with a high-pressure treatment (20 bar, 500°C, with a duration ranging from 1 h to 3 days) and studied their PL emission with 375 nm excitation in air, compared to that of non-hydrogenated nanoparticles; in both cases a broad emission with a maximum in the range 600-700 nm was found and it was ascribed to a superposition between self-trapped exciton recombinations and defect-related emissions. However, for the hydrogenated nanoparticles, an additional peak in the range 400–450 nm appeared, and it was attributed to some specific defect states introduced by H_2 annealing (rather than self-trapped excitons as suggested, instead, by McHale and co-workers). Finally, Gurylev *et al.*[86] reported the PL emission of hydrogenated TiO_2 thin films with 310 nm excitation, which appeared as a broad band in the visible range with defined peaks at various energies, attributed to self-trapped excitons, oxygen vacancies and surface defects; in addition, the PL intensity decreased after hydrogen treatment because oxygen vacancies acted mostly as non-radiative centers.

The brief review on state-of-the-art knowledge on PL properties of anantase nanomaterials can suggest that some open issues are still present in literature. First, PL results vary according to the material porosity, morphology and defectivity[184]. Second, few studies compared above-bandgap to below-bandgap excitations with the aim of probing different trap/defect states in the bandgap; some examples, both with blue excitation (442 nm), are the already mentioned works of Preclíková *et al.*[206], who observed a wide band centered around 2.2-2.4 eV, attributed to radiative recombinations mediated by trap states in the anatase bandgap, and Pallotti *et al.*[218], who reported a "red PL" mechanism, related to sub-surface oxygen vacancies. Third, in the specific case of black titania, a lack of detailed investigations appear evident, and the typical "PL-active" defect states are the same expected in unmodified TiO_2 (i.e. oxygen vacancies, Ti^{3+} ions), with an increased concentration upon hydrogenation.

6.3 Experimental results

As motivated at the beginning of this chapter and by the above discussion, in this section the PL properties of hydrogenated/reduced TiO_2 hierarchical films with [Air], [Air+Ar/H_2] and [Air+Vac] annealing treatments is reported, following the experimental strategy presented in Section 6.1.

The PL spectra for the three annealed films with UV, blue, green and red excitation wavelengths are shown in Figure 6.3, in which each subfigure compares the results for [Air]-, [Air+Ar/H_2]- and [Air+Vac]-annealed films with the same excitation energy.

- Figure 6.3A shows PL spectra obtained with UV excitation, which are rather similar to each other for all three films and the highest intensity is exhibited by the [Air+Ar/H_2]-annealed film. For the three curves, indeed, the maximum is found approximately at 2.0 eV (with a large Stokes shift with respect to the excitation energy).
- Figure 6.3B, on the other hand, shows the results for blue excitation; in this case, the [Air+Ar/H_2]-annealed film still exhibits the highest intensity, but the maximum of its PL curve (about 2.0 eV) is slightly shifted with respect to that of the [Air+Vac]-annealed film (about 2.2 eV); moreover, the [Air]-annealed film does not show any signal at all.
- A somehow similar outcome is found with green excitation, as illustrated in Figure 6.3C, in which again the [Air+Ar/H_2] film exhibits the highest intensity, clearly higher than the [Air+Vac] film, while the [Air] film has no signal as well. The PL emissions peak at about 1.8-1.9 eV in this case.
- Finally, Figure 6.3D shows the results obtained with red excitation; also in this case, the [Air+Ar/H_2]-annealed film exhibits the highest intensity and the [Air]-annealed one does not show any PL emission (indeed, the signal at energy lower than 1.3 eV is due to the PL of silicon substrate[200]).

In general, it can be concluded that all the investigated films exhibit a wide PL band centered at about 1.8–2.2 eV, thus in the red-yellow region of the visible electromagnetic spectrum, with the exception of the [Air]-annealed film, which does not show any signal with below bandgap excitations. These results are consistent with those presented in previous chapters for thicker films, as in Figures 4.6 and 4.15, in which an accurate spectral fitting was not straightforward due to interference fringes (a method to overcome this issue is discussed in ref. [199]).

The low thickness (about 280 nm) of the films considered in this study, conversely, prevented any interference effect, being lower even than the UV wavelength (325 nm); for this reason, PL curves were fitted with a superposition of Gaussian curves without any further data processing; as an example of this

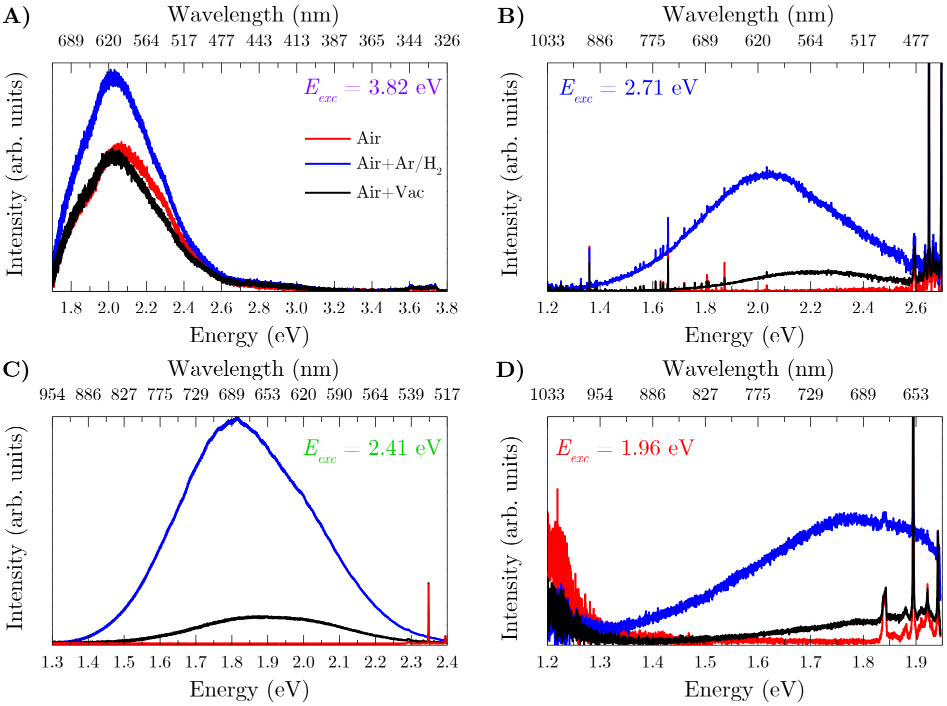

Figure 6.3: Photoluminescence spectra of annealed TiO_2 films (red: [Air]; blue: [Air+Ar/H_2]; black: [Air+Vac]) with different excitation energies: **A)** 3.82 eV (UV), **B)** 2.71 eV (blue), **C)** 2.41 eV (green), **D)** 1.96 eV (red). In **A)** the intensity of the three films was normalized by substracting the signal obtained with the bare Si substrate, while in **B)**, **C)** and **D)** by setting as equal to 1 the intensity of the Raman $E_g(1)$ peak of anatase (Raman peaks appear on the right of each figure).

procedure, Figure 6.4 shows the multi-Gaussian fit of PL spectra excited with the UV laser line for the [Air] film (Figure 6.4A) and for the [Air+Ar/H_2] film (Figure 6.4B; very similar results are found for the [Air+Vac] film). For both films, a good fit of the experimental data was obtained with four Gaussians, peaked in the red, orange, yellow and green/light blue regions of the visible spectrum. The values obtained for these peaks and for all the other fits of PL spectra shown in Figure 6.3 is reported in Table 6.1. The first three of them exhibit almost identical peak positions for the two films (1.80 eV, 1.97 eV and 2.16-2.17 eV for the red, orange and yellow components, respectively) with slight differences in relative intensities, e.g. the yellow component is more intense than the orange one for the [Air]-annealed film, while they show the same height for the [Air+Ar/H_2]-annealed film. On the other hand, the fourth component is very broad and is located at slightly higher energy for the [Air+Ar/H_2]-annealed film (2.54 eV) than for the [Air]-annealed film (2.46 eV).

By overall considering the experimental data in Figure 6.3 and the fitting analysis of Table 6.1, some observations can be pointed out:

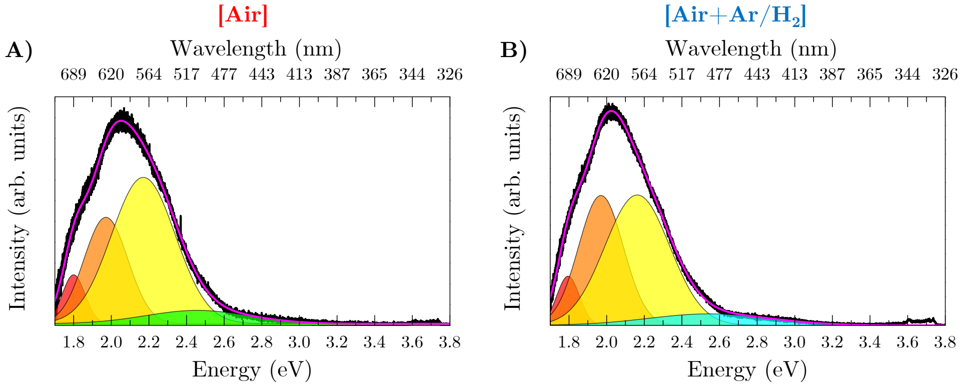

Figure 6.4: Multi-gaussian fit of photoluminescence spectra excited with UV laser line. **A)** [Air]-annealed film; **B)** [Air+Ar/H_2]-annealed film. The individual Gaussian peaks are colored to easily visualize their corresponding region of the electromagnetic spectrum.

Table 6.1: Peak position values obtained from the multi-Gaussian fit of PL spectra presented in Figure 6.3.

Excitation	PL peaks	[Air]	[Air+Ar/H_2]	[Air+Vac]
UV	$PL1_{UV}$	1.80 eV	1.80 eV	1.80 eV
	$PL2_{UV}$	1.97 eV	1.97 eV	1.97 eV
	$PL3_{UV}$	2.17 eV	2.16 eV	2.17 eV
	$PL4_{UV}$	2.46 eV	2.54 eV	2.56 eV
Blue	$PL1_{blue}$	-	2.01 eV	2.23 eV
	$PL2_{blue}$	-	2.40 eV	-
Green	$PL1_{green}$	-	1.79 eV	1.85 eV
	$PL2_{green}$	-	2.05 eV	2.06 eV
Red	$PL1_{red}$	-	1.80 eV	1.82 eV

- for UV excitation, comparable results for all three films have been obtained, as indicated by the similar values of peak positions (with the only exception of the $PL4_{UV}$ for the [Air]-annealed film);
- the [Air+Ar/H_2]- and [Air+Vac]-annealed films exhibit PL peaks with very similar energies but quite different intensities (higher for the [Air+Ar/H_2]-annealed film); this occurs at any excitation wavelength, except for the blue laser line;
- for the [Air+Ar/H_2]- and [Air+Vac]-annealed films, some peaks with very similar energies are found with different excitation wavelengths: $PL1_{UV}$~$PL1_{green}$~$PL1_{red}$, while $PL2_{UV}$~$PL1_{blue}$ (only for the [Air+Ar/H_2]-annealed film) ~$PL2_{green}$.

As pointed out by the above analysis, the [Air+Ar/H_2] and [Air+Vac] films exhibit a PL emission at any investigated excitation wavelength; for this reason, Figure 6.5 shows the PL spectra with the peak normalized at unity for these two films. Figure 6.5A shows the results for the [Air+Ar/H_2] film, both considering the measured spectra (top figure) and their corresponding multi-Gaussian cumulative fits (bottom figure); it can be noted that the PL curves with UV and blue excitations show the same maximum, as well as those with green and red excitations. On the contrary, Figure 6.5B shows that for the [Air+Vac] film the PL maxima with blue and UV excitations are shifted relative to one another (about 0.25 eV) and the same occurs for the PL curves for green and red excitations, even though in this case the shift is only 0.1 eV. In the case of [Air+Ar/H_2]-annealed film (Figure 6.5), the superposition of PL curves may be attributed to the activation of similar radiative recombination pathways, while in the case of [Air+Vac]-annealed film the slight shift appearing between each curve may be related to a wider population of defect states suitable for luminescence[203,223]. However, it must be noted that the signal/noise ratio in Figure 6.5B is lower than in Figure 6.5A due to the lower intensity of PL signal for the [Air+Vac]-annealed film, which may affect the reliability of the multi-Gaussian cumulative fits shown in the bottom figure. At this point, no further considerations can be made and confirmation of these results are needed.

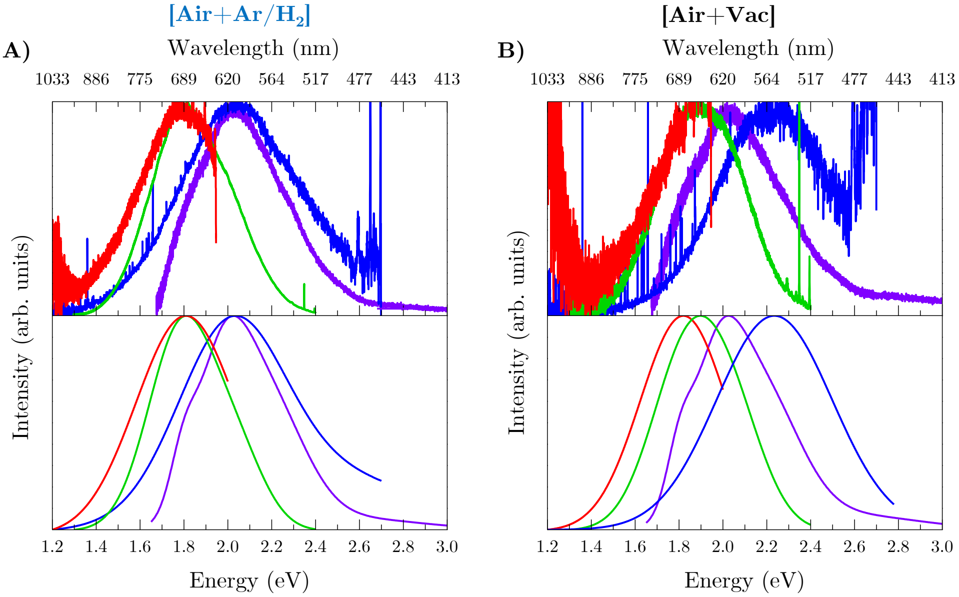

Figure 6.5: Comparison between normalized PL spectra (top) and their multi-Gaussian cumulative fit (bottom) for **A)** [Air+Ar/H_2]- and **B)** [Air+Vac]-annealed films. In all cases, each color corresponds to a different excitation energy: violet for 3.82 eV (UV), blue for 2.71 eV, green for 2.41 eV, red for 1.96 eV.

The overall results discussed above essentially evidence that TiO_2 hierarchical nanostructures exhibit a broad PL emission made up of few components in the red, orange and yellow region of the visible electromagnetic spectrum, with an additional broad and weak emission in the green region; these components can be probed depending on the excitation wavelength and, in general, the maximum of the PL emission falls in the orange-red region of the visible electromagnetic spectrum. Notably, for the [Air]-annealed film no emission is found with excitation energy lower than the bandgap. A comparison of these results with the already existing literature, mostly concerning compact thin TiO_2 films, can be carefully performed as suggested by Pallotti *et al.*[218], who showed that, at least qualitatively, hierarchical films deposited by PLD (but only air-annealed) exhibited similar results to pellets obtained by cold-pressing commercial TiO_2 nanopowders at equal crystalline phase and measurement conditions. As a consequence, it is possible to compare the results presented above with those obtained by McHale and co-workers[208] and Pallotti *et al.*[218] in terms of the so-called "red PL" (see Figure 6.2). According to these authors, PL measurements in air show the prevalence of this emission and a quenching of the "green PL", as discussed in Section 6.2; a similar mechanism, thus, could explain the results obtained for all the films with UV excitation (Figure 6.3A). Moreover, a red PL actually composed by two discernible components, in the yellow and red regions, was reported by McHale and co-workers[211].

On the other hand, PL emissions with blue excitation has already been observed by few authors[206,218]; Pallotti *et al.*, in particular, suggest that below-bandgap excitation can promote electrons to shallow states which, then, can migrate into deeper traps and, eventually, radiatively recombine with valence band holes according to the red PL mechanism[218]. Excitation with green wavelengths, in addition, were employed by few authors as well[203,223]; in both cases, the lowest energy employed, 2.4 eV, produced a PL emission with a maximum at 2.15 eV (yellow), as mentioned in Section 6.2. The results of Pallotti *et al.*[218] may again be compared to those obtained in this study for the "red-like" PL emission of [Air+Ar/H_2]-annealed film with blue excitation (Figure 6.3B), while those of Zhang *et al.*[203] and Šćepanović *et al.*[223] evidence a more "yellow-like" PL than that observed for both [Air+Ar/H_2]- and [Air+Vac]-annealed films with green excitation (Figure 6.3C). A fundamental difference between these studies and the present one, however, is the already mentioned absence of PL emission for the [Air]-annealed film for below-bandgap excitation. Moreover, no previous studies concerning an excitation energy as low as in this case (1.96 eV, in the red region) are available, at least to this author's knowledge.

By taking into account the above considerations, it can be hypothesized that the [Air+Ar/H_2] and [Air+Vac] thermal treatments intensify the presence defect states in the bandgap, such as the "usual suspect" oxygen vacancies, in two ways:

- by increasing their concentration without changing their chemical nature (thus their energy levels in the bandgap), which could explain the increase of PL intensity with respect to the negligible signal for the [Air]-annealed film;
- by extending the population of defect states in the bandgap, which would allow additional excitation and recombination pathways for electron-hole pairs.

Assuming the correctness of these hypotheses, at this point it is not possible to state which of these mechanisms prevails only based on the experimental results discussed above. For instance, the spectral similarities emerged with UV excitation (Figure 6.3A) could favor the idea of similar defects for all the investigated films, while the results obtained with visible excitation could instead suggest additional defect states introduced by reducing thermal treatments (Figure 6.3B–6.3D). An alternative point of view, moreover, would be to consider non-radiative recombinations, which are indeed significant in anatase TiO_2[208]; the lower PL signal obtained for the [Air+Vac]-annealed film with respect to the [Air+Ar/H_2]-annealed one, for instance, may indicate a higher degree of non-radiative recombinations for the former, and an even higher for the [Air]-annealed excited film with visible excitation (so high that it completely overcomes radiative pathways).

Finally, the few literature studies critically discussing the PL properties of hydrogen-treated TiO_2 nanomaterials mostly evoke the role of oxygen vacancies in increasing radiative recombinations in the green region of the visible spectrum[219,221]; however, these works consider either the rutile phase[219] or a nanopowder morphology[221], thus preventing a straightforward comparison with the results for the [Air+Ar/H_2]-annealed film (and, further, for the [Air+Vac]-annealed one). Moreover, the great variability in outcomes obtained for black titania nanomaterials depending on the experimental procedure has already been stressed out in Chapter 2, which should also be taken into account for this analysis.

6.4 Summary

As reviewed in the first part of this chapter, several works have considered the photoluminescence (PL) properties of TiO_2 nanomaterials, with varying spectral shapes, intensities and assignments for the obtained results (self-trapped excitons, surface states, oxygen vacancies/Ti^{3+} sites, under-coordinated Ti atoms). Very few works have thoroughly investigated the PL properties of hydrogen-treated TiO_2, especially considering the anatase phase. Considering, instead, the framework of this thesis work, a clear understanding of the chemical nature of defects introduced with the reducing deposition/annealing conditions discussed in Chapters 4 and 5 was not addressed. For all of these reasons, PL measurements on three thin TiO_2 films deposited in Ar/O_2 (50:50) atmosphere and annealed with [Air], [Air+Ar/H_2] and [Air+Vac] treatments have been performed in air with four excitation energies, one above bandgap (in the UV region of the electromagnetic spectrum) and three below (in the blue, green and red regions). While with UV excitation all the three films exhibit comparable PL spectra, with visible excitation no emission is obtained for the [Air]-annealed film (as already noted in Chapter 4). In most cases, PL emission is maximum in the orange-red region of the electromagnetic spectrum and the highest intensity is exhibited by the [Air+Ar/H_2]-annealed film. Even though the presence of some components in PL bands has been elucidated with a multi-Gaussian spectral fitting and the reasonable contribution of oxygen vacancies can be supposed, no further hypotheses can be made at present due to the need of additional experiments. Indeed, the investigation reported in this chapter is only preliminary and can be improved with several strategies, to gain more information on the defect states in the bandgap of TiO_2, such as:

- PL spectra at a chosen wavelength in other environments than air, as performed by McHale and co-workers[208], to selectively quench some recombination pathways and, at the same time, favor others;
- time-resolved and temperature-dependent experiments (e.g. at cryogenic temperatures)[176];
- additional excitation energies (or better, photoluminescence excitation spectroscopy, PLE[176,218]);
- PL measurements at varying incident power, which could elucidate the saturation of defect states at increasing power, thus aiding their identification[203].

On the other hand, PL measurements could be coupled with other spectroscopic techniques, such as electron paramagnetic resonance (EPR), to explicitly detect species such as Ti^{3+}, or Fourier transform infrared spectroscopy (FTIR), to evidence the presence of surface Ti–OH or Ti–H bonds in hydrogen-treated films. Finally, hydrogenated films prepared with a pure hydrogen atmosphere could be investigated, in order to elucidate the effects of a different hydrogen content in the reducing environment. Some of these perspectives are foreseen after this thesis work, including: the effect of a different contacting medium, i.e. ethanol and water, the use of other characterization techniques (FTIR measurements in collaboration with G. Terraneo, Department of Chemistry, Materials and Chemical Engineering "G. Natta", Politecnico di Milano) and the analysis of a pure-hydrogen annealed

TiO_2 film (in collaboration with A. Naldoni, Regional Centre of Advanced Technologies and Materials, Olomuc, Czech Republic).

7

Integration of TiO_2 hierarchical films with plasmonic Au nanoparticles

This chapter reports on the preliminary investigations concerning the integration of plasmonic noble metal nanoparticles in TiO_2 hierarchical nanostructured films. The motivations leading to this additional research work, going further than the investigations discussed in the previous chapters, are clarified in Section 7.1. First, the control of morphological and plasmonic properties of metal nanoparticles by means of Pulsed Laser Deposition, on the basis of previous literature studies, is presented in Section 7.2. These experiments were mandatory in order to successfully address the integration of these nanoparticles with TiO_2 hierarchical films, which is presented in Sections 7.3 to 7.5. Moreover, some preliminary tests in photoelectrochemical water splitting cells (with the same conditions as for the hydrogen-treated TiO_2 films) on selected photoanodes are presented in Section 7.6. The chapter is closed by summarizing the main findings and by highlighting the perspectives (most of them already ongoing) of this investigation (Section 7.7).

7.1 Experimental strategy

As discussed in Section 2.2.3, some studies have been proposed in the literature regarding the integration between TiO_2 (or other oxides) and plasmonic metal nanoparticles (NPs). As a plasmonic metal, gold (Au) in most cases is preferred to silver (Ag) since the latter can be easily oxidized when exposed to oxygen at room temperature, producing a redshift of the localized surface plasmon resonance[224], even though some remarkable studies on Ag-TiO_2 have also been mentioned (e.g. plasmon resonant energy transfer mechanism for the system Ag/N-TiO_2[122] presented in Section 2.2.3). In most of the previous studies, the preparation of Au NPs is performed on the surface of a TiO_2 film by means of a photoreduction method in the liquid phase starting from the $HAuCl_4$ precursor[114,115,118,119]. More generally, chemical methods allow a fine tuning of the morphology and size distribution of metal NPs[225]. On the contrary, in order to prevent residual chemical agents or the use of toxic precursors, vapor phase methods have been proposed, which typically involve the evaporation or sputtering of a gold nm-thick film on TiO_2 and its subsequent transformation into nanoparticles by means of a thermal treatment (i.e. *dewetting* effect)[226–228].

On the other hand, pulsed laser deposition (PLD) has also been exploited for the production of surface-supported noble metal nanoparticles; specifically, Au NPs have been reported for surface-enhanced Raman scattering (SERS) applications[229–232]; moreover, their growth dynamics[231,233,234] has also been investigated, but only few studies concerned the influence of the PLD process parameters on the plasmonic resonance frequency of the NPs[235–237]. Considering the findings presented in these studies, PLD shows the potentiality of obtaining NPs with a desired size and controllable plasmonic resonance frequency by controlling its process parameters, also exploiting *in-plume* cluster nucleation phenomena at high pressures[238] to avoid subsequent thermal treatments and to obtain size distributions independent from the substrate. For instance, a control on the localized surface plasmon resonance (LSPR) wavelength in the range 550–700 nm has been reported depending on synthesis conditions, such as target-to-substrate distance (d_{T-S}), laser fluence, background gas pressure, number of shots and substrate temperature[235–237].

The use of PLD to sythesize plasmonic nanoparticles, thus, avoids the use of aggressive solvents[239], allows to employ the same technique for the synthesis of both Au NPs and TiO_2 hierarchical films and, more interestingly, allows the direct growth of an integrated Au-TiO_2 film in a single experimental run (i.e. the *co-deposition*), ensuring a satisfactory infiltration of Au NPs in TiO_2, otherwise extremely challenging with chemical methods or other techniques. Accordingly, very few works employing PLD for the synthesis of Au NPs on TiO_2 have been reported[240,241]. Consequently, a further development of this Ph.D. project was related to the conception and the first investigations on plasmonic Au-TiO_2 hierarchical nanostructured films; as mentioned also in Section 3.1, this work was performed in collaboration with a student who developed her Master thesis work in this regard[169]. Accordingly, in this chapter only the results pertaining to my personal activity will be reported.

The strategy was developed as follows:

1. exploration of various PLD conditions for the deposition of Au NPs on bare substrates (silicon and glass) to obtain a satisfactory control on the Au NP size, which in turn is related to their plasmonic properties;
2. integration of Au NPs, obtained in selected conditions, with TiO_2 hierarchical films according to three approaches, as illustrated in

Figure 7.1: Au NPs on top of the TiO_2 film, hereinafter labeled as **Au/TiO$_2$** (Figure 7.1A), Au NPs at the bottom of the TiO_2 film, labeled as **TiO$_2$/Au** (Figure 7.1B) and co-deposition, i.e. Au NPs dispersed within the TiO_2 film thanks to the simultaneous growht, labeled as **Au-TiO$_2$** (Figure 7.1C).

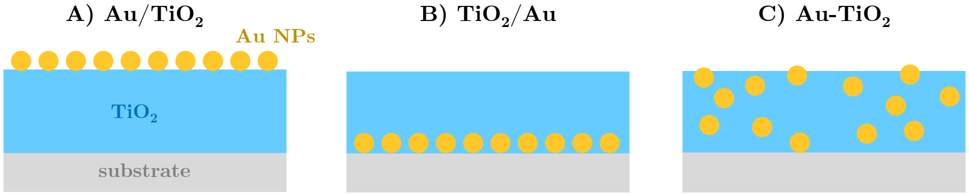

Figure 7.1: Schematic illustration of the integration strategies between Au nanoparticles and TiO_2 hierarchical films: **A)** Au NPs on top of TiO_2, **B)** Au NPs at the bottom of TiO_2 and **C)** co-deposition (Au NPs intermixed with TiO_2).

The detailed experimental parameters of both these steps are reported in Sections 7.1.1 and 7.1.2, respectively, while the results are presented in the following sections as already clarified above.

7.1.1 Deposition parameters of Au nanoparticles

Au NPs were deposited by ablating an Au (99.99%) target with the ns-PLD system described in Section 3.2.1 (using $\lambda = 532$ nm and repetition rate 1 or 10 Hz). The laser fluence on the target was set at about 2.0 J/cm^2 (comparable to literature data, in which values in the range 1–4 J/cm^2 are reported[230,235,236]) and the laser pulse energy was 100 mJ. Si(100) (University Wafer, thickness 0.5 mm) and soda-lime glass (thickness 1 mm) were used as substrates, mounted on an in-axis rotating sample holder at a fixed $d_{T-S} = 50$ and 100 mm. All the depositions were carried out at room temperature with a pure Ar background gas (as also performed in previous studies[230,231]), varying the pressure in the range 10–1000 Pa as well as the number of laser pulses (10, 50, 100, 1000) to explore different coverage degrees and different growth conditions. For selected samples, post-deposition annealing treatments were performed in air in a Lenton muffle furnace (see Section 3.2.2) with 4°C/min heating ramp and 2 h dwell at 500°C, labeled as **[Air]** (as in Section 4.1).

7.1.2 Deposition parameters of integrated Au-TiO$_2$ films

For the integration between Au NPs and TiO_2 films, some PLD parameters were kept fixed, such as the wavelength ($\lambda = 532$ nm), the target-to-substrate distance ($d_{T-S} = 50$ mm), the room temperature conditions, the targets (Au 99.99% and TiO_2 99.9%, except for the Au-TiO_2

films) and the substrates (silicon, glass and half-masked Ti plates as in previous chapters, see Sections 4.1.1 and 5.1.1). The specific parameters employed for the three different integration strategies are instead reported below.

Au/TiO_2. For these films, the integration was performed by means of successive depositions:

1. TiO_2 deposited with fluence of 3.5 J/cm^2, pure O_2 background pressure of 5 Pa and 8 Pa, nominal thickness 1 µm, [Air] thermal treatment; the pressure of 8 Pa was motivated by the need of a more open-porous morphology (see Section 5.3) for the infiltration of Au NPs.
2. Au NPs deposited on TiO_2 with fluence 2.0 J/cm^2, pure Ar background pressure of 1000 Pa, 150 laser shots, aiming at a nominal average diameter of 5 nm, favorable for plasmonic phenomena such as hot electron injection (see Section 2.2.3).

TiO_2/Au. This integration strategy basically followed the reverse procedure than the former case:

1. Au NPs obtained by a deposition with fluence 2.0 J/cm^2, pure Ar background pressure of 1000 Pa, 1000 laser shots, [Air] thermal treatment, aiming at a nominal average size of about 20-25 nm, favorable for PRET mechanism (see Section 2.2.3);
2. TiO_2 deposited on Au NPs with fluence of 3.5 J/cm^2, pure O_2 background pressure of 5 Pa, nominal thickness 1 µm, [Air] thermal treatment.

Au-TiO_2. This strategy was based on the ablation of a composite Au-TiO_2 target obtained by attaching on the surface of the already employed TiO_2 target few Au lamellae (as illustrated in Figure 7.2), placed near the center to obtain few subsequent laser shots only on Au during the roto-translational motion of the target. Thus, Au-TiO_2 films were deposited exploring two different gold amounts with fluence of 3.5 J/cm^2, pure O_2 background pressure of 5 Pa and 8 Pa, nominal thickness 1 µm, [Air] thermal treatment. The relative Au/TiO_2 in the deposited film (shown on the right of Figure 7.2) was calculated knowing empirically the ablation rate of the two materials and the relative target surface covering, as shown in the table on the right of Figure 7.2.

7.2 Pulsed laser deposition of gold nanoparticles

The discussion on the growth of Au NPs with PLD and their corresponding plasmonic properties is focused on the effects of pressure and number of shots at fixed d_{T-S} (5 cm). The morphological analysis was performed by SEM images of NPs grown on Si substrates, as illustrated in Figure 7.3, which shows

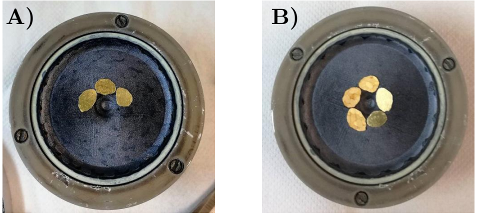

Target	% Au (area)	P (Pa)	% Au (vol.)
A)	4	5	3.2
		8	1.8
B)	6.6	5	5
		8	3.3

Figure 7.2: Left. Digital pictures of targets employed for co-depositions (Au-TiO_2): **A)** 4% and **B)** 6.6% surface covered by Au lamellae. **Right.** Corresponding expected amounts of Au in the deposited Au-TiO_2 film for all the explored conditions.

the results as a function of pressure (10, 100, 300, 500 and 1000 Pa of Ar) and of the laser pulses (50, 100 and 1000). By observing the set of SEM images presented in Figure 7.3, some considerations can be made: first, as expected, by increasing the number of shots (i.e. the deposition time), the coverage increases, leading to film growth for 1000 laser pulses; second, the morphological evolution depends on the pressure value, as the film growth is retarded at high values (i.e. above 300 Pa) and is preceded by the formation of percolated domains; third, by increasing the background gas pressure, the coverage decreases. These observations are confirmed by the average NP size values, shown per each condition in Figure 7.3), and are related to the different deposition regimes occurring for different pressure values:

1. at low pressure (10–100 Pa), ablated Au species proceed from the target to the substrate with a limited amount of collisions, thus with high kinetic energy and leading to atom-by-atom deposition; the NPs growth, as a consequence, occurs on the substrate surface upon diffusion phenomena, which results in an average NP size increase with the increasing coverage (i.e. by increasing the number of shots);
2. at high pressure (300–1000 Pa), ablated Au species strongly interact with the gas, their kinetic energy is reduced, leading to larger plume confinement and NP/cluster nucleation in the plume[131,173,238]; accordingly, already-formed clusters slowly diffuse on the substrate due to the higher interaction with the latter[131]; as a consequence, the average NP size is (almost) independent on the substrate material, i.e. it does not depend on the number of shots until coalescence occurs, promoting the film growth.

In addition, from Figure 7.3 it can also be observed that the Au NPs exhibit a rounded shape; considering that an amorphous oxide overlayer is expected on Si, this observation is consistent with the well-reported knowledge on quasi-spherical NPs growth for low metal contents and irregular shapes due to coalescence for higher values on amorphous substrates[233,242]. Actually, a further analysis with atomic force microscopy (AFM) has revealed

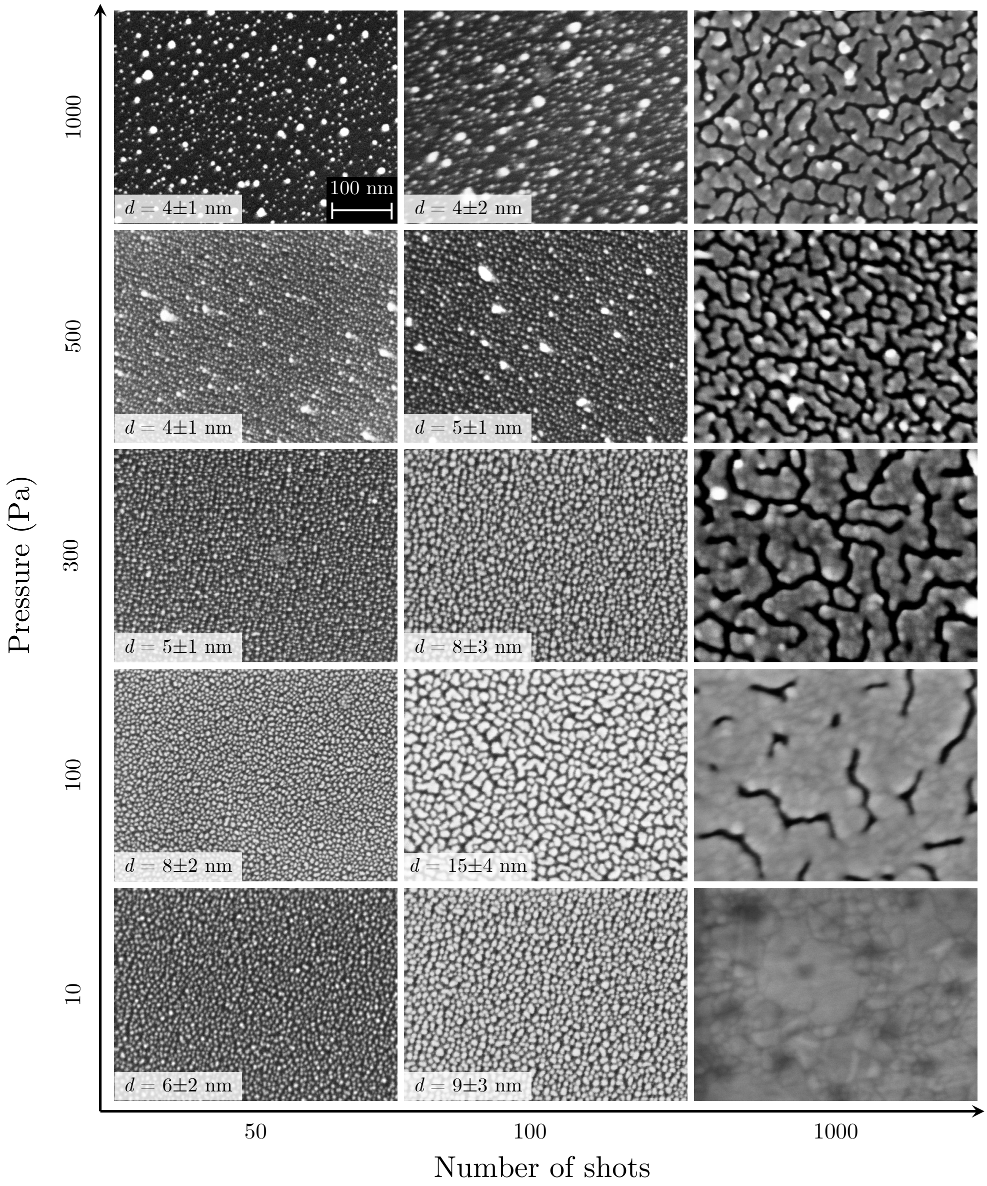

Figure 7.3: SEM images of various Au NPs/nanostructures by varying Ar background pressure and number of laser pulses (the scale bar for all the images is reported in the top-left figure). For each condition, the average area of NPs was obtained by processing the SEM images with the open-source ImageJ software, deriving an equivalent average spherical diameter, which defines the average size *d*.

a slightly "flattened" morphology (not shown as not related to my activity). Finally, the maximum NP size obtained in this set of experiments is about 15 nm, as shown by the SEM image in Figure 7.3 for the deposition at 100 Pa of Ar with 100 shots, which also shows the beginning of particle coalescence.

The different sizes of Au NPs affect their plasmonic properties, as well-known in literature[106]; accordingly, Figure 7.4 shows total transmittance (Figure 7.4A) and absorbance (Figure 7.4B) of selected Au NPs samples (i.e. deposited at 100 and 500 Pa with 50 and 100 shots), the latter evaluated as $A \simeq 1 - T$ due to the limited contribution of reflectance (around 5%). Absorbance spectra in Figure 7.4B allow a more direct evaluation of the LSPR peak position; however, it should be noted that the contribution of interband transitions (from 5d to 6sp bands[243,244]) for Au partially overlaps with the LSPR for $\lambda < 600$ nm and dominates for $\lambda < 400$ nm[106], which explains the increasing trend of absorbance at lower wavelengths. Nevertheless, the LSPR wavelength is located at about 540 nm for the NPs deposited at 500 Pa, at 567 nm for those deposited at 100 Pa with 50 shots and 622 nm for those deposited at 100 Pa with 100 shots. These values are consistent with a redshift of the LSPR wavelength for increasing average diameters (which are also reported in Figure 7.4B). Moreover, Au NPs deposited at 500 Pa with 50 and 100 shots do not exhibit any LSPR redshift, which can be reasonably related to their equal average sizes ($d = 4nm$), which in turn is related to in-plume cluster nucleation and growth phenomena occurring at high background pressures[131].

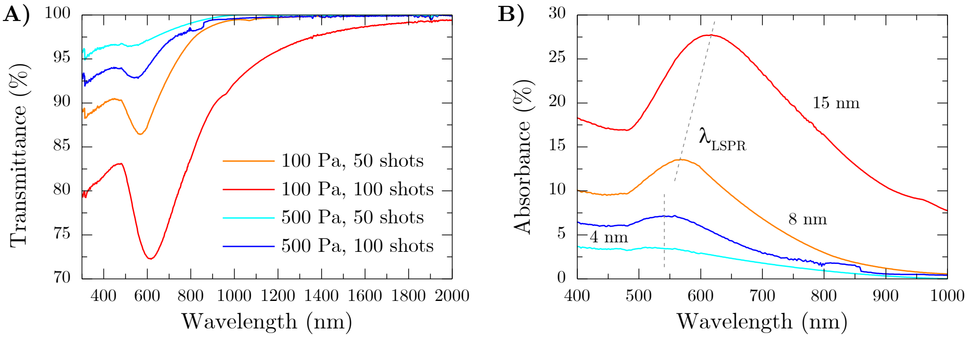

Figure 7.4: Optical analysis of Au NPs obtained in selected conditions (light blue: 100 Pa, 50 shots; blue: 100 Pa, 100 shots; orange: 500 Pa, 50 shots; red: 500 Pa, 100 shots). **A)** Transmittance curves; **B)** absorbance curves, evaluated as $A \simeq 1 - T$; the average sizes d for Au NPs are also reported.

In this discussion, it is assumed that the growth mechanism is not strongly dependent on the substrate (i.e. NPs size measured on Si is assumed comparable to that on glass, not measured). Atomic force microscopy (AFM) measurements of NPs size on glass substrate are indeed difficult due to the small length scales (less than 10 nm) and the high density of NPs, which induces tip convolution effects (AFM measurements on bigger NPs have been reported in ref. [245]). Finally, the values of λ_{LSPR} obtained in this analysis and their relation with the average size of NPs (a redshift with increasing size) are in agreement with previous studies[236,237].

The results illustrated above show that a systematic analysis of the PLD conditions for the growth of Au NPs allowed a satisfactory control on their plasmonic resonance, at least in the 500–700 nm range. As explained in Section 7.1, three strategies for the integration of these NPs in TiO_2 hierarchical films were explored, two of them consisting in subsequent deposition of the two materials. Thus, for the Au/TiO_2 film (i.e. Au NPs on top of the TiO_2 film), the growth of NPs was performed at 1000 Pa (i.e. top row of Figure 7.3) with the aim of exploiting the clustering mechanism in the ablation plume and avoiding the dependence on substrate (in this case the porous surface of hierarchical TiO_2); 150 laser pulses were employed in order to discern the NPs with SEM images but avoid a complete covering of the TiO_2 surface as well. Accordingly, Figure 7.5A shows the morphological results for these growth conditions on Si substrate (the average diameter is 5 nm), resulting in the absorption spectrum shown in Figure 7.5C (blue line). This average size was desired as more favorable for hot electron injection effects[246] (see Section 2.2.3).

On the other hand, for the TiO_2/Au film (i.e. Au NPs on substrate, at the bottom of the TiO_2 hierarchical film), larger particles (i.e. $\simeq 25$ nm) were desired in order to induce effects such as PRET or enhanced light scattering (Section 2.2.3), but the maximum size obtained by PLD was about 15 nm (see Figure 7.3); consequently, the increase of NP size was pursued by exploiting the already mentioned *dewetting* effect, which consists in the formation of NPs by annealing a nm-thick film. This strategy is typically employed starting from evaporated films[247–250] and the obtainment of nanoparticles is attributed to the difference in thermal expansion coefficient between the gold film and substrate[248]. In this work, the "standard" [Air] annealing was employed for Au films with percolating domains obtained by deposition at 1000 Pa with 1000 shots (SEM image in the top-right corner of Figure 7.3) and the result is shown in Figure 7.5B: NPs with an average size of 23 nm were obtained, with irregular shapes related to the interface chemistry between Au and the SiO_2 layer on Si substrate[250]. Accordingly, their optical spectrum is shown in Figure 7.5C, with a $\lambda_{LSPR} \simeq 550$ nm, which is comparable to the value for smaller NPs, as reported above. This blueshift can be related to the change in the inter-particle distance[248,249] or to the NP shape and aspect ratio[247].

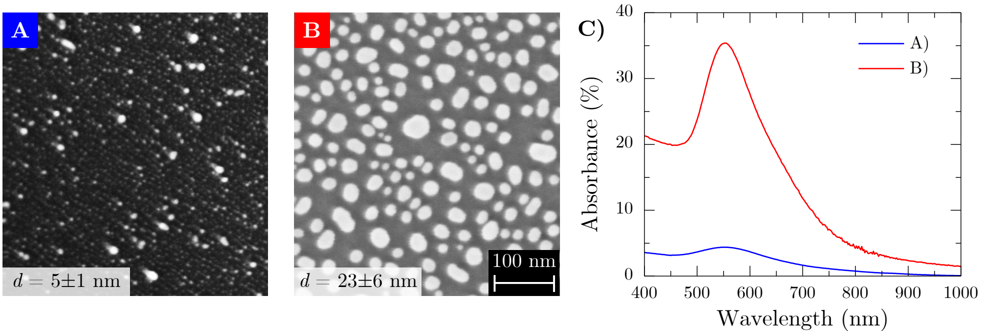

Figure 7.5: Morphological (SEM images, scale bar in **B**) and optical analysis of Au NPs employed for integration with TiO_2. **A)** Au NPs deposited at 1000 Pa, 100 shots. **B)** Au NPs obtained by deposition at 1000 Pa, 1000 shots and [Air] annealing. **C)** Absorbance spectra of Au NPs in A) (blue) and B) (red).

7.3 Au/TiO_2 films

The details of the synthesis process of Au/TiO_2 films are reported in Section 7.1.2; in this section, the morphological and optical analysis of an Au/TiO_2 film, with TiO_2 deposited at 8 Pa, is discussed (the Au/TiO_2 film with TiO_2 deposited at 5 Pa is not considered for the sake of brevity). Raman spectroscopy results are not reported (neither in Sections 7.4 and 7.5) due to the absence of relevant effects of thermal treatments beyond the crystallization in anatase phase (as observed for TiO_2 films without the presence of Au).

Figure 7.6 presents the overall morphological and optical results for the Au/TiO_2 film. Figure 7.6A shows a top-view SEM image of the film, in which the Au NPs are clearly distinguishable, characterized by an average size of about 5 nm, confirming the hypothesis of independence on the substrate for these PLD conditions (i.e. 1000 Pa of Ar). SEM cross-sectional images are shown in Figure 7.6B and 7.6C; the former illustrates the overall film morphology (with a thickness of 1 µm), while the latter reveals the penetration of Au NPs up to about 200 nm below the film surface, which is allowed by the relatively high porosity of TiO_2 deposited at 8 Pa. Figure 7.6D, on the other hand, shows the transmittance spectrum of the Au/TiO_2 film compared to the spectra of the Au NPs on glass substrate and of TiO_2 without nanoparticles (the films were [Air]-annealed). The effect of the NPs on the TiO_2 film is that of a limited transmittance decrease in the range 400-700 nm, without evident fingerprint of the LSPR, probably due to the low intensity of the plasmonic peak of the NPs alone. This outcome is confirmed by absorbance spectra in Figure 7.6E; moreover, no change in the absorption onset is evidenced, as expected.

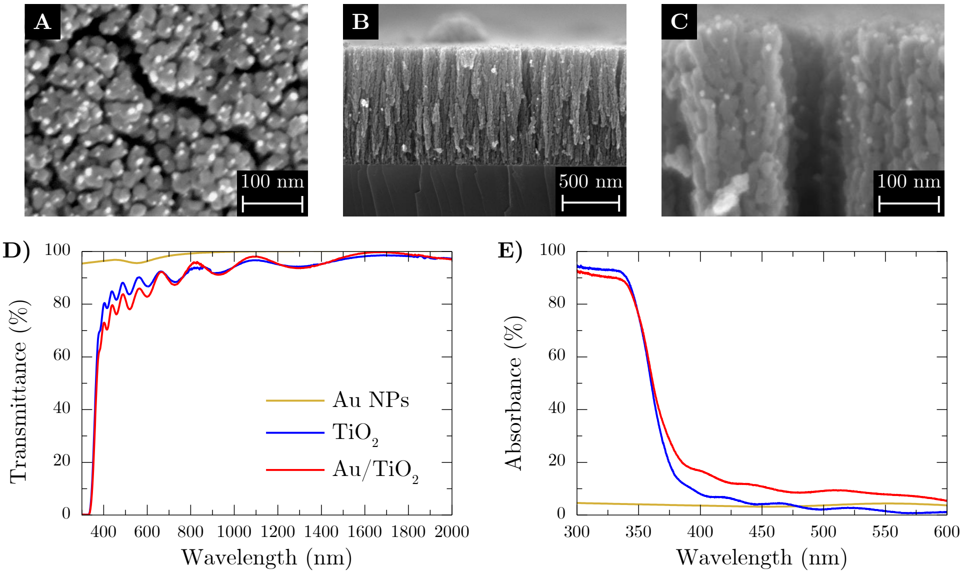

Figure 7.6: Morphological and optical analysis of Au/TiO_2 film. **A–C)** SEM images. **D)** Transmittance and **E)** absorbance curves of Au/TiO_2 with bare Au NPs and TiO_2 w/o Au NPs as references.

7.4 TiO_2/Au films

The TiO_2/Au film was based on the “reverse” approach than the Au/TiO_2 film; the synthesis conditions for these films have already been reported in Section 7.1.2; briefly, a percolated Au film was [Air]-annealed, obtaining NPs as shown in Figure 7.5B, on which a TiO_2 film was deposited at 5 Pa of pure O_2, reaching a thickness of 1 µm.

The morphological and optical analysis was performed for the as-deposited and [Air]-annealed TiO_2/Au films, as illustrated in Figure 7.7. The as-deposited film exhibits the same morphology as a “regular” 5 Pa-deposited TiO_2 film (compare Figure 7.7A to Figures 4.1 and 5.1), but observing at higher magnification the film bottom (Figure 7.7B) the Au NPs are evident, which do not hinder the hierarchical growth of the TiO_2 nanostructured film, but, instead, they seem to act as nucleation centers (this hypothesis was confirmed by further investigations[251]). [Air] annealing promotes the formation of nanocrystalline domains with a high degree of connectivity, as shown in Figure 7.7C; moreover, a SEM image recorded with back-scattered electrons is shown in Figure 7.7D, which allows to easily discern the layer formed by Au NPs, having a thickness of approximately 25-30 nm (as indicated by the yellow bar).

The optical analysis is presented in Figure 7.7E with transmittance curves and Figure 7.7F with absorbance profiles. In both of them, the spectra of the as-deposited and [Air]-annealed TiO_2/Au films are presented, together with those of an [Air]-annealed TiO_2 film deposited at 5 Pa on bare glass substrate and of uncovered Au NPs (the same as in Figure 7.5C). Digital pictures of all these samples are also reported, showing that by unaided eye a clear color difference is evident between all of them (on the contrary, the Au/TiO_2 film was not discernible from a TiO_2 film). This qualitative color difference is confirmed by the optical measurements. The transmittance spectrum of the TiO_2/Au film (green line in Figure 7.7E) shows a clear feature of the LSPR resonance, redshifted with respect to that of the Au NPs alone (about 550 nm), even though a precise peak position is not easily found due to the interference fringes of TiO_2. This effect is consistent with the different surrounding medium around the Au NPs (see Section 2.2.3), as $\lambda_{LSPR} \propto \sqrt{1+2\epsilon_d}$ (where ϵ_d is the medium relative permittivity) according to the simple Frölich condition[106]. On the other hand, the interference fringes of TiO_2 increase with respect to the reference TiO_2 film, which could be ascribed to stronger interference effects in the film promoted by the Au NPs layer (however, a scattering effect is expected for bigger NPs[108]). In addition, the [Air]-annealed film exhibits even stronger absorption in the LSPR region as well as more intense interference fringes. Absorbance spectra in Figure 7.7F, calculated from transmittance and reflectance measurements, confirm these findings, suggesting that the presence of Au NPs at the bottom of the TiO_2 film increases its light absorption in the visible range, especially in the spectral region of the LSPR, without affecting its bandgap value of 3.2 eV (not shown) for both the as-deposited and [Air]-annealed films.

7.5 Au-TiO_2 films: co-depositions

The last, but the most innovative, integration strategy consisted in the co-deposition of Au and TiO_2 in the same experimental process, with the details reported in Section 7.1.2. Among the investigated parameters, for the reasons discussed at the beginning of this chapter, only one example will be considered in this section, i.e. Au-TiO_2 film deposited at 8 Pa with 1.8% vol. Au (i.e. using the target with 3 Au lamellae shown in Figure 7.1), in particular examining the effect of [Air] annealing.

The overall results for this film are reported in Figure 7.8. The morphological analysis is presented with SEM images in Figure 7.8A–7.8E; from the cross-sectional (Figure 7.8A and 7.8D) and top-view (Figure 7.8B) points of view, the as-deposited film exhibits a comparable hierarchical organization to an unmodified TiO_2 film deposited at the same pressure (8 Pa); indeed, the presence of Au NPs is not evident, which could be ascribed to a dispersion of gold within the overall thickness of TiO_2. However, upon [Air] annealing, Au NPs become clearly visible in cross-sectional SEM

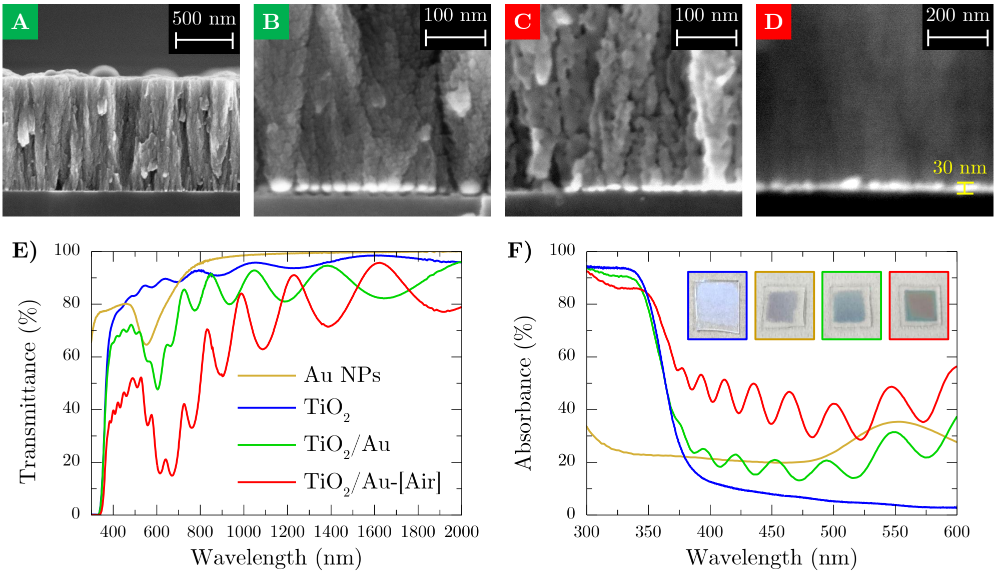

Figure 7.7: Morphological and optical analysis of TiO$_2$/Au film. **A, B)** SEM images of as-deposited TiO$_2$/Au film. **C, D)** SEM images of TiO$_2$/Au-[Air] (**D** with back-scattered electrons). **E)** Transmittance and **F)** absorbance curves of as-deposited and [Air]-annealed TiO$_2$/Au with bare Au NPs and TiO$_2$ w/o Au NPs as references (digital pictures of the samples are also shown as insets).

images (Figure 7.8E), while from the top-view only few small NPs are hardly detectable (Figure 7.8C). The NPs have diameters in the range 2–25 nm (Figure 7.8E).

These morphological observations can be related to transmittance spectra of Au-TiO$_2$ films shown in Figure 7.8F, which reports also the spectrum of TiO$_2$ (deposited also at 8 Pa) as reference. It can be observed that the fingerprint of the plasmon resonance in the spectrum of the as-deposited film is not clear, while it becomes much more evident after [Air] annealing; an increase of transmittance in the IR region occurs as well after thermal treatment. Thus, by considering both morphological and optical results, it can be suggested that Au NPs are extremely small in the as-deposited film, if not completely dispersed as few atomic aggregates, and that they grow and coalesce (such as via Ostwald ripening) during thermal treatment, giving rise to a well-defined LSPR. This hypothesis is in agreement with previous studies concerning the morphological and optical evolution of Au-TiO$_2$ composite films prepared with magnetron sputtering[252–256]; also, a redshift of the LSPR is expected passing from amorphous to anatase TiO$_2$ due to the different dielectric constant[253]. Accordingly, the color appereance of the films change with thermal treatment, as shown by the inset photographs in Figure 7.8F: the Au-TiO$_2$-[Air] exhibits a black color, darker than the as-deposited film (grey-green), due to the increased absorption in the visible range (corresponding to the LSPR peak).

Figure 7.8F, in addition, illustrates also the haze factor curves for TiO_2 and Au-TiO_2 (as-deposited and annealed) films; these show the reduction in light scattering ability for the Au-TiO_2 film with respect to pure TiO_2, probably related to the absorption of dispersed Au particles/atoms; however, the haze factor slightly increases for the [Air]-annealed film, which also occurs for a pure [Air]-annealed TiO_2 with respect to the as-deposited one.

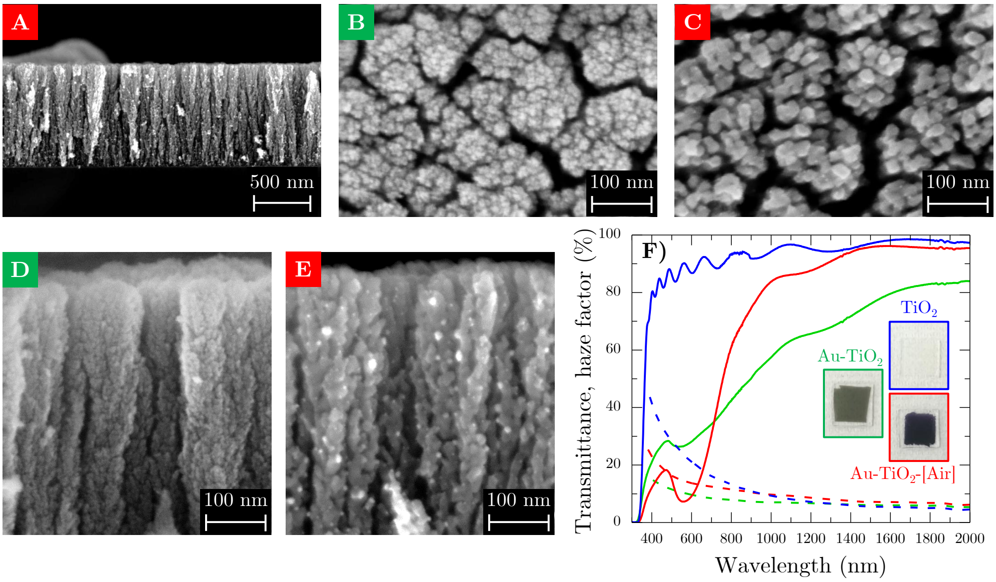

Figure 7.8: Morphological and optical analysis of Au-TiO_2 film deposited at 8 Pa (blue: TiO_2, as reference; green: as-deposited; red: [Air] annealed; the color coding for all the figures). **A–E)** SEM images of the as-deposited (**B**, top-view and **D**, cross-sectional) and the [Air]-annealed (**A** and **E**, cross-sectional and **C**, top-view). **F)** Transmittance spectra (solid lines) and haze factor curves (dashed lines).

Finally, it should be noted that the bandgap of the Au-TiO_2-[Air] film was not evaluated due to the lack of a sharp transition from the high-absorbance region to the transparency one, thus preventing an accurate linear fit with the Tauc plot method[179].

In conclusion, the co-deposition approach resulted in an effective intermixing between Au NPs and TiO_2 hierarchical nanostructures, with evident effects on the optical properties of the composite film. Even though other strategies to obtain Au NPs throughout the whole TiO_2 film have been reported (such as magnetron sputtering[252–256] or annealing an Au film on top of TiO_2 nanotubes to promote dewetting and diffusion effects[257]), the co-deposition fully exploits the versatility of the PLD process, as an intermixed Au-TiO_2 film can be obtained directly in the synthesis step with tuneable relative amount between the two materials and morphology.

7.6 Photoelectrochemical measurements

This section illustrates the first tests in a PEC cell (with the same setup described in Section 3.4) of three TiO_2 hierarchical films integrated with Au NPs, namely:

- a Au/TiO_2 film with TiO_2 deposited at 8 Pa (the same as in Section 7.3);
- a TiO_2/Au film with TiO_2 deposited at 5 Pa (the same as in Section 7.4);
- a Au-TiO_2 film deposited at 8 Pa with 3.3% vol. Au (i.e. with a higher Au content than the film presented in Section 7.5).

In the following, it is implicitly understood that all these films were [Air]-annealed before testing (see the detailed preparation procedures reported in Section 7.1.2), in order to obtain an anatase crystalline phase. The photoelectrochemical results, accordingly, are shown in Figure 7.9, which is divided into two panels according to the deposition background O_2 pressure for the TiO_2 layer. Indeed, Figure 7.9A shows the results for the films deposited at 5 Pa, i.e. the TiO_2/Au and the reference TiO_2 photoanodes. The latter exhibits comparable results to the O_2-TiO_2-[Air] films in Chapters 4 and 5 (see Figures 4.11 and 5.7), with a photocurrent onset at about −0.75 V vs. SCE and a saturated photocurrent value of 50 $\mu A\,cm^{-2}$. On the other hand, the TiO_2/Au film exhibits a different behavior, as the photocurrent onset is anodically shifted to about −0.44 V vs. SCE and the saturated photocurrent value increases up to 60 $\mu A\,cm^{-2}$. On the other hand, Figure 7.9B shows the photocurrents recorded for photoanodes in which TiO_2 was deposited at 8 Pa, i.e. the Au/TiO_2, the Au-TiO_2 and a reference TiO_2 films. The latter exhibits the same photocurrent onset but a lower saturated value (25 $\mu A\,cm^{-2}$) than the reference film deposited at 5 Pa, in agreement with previous results (Figure 5.12). On the other hand, the Au/TiO_2 shows both lower photocurrent onset (−0.6 V vs. SCE) and saturated value (20 $\mu A\,cm^{-2}$) than the reference film; moreover, the Au-TiO_2 film exhibits even lower photoresponse, with an onset at −0.17 V vs. SCE and a saturated value at almost 9 $\mu A\,cm^{-2}$.

From Figure 7.9, therefore, it appears that the integration between Au and TiO_2 does not lead to satisfactory results so far.

A possible mechanism leading to poorer photoelectrochemical performance can be the formation of a Schottky barrier between Au and TiO_2, as predicted by the Schottky-Mott rule[258,259]:

$$\Phi_B^n = \phi_{Au} - \chi_{TiO_2} = 5.1\text{ eV} - 4.0\text{ eV} = 1.1\text{ eV} \tag{7.1}$$

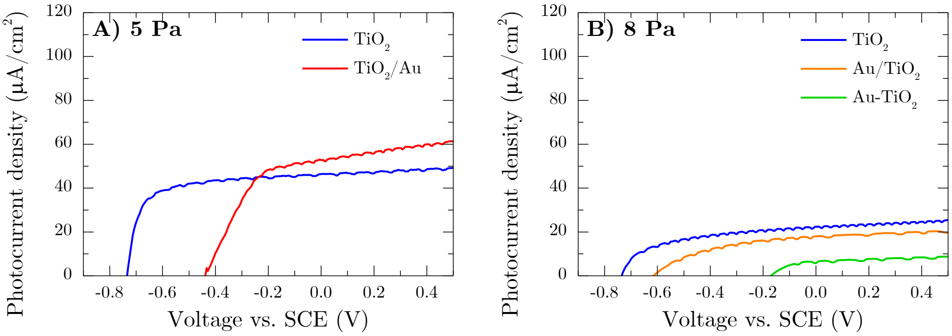

Figure 7.9: Preliminary photoelectrochemical results of TiO_2 photoanodes integrated with Au NPs. **A)** Depositions performed at 5 Pa: TiO_2 (blue) and TiO_2/Au (red). **B)** Depositions performed at 8 Pa: TiO_2 (blue), Au/TiO_2 (orange) and Au-TiO_2 (Au 3% vol., green).

where ϕ_{Au} is the work function of gold and χ_{TiO_2} is the electron affinity of TiO_2 (the work function of TiO_2 instead is $\phi_{TiO_2} = 4.8$ eV). Even though the formation of a Schottky barrier is a quite complex subject[260], a potential barrier of 1.1 eV predicted by this simple argument may play a role; indeed, Zhao *et al.*[261] suggested that a decrease in photocurrent for a TiO_2 electrode modified with Au NPs could be related to a reduction in mobility of electrons and holes due to the presence of a Schottky barrier between Au and TiO_2. This barrier may be useful at the surface of the semiconductor as it favors the separation between photoexcited electrons and holes (acting in the same way as the built-in electric field in the space charge region at the semiconductor/electrolyte interface, see Section 1.3.1); on the other hand, a Schottky barrier due to Au NPs at the bottom of TiO_2, thus in between the semiconductor and the metal back-contact, may prevent electrons from the conduction band of TiO_2 to reach the substrate, which may explain (at least qualitatively) the increase of photocurrent onset for the TiO_2/Au film (which, besides, do not exhibit a drop in the photocurrent value). This is also supported by the fact that NPs larger than 10 nm (as for the TiO_2/Au film) exhibit the same Schottky barrier as in the macroscopic case[262]. A lower (cathodic) onset potential, instead, would suggest a catalytic effect by Au NPs towards the water oxidation reaction[104,262].

Other mechanisms playing a role in all the three cases (Au/TiO_2, TiO_2/Au and Au-TiO_2) may also be an increased recombination of electron/hole pairs at the surface of metal NPs, reducing the photocurrent values[261,263], or parasitic surface reactions, such as O_2 reduction by photogenerated electrons in the conduction band of TiO_2[263], which could also lead to an anodic shift in the open circuit potential[263]. Considering the Au-TiO_2 film, in particular, this effect could be related to an excessive amount of gold in the integrated material, so that recombination pathways would overcome the positive effects related to plasmonic mechanisms. In that case, a straightforward method to lower the Au content in the material would be to decrease the fraction of target area covered by Au lamellae.

Finally, it should be pointed out that in the photoelectrochemical tests presented in Figure 7.9 no clear effects of the LSPR of Au NPs could be discerned, as they were performed under AM 1.5G illumination, which on the one hand is a useful standard illumination condition, but, on the other hand, does not allow to ascertain visible-light activity induced by the plasmonic resonance; thus, a precise explanation of the photocurrents reported in Figure 7.9, both taking into account "positive" plasmonic effects and "negative" side effects (as those mentioned above) is not possible with further data, such as IPCE measurements.

7.7 Summary

This chapter presented the first development of three integration strategies between gold nanoparticles, exhibiting the localized surface plasmon resonance, and TiO_2 hierarchically organized films, employing pulsed laser deposition as a synthesis technique for both materials.

First, an appropriate control of gold nanoparticles size was mandatory, as it is strictly related to their plasmonic properties, which was achieved by a systematic campaign of PLD experiments, in which some of the possible process parameters (such as the background gas pressure and the number of laser pulses) were varied and the resulting morphological and optical properties of gold nanoparticles were assessed. Thus, two different conditions were chosen for nanoparticles to be deposited on top of TiO_2 (i.e. Au/TiO_2) or at the bottom, thus performing the deposition of TiO_2 subsequently (i.e. TiO_2/Au).

Second, the morphological and optical properties of thee kinds of TiO_2 films with integrated Au nanoparticles were investigated, i.e. the two mentioned above and the co-deposition, Au-TiO_2, which was obtained by ablating a composite target made of a standard TiO_2 target covered with Au lamellae, allowing the simultaneous growth of both materials and a good intermixing between them. Indeed, this third strategies led to the most interesting results and can be more easily tuned by playing with the PLD conditions.

The preliminary tests in photoelectrochemical cells of these materials generally showed a performance decrease with respect to reference TiO_2 films. Therefore, these results suggest that a finer tuning of the integrated films should be obtained, for instance by varying the relative Au/TiO_2 amount. Further experiments, indeed, have been recently performed following this approach, obtaining two sets of co-deposited Au-TiO_2 films at 5 and 8 Pa with decreasing Au/TiO_2 relative content. On the other hand, an appropriate evaluation of the plasmonic mechanism activated by visible light illumination should be assessed (see discussion in Section 2.2.3). Moreover, the development of the integrated Au/TiO_2 nanostructured films should be not limited to water splitting applications (which was the main purpose of this thesis work), but can be easily extended to other ones, such as photocatalytic degradation of organic compounds or sensors.

8

Conclusions and perspectives

Photoelectrochemical (PEC) water splitting is a promising method for the renewable production of hydrogen gas (H_2), as it only involves the use of an electrochemical cell and it requires water and solar energy to obtain this fuel. In this method, a semiconductor material absorbs solar energy and delivers it to water, promoting its decomposition into H_2 and O_2: $2h\nu + H_2O\ (l) \rightarrow 1/2\ O_2\ (g) + H_2\ (g)$; the threshold energy for this reaction is 1.23 eV from the thermodynamic point of view, but this value is raised to about 2 eV considering various loss factors; in turn, this corresponds to the minimum bandgap energy (E_g) of the semiconductor. Upon photon absorption, electrons in the conduction band (CB) and holes in the valence band (VB) are generated; the former are transported to the metal contact (cathode), leading to the evolution of H_2, while the latter oxidize water at the photoanode surface (other architectures, such as metal anode/photocathode and photoanode/photocathode can be employed as well).

Titanium dioxide (TiO_2) was the material employed as photoanode for the first demonstration of PEC water splitting and its bandgap is 3.2 eV (in the anatase phase), which limits its light absorption only to the UV region, leading to unsatisfactory solar-to-hydrogen efficiency (max. 1%). Also, TiO_2 shows a low quantum efficiency for the water splitting process. Nevertheless, a material which meets all the requirements for this complex reaction has not been found yet, thus TiO_2 is still being investigated at the research scale thanks to its excellent chemical stability and relatively low cost. In order to address its limitations, several strategies have been proposed, and are still being studied, in literature. Some of them aim to increase of TiO_2 light absorption. For instance, in 2011 the first reports on the so-called *black titania* showed an evident darkening of TiO_2 after a hydrogenation process by means of thermal treatments in H_2 atmosphere at high temperature leading to remarkable enhancements in photoactivity. These findings triggered a great interest in the scientific community and several other studies have addressed the hydrogenation/reduction of TiO_2; however, results are strongly dependent on the starting material and the experimental procedure, thus a complete understanding on black titania, despite some theoretical studies, is still lacking. For instance, it has been shown that the dark color by itself does not correspond to actual visible-light activity. On the other hand, TiO_2 has been combined with noble-metal nanoparticles exhibiting the *localized surface plasmon resonance* (LSPR), which roughly consists in an absorption peak in the visible range, which can be exploited to extend the absorption of wide-bandgap semiconductors. Finally, in order to improve TiO_2 charge transport and reduce recombinations, one-dimensional (1D) or quasi-1D nanostructures have been proposed, such as nanowires, nanotubes and hierarchical nanostructures. The latter have been obtained for instance with Pulsed Laser Deposition (PLD), a physical vapor deposition technique, and employed in energy conversion applications thanks to their high surface area, effective light scattering and preferential charge transport along the growth direction. Whatever the strategy choice for improving the TiO_2 properties, a suitable control on its defect chemistry should be taken into account; indeed, this material is typically an *n*-type semiconductor thanks to oxygen vacancies/Ti^{3+} ions, but thermal treatments can increase their concentration or even induce additional defects depending on the specific conditions, which is of great relevance for experiments aimed at obtaining black titania.

Taking into account these strategies proposed in literature, this thesis work consisted in a material science study on hydrogenated/reduced TiO_2 hierarchically structured films prepared by PLD and tested in PEC water splitting experiments; in particular, it was developed by means of experimental investigation focused on the introduction of defects by deposition or thermal treatment in (partially) reducing conditions. More specifically, first the controlled introduction of defects and their influence on the morphological, structural, optical and photoelectrochemical properties was studied; then, the synthesis conditions and their relation to the material photoactivity were studied in detail to find an optimization of the experimental strategy; a further direction of studying hydrogenated/reduced TiO_2 hierarchical materials consisted in investigating with dedicated experiments these defects. On the other hand, an additional research strategy, i.e. the integration of TiO_2 with Au nanoparticles with plasmonic properties, was also developed. As characterization techniques, scanning electron microscopy (SEM), Raman spectroscopy, photoluminescence (PL) spectroscopy, X-ray diffraction (XRD), UV-visible-IR spectroscopy were employed and TiO_2 films were tested as photoanodes in a three-electrode PEC cell at the Laboratory of Catalysis an Catalytic Processes (LCCP) of Department of Energy, Politecnico di Milano.

First, the controlled introduction of defects was explored as follows: on the one hand, ablating a TiO_2 target with 5 Pa of background gas with pure O_2 (corresponding to previous investigations) and in atmospheres with reduced oxygen content (Ar/O_2 50%-50% mixture) or even without (Ar/H_2

97%-3% mixture); on the other hand, annealing the as-deposited films at 500°C in air (again as reference) and in Ar/H_2 mixture at atmospheric pressure in substitution to or in combination with the former; these thermal treatments were labeled as [Air], [Ar/H_2] and [Air+Ar/H_2]. TiO_2 films deposited in O_2 or in Ar/O_2 exhibited comparable morphological, structural and optical properties; in particular, thermal treatments in the presence of hydrogen did not affect crystallization in anatase and induced a slight absorption increase in the visible range with respect to the [Air]-annealed film; in addition, PL spectra for these films excited with 2.41 eV energy showed a broad emission around 1.8 eV, on the contrary of the [Air]-annealed film. These observations suggested that thermal treatments induce a limited amount of defect states in the bandgap of TiO_2 (such as oxygen vacancies). Films deposited in Ar/H_2 mixture, on the other hand, showed a more compact morphology, ascribed to the different interaction mechanisms of the ablated species with the background gas during deposition. Photocurrent measurements showed that both annealing treatments and synthesis conditions affected the material photoactivity (a sort of “memory effect”): a shortage of oxygen (but not absence) in the deposition step with the [Air+Ar/H_2] annealing led to an evident photocurrent increase with respect to all the other investigated conditions, which was ascribed to defects introduced by the synthesis conditions as well as by thermal treatments leading to better conduction or reduced recombinations.

A further experimental campaign was undertaken starting from these results, with the aim of better understanding the effect of synthesis conditions and developing the approach discussed above. This was addressed by finely tuning the oxygen content in the deposition step, either in the gas phase, employing Ar/O_2 mixtures from pure Ar to pure O_2, or in the target, comparing the results for a Ti target instead of TiO_2; all the films were annealed with [Air] and [Air+Ar/H_2] thermal treatments. Accordingly, clear trends in photoelectrochemical results for all these films were found, showing two optimized deposition background atmosphere compositions for the [Air+Ar/H_2]-annealed photoanodes, one starting from TiO_2 target (Ar/O_2 50%-50%) and one from Ti target (Ar/O_2 25%-75%); these results were interpreted with the same arguments as above. In addition, other investigations related to the control of photoelectrochemical properties were investigated, such as the effect of a higher deposition pressure (8 Pa) and the effect of thermal treatments in other reducing conditions (in vacuum at 10^{-4} Pa or in pure Ar atmosphere instead of Ar/H_2) or at higher temperature (650°C instead of 500°C).

With the aim of gaining a better understanding on the defects introduced by reducing thermal treatments, dedicated experiments on thin TiO_2 films annealed with [Air], [Air+Ar/H_2] and [Air+Vac] (air annealing followed by vacuum annealing) were performed by means of photoluminescence (PL) studies employing Raman spectrometers with four different excitation laser lines: UV (325 nm or 3.82 eV), blue (457 nm or 2.71 eV), green (514.5 nm or 2.41 eV) and red (633 nm or 1.96 eV). This study was further motivated by the lack of an univocal interpretation of PL properties of anatase nanomaterials with UV excitation; fewer studies, moreover, have been dedicated to hydrogenated TiO_2 or to the analysis of PL emission with several excitation energies, such as in this case. UV (above-bandgap) excitation of the three aforementioned films resulted in a broad emission peaking in the orange-red region of the electromagnetic spectrum, while below-bandgap excitation produced analogous emissions only for [Air+Ar/H_2]- and [Air+Vac]-annealed films, while no emission was found for the [Air]-annealed film. These outcomes suggested that defect concentration increased after reducing thermal treatments, as hypothesized to explain the results of water splitting tests discussed above. Oxygen vacancies have been frequently proposed in literature to explain PL emissions similar to these results, but additional experiments are needed to better determine the nature of these defects. Some of the foreseen experiments in this regard include PL studies with liquid contacting media (such as ethanol or water) able to quench radiative decay pathways peculiar of certain species of defects, the study of pure H_2-annealed TiO_2 films (in contrast to Ar/H_2-annealed ones), in order to gain more information of the specific role of the thermal treatment atmosphere, and the exploitation of other characterization techniques, such as Fourier transform infrared spectroscopy (FTIR), to probe surface bonds such as Ti–OH or Ti–H related to the hydrogenation treatment.

Apart from the open challenge related to a deeper understanding of the defect states in hydrogenated/reduced TiO_2 hierarchical nanostructures, this research approach showed the potentiality and versatility of PLD in realizing photoanode materials with tuneable properties. This suggests that further studies concerning different materials with a lower bandgap than TiO_2, such as α-Fe_2O_3, or even ternary oxides, such as $CuFeO_2$ or TaON, could be prepared with this technique. Alternatively, the TiO_2 hierarchical materials considered for PEC water splitting applications could be utilized as photoanodes in solid-state dye-sensitized solar cells or in lithium-ion batteries.

An additional research pathway developed in this Ph.D. work, in collaboration with Master thesis students, consisted in the integration of TiO_2 with plasmonic Au nanoparticles, in order to exploit their localized surface plasmon resonance (LSPR) to harvest photons in the visible region of the electromagnetic spectrum (hot electron injection mechanism) or to increase the generation of electron/hole pairs (a sort of "antenna" mechanism). First, an appropriate control of Au nanoparticles LSPR, closely related to their size, was addressed by a systematic campaign of PLD experiments, which illustrated the possibility of controlling the Au nanoparticles size by controlling (for instance) the background gas pressure, the number of laser pulses or post-deposition annealing treatments. Second, three different integration strategies were explored: Au nanoparticles on top of TiO_2 (Au/TiO_2), the reverse (TiO_2/Au) and Au nanoparticles intermixed with TiO_2 (Au-TiO_2) by means of a simultaneous deposition of both materials (co-deposition), achieved by means of a composite target. The TiO_2/Au and Au-TiO_2 films, in particular, showed a clear increase of optical absorption in the 500–700 nm region due to the Au LSPR; the co-deposition approach resulted in the most interesting strategy thanks to a good intermixing between the two materials ensured by their simultaneous growth. As the preliminary PEC tests of these films did not evidence a positive effect of the Au nanoparticles on the photocurrent response of TiO_2 photoanodes, a fine tuning of the composite materials should be obtained and, in particular, a systematic control of the relative Au/TiO_2 content is currently being addressed by means of other co-depositions experiments.

The achievement of a satisfactory control on the size and plasmonic properties of Au nanoparticles (or, more generally, nanostructured surfaces) and the possibility of obtaining Au-TiO_2 co-depositions has already triggered their study in further applications thanks to external collaborations, based on their integration with other materials: for instance, Au nanoparticles deposited on *p*-type Si photocathodes for CO_2 reduction (in collaboration with S. Berardi, University of Ferrara) and co-depositions deposited on micrometric SiO_2/TiO_2 core/shell spheres for the degradation of organic compounds (in collaboration with I. Alessandri, University of Brescia). These projects are being developed as a team work, involving Master and Ph.D. students as well as post-doc researchers, under the supervision of Prof. A. Li Bassi. On the other hand, the well-known versatility of PLD as a synthesis technique allows to obtain plasmonic materials in various nanostructured forms: for instance, porous Au nanostructures, characterized by a broadband solar absorption in the visible region, have been considered for surface-enhanced Raman scattering (SERS) or CO_2 reduction applications and their realization with PLD has already been successfully tested in preliminary experiments. Finally, alternative plasmonic materials beyond noble metals, such as titanium nitride (TiN), could be realized by properly tuning PLD deposition conditions and tested in energy-related experiments thanks to their advantages, such as high temperature durability, lower cost and mechanical hardness.

List of Figures

List of Tables

Bibliography

(1) Hosseini, S. E.; Wahid, M. A. *Renew. Sust. Energ. Rev.* **2016**, *57*, 850–866.

(2) Lewis, N. S.; Crabtree, G. *Basic research needs for solar energy utilization*, workshop on solar energy utilization, April 18-21, 2005, Washington, DC.

(3) *Key World Energy Statistics 2017*, International Energy Agency, 2017.

(4) Walter, M. G.; Warren, E. L.; McKone, J. R.; Boettcher, S. W.; Mi, Q.; Santori, E. A.; Lewis, N. S. *Chem. Rev.* **2010**, *110*, 6446–6473.

(5) Fujishima, A.; Honda, K. *Nature* **1972**, *238*, 37–38.

(6) Ohtani, B. *Electrochemistry* **2014**, *82*, 414–425.

(7) Bak, T; Nowotny, J; Rekas, M; Sorrell, C. C *Int. J. Hydrogen Energ.* **2002**, *27*, 991–1022.

(8) Kittel, C., *Introduction to Solid State Physics*, 8th ed.; Wiley: 2004.

(9) Trasatti, S. *Pure Appl. Chem.* **1986**, *58*, 955–966.

(10) Nowotny, J.; Sorrell, C. C.; Sheppard, L. R.; Bak, T *Int. J. Hydrogen Energ.* **2005**, *30*, 521–544.

(11) Weber, M. F.; Dignam, M. J. *Int. J. Hydrogen Energ.* **1986**, *11*, 225–232.

(12) Bolton, J. R.; Strickler, S. J.; Connolly, J. S. *Nature* **1985**, *316*, 495–500.

(13) Vayssieres, L., *On Solar Hydrogen and Nanotechnology*; John Wiley & Sons: Singapore, 2010.

(14) Van de Krol, R.; Grätzel, M., *Photoelectrochemical Hydrogen Production*; Electronic Materials: Science & Technology, Vol. 102; Springer: 2012.

(15) Gerischer, H. *Electrochim. Acta* **1990**, *35*, 1677–1699.

(16) Kumar, A.; Santangelo, P. G.; Lewis, N. S. *J. Phys. Chem.* **1992**, *96*, 834–842.

(17) Salvador, P. *J. Phys. Chem. B* **2001**, *105*, 6128–6141.

(18) Bisquert, J.; Cendula, P.; Bertoluzzi, L.; Gimenez, S. *J. Phys. Chem. Lett.* **2014**, *5*, 205–207.

(19) Cendula, P.; Tilley, S. D.; Gimenez, S.; Bisquert, J.; Schmid, M.; Grätzel, M.; Schumacher, J. O. *J. Phys. Chem. C* **2014**, *118*, 29599–29607.

(20) Nozik, A. J.; Memming, R. *J. Phys. Chem.* **1996**, *100*, 13061–13078.

(21) Bard, A. J.; Bocarsly, A. B.; Fan, F. R. F.; Walton, E. G.; Wrighton, M. S. *J. Am. Chem. Soc.* **1980**, *102*, 3671–3677.

(22) Lewis, N. S. *Inorg. Chem.* **2005**, *44*, 6900–6911.

(23) Nelson, J., *The Physics of Solar Cells*; Series on Properties of Semiconductor Materials, Vol. 2; Imperial College Press: 2003.

(24) Sivula, K. *J. Phys. Chem. Lett.* **2013**, *4*, 1624–1633.

(25) Liu, B.; Zhao, X.; Terashima, C.; Fujishima, A.; Nakata, K. *Phys. Chem. Chem. Phys.* **2014**, *16*, 8751–8760.

(26) Kavan, L.; Grätzel, M.; Gilbert, S. E.; Klemenz, C.; Scheel, H. J. *J. Am. Chem. Soc.* **1996**, *118*, 6716–6723.

(27) Hodes, G. *J. Phys. Chem. Lett.* **2012**, *3*, 1208–1213.

(28) Varghese, O. K.; Grimes, C. A. *Sol. Energy Mater. Sol. Cells* **2008**, *92*, 374–384.

(29) Chen, Z.; Jaramillo, T. F.; Deutsch, T. G.; Kleiman-Shwarsctein, A.; Forman, A. J.; Gaillard, N.; Garland, R.; Takanabe, K.; Heske, C.; Sunkara, M.; McFarland, E. W.; Domen, K.; Miller, E. L.; Turner, J. A.; Dinh, H. N. *J. Mater. Res.* **2010**, *25*, 3–16.

(30) Chen, Z.; Dinh, H.; Miller, E., *Photoelectrochemical Water Splitting: Standards, Experimental Methods, and Protocols*; Springer Science & Business Media: 2013.

(31) Li, J.; Wu, N. *Catal. Sci. Technol.* **2015**, *5*, 1360–1384.

(32) Mavroides, J. G.; Kafalas, J. A.; Kolesar, D. F. *Appl. Phys. Lett.* **1976**, *28*, 241–243.

(33) Ellis, A. B.; Kaiser, S. W.; Wrighton, M. S. *J. Phys. Chem.* **1976**, *80*, 1325–1328.

(34) Paracchino, A.; Laporte, V.; Sivula, K.; Grätzel, M.; Thimsen, E. *Nat. Mater.* **2011**, *10*, 456–461.

(35) Sivula, K.; van de Krol, R. *Nat. Rev. Mater.* **2016**, *1*, 15010.

(36) Benck, J. D.; Pinaud, B. A.; Gorlin, Y.; Jaramillo, T. F. *PLOS One* **2014**, *9*, e107942.

(37) Peter, L. M. In *Photoelectrochemical Solar Fuel Production*, Giménez, S., Bisquert, J., Eds.; Springer: 2016, pp 3–40.

(38) Albery, W. J.; Bartlett, P. N. *J. Electrochem. Soc.* **1984**, *131*, 315–325.

(39) Goossens, A. *J. Electrochem. Soc.* **1996**, *143*, L131–L133.

(40) Meinhold, G. *Earth-Sci. Rev.* **2010**, *102*, 1–28.

(41) Diebold, U. *Surf. Sci. Rep.* **2003**, *48*, 53–229.

(42) *WWW-MINCRYST - Cristallographic database for minerals*, `http://database.iem.ac.ru/mincryst/` (accessed 06/23/2017).

(43) Ranade, M. R.; Navrotsky, A.; Zhang, H. Z.; Banfield, J. F.; Elder, S. H.; Zaban, A.; Borse, P. H.; Kulkarni, S. K.; Doran, G. S.; Whitfield, H. J. *Proc. Natl. Acad. Sci. USA* **2002**, *99*, 6476–6481.

(44) Hanaor, D. A. H.; Sorrell, C. C. *J. Mater. Sci.* **2011**, *46*, 855–874.

(45) Ohsaka, T.; Izumi, F.; Fujiki, Y. *J. Raman Spectrosc.* **1978**, *7*, 321–324.

(46) Balachandran, U.; Eror, N. G. *J. Solid State Chem.* **1982**, *42*, 276–282.

(47) Porto, S. P. S.; Fleury, P. A.; Damen, T. C. *Phys. Rev.* **1967**, *154*, 522–526.

(48) Tompsett, G. A.; Bowmaker, G. A.; Cooney, R. P.; Metson, J. B.; Rodgers, K. A.; Seakins, J. M. *J. Raman Spectrosc.* **1995**, *26*, 57–62.

(49) Li Bassi, A.; Cattaneo, D.; Russo, V.; Bottani, C. E.; Barborini, E.; Mazza, T.; Piseri, P.; Milani, P.; Ernst, F. O.; Wegner, K.; Pratsinis, S. E. *J. Appl. Phys.* **2005**, *98*, 074305.

(50) Zhang, W. F.; He, Y. L.; Zhang, M. S.; Yin, Z.; Chen, Q. *J. Phys. D: Appl. Phys.* **2000**, *33*, 912.

(51) Mazzolini, P.; Russo, V.; Casari, C. S.; Hitosugi, T.; Nakao, S.; Hasegawa, T.; Li Bassi, A. *J. Phys. Chem. C* **2016**, *120*, 18878–18886.

(52) Parker, J. C.; Siegel, R. W. *Appl. Phys. Lett.* **1990**, *57*, 943–945.

(53) Spurr, R. A.; Myers, H. *Anal. Chem.* **1957**, *29*, 760–762.

(54) *Database of Raman spectroscopy, X-ray diffraction and chemistry of minerals*, `http://rruff.info/` (accessed 05/31/2017).

(55) Asahi, R.; Taga, Y.; Mannstadt, W.; Freeman, A. J. *Phys. Rev. B* **2000**, *61*, 7459–7465.

(56) Landmann, M.; Rauls, E.; Schmidt, W. G. *J. Phys.: Condens. Matter* **2012**, *24*, 195503.

(57) Tang, H.; Prasad, K.; Sanjinès, R.; Schmid, P. E.; Lévy, F. *J. Appl. Phys.* **1994**, *75*, 2042–2047.

(58) Cronemeyer, D. C. *Phys. Rev.* **1952**, *87*, 876–886.

(59) Koelsch, M; Cassaignon, S; Guillemoles, J. F; Jolivet, J. P *Thin Solid Films* **2002**, *403*, 312–319.

(60) Fujishima, A.; Zhang, X.; Tryk, D. A. *Surf. Sci. Rep.* **2008**, *63*, 515–582.

(61) Schneider, J.; Matsuoka, M.; Takeuchi, M.; Zhang, J.; Horiuchi, Y.; Anpo, M.; Bahnemann, D. W. *Chem. Rev.* **2014**, *114*, 9919–9986.

(62) Etacheri, V.; Di Valentin, C.; Schneider, J.; Bahnemann, D.; Pillai, S. C. *J. Photochem. Photobiol. C* **2015**, *25*, 1–29.

(63) Di Valentin, C.; Selloni, A. *J. Phys. Chem. Lett.* **2011**, *2*, 2223–2228.

(64) Zawadzki, P.; Laursen, A. B.; Jacobsen, K. W.; Dahl, S.; Rossmeisl, J. *Energy Environ. Sci.* **2012**, *5*, 9866–9869.

(65) Yamakata, A.; Ishibashi, T.-a.; Onishi, H. *J. Phys. Chem. B* **2001**, *105*, 7258–7262.

(66) Tang, J.; Durrant, J. R.; Klug, D. R. *J. Am. Chem. Soc.* **2008**, *130*, 13885–13891.

(67) Nakamura, R.; Nakato, Y. *J. Am. Chem. Soc.* **2004**, *126*, 1290–1298.

(68) Nakamura, R.; Okamura, T.; Ohashi, N.; Imanishi, A.; Nakato, Y. *J. Am. Chem. Soc.* **2005**, *127*, 12975–12983.

(69) Imanishi, A.; Okamura, T.; Ohashi, N.; Nakamura, R.; Nakato, Y. *J. Am. Chem. Soc.* **2007**, *129*, 11569–11578.

(70) Chen, H. M.; Chen, C. K.; Liu, R.-S.; Zhang, L.; Zhang, J.; Wilkinson, D. P. *Chem. Soc. Rev.* **2012**, *41*, 5654–5671.

(71) Chen, X.; Shen, S.; Guo, L.; Mao, S. S. *Chem. Rev.* **2010**, *110*, 6503–6570.

(72) Anpo, M.; Takeuchi, M. *J. Catal.* **2003**, *216*, 505–516.

(73) Umebayashi, T.; Yamaki, T.; Itoh, H.; Asai, K. *J. Phys. Chem. Solids* **2002**, *63*, 1909–1920.

(74) Chen, X.; Burda, C. *J. Am. Chem. Soc.* **2008**, *130*, 5018–5019.

(75) Asahi, R.; Morikawa, T.; Ohwaki, T.; Aoki, K.; Taga, Y. *Science* **2001**, *293*, 269–271.

(76) Asahi, R.; Morikawa, T.; Irie, H.; Ohwaki, T. *Chem. Rev.* **2014**, *114*, 9824–9852.

(77) Liu, G.; Yin, L.-C.; Wang, J.; Niu, P.; Zhen, C.; Xie, Y.; Cheng, H.-M. *Energy Environ. Sci.* **2012**, *5*, 9603–9610.

(78) Chen, X.; Liu, L.; Huang, F. *Chem. Soc. Rev.* **2015**, *44*, 1861–1885.

(79) Liu, X.; Zhu, G.; Wang, X.; Yuan, X.; Lin, T.; Huang, F. *Adv. Energy Mater.* **2016**, *6*, 1600452.

(80) *Black TiO_2 Nanomaterials for Energy Applications*; Chen, X., Cui, Y., Eds.; World Scientific: 2016, 330 pp.

(81) Cronemeyer, D. C.; Gilleo, M. A. *Phys. Rev.* **1951**, *82*, 975–976.

(82) Cronemeyer, D. C. *Phys. Rev.* **1959**, *113*, 1222–1226.

(83) Chen, X.; Liu, L.; Yu, P. Y.; Mao, S. S. *Science* **2011**, *331*, 746–750.

(84) Wang, G.; Wang, H.; Ling, Y.; Tang, Y.; Yang, X.; Fitzmorris, R. C.; Wang, C.; Zhang, J. Z.; Li, Y. *Nano Lett.* **2011**, *11*, 3026–3033.

(85) Liu, N.; Schneider, C.; Freitag, D.; Hartmann, M.; Venkatesan, U.; Müller, J.; Spiecker, E.; Schmuki, P. *Nano Lett.* **2014**, *14*, 3309–3313.

(86) Gurylev, V.; Su, C.-Y.; Perng, T.-P. *J. Catal.* **2015**, *330*, 177–186.

(87) Pesci, F. M.; Wang, G.; Klug, D. R.; Li, Y.; Cowan, A. J. *J. Phys. Chem. C* **2013**, *117*, 25837–25844.

(88) Yang, Y.; Ling, Y.; Wang, G.; Li, Y. *Eur. J. Inorg. Chem.* **2014**, *2014*, 760–766.

(89) Zhou, W.; Li, W.; Wang, J.-Q.; Qu, Y.; Yang, Y.; Xie, Y.; Zhang, K.; Wang, L.; Fu, H.; Zhao, D. *J. Am. Chem. Soc.* **2014**, *136*, 9280–9283.

(90) Hoang, S.; Berglund, S. P.; Hahn, N. T.; Bard, A. J.; Mullins, C. B. *J. Am. Chem. Soc.* **2012**, *134*, 3659–3662.

(91) Zhang, S.; Zhang, S.; Peng, B.; Wang, H.; Yu, H.; Wang, H.; Peng, F. *Electrochem. Commun.* **2014**, *40*, 24–27.

(92) Wang, D.; Zhang, X.; Sun, P.; Lu, S.; Wang, L.; Wang, C.; Liu, Y. *Electrochim. Acta* **2014**, *130*, 290–295.

(93) Wang, C.-C.; Chou, P.-H. *Nanotechnology* **2016**, *27*, 325401.

(94) Wang, X.; Zhang, S.; Xie, Y.; Wang, H.; Yu, H.; Shen, Y.; Li, Z.; Zhang, S.; Peng, F. *Int. J. Hydrogen Energ.* **2016**, *41*, 20192–20197.

(95) Mohajernia, S.; Hejazi, S.; Mazare, A.; Nguyen, N. T.; Schmuki, P. *Chem. Eur. J.* **2017**, *23*, 12406–12411.

(96) Cai, J.; Wu, M.; Wang, Y.; Zhang, H.; Meng, M.; Tian, Y.; Li, X.; Zhang, J.; Zheng, L.; Gong, J. *Chem* **2017**, *2*, 877–892.

(97) Chen, B.; Beach, J. A.; Maurya, D.; Moore, R. B.; Priya, S. *RSC Adv.* **2014**, *4*, 29443–29449.

(98) Liu, N.; Schneider, C.; Freitag, D.; Zolnhofer, E. M.; Meyer, K.; Schmuki, P. *Chem. Eur. J.* **2016**, *22*, 13810–13814.

(99) Xu, C.; Song, Y.; Lu, L.; Cheng, C.; Liu, D.; Fang, X.; Chen, X.; Zhu, X.; Li, D. *Nanoscale Res. Lett.* **2013**, *8*, 391.

(100) Chen, H.; Wei, Z.; Yan, K.; Bai, Y.; Yang, S. *J. Phys. Chem. Lett.* **2014**, *5*, 2890–2896.

(101) Cui, H.; Zhao, W.; Yang, C.; Yin, H.; Lin, T.; Shan, Y.; Xie, Y.; Gu, H.; Huang, F. *J. Mater. Chem. A* **2014**, *2*, 8612–8616.

(102) Shen, S.; Mao, S. S. *Nanophotonics* **2012**, *1*, 31–50.

(103) Linic, S.; Christopher, P.; Ingram, D. B. *Nat. Mater.* **2011**, *10*, 911–921.

(104) Warren, S. C.; Thimsen, E. *Energy Environ. Sci.* **2012**, *5*, 5133–5146.

(105) Zhang, X.; Chen, Y. L.; Liu, R.-S.; Tsai, D. P. *Rep. Prog. Phys.* **2013**, *76*, 046401.

(106) Kreibig, U.; Vollmer, M., *Optical properties of metal clusters*; Springer Series in Material Science, Vol. 25; Springer: 1995; 568 pp.

(107) Maier, S. A., *Plasmonics: Fundamentals and Applications*; Springer Science & Business Media: 2007; 234 pp.

(108) Jain, P. K.; Lee, K. S.; El-Sayed, I. H.; El-Sayed, M. A. *J. Phys. Chem. B* **2006**, *110*, 7238–7248.

(109) Atwater, H. A.; Polman, A. *Nat. Mater.* **2010**, *9*, 205–213.

(110) Zhang, P.; Wang, T.; Gong, J. *Adv. Mater.* **2015**, *27*, 5328–5342.

(111) Naldoni, A.; Riboni, F.; Guler, U.; Boltasseva, A.; Shalaev, V. M.; Kildishev, A. V. *Nanophotonics* **2016**, *5*, 112–133.

(112) Marchuk, K.; Willets, K. A. *Chem. Phys.* **2014**, *445*, 95–104.

(113) Govorov, A. O.; Zhang, H.; Gun'ko, Y. K. *J. Phys. Chem. C* **2013**, *117*, 16616–16631.

(114) Tian, Y.; Tatsuma, T. *J. Am. Chem. Soc.* **2005**, *127*, 7632–7637.

(115) Gomes Silva, C.; Juárez, R.; Marino, T.; Molinari, R.; García, H. *J. Am. Chem. Soc.* **2011**, *133*, 595–602.

(116) Lee, J.; Mubeen, S.; Ji, X.; Stucky, G. D.; Moskovits, M. *Nano Lett.* **2012**, *12*, 5014–5019.

(117) Mubeen, S.; Lee, J.; Singh, N.; Krämer, S.; Stucky, G. D.; Moskovits, M. *Nat. Nano.* **2013**, *8*, 247–251.

(118) Su, F.; Wang, T.; Lv, R.; Zhang, J.; Zhang, P.; Lu, J.; Gong, J. *Nanoscale* **2013**, *5*, 9001–9009.

(119) DuChene, J. S.; Sweeny, B. C.; Johnston-Peck, A. C.; Su, D.; Stach, E. A.; Wei, W. D. *Angew. Chem. Int. Ed.* **2014**, *53*, 7887–7891.

(120) Li, J.; Cushing, S. K.; Meng, F.; Senty, T. R.; Bristow, A. D.; Wu, N. *Nat. Photon.* **2015**, *9*, 601–607.

(121) Cushing, S. K.; Li, J.; Meng, F.; Senty, T. R.; Suri, S.; Zhi, M.; Li, M.; Bristow, A. D.; Wu, N. *J. Am. Chem. Soc.* **2012**, *134*, 15033–15041.

(122) Ingram, D. B.; Linic, S. *J. Am. Chem. Soc.* **2011**, *133*, 5202–5205.

(123) Liu, Z.; Hou, W.; Pavaskar, P.; Aykol, M.; Cronin, S. B. *Nano Lett.* **2011**, *11*, 1111–1116.

(124) Pu, Y.-C.; Wang, G.; Chang, K.-D.; Ling, Y.; Lin, Y.-K.; Fitzmorris, B. C.; Liu, C.-M.; Lu, X.; Tong, Y.; Zhang, J. Z.; Hsu, Y.-J.; Li, Y. *Nano Lett.* **2013**, *13*, 3817–3823.

(125) Eftekhari, A.; Babu, V. J.; Ramakrishna, S. *Int. J. Hydrogen Energ.* **2017**, *42*, 11078–11109.

(126) Pan, J.; Liu, G.; Lu, G. Q. M.; Cheng, H.-M. *Angew. Chem. Int. Ed.* **2011**, *50*, 2133–2137.

(127) Paulose, M.; Shankar, K.; Yoriya, S.; Prakasam, H. E.; Varghese, O. K.; Mor, G. K.; Latempa, T. A.; Fitzgerald, A.; Grimes, C. A. *J. Phys. Chem. B* **2006**, *110*, 16179–16184.

(128) Roy, P.; Berger, S.; Schmuki, P. *Angew. Chem. Int. Ed.* **2011**, *50*, 2904–2939.

(129) Riboni, F.; Truong Nguyen, N.; So, S.; Schmuki, P. *Nanoscale Horiz.* **2016**, *1*, 445–466.

(130) Kharisov, B. I.; Kharissova, O. V.; García, B. O.; Méndez, Y. P.; de la Fuente, I. G. *RSC Adv.* **2015**, *5*, 105507–105523.

(131) Casari, C. S.; Li Bassi, A. In *Advances in Laser and Optics Research. Volume 7*, Arkin, W. T., Ed.; Nova Science Publishers: 2011, pp 65–100.

(132) Divitini, G.; Stenzel, O.; Ghadirzadeh, A.; Guarnera, S.; Russo, V.; Casari, C. S.; Li Bassi, A.; Petrozza, A.; Di Fonzo, F.; Schmidt, V.; Ducati, C. *Adv. Funct. Mater.* **2014**, *24*, 3043–3050.

(133) Di Fonzo, F.; Casari, C. S.; Russo, V.; Brunella, M. F.; Li Bassi, A.; Bottani, C. E. *Nanotechnology* **2009**, *20*, 015604.

(134) Fusi, M.; Russo, V.; Casari, C. S.; Li Bassi, A.; Bottani, C. E. *Appl. Surf. Sci.* **2009**, *255*, 5334–5337.

(135) Sauvage, F.; Di Fonzo, F.; Li Bassi, A.; Casari, C. S.; Russo, V.; Divitini, G.; Ducati, C.; Bottani, C. E.; Comte, P.; Grätzel, M. *Nano Lett.* **2010**, *10*, 2562–2567.

(136) Fusi, M.; Maccallini, E.; Caruso, T.; Casari, C. S.; Li Bassi, A.; Bottani, C. E.; Rudolf, P.; Prince, K. C.; Agostino, R. G. *Surf. Sci.* **2011**, *605*, 333–340.

(137) Matarrese, R.; Nova, I.; Li Bassi, A. L.; Casari, C. S.; Russo, V. *Chem. Eng. Trans.* **2014**, *41*, 313–318.

(138) Matarrese, R.; Nova, I.; Li Bassi, A.; Casari, C. S.; Russo, V.; Palmas, S. *J. Solid State Electrochem.* **2017**, 1–16.

(139) Ghosh, R.; Hara, Y.; Alibabaei, L.; Hanson, K.; Rangan, S.; Bartynski, R.; Meyer, T. J.; Lopez, R. *ACS Appl. Mater. Interfaces* **2012**, *4*, 4566–4570.

(140) Noh, J. H.; Park, J. H.; Han, H. S.; Kim, D. H.; Han, B. S.; Lee, S.; Kim, J. Y.; Jung, H. S.; Hong, K. S. *J. Phys. Chem. C* **2012**, *116*, 8102–8110.

(141) Passoni, L.; Ghods, F.; Docampo, P.; Abrusci, A.; Martí-Rujas, J.; Ghidelli, M.; Divitini, G.; Ducati, C.; Binda, M.; Guarnera, S.; Li Bassi, A.; Casari, C. S.; Snaith, H. J.; Petrozza, A.; Di Fonzo, F. *ACS Nano* **2013**, *7*, 10023–10031.

(142) Passoni, L.; Giordano, F.; Zakeeruddin, S. M.; Grätzel, M.; Fonzo, F. D. *RSC Adv.* **2015**, *5*, 93180–93186.

(143) Nowotny, J.; Bak, T.; Nowotny, M. K.; Sheppard, L. R. *Int. J. Hydrogen Energ.* **2007**, *32*, 2630–2643.

(144) Koch, D.; Manzhos, S. *J. Phys. Chem. Lett.* **2017**, *8*, 1593–1598.

(145) Walsh, A.; Sokol, A. A.; Buckeridge, J.; Scanlon, D. O.; Catlow, C. R. A. *J. Phys. Chem. Lett.* **2017**, *8*, 2074–2075.

(146) Koch, D.; Manzhos, S. *J. Phys. Chem. Lett.* **2017**, *8*, 3945–3946.

(147) Kröger, F. A.; Vink, H. J. In *Solid State Physics*, Seitz, F., Turnbull, D., Eds., Supplement C vols.; Academic Press: 1956; Vol. 3, pp 307–435.

(148) Pan, X.; Yang, M.-Q.; Fu, X.; Zhang, N.; Xu, Y.-J. *Nanoscale* **2013**, *5*, 3601–3614.

(149) Nowotny, J.; Alim, M. A.; Bak, T.; Idris, M. A.; Ionescu, M.; Prince, K.; Sahdan, M. Z.; Sopian, K.; Teridi, M. A. M.; Sigmund, W. *Chem. Soc. Rev.* **2015**, *44*, 8424–8442.

(150) Serpone, N.; Lawless, D.; Khairutdinov, R. *J. Phys. Chem.* **1995**, *99*, 16646–16654.

(151) Hoffmann, M. R.; Martin, S. T.; Choi, W.; Bahnemann, D. W. *Chem. Rev.* **1995**, *95*, 69–96.

(152) Di Valentin, C.; Pacchioni, G.; Selloni, A. *J. Phys. Chem. C* **2009**, *113*, 20543–20552.

(153) Cheng, H.; Selloni, A. *Phys. Rev. B* **2009**, *79*, 092101.

(154) Mattioli, G.; Alippi, P.; Filippone, F.; Caminiti, R.; Amore Bonapasta, A. *J. Phys. Chem. C* **2010**, *114*, 21694–21704.

(155) Deák, P.; Aradi, B.; Frauenheim, T. *Phys. Rev. B* **2012**, *86*, 195206.

(156) Gerosa, M.; Bottani, C. E.; Caramella, L.; Onida, G.; Di Valentin, C.; Pacchioni, G. *J. Chem. Phys.* **2015**, *143*, 134702.

(157) De Angelis, F.; Di Valentin, C.; Fantacci, S.; Vittadini, A.; Selloni, A. *Chem. Rev.* **2014**, *114*, 9708–9753.

(158) Schaub, R.; Thostrup, P.; Lopez, N.; Lægsgaard, E.; Stensgaard, I.; Nørskov, J. K.; Besenbacher, F. *Phys. Rev. Lett.* **2001**, *87*, 266104.

(159) Bikondoa, O.; Pang, C. L.; Ithnin, R.; Muryn, C. A.; Onishi, H.; Thornton, G. *Nat. Mater.* **2006**, *5*, 189–192.

(160) Nakamura, I.; Negishi, N.; Kutsuna, S.; Ihara, T.; Sugihara, S.; Takeuchi, K. *J. Mol. Catal. A Chem.* **2000**, *161*, 205–212.

(161) Liu, H.; Ma, H. T.; Li, X. Z.; Li, W. Z.; Wu, M.; Bao, X. H. *Chemosphere* **2003**, *50*, 39–46.

(162) Naldoni, A.; Allieta, M.; Santangelo, S.; Marelli, M.; Fabbri, F.; Cappelli, S.; Bianchi, C. L.; Psaro, R.; Dal Santo, V. *J. Am. Chem. Soc.* **2012**, *134*, 7600–7603.

(163) Liu, L.; Yu, P. Y.; Chen, X.; Mao, S. S.; Shen, D. Z. *Phys. Rev. Lett.* **2013**, *111*, 065505.

(164) Chen, X.; Liu, L.; Liu, Z.; Marcus, M. A.; Wang, W.-C.; Oyler, N. A.; Grass, M. E.; Mao, B.; Glans, P.-A.; Yu, P. Y.; Guo, J.; Mao, S. S. *Sci. Rep.* **2013**, *3*, DOI: `10.1038/srep01510`.

(165) Liu, N.; Häublein, V.; Zhou, X.; Venkatesan, U.; Hartmann, M.; Mačković, M.; Nakajima, T.; Spiecker, E.; Osvet, A.; Frey, L.; Schmuki, P. *Nano Lett.* **2015**, *15*, 6815–6820.

(166) Xia, T.; Zhang, Y.; Murowchick, J.; Chen, X. *Catal. Today* **2014**, *225*, 2–9.

(167) Gondoni, P.; Mazzolini, P.; Russo, V.; Diani, M.; Amati, M.; Gregoratti, L.; De Renzi, V.; Gazzadi, G. C.; Martí-Rujas, J.; Li Bassi, A.; Casari, C. S. *Thin Solid Films* **2015**, *594*, 12–17.

(168) Ferrulli, S. "Hydrogen treated Titania for photoelectrochemical (PEC) water splitting", Master thesis, Politecnico di Milano, 2015.

(169) Bricchi, B. R. "Integration of gold nanoparticles in hierarchical titania nanostructures for photoelectrochemical water splitting", Master thesis, Politecnico di Milano, 2017.

(170) *Pulsed Laser Deposition of Thin Films*; Chrisey, D. B., Hubler, G. K., Eds.; Wiley: 1994, 648 pp.

(171) *Pulsed Laser Deposition of Thin Films: Applications-Led Growth of Functional Materials*; Eason, R., Ed.; John Wiley & Sons: 2007.

(172) Amoruso, S.; Toftmann, B.; Schou, J. *Phys. Rev. E* **2004**, *69*, 056403.

(173) Geohegan, D. B.; Puretzky, A. A.; Duscher, G.; Pennycook, S. J. *Appl. Phys. Lett.* **1998**, *72*, 2987–2989.

(174) Schou, J. *Appl. Surf. Sci.* **2009**, *255*, 5191–5198.

(175) Brüesch, P., *Phonons: Theory and Experiments II: Experiments and Interpretation of Experimental Results*; Springer Series in Solid-State Sciences, Vol. 65; Springer Science & Business Media: 1986.

(176) Gfroerer, T. H. In *Encyclopedia of Analytical Chemistry*, Meyers, R. A., Ed., DOI:10.1002/9780470027318.a2510; John Wiley & Sons, Ltd: 2006, pp 9209–9231.

(177) Bergman, L.; McHale, J. L., *Handbook of Luminescent Semiconductor Materials*; CRC Press: 2012; 460 pp.

(178) Scherrer, P. *Göttinger Nachrichten Math. Phys.* **1918**, *2*, 98–100.

(179) Tauc, J.; Grigorovici, R.; Vancu, A. *Phys. Status Solidi B* **1966**, *15*, 627–637.

(180) Buchholz, D. B.; Liu, J.; Marks, T. J.; Zhang, M.; Chang, R. P. H. *ACS Appl. Mater. Interfaces* **2009**, *1*, 2147–2153.

(181) Mascaretti, L.; Ferrulli, S.; Mazzolini, P.; Casari, C. S.; Russo, V.; Matarrese, R.; Nova, I.; Terraneo, G.; Liu, N.; Schmuki, P.; Li Bassi, A. *Sol. Energy Mater. Sol. Cells* **2017**, *169*, 19–27.

(182) Bailini, A.; Di Fonzo, F.; Fusi, M.; Casari, C. S.; Li Bassi, A.; Russo, V.; Baserga, A.; Bottani, C. E. *Appl. Surf. Sci* **2007**, *253*, 8130–8135.

(183) Frank, O.; Zukalova, M.; Laskova, B.; Kürti, J.; Koltai, J.; Kavan, L. *Phys. Chem. Chem. Phys.* **2012**, *14*, 14567–14572.

(184) McHale, J. L.; Knorr, F. J. In *Handbook of Luminescent Semiconductor Materials*, DOI:10.1201/b11201-14; CRC Press: 2011, pp 365–390.

(185) Zhou, B.; Schulz, M.; Lin, H. Y.; Shah, S. I.; Qu, J.; Huang, C. P. *Appl. Catal. B-Environ.* **2009**, *92*, 41–49.

(186) Cowan, A. J.; Tang, J.; Leng, W.; Durrant, J. R.; Klug, D. R. *J. Phys. Chem. C* **2010**, *114*, 4208–4214.

(187) Spadavecchia, F.; Ardizzone, S.; Cappelletti, G.; Falciola, L.; Ceotto, M.; Lotti, D. *J. Appl. Electrochem.* **2013**, *43*, 217–225.

(188) Song, X.-M.; Wu, J.-M.; Tang, M.-Z.; Qi, B.; Yan, M. *J. Phys. Chem. C* **2008**, *112*, 19484–19492.

(189) Xu, Z.; Yu, J. *Nanoscale* **2011**, *3*, 3138–3144.

(190) Zhang, K.; Shi, X.-J.; Kim, J. K.; Park, J. H. *Phys. Chem. Chem. Phys.* **2012**, *14*, 11119–11124.

(191) Lu, Z.; Yip, C.-T.; Wang, L.; Huang, H.; Zhou, L. *ChemPlusChem* **2012**, *77*, 991–1000.

(192) Mascaretti, L.; Matarrese, R.; Ravanelli, A.; Isacchi, M.; Mazzolini, P.; Casari, C. S.; Russo, V.; Nova, I.; Terraneo, G.; Ducati, C.; Li Bassi, A. *Int. J. Hydrogen Energ.* **2017**, *42*, 26639–26651.

(193) Long, H.; Yang, G.; Chen, A.; Li, Y.; Lu, P. *Thin Solid Films* **2008**, *517*, 745–749.

(194) Mazzolini, P.; Gondoni, P.; Russo, V.; Chrastina, D.; Casari, C. S.; Li Bassi, A. *J. Phys. Chem. C* **2015**, *119*, 6988–6997.

(195) Mazzolini, P.; Acartürk, T.; Chrastina, D.; Starke, U.; Casari, C. S.; Gregori, G.; Li Bassi, A. *Adv. Electron. Mater.* **2016**, *2*, 1500316.

(196) Guillemot, F; Porté, M. C; Labrugère, C; Baquey, C. *J. Colloid Interface Sci.* **2002**, *255*, 75–78.

(197) Iliev, M. N.; Hadjiev, V. G.; Litvinchuk, A. P. *Vib. Spectrosc.* **2013**, *64*, 148–152.

(198) Tian, M.; Mahjouri-Samani, M.; Eres, G.; Sachan, R.; Yoon, M.; Chisholm, M. F.; Wang, K.; Puretzky, A. A.; Rouleau, C. M.; Geohegan, D. B.; Duscher, G. *ACS Nano* **2015**, *9*, 10482–10488.

(199) Larsen, J. K.; Li, S.-Y.; Scragg, J. J. S.; Ren, Y.; Hägglund, C.; Heinemann, M. D.; Kretzschmar, S.; Unold, T.; Platzer-Björkman, C. *J. Appl. Phys.* **2015**, *118*, 035307.

(200) Tajima, M.; Ogura, A.; Karasawa, T.; Mizoguchi, A. *Jpn. J. Appl. Phys.* **1998**, *37*, L1199.

(201) Tang, H.; Berger, H.; Schmid, P. E.; Lévy, F.; Burri, G. *Solid State Commun.* **1993**, *87*, 847–850.

(202) Sekiya, T.; Kamei, S.; Kurita, S. *J. Lumin.* **2000**, *87*, 1140–1142.

(203) Zhang, W. F.; Zhang, M. S.; Yin, Z.; Chen, Q. *Appl. Phys. B* **2000**, *70*, 261–265.

(204) Shi, J.; Chen, J.; Feng, Z.; Chen, T.; Lian, Y.; Wang, X.; Li, C. *J. Phys. Chem. C* **2007**, *111*, 693–699.

(205) Cavigli, L.; Bogani, F.; Vinattieri, A.; Faso, V.; Baldi, G. *J. Appl. Phys.* **2009**, *106*, 053516.

(206) Preclíková, J.; Galář, P.; Trojánek, F.; Daniš, S.; Rezek, B.; Gregora, I.; Němcová, Y.; Malý, P. *J. Appl. Phys.* **2010**, *108*, 113502.

(207) Knorr, F. J.; Zhang, D.; McHale, J. L. *Langmuir* **2007**, *23*, 8686–8690.

(208) Knorr, F. J.; Mercado, C. C.; McHale, J. L. *J. Phys. Chem. C* **2008**, *112*, 12786–12794.

(209) Mercado, C.; Seeley, Z.; Bandyopadhyay, A.; Bose, S.; McHale, J. L. *ACS Appl. Mater. Interfaces* **2011**, *3*, 2281–2288.

(210) Mercado, C. C.; Knorr, F. J.; McHale, J. L.; Usmani, S. M.; Ichimura, A. S.; Saraf, L. V. *J. Phys. Chem. C* **2012**, *116*, 10796–10804.

(211) Knorr, F. J.; McHale, J. L. *J. Phys. Chem. C* **2013**, *117*, 13654–13662.

(212) Rex, R. E.; Knorr, F. J.; McHale, J. L. *J. Phys. Chem. C* **2014**, *118*, 16831–16841.

(213) Tang, H.; Lévy, F.; Berger, H.; Schmid, P. E. *Phys. Rev. B* **1995**, *52*, 7771–7774.

(214) Stevanovic, A.; Büttner, M.; Zhang, Z.; Yates, J. T. *J. Am. Chem. Soc.* **2012**, *134*, 324–332.

(215) Stevanovic, A.; Yates, J. T. *J. Phys. Chem. C* **2013**, *117*, 24189–24195.

(216) Ma, S.; Reish, M. E.; Zhang, Z.; Harrison, I.; Yates, J. T. *J. Phys. Chem. C* **2017**, *121*, 1263–1271.

(217) Pallotti, D. K.; Orabona, E.; Amoruso, S.; Bruzzese, R.; Chiarella, F.; Tuzi, S.; Maddalena, P.; Lettieri, S. *J. Appl. Phys.* **2013**, *114*, 043503.

(218) Pallotti, D. K.; Passoni, L.; Maddalena, P.; Di Fonzo, F.; Lettieri, S. *J. Phys. Chem. C* **2017**, *121*, 9011–9021.

(219) Rex, R. E.; Yang, Y.; Knorr, F. J.; Zhang, J. Z.; Li, Y.; McHale, J. L. *J. Phys. Chem. C* **2016**, *120*, 3530–3541.

(220) Rex, R. E.; Knorr, F. J.; McHale, J. L. *J. Phys. Chem. C* **2013**, *117*, 7949–7951.

(221) Yan, Y.; Han, M.; Konkin, A.; Koppe, T.; Wang, D.; Andreu, T.; Chen, G.; Vetter, U.; Morante, J. R.; Schaaf, P. *J. Mater. Chem. A* **2014**, *2*, 12708–12716.

(222) Liu, N.; Schneider, C.; Freitag, D.; Venkatesan, U.; Marthala, V. R. R.; Hartmann, M.; Winter, B.; Spiecker, E.; Osvet, A.; Zolnhofer, E. M.; Meyer, K.; Nakajima, T.; Zhou, X.; Schmuki, P. *Angew. Chem.* **2014**, *126*, 14425–14429.

(223) Šćepanović, M.; Dohčević-Mitrović, Z.; Hinić, I.; Grujić-Brojčin, M.; Stanišić, G.; Popović, Z. V. *Mater. Sci. Forum* **2005**, *494*, 265–270.

(224) Levard, C.; Hotze, E. M.; Lowry, G. V.; Brown, G. E. *Environ. Sci. Technol.* **2012**, *46*, 6900–6914.

(225) You, H.; Yang, S.; Ding, B.; Yang, H. *Chem. Soc. Rev.* **2013**, *42*, 2880–2904.

(226) Mubeen, S.; Hernandez-Sosa, G.; Moses, D.; Lee, J.; Moskovits, M. *Nano Lett.* **2011**, *11*, 5548–5552.

(227) Kim, H.; Choi, C.; Khamwannah, J.; Noh, S. Y.; Zhang, Y.; Seong, T.-Y.; Jin, S. *J. Ren. Sust. Energ.* **2013**, *5*, 053104.

(228) Yoshida, T.; Watanabe, T.; Kikuchi, F.; Tabuchi, T.; Umezu, I.; Haraguchi, M. *Appl. Phys. A* **2016**, *122*, 510.

(229) Domingo, C.; Resta, V.; Sanchez-Cortes, S.; García-Ramos, J. V.; Gonzalo, J. *J. Phys. Chem. C* **2007**, *111*, 8149–8152.

(230) Agarwal, N. R.; Fazio, E.; Neri, F.; Trusso, S.; Castiglioni, C.; Lucotti, A.; Santo, N.; Ossi, P. M. *Cryst. Res. Technol.* **2011**, *46*, 836–840.

(231) Ossi, P. M.; Neri, F.; Santo, N.; Trusso, S. *Appl. Phys. A* **2011**, *104*, 829–837.

(232) Agarwal, N. R.; Neri, F.; Trusso, S.; Lucotti, A.; Ossi, P. M. *Appl. Surf. Sci.* **2012**, *258*, 9148–9152.

(233) Gonzalo, J.; Perea, A.; Babonneau, D.; Afonso, C. N.; Beer, N.; Barnes, J.-P.; Petford-Long, A. K.; Hole, D. E.; Townsend, P. D. *Phys. Rev. B* **2005**, *71*, 125420.

(234) Agarwal, N. R.; Neri, F.; Trusso, S.; Ossi, P. M. *Plasmonics* **2013**, *8*, 1707–1712.

(235) Donnelly, T.; Krishnamurthy, S.; Carney, K.; McEvoy, N.; Lunney, J. G. *Appl. Surf. Sci.* **2007**, *254*, 1303–1306.

(236) Verma, S.; Tirumala Rao, B.; Rai, S.; Ganesan, V.; Kukreja, L. M. *Appl. Surf. Sci.* **2012**, *258*, 4898–4905.

(237) Kukreja, L. M.; Verma, S.; Pathrose, D. A.; Rao, B. T. *J. Phys. D: Appl. Phys.* **2014**, *47*, 034015.

(238) Wood, R. F.; Leboeuf, J. N.; Chen, K. R.; Geohegan, D. B.; Puretzky, A. A. *Appl. Surf. Sci.* **1998**, *127-129*, 151–158.

(239) Cushing, B. L.; Kolesnichenko, V. L.; O'Connor, C. J. *Chem. Rev.* **2004**, *104*, 3893–3946.

(240) Ito, A.; Masumoto, H.; Goto, T. *Mater. Trans.* **2003**, *44*, 1599–1603.

(241) Yoshida, T.; Watanabe, T.; Kikuchi, F.; Tabuchi, T.; Umezu, I.; Haraguchi, M. *Applied Physics A* **2016**, *122*, 510.

(242) Resta, V.; Afonso, C. N.; Piscopiello, E.; Van Tendeloo, G. *Phys. Rev. B* **2009**, *79*, 235409.

(243) Christensen, N. E.; Seraphin, B. O. *Phys. Rev. B* **1971**, *4*, 3321–3344.

(244) Rangel, T.; Kecik, D.; Trevisanutto, P. E.; Rignanese, G.-M.; Van Swygenhoven, H.; Olevano, V. *Phys. Rev. B* **2012**, *86*, 125125.

(245) Ghidelli, M.; Mascaretti, L.; Bricchi, B. R.; Zapelli, A.; Russo, V.; Casari, C. S.; Li Bassi, A. *Appl. Surf. Sci.* **2018**, *434*, 1064–1073.

(246) Govorov, A. O.; Zhang, H.; Demir, H. V.; Gun'ko, Y. K. *Nano Today* **2014**, *9*, 85–101.

(247) Gupta, G.; Tanaka, D.; Ito, Y.; Shibata, D.; Shimojo, M.; Furuya, K.; Mitsui, K.; Kajikawa, K. *Nanotechnology* **2009**, *20*, 025703.

(248) Serrano, A.; Rodríguez de la Fuente, O.; García, M. A. *J. Appl. Phys.* **2010**, *108*, 074303.

(249) Menegotto, T.; Pereira, M. B.; Correia, R. R. B.; Horowitz, F. *Appl. Opt.* **2011**, *50*, C27–C30.

(250) Tanyeli, I.; Nasser, H.; Es, F.; Bek, A.; Turan, R. *Opt. Express* **2013**, *21*, A798–A807.

(251) Afifi Afifi, T. "Fabrication and characterization of plasmonic gold nanoparticles in titanium dioxide photoanodes for photoelectrochemical water splitting", Master thesis, Politecnico di Milano, 2017.

(252) Torrell, M.; Cunha, L.; Kabir, M. R.; Cavaleiro, A.; Vasilevskiy, M. I.; Vaz, F. *Materi. Lett.* **2010**, *64*, 2624–2626.

(253) Borges, J.; Buljan, M.; Sancho-Parramon, J.; Bogdanovic-Radovic, I.; Siketic, Z.; Scherer, T.; Kübel, C.; Bernstorff, S.; Cavaleiro, A.; Vaz, F.; Rolo, A. G. *J. Nanopart. Res.* **2014**, *16*, 2790.

(254) Reymond-Laruinaz, S.; Saviot, L.; Potin, V.; Lopes, C.; Vaz, F.; Marco de Lucas, M. C. *Thin Solid Films* **2014**, *553*, 138–143.

(255) Borges, J.; Rodrigues, M. S.; Kubart, T.; Kumar, S.; Leifer, K.; Evaristo, M.; Cavaleiro, A.; Apreutesei, M.; Pereira, R. M. S.; Vasilevskiy, M. I.; Polcar, T.; Vaz, F. *Thin Solid Films* **2015**, *596*, 8–17.

(256) Rodrigues, M. S.; Costa, D.; Domingues, R. P.; Apreutesei, M.; Pedrosa, P.; Martin, N.; Correlo, V. M.; Reis, R. L.; Alves, E.; Barradas, N. P.; Sampaio, P.; Borges, J.; Vaz, F. *Appl. Surf. Sci.* **2017**, in press, DOI: `10.1016/j.apsusc.2017.09.162`.

(257) Zhang, W.; Liu, Y.; Zhou, D.; Wen, J.; Zheng, L.; Liang, W.; Yang, F. *RSC Adv.* **2016**, *6*, 48580–48588.

(258) Schottky, W. *Z. Phys.* **1939**, *113*, 367–414.

(259) Mott, N. F. *Proc. Royal Soc. A* **1939**, *171*, 27–38.

(260) Tung, R. T. *Appl. Phys. Rev.* **2014**, *1*, 011304.

(261) Zhao, G.; Kozuka, H.; Yoko, T. *Thin Solid Films* **1996**, *277*, 147–154.

(262) Thimsen, E.; Le Formal, F.; Grätzel, M.; Warren, S. C. *Nano Lett.* **2011**, *11*, 35–43.

(263) Reichert, R.; Jusys, Z.; Behm, R. J. *J. Phys. Chem. C* **2015**, *119*, 24750–24759.